EXPERIMENTAL STUDY OF SHALLOW FLOWS OVER PERMEABLE ROUGH BED

NGUYEN BA TUYEN

SCHOOL OF CIVIL AND ENVIRONMENTAL ENGINEERING

2014

Experimental Study of Shallow Flows over Permeable Rough Bed

Nguyen Ba Tuyen

School of Civil and Environmental Engineering

A Thesis submitted to the Nanyang Technological University
in fulfilment of the requirement for the degree of
Doctor of Philosophy.

2014

To my family

ACKNOWLEDGEMENTS

The author would like to express his deepest appreciation to his supervisor, Associate Professor Cheng Nian Sheng for his valuable guidance, advice, and encouragement throughout the years.

This research work was conducted in the School of Civil & Environmental Engineering, and the research scholarship awarded by Nanyang Technological University is gratefully acknowledged. The authors would like to thank MRC and DHI-NTU Centres for their valuable supports during the course of this study.

The author would also like to express his gratitude to all those who provided him the possibility to complete this study - Assoc. Prof. Tan Soon Keat for the valuable discussions and suggestions; to Mr. Foo Shiang Kim, Mr. Lim Kok Hin and other Hydraulics Laboratory staff; to his colleagues Qiao Changkai, Zhou Zingmin and Adel Emadzadeh for their assistance in experimental works.

Finally, a special thank to his family and friends for their invaluable encouragement and supports.

TABLE OF CONTENTS

SUMMARY

First of all, this research work presents a new and simple calculation for resistance coefficient and mean velocity in shallow flow over rough beds, as observed in mountain streams. An examination of the available formulations from published studies regarding this emerging research topic has revealed that currently there is no standard formula for calculating the flow quantities in a consistent and accurate manner. Using a heuristic approach, this study first justified a theoretical analysis for the derivation of a modified Manning's formula in a dimensionally consistent form. An exponential function of the roughness submergence was introduced to account for the effect of the shallowness on roughness coefficient. The new resistance equation was then calibrated by using a large compilation of existing data, from a wide variety of available sources and also this study. The proposed formula performs better than those currently available in literature particularly for estimating the resistance to flows with the roughness submergence smaller than five.

This study also presents an approach that is useful for scaling the mean velocity profiles in the outer region of turbulent open channel flows over a porous rough bed with small roughness submergence. Using the plane mixing layer analogy, this study's scaling analysis shows that the velocity profiles can be well normalised using the maximum velocity and a characteristic flow depth at which the flow velocity reduces to half of the maximum velocity. In order to validate the proposed scaling method, a series of velocity measurements were conducted for flows over a rough bed composed of layers of glass beads (with the aid of laser-based imaging techniques) and weathered gravels (with point measurement instrument). A double-averaging method was applied to gain statistics of flow velocities. Comparisons with the measurements show that the proposed scaling argument performs very well in collapsing the vertical velocity profiles, providing an effective way to represent the flow velocity profile from the

more readily observable flow parameters. Finally, an eddy viscosity model was also developed to justify the scaling argument and further validation was conducted with other datasets reported in the literature.

This study also made use of the state-of-the-art non-intrusive measurement techniques including PIV, PTV and other image processing tools to study the flow structure. Subsequent data analysis has found that the shear velocity derived from the total fluid shear stress acting at the roughness crest level could be used to scale and collapse the measurement of higher velocity moments. The turbulence intensity and Reynolds shear stress are independent of the boundary condition for $y/H_s > 0.2$. In general, the normalised turbulent intensities were found to linearly increase towards the bed and attain their peak values just above the roughness top, at a height of approximately $D/5$, where D is the roughness size. Furthermore, investigation has found that a decrease in the streamwise turbulence intensity with increasing number of roughness layers. Instantaneous visualization of shallow flows over permeable rough bed also revealed the extensive action of coherent structures in the first and fourth quadrant, i.e. the ejection and sweep events. Near the roughness element, the ejection happens more frequently, while the role of sweep events gradually takes over when moving away from the bed.

LIST OF TABLES

The following tables are used in this thesis:

LIST OF FIGURES

The following figures are used in this thesis:

LIST OF SYMBOLS

The following symbols, subscripts/superscripts and other abbreviations are used in this thesis:

Symbol	**Dimension**	**Description**
B	[m]	channel width
B/H_s	[-]	channel's aspect ratio (width-to-depth ratio)
C	[$L^{1/2}s^{-1}$]	Chézy's resistance coefficient
d	[m]	diameter of the roughness element
D_{50}	[mm]	average bed material size
D_i	[m]	particle size for which i % of the bed material is finer
D	[m]	general particle diameter (glass beads, polystyrene tracer particles)
D_t	[m]	diameter of polystyrene tracer particles
Fr	[-]	Froude number
f	[-]	friction factor; Darcy-Weisbach's resistance coefficient
f_s	[-]	pore-based friction factor
g	[m s^{-2}]	gravitational acceleration, g = 9.81 m/s^2
H_s	[m]	surface layer flow depth (the depth measured from water surface down to the mean elevation of the rough bed)
H_s/k	[-]	Roughness submergence
H_p	[m]	thickness of the subsurface layer, or average height of the porous bed

H_0	[m]	depth measured from water surface down to the steel bottom of flume
i_s	[-]	hydraulic gradient
k_s	[m]	roughness size
K	[m^2]	permeability
K_u	[m^2]	unit conversion constant
l_p	[m]	characteristic dimension (usually the hydraulic diameter) of the cross section of porous bed, $L_p = 4R_h$
L	[m]	Length
n	[L$^{-1/3}$s]	Manning's resistance coefficient
Q	[m^3 s^{-1}]	total flow rate
q	[m^2 s^{-1}]	total flow rate per unit width
Q_s	[m^3 s^{-1}]	flow rate through the surface layer
Q_p	[m^3 s^{-1}]	flow rate through the porous bed
R_h	[m]	hydraulic radius
R	[m]	characteristic length of the cross-section
Re	[-]	Reynolds number
Re_s	[-]	pore-based Reynolds number
S	[-]	bed slope
S_f	[-]	friction slope
t	[m]	thickness of the transition zone
t_e	[s]	eddy turn-over time
T	[^{0}C]	Temperature

u, v, w	[m s^{-1}]	streamwise, bottom-normal and transversal velocity components
u_*	[m s^{-1}]	shear velocity
U	[m s^{-1}]	mean streamwise flow velocity
U_{CL}	[m s^{-1}]	centreline (streamwise) velocity
U_0	[m s^{-1}]	(streamwise) slip velocity at the interface level (y = 0)
U_p	[m s^{-1}]	bulk or superficial seepage velocity
ua_p	[m s^{-1}]	intrinsic seepage (pore) velocity
V_f	[m^3]	Volume of fluid
V_0	[m^3]	Total volume of the porous medium
u_{rms}, v_{rms}	[m s^{-1}]	fluctuation intensity of u and v velocity components
ν	[m^2 s^{-1}]	kinematic viscosity
u_n , u_t	[m s^{-1}]	fluctuating velocities normal and tangent to a surface T
u_D	[m s^{-1}]	characteristic velocity associated with the eddies of size D
x, y, z	[m]	Cartesian coordinates (streamwise, bottom-normal and transversal, respectively)
ψ	[m]	Bottom-normal coordinate, with its origin at the free water surface (i.e., an inverse coordinate for y)
y_0	[m]	zero velocity height according to the law of the wall
Re_K	[-]	permeability Reynolds number
$-\overline{u'v'}$	[m^2 s^{-2}]	Reynolds shear stress
u_s	[m s^{-1}]	bulk or superficial seepage velocity
ΔP	[m water]	pressure drop
Δ_p	[μs]	time span between two frames of a double-frame image

ΔH	[m]	(water) head loss
u', v'	[m s^{-1}]	fluctuation velocity components (of u and v)
α	[-]	general exponent
ε	[-]	porosity
ε_d	[m^2 s^{-3}]	turbulent energy dissipation rate
m, α, β	[-]	(localized) exponents
δ	[m]	boundary layer thickness
κ	[-]	von Karman constant: $\kappa \approx 0.4$
ρ	[kg m^{-3}]	density
τ	[N m^{-2}]	shear stress
τ_0	[N m^{-2}]	bed shear stress (at y = 0)
σ	[-]	standard deviation

Subscript/ superscript	**Description**
*	(quantities) belong or related to shear (e.g. velocity, Re, τ, etc)
+	normalised quantities
b	pertain to the bulk flow characteristics
m	pertain to the mean value
p	(quantities) pertain to the subsurface layer of the flow (i.e., the porous bed)
s	(quantities) pertain to the surface layer of the flow

Abbreviation	Description
IA	Interrogation Area
PIV	Particle Image Velocimetry
PTV	Particle Tracking Velocimetry
Q1, Q2, Q3, Q4	First quadrant, second quadrant, third quadrant, fourth quadrant

Chapter 1

Introduction

This thesis addresses the need for a better understanding of the characteristics of shallow open channel flows over different types of permeable beds comprise of large-scale roughness. The study made use of experimental and theoretical analyses to draw attention to the effect of the permeable bed and small roughness submergence on the hydraulic resistance, velocity distribution and turbulence structure of the flow. In fact, these topics have been receiving much interest over the last decades as they are of increasingly importance in practice.

1.1. Motivation

The present study aimed to investigate major characteristics of shallow open channel flow above permeable beds composing of coarse materials. Such flows are of interest to hydrologists, geomorphologists, and hydraulic researchers due to its widespread occurrence in various environments. Typical examples are gravel-bed streams in mountainous areas and other artificial coarse-bed channels.

Turbulent flows over permeable rough bed in general have been the subject for intensive study for the last few decades, as exemplified by the International Gravel Bed Rivers workshop series dated back to 1980. Although there has been consistent focus on the flow characteristics, still many problems remain unsolved. This is particularly the case for the hydraulically rough flows with small roughness submergence, i.e. the roughness elements being of the same order of magnitude as the flow depth, as observed in mountain streams [*Aberle and Smart*, 2003; *Buschmann and Gad-el-Hak*, 2007; *Ferguson*, 2007; *Manes et al.*, 2007; *Nezu and Nakagawa*, 1993; *Wohl*, 2000] (see Fig. 1.1 for an example).

Fig. 1.1: Vermont stream near Rochester, USA (photo by Towboat Garage)

With an appreciation of the major controversial topics and the information deficiency being faced, the present study aimed at gaining a further understanding of the flow velocity and turbulence characteristics. Subsurface portion of the flow through the porous bed would also be considered as an integral part of the shallow, turbulent flow over permeable rough beds.

1.2. Flow resistance

Perhaps the most fundamental and important bulk characteristic of open channel flow over permeable rough bed is the hydraulic resistance. Quantifying the flow resistance is generally required for designing purpose of channels, for prediction of flow depth, average velocity, sediment transport and flood routing.

Due to numerous scientific and practical applications, flow resistance has gained a significant theoretical interest over the last two and a half centuries [*Montes*, 1998]. The conventional way to describe the hydraulic resistance is to use friction factor, or roughness coefficient. This coefficient can be defined in a variety of ways and there have been a wide range of equations being proposed to relate the mean channel flow velocity to flow resistance, especially for the case of shallow flow over rough surfaces. Hence, this study would focus on providing a reliable way to predict resistance from the observable flow and bed properties.

This thesis first provides a brief review on published relationships for hydraulic resistance, particularly those for flows over rough bed with small roughness submergence (say, $H/k < 5 - 10$, where H is the mean flow depth and k is a representative bed roughness height). A conceptual model for flow resistance will then be introduced prior to the derivation of a new, simple semi-empirical relationship to predict the friction. A large set of calibration data collected from available sources in literature as well as from this study has been used for the calibration of the proposed formula. By combining these steps, the present study aims at introducing an equation that has both a theoretical basis and generic validity. Lastly, discussions on the resulting formula and its applicability will be presented. However, to minimize the complexity, the proposed model would not address some complex traits of real mountain streams such as bank effect, sediment mobility, submerged vegetation, bed-forms and larger scale bed features (e.g., step-pool morphology). Flow resistance is hereby considered solely due to the grain roughness of the bed material.

1.3. Velocity profile and scaling

Of practical importance to environmental and hydraulic engineers is the mean velocity profile as it can provide information relevant to flow resistance, conveyance capacity and sediment transport. However, the understanding of velocity distribution over the whole flow depth in such conditions is still limited and there are ongoing debates on the underlying mechanism. The ability to describe the flow velocity profile is, therefore, a major concern over the past decades.

Meanwhile, it is known that scaling of fluid flow is a powerful technique as it can provide convenient, dimensionless representation for similar flow conditions. It can also be useful in extrapolating the typically low Reynolds number laboratory tests to the high Reynolds number field conditions. Proper scaling of a fluid flow is a particularly powerful technique for turbulent flows where analytical solutions derived from first principles are not available.

This study aims at contributing to the ability to describe the flow velocity profiles by proposing a simple yet acceptable scaling method that is capable of scaling the flow velocity profile in the surface layer, especially for shallow flow conditions. It will also discusses a method to estimate the average velocity in the sublayer and develops a simple eddy viscosity model is developed to justify the scaling argument.

1.4. Turbulence characteristics

The majority of flows over large-scale roughness in nature and engineering practice are turbulent, which has been known to be a challenging topic. The presence of a permeable bed and small roughness submergence causes the turbulence structure to be quite different from that in a flow with smooth bed and sufficient submergence, adding to the complexity of the problem. This study aim to provide a better understanding on the effect of bed permeability as well as the small roughness submergence on the structure of the flow turbulence.

Since turbulence is difficult to be defined precisely and in fact, unable to be solved analytically, researchers have been relying on physical intuition and dimensional arguments to address the problem. This study, therefore, makes use of experimental investigation and dimensional analysis to investigate the turbulence characteristics and discusses the effects of the bed permeability as well as the small roughness submergence. Measurements were carried out to probe the shallow flows over permeable rough bed composed of glass spheres (marbles) as well as gravel beds.

1.5. Objectives and scope

This study sets out to investigate the shallow open channel flows over different permeable rough beds, excluding rill flows and sandy beds where surface tension plays a significant role, in order to gain further understanding and provide practical approaches to interpret the flow characteristics. More specifically, it aims to:

1) Observe the flow velocity profiles and turbulence structure and investigate the influence of bed permeability and small roughness submergence on characteristics of the surface flow.
2) Find a new approach for a more accurate and consistent calculation of the hydraulic resistance and mean velocity for very shallow flow over permeable rough beds, of which the roughness submergence is smaller than five.
3) Identify an appropriate velocity and length scale that well perform in scaling the mean velocity profiles in the outer region of turbulent open channel flows over a permeable rough bed with small roughness submergence.

1.6. Outline of the thesis

This thesis is organized into seven chapters, of which this chapter introduces the background, objectives and scope of the present study. The remaining chapters are laid out as follows:

Chapter 2 reviews the relevant analytical, numerical simulation and experimental works in literature, focusing on the effect of the permeable bed and the small roughness submergence on the hydraulic resistance, velocity distribution and turbulence structure of the flow. The methodology, findings and shortfalls of certain studies regarding the characteristics of shallow open channel flow over permeable rough beds are briefly discussed.

Chapter 3 describes the experimental setups and procedures, together with data analysis techniques employed in the present study. Laboratory experiments cover a range of flume facilities, bed materials, bed porosities, roughness submergences and flow conditions that are considered necessary. Besides, it also presents the results obtained from the measurements of flow through porous bed and the estimation of subsurface flow, which would facilitate the study's subsequent analyses.

Chapter 4 introduces a new and simple calculation for resistance coefficient and mean velocity in a very shallow flow over permeable rough beds. It first justifies a theoretical analysis, then introduces an exponential function to better account for the roughness submergence, and finally calibrates the proposed formulae by using a large compilation of data from a wide variety of sources including those from the present study.

Chapter 5 proposes an approach that is useful for scaling the mean velocity profiles in the outer region of turbulent open channel flows over a porous rough bed comprising large scale roughness by using the plane mixing layer analogy. The statistics of the flow velocities obtained through experiments and literature were then used to validate the proposed scaling method. Finally, it introduces an eddy viscosity model to justify the scaling arguments.

Chapter 6 is devoted to the description and interpretation of the flow measurement, using Particle Image Velocimetry (PIV) and other image processing techniques. Investigation of turbulence characteristics and flow structures reveals the influences of the bed permeability as well as the small roughness submergence on the flow. Comparison with those characteristics in flow with sufficient submergence and/or flow over impermeable rough bed signifies the difference attributed to the specific flow conditions under consideration.

Chapter 7 summarizes all the major findings of this study and concludes the thesis with recommendations for possible future studies.

Chapter 2

Literature Review

This chapter reviews relevant analytical, experimental and numerical simulation works regarding the characteristics of shallow open channel flow over permeable rough beds. The emphasis of this review is on the effect of the permeable bed and the small roughness submergence (or large roughness) of the flow on the hydraulic resistance, velocity distribution and turbulence structure of the flow.

2.1. Shallow flow over permeable rough bed

2.1.1 The context

Shallow flows, featured by two much larger dimensions of the flow domain than the third one, are widely observed in practice. Many kinds of hydraulic, environmental and geophysical flows can be considered as shallow, such as flows in gravel-bed mountain rivers, wide low land rivers, estuaries and coastal areas, as well as shallow mixing layers.

Notwithstanding that, shallow flows are largely unidirectional, turbulent and shear-driven by a piezometric gradient [*Jirka and Uijttewaal*, 2004]. They are often bounded in a domain where the length scales in the streamwise and transverse direction greatly exceed the third length scales, often in the vertical direction. The typical environmental or geophysical setting of gravel-bed river flows can be depicted by Fig. 2.1, whereby the transverse length scale *B* is greatly larger than the confined flow depth *H*. This is known as the primary kinematic condition for shallow flows.

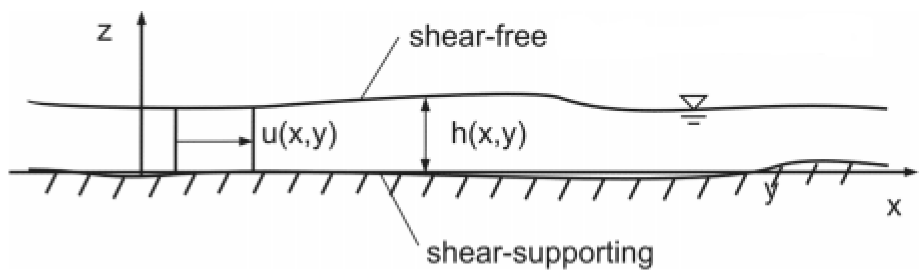

Fig. 2.1: Schematics of a shallow flow (after Jirka and Uijttewaal, 2004)

Flow in gravel-bed rivers is usually shallow, or in other words, it is characterized by relative large-scale roughness. The flow's roughness submergence, defined as the ratio of depth to roughness height, is typically less than 4–5 during low flow conditions and less than 10-20 during flood conditions (e.g., Bathurst [1985], Charlton et al. [1978], Ferro and Pecoraro [2000], Hardy et al. [2010], Wohl [2000]).

2.1.2 Subdivision of the flow field

To facilitate the subsequent analysis, this study starts off with a division of the turbulent structure of an open channel flow into its different characteristic layers, as shown in Fig. 2.2. There have been several methods to define the sublayers of a flow field and reference would first be made to a prevailing subdivision method (used by, for example, *Nikora et al.* [2001]). Subsequently, necessary adaptations to shallow flows over permeable rough beds would then be discussed throughout the study.

The entire structure of an open channel flow over porous bed can be vertically subdivided into four major layers, namely the outer, the inertial, the roughness, and the subsurface ones. Hereafter a brief description, together with some conventional dimensionless parameters of mean flow velocity profiles, is given to each of the layers. Note that for the rough-bed flows, the velocity scales are defined in terms of double averaged velocities. The reference bed level (y = 0) is chosen to be the tangential surface at the crest of the top layer of roughness elements. Reason being, it would facilitate the interpretation of the Reynolds shear stress profiles later on, and also it yields consistency between vertical velocity profiles and turbulence intensities profiles. This is also in agreement with many other studies such as Nakagawa et al. [1991], Manes et al. [2009], and Dey and Das [2012].

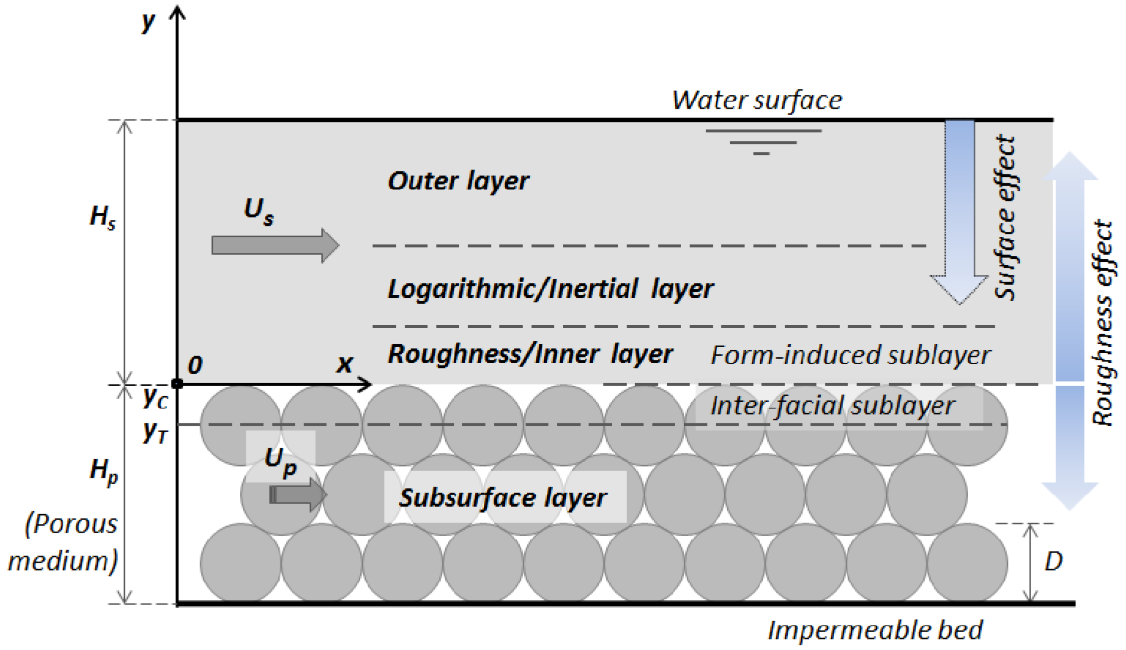

Fig. 2.2: Subdivision of flow over a permeable rough bed

1. The *outer layer*. Relatively far from the rough bed, the viscous effects and form-induced fluxes are negligible in this layer and the flow structure here is controlled by the outer variables. The length and velocity scales are characterized by the flow depth H_s and the maximum mainstream velocity U_{max}, respectively. A log-wake law can be applied in this region to describe the velocity distribution [*Nezu and Nakagawa*, 1993].

2. The *logarithmic (log) layer*, or *inertial layer*. This layer, which exists in flows with large roughness submergence, occupies the overlapping region between the outer layer and inner layer. It corresponds loosely to the inertial subrange of the spectral distribution, and is where the log-law valid [*Hinze*,

1975; *Kundu and Cohen*, 2008]. This layer may be identified as the equilibrium layer where the energy production and dissipation rates are balanced [*Townsend*, 1961]. Its characteristic velocity scale is u_*, and its length scales can be the distance from the bed y and/or the characteristic length of the bed topography (the representative roughness height k).

3. The *roughness layer*, or *inner layer*. Below the log layer there is a flow region influenced predominantly by the roughness elements, called the roughness layer. The flow, directly influenced by individual roughness elements, are spatially inhomogeneous. This is where the wall effect is strong and free surface effect is negligible. It can be further divided into an *interfacial sublayer* (which occupies the flow region between roughness crest and troughs) and a *form-induced sublayer* (which occupies the region just above the roughness crest, where the flow is influenced by individual roughness elements). This layer can be interpreted by an analogy to the classical boundary layer theory for smooth bed, where the interfacial and form-induced sublayers play the role of the viscous and buffer sublayers, respectively [*Nikora et al.*, 2001; *Raupach et al.*, 1991]. Both the roughness layer and logarithmic layer fall into the conventional wall region in the boundary layer approach [*Nezu and Nakagawa*, 1993], thus they are expected to share similar velocity and length scales.

4. The *subsurface layer*. In the presence of a permeable bed (or a canopy composed of large-scale roughness elements), the flow in this layer takes place in the pores between solid grains and is driven by the gravity and momentum fluxes from the above layers [*Nikora et al.*, 2001]. For a porous media composed of regular spherical beads, with the reference level taken at the crest level of the roughness elements ($y = y_c = 0$), the interfacial sublayer occupies the region of $y_t \leq y \leq 0$, where y_t ($= -D/2$) is the elevation of the trough. The subsurface layer falls right below the interfacial sublayer, both forming the so-called *porous layer*.

The above four major layers cover the whole depth of open channel flow over a permeable rough bed. It should be noted that, the layers are overlapping in part and it is difficult to define a clear range for each of them. Therefore, several researchers, including *Nezu and Nakagawa* [1993], used to term layer (2) the *intermediate region*; layers (1) and (2) the *outer region*; and layers (2) and (3) the *inner region* (or *wall region*).

The flows investigated in the present study generally fall under shallow flow condition whereby the flow depth is relatively small (in comparison with the roughness size) to limit the formation of a major logarithmic layer. They are, however, generally sufficiently deep to accommodate an outer layer where the influence of roughness elements does not solely overrule.

2.2. Flow resistance

2.2.1 Background

Due to a multitude of factors influencing roughness, the quantification of hydraulic resistance has been known not to be a trivial task [*McKay and Fischenich*, 2011]. A few of these factors can be named such as geometrical channel characteristics, streamwise gradient, bed materials, bed forms, and flow condition. In fact, it is surprising to know that engineering practice has depended to a considerable extent on many of the empirically derived formulae, introduced as early as more than a century ago, such as the Manning's one [*Yen*, 1992]. However, the hydraulics has been evolving from empirically-based approach to fluid mechanics-based science and recently, several researchers have proposed conceptual and heuristic methods to address the problem. Ferro and Pecoraro [2000], Gioia and Bombardelli [2002], Katul *et al.* [2002] and Lawrence [1997] are among them.

In spite of the well-established study and a broad literature on open channel flow hydraulics, the hydraulics of steep mountain streams is so far poorly understood compared to that of lowland, fluvial streams. Only during the last three decades have the mountain rivers begun to receive increasing attention as a subset of rivers [*Wohl*, 2000].

Recent reviews have concluded that there is no standard formula for calculating the resistance of mountain streams in a consistent and accurate manner [*Aberle and Smart*, 2003; *Ferguson*, 2007; *Wohl*, 2000]. Most equations derived from boundary layer theory work well for low-gradient sand-bed alluvial rivers. However, they show some systematic deviation when being extrapolated to apply in mountain rivers, which are characterized by higher gradient, turbulent flow, large size and heterogeneous bed material, and relatively shallow flow depth [*Alonso et al.*, 2009; *Bathurst*, 2002; *Ferguson*, 2007; *Jordanova and James*, 2010; *D. Rickenmann and Recking*, 2011].

There have been numerous modifications of resistance coefficients such as Manning's n, Chézy C and the Darcy-Weisbach f for application in shallow flow over rough beds. However, the greater complexity in the hydro-geomorphologic processes of these flows has caused the proposed governing equations virtually empirical. The strong variation of their coefficients suggests that their applicability and accuracy are somehow limited, subjected to the data set used for calibration [*Bathurst*, 2002; *Froehlich*, 2012; *Jordanova and James*, 2010; *Katul et al.*, 2002; *D. Rickenmann and Recking*, 2011].

From another angle, there is a consensus on the influence of bed permeability on the flow resistance. Several studies have reported the significant increase in friction factors of the turbulent flows over permeable walls compared to that in impermeable walls with the same surface roughness. Among those are the works done by Grass [1971], Zagni and Smith [1976], Stoesser et al. [2007], Hardy et al. [2009], Manes et al. [2009], and Suga et al. [2010]. This increase is resulted from the additional dissipation of turbulent kinetic energy, which is often attributed to the shear penetration into the permeable bed, or in other words, the exchange of flow momentum between the surface and subsurface flows across the permeable interface. Furthermore, the friction factor was found to be Reynolds number dependent in the hydraulically rough flow conditions (e.g., Manes et al. [2009] and Suga et al. [2010]).

Through the following sections, this study attempts to show and categorize the connection among the available resistance formulations. The review to be presented was composed in the same spirit as the excellent works done by Ferguson [2007], Aberle [2003], Bathurst et al. [2002; 1981]. This review would facilitate the subsequent derivation of a modified Manning's formula, which was extended from the theoretical justification of Gioia and Bombardelli [2002], to calculate the resistance coefficient.

2.2.2 Theoretical consideration

Except for the flood routing and mobile bed problems, flow resistance is usually investigated based on a balance between the driving force caused by gravitational acceleration and the frictional resistance on the water body. The flow resistance needs to be predicted from time-invariant channel properties (slope, shape and dimensions) and other readily observable flow characteristics (depth, discharge and/or mean velocity). The use of dimensionless resistance coefficients and hydraulic geometry has also facilitated the formulation of flow resistance.

A variety of relationships have emerged from nineteenth and twentieth century to characterize the flow resistance. When bed gradient is low and the flow is relatively deep (fine bed material), popular relationships linking velocity and flow resistance such as Manning, Chézy and Darcy-Weisbach equations can be applied

$$U = \frac{1}{n} R^{2/3} S_f^{1/2} = C\left(RS_f\right)^{1/2} = \left(\frac{8gRS_f}{f}\right)^{1/2} \tag{2.1}$$

where n ($L^{-1/3}T$), C ($L^{1/2}T^{-1}$) and f (dimensionless) are the Manning, Chezy and Darcy-Weisbach coefficients, respectively; U = mean velocity, R = hydraulic radius, S_f = friction slope, and g = gravitational acceleration. For shallow flows over rough bed, the surface flow depth H_s is usually used instead of R.

The central problem in applying resistance equations is to evaluate the coefficients. Although the Chézy coefficient is simplest and has the longest history [*Yen*, 1992], f and n has been used more frequently for engineering purpose. The value of f can be retrieved from the Moody diagram, while n values can be obtained from a variety of text books (e.g., Chow [1959]). Manning's n

has an approximately constant value for comparatively deep flows, but increases rapidly with decreasing water depth in shallow flow. The value of f also varies significantly with the flow depth under low flow conditions. The use of the resistance equations in their original form is inappropriate for shallow flows [*Froehlich*, 2012; *Jarrett*, 1984b; *Jordanova and James*, 2010].

Besides, the relatively deep flows (i.e., small-scale roughness) may be described by boundary-layer theory, so that n and f can be explicitly expressed in term of the hydrodynamic roughness height y_0 in the log-law for turbulent boundary layers [*Bathurst et al.*, 1981; *Jordanova and James*, 2010; *Katul et al.*, 2002]. However, it is not appropriate to use the same theory to describe the flow with large-scale roughness as a significant portion of the flow takes place within and near the roughness layer.

Mountain streams and other artificial coarse-bed channels are characterized by the development of an armour layer with a wide range of gravels, cobbles and boulders. With respect to the roughness submergence H_s/k, the roughness can be divided into large-scale (i.e. small submergence, H_s/k generally smaller than about 4 – 5), intermediate-scale ($4 < H_s/k < 15$), and small-scale roughness otherwise [*Bathurst et al.*, 1981]. The large-scale roughness elements affect the whole flow depth and skin friction is then dominated by form drag, wake vortices, local contraction, expansion and other resistance processes [*Bathurst*, 2002; *Ferguson*, 2007].

In developing a process-based resistance equation for large-scale roughness, Bathurst *et al.* [1981] have identified the processes that determine the drag of an individual element (those related to Reynolds number and Froude number), and the processes that determine the effect of roughness elements on the flow (roughness geometry and channel geometry). Considering only the roughness of the bed elements (k), their effect on the flow resistance depends on the proportion of the bed material which has a significant form drag [*Bathurst*, 2002]. Following the concept of equivalent grain roughness introduced by Nikuradse, k is usually assumed to be proportional to a representative sediment size, $k = \alpha_i D_i$, where D_i = bed material size for which $i\%$ of the bed material is finer, and α_i = multiplication factor, typically within the range of 1–8. The choice of a representative D_i and its associated α_i is not a trivial matter and has been addressed in a multitude of studies [*Simões*, 2010; *Yen*, 2002]. The principal factor that most resistance equations have used to account for the roughness geometry in natural and artificial coarse-bed channels is the roughness submergence, H_s/D_{50} or H_s/D_{84}.

Among the common friction factors *f*, *C* and *n*, there is no clear advantage of one over another, and they are interchangeable via Eq. (2.1) [*Yen*, 2002]. However, *f* has two advantages that make it the popular choice: it is dimensionless and physically interpretable as a drag coefficient. The function $\sqrt{8/f}$, which is inversely proportional to resistance, is often used instead of the simple coefficient *f* in resistance expressions because it is interchangeable with the dimensionless velocity U/u_*, where $u_* = \sqrt{gH_sS}$ is the shear velocity. This can be shown by applying the general concept of bed shear stress (τ_0), originally developed for uniform flows with small-scale roughness and gentle slopes. The relationship could be derived by equating τ_0 with the streamwise component of the gravitational force per unit bed area and assuming that τ_0 is proportional to the square of velocity

$$\tau_0 = \rho u_*^2 = \rho g H_s S = \rho U^2 \frac{f}{8} \tag{2.2}$$

This is also the clue for the interchangeable dimensionless groups, which are extensively used in literature

$$\sqrt{\frac{8}{f}} = \frac{U}{u_*} = \frac{C}{\sqrt{g}} \tag{2.3}$$

2.2.3 Flow resistance equations

Extensive reviews on flow resistance has been documented earlier by Ferguson [2007], Yen [2002], and Bathurst [2002; 1981]. In the following, this study attempts to classify and provide a brief perspective of the formulae found in literature. The list is not complete, but provides the basis to justify the idea developed in this study.

Resistance equations for shallow flows over rough beds may generally be divided into three categories. They are based on the logarithmic law of the wall, power law, or other heuristic approaches. Several authors have proposed resistance equations specifically for shallow flows using both empirical and semi-empirical approaches. Recent studies also adopted semi-empirical approaches to modify the log and/or power law velocity distribution to for their resistance models.

Approaches based on logarithmic law

By integrating the Karman-Prandtl-Nikuradse logarithmic velocity distribution, Keulegan [1938] arrived with the pioneering logarithmic equation for turbulent, which was later simplified by Chow [1959]. They applies for uniform flow in open channels with hydraulically rough boundary surfaces and can be expressed in the following general form

$$\sqrt{\frac{8}{f}} = \frac{1}{\kappa}\ln\left(\frac{H_s}{ey_0}\right) = \frac{1}{\kappa}\ln\frac{H_s}{k} + a_1 = a_2\log\left(\frac{H_s}{k}\right) + a_3 \tag{2.4}$$

where κ = von Karman's coefficient, often taken to be 0.4; e is the base of natural logarithms; y_0 is the zero velocity height according to the law of the wall ($k = 30y_0$ as proposed by Nikuradse); a_1, a_2 and a_3 are dimensionless coefficients, where $a_2 = 5.75$ and a_3 varies with the shape of the channel cross-section [*Hey*, 1979; *Keulegan*, 1938]. Keulegan initially proposed to use the median diameter D_{50} for k. However, using the equivalent grain roughness concept, $k = \alpha_i D_i$, many formulations have been derived, with the coefficients and choice of D_i being determined by optimizing the fitting to data (Eq. A1-A10, listed in Table 2.1). These semi-logarithmic relationships are able to account for the considerable deviation of velocity profile in shallow flows from the logarithmic law and provide adequate prediction for certain conditions.

Table 2.1: Flow resistance relationships based on logarithmic law

Eq.	**Reference**	**Formula (or equivalent)**	**Remarks**
A1	Keulegan [1938]	$\sqrt{\frac{8}{f}} = 5.75\log\left(\frac{H_s}{D_{50}}\right) + 6.25$	
A2	Hey [1979]	$\sqrt{\frac{8}{f}} = 5.74\log\left(\frac{aR}{3.5D_{84}}\right)$	a = function of cross-sectional shape = 11.1–13.46 (11.37 for rectangular channel.)
A3	Bathurst [1985]	$\sqrt{\frac{8}{f}} = 5.62\log\left(\frac{H_s}{D_{84}}\right) + 4$	
A4	Froehlich [2012]	$\sqrt{\frac{8}{f}} = 5.62\log\left(\frac{H_s}{1.7D_{50}}\right) + 6.25$	For riprap-lined channels, with $0.1 \leq H/D_{50} \leq 30$
A5	Smart [1984]	$\sqrt{\frac{8}{f}} = 5.75\left[1 - e^{\frac{-0.05Z_{90}}{S_0^{0.5}}}\right]^{0.5} \log\left(8.2\frac{H_s}{D_{90}}\right)$	
A6	Bray [1979]	$\sqrt{\frac{8}{f}} = 6.11\log\left(\frac{H_s}{D_{90}}\right) + 3.56$	
A7	Millar [1999]	$\sqrt{\frac{8}{f}} = 5.74\log\left(\frac{12.2H_s}{D_{50}}\right)$	For grain resistance component
A8	Ferro and Pecoraro [2000]	$\sqrt{\frac{8}{f}} = 4.446\log\left(\frac{H_s}{D_{84}}\right) + 0.8616$	
A9	Thompson and Campbell [1979]	$\sqrt{\frac{8}{f}} = 2.5\left(1 - 0.1\frac{k}{R}\right)\ln\left(\frac{12R}{k}\right)$	$k = 4.5D_{50} = 2.37D_{84}$ at their site.
A10	Aberle and Smart [2003]	$\sqrt{\frac{8}{f}} = 4.41 + 3.54\ln\left(\frac{H_s}{D_{84}}\right)$ $\sqrt{\frac{8}{f}} = 3.86\ln\left(\frac{H_s}{\sigma}\right) - 1.19$	σ is the standard deviation of the bed material size.

Approaches based on power law

Semi-logarithmic relationships have been empirically proposed because the logarithmic law is essentially not relevant for flows with large-scale roughness. However, it has been pointed out that for these conditions, a power law is even more appropriate and can describe the dependency of the resistance function $(8/f)^{1/2}$ on H_s/k more accurately [*Bathurst et al.*, 1981; *Ferguson*, 2007; *D. Rickenmann and Recking*, 2011]. It was also noted that logarithmic function discussed earlier can be effectively approximated by a power law relationship, with the exponent of 1/7 [*Hinze*, 1975; *Katul et al.*, 2002], and 1/6 – 1 for different ranges of H_s/k [*Carson and Kirkby*, 1972].

Many researchers have proposed resistance equations by linking the dimensionless friction factor to the flow depth and bed material size (Eq. A11-A17, Table 2.2), with the general power form of

$$\sqrt{\frac{8}{f}} = b_1 \left(\frac{H_s}{k} \right)^{m_1} \tag{2.5}$$

This is an empirical way to define a resistance relationship and therefore, coefficient b_1 and exponent m_1 need to be determined by fitting to the calibration data. The Manning-Strickler relation, which relates the Manning's n to the 1/6 power of D, also implies this power relationship with m_1 = 1/6 and b_1 = 6.7 if D_{50} is used as roughness size, or 8.2 if D_{84} or D_{90} is used [*Ferguson*, 2007].

Table 2.2: Flow resistance relationships based on power law

Eq.	**Reference**	**Formula (or equivalent)**	**Remarks**
A11	Manning-Strickler	$\sqrt{\frac{8}{f}} = a_1 \left(\frac{H_s}{D_i} \right)^{1/6}$	$a_1 \cong 6.7$ for D_{50}; $a_1 \cong 8.2$ for D_{84} or D_{90}
A12	Bathurst [2002]	$\sqrt{\frac{8}{f}} = a \left(\frac{H_s}{D_{84}} \right)^{b}$	a = 3.84, b = 0.547 for S < 0.8% a = 3.10, b = 0.93 for S > 0.8%

Eq.	Reference	Formula (or equivalent)	Remarks
A13	Parker [1991]	$\sqrt{\frac{8}{f}} = 8.1\left(\frac{H_s}{2D_{84}}\right)^{1/6}$	
A14	Maynord (1991)	$\sqrt{\frac{8}{f}} = 7.92\left(\frac{H_s}{D_{90}}\right)^{0.1664}$ $\sqrt{\frac{8}{f}} = 6.89\left(\frac{H_s}{D_{50}}\right)^{1/6}$	For riprapped surfaces.
A15	Griffiths [1981]	$\sqrt{\frac{8}{f}} = 3.54\left(\frac{H_s}{D_{50}}\right)^{0.287}$	0.0085 < S < 1.1%
A16	Bray [1979]	$\sqrt{\frac{8}{f}} = 5.03\left(\frac{H_s}{D_{90}}\right)^{0.268}$	0.0035 < S < 1.5%
A17	Ferguson [2007]	$\sqrt{\frac{8}{f}} = \frac{c_1 c_2 (H_s/D_{84})}{\sqrt{c_1^2 + c_2^2 \left(H_s/D_{84}\right)^{5/3}}}$	(variable-power equation) $a1 \approx$ 7–8; $a2 \approx$ 1–4
A18	Bjerklie et al. [2005]	$U = k_1 H_s^{0.67} S^{0.33}$ (modified Manning eq.) $U = k_2 g^{0.5} H_s^{0.5} S^{0.33}$ (modified Chezy eq.) $U = 4.24 \cdot B^{0.1} H_s^{0.63} S^{0.33}$ (regression model)	B is the flume width; Multiple regression analyses reached a common exponent of 0.33.
A19	Rickenmann [1991]	$U = 1.3 q^{0.6} \left(gS\right)^{0.2} D_{90}^{-0.4}$	3% < S < 40%; q is the discharge per unit width.
A20	Rickenmann (1996)	$U = 0.37 g^{0.33} Q^{0.34} S^{0.20} D_{90}^{-0.35}$ $U = 0.96 g^{0.36} Q^{0.29} S^{0.35} D_{90}^{-0.23}$	S > 0.8% S < 1%
A21	Jarrett [1984a]	$U = 3.81 R^{0.83} S^{0.12}$, for S > 0.002.	From 75 measurements of discharge made on 21 high-gradient streams
A22	Ferguson [2007]	$U_+ = a_2^{0.4} q_+^{0.6} S^{0.2}$ (shallow flows) $U_+ = a_2^{0.6} q_+^{0.4} S^{0.3}$ (deep flows)	where $a1 \approx$ 7–8; $a2 \approx$ 1–4, $U_+ = U/\left(gD_{84}\right)^{0.5}$ and $q_+ = q/\left(gD_{84}^3\right)^{0.5}$

Another popular approach is to derive a relationship between the mean velocity and the flow discharge, where the slope is often included (Eq. A18). A more general power form of many resistance equations was arrived by including the characteristic roughness size (Eq. A19-A20)

$$U = b_3 Q^{m3} g^{m4} S^{m5} D_i^{m6} \tag{2.6}$$

There were also other formulations available, such as the one proposed by Jarret (1984) who found that *n* can be estimated better from *S* and *R* than from *D* (Eq. A21).

Many of these equations can also be given in nondimensional hydraulic geometry terms and show better performance, for example those from Eq. A22 and A23 [*Aberle and Smart*, 2003; *Ferguson*, 2007; *D. Rickenmann and Recking*, 2011; *Zimmermann*, 2010], i.e.

$$U_+ = b_4 q_+^{m_7} \text{, or} \tag{2.7}$$

$$U_+ = b_4 Q_+^{m_8} S^{(1-m_8)/2} \tag{2.8}$$

where $U_+ = U/\left(gD_{84}\right)^{0.5}$ and $q_+ = q/\left(gD_{84}^3\right)^{0.5}$.

Other heuristic approaches

There have been a number of heuristic approaches proposed, where a resistance equation was introduced together with a supporting theory other than the boundary-layer. They may be very different in nature, with complex form, but all were derived with a certain level of theoretical analysis and reached about the same conclusions on bulk flow resistance. These formulae are also summarized in Table 2.3 (Eq. A23-A27).

Table 2.3: Other heuristic/empirical flow resistance relationships

Eq.	**Reference**	**Formula (or equivalent)**	**Remarks**
A23	Rickenmann		where $U_{++} = U/\left(gSD_{84}\right)^{0.5}$

Eq.	**Reference**	**Formula (or equivalent)**	**Remarks**
	[2011]	$U_{++}=1.5471q_{++}^{0.7062}\left[1+\left(\frac{q_{++}}{10.31}\right)^{0.6317}\right]^{-0.49}$ $\sqrt{\frac{8}{f}}=4.416\left(\frac{H_s}{D_{84}}\right)^{1.904}$ $\times\left[1+\left(\frac{H_s}{1.283D_{84}}\right)^{1.618}\right]^{-1.083}$	and $q_{++}=q/\left(gSD_{84}^{3}\right)^{0.5}$
A24	Smart et al. (2002)	$\sqrt{\frac{8}{f}}=a\left(\frac{R}{\sigma_z}\right)^{0.5}\left(\frac{D_x}{\sigma_z}\right)^{0.5}$ for $\sigma_z/R<0.03$ $\sqrt{\frac{8}{f}}=a\left(\frac{R}{\sigma_z}\right)^{1.25}\left(\frac{D_x}{\sigma_z}\right)^{0.5}$ for $\sigma_z/R\geq 0.03$	D_x >≈ D_{50}; σ_z = (1/5–1/17)·D_{84} is the standard deviation of granular surface elevation.
A25	Katul [2002]	$\sqrt{\frac{8}{f}}\propto\left\{1+\frac{k}{H_s}\ln\left[0.65\cosh\left(\frac{H_s}{k}-1\right)\right]\right\}$	0.2 < H/k <7
A26	Bathurst et al. [1981]	$\sqrt{\frac{8}{f}}=\left(\frac{0.28}{b}Fr\right)^{\log(0.755/b)}\times\frac{A_w}{BH_s^{'}}$ $\times\left[13.434\left(\frac{B}{Y_{50}}\right)^{0.492}b^{1.025(B/Y_{50})^{0.118}}\right]$	Combining effect of Reynolds number, Froude number (Fr), relative roughness area (A_w/BH'); and roughness concentration (quantified by the function b). Here, Y_{50} = average of the long and median axes of sediment particles.
A27	Manes [2011b]	$\sqrt{\frac{8}{f}}=\frac{U}{u_*}=\frac{U_cH_s+U_LH_i}{\sqrt{gS}\left(H_s+H_i\right)^{3/2}}$	where H_i is the depth of the interface region, U_L is the bulk mean velocity in that region; U_c is the bulk mean velocity in the surface flow region

Ferro and Pecoraro [2000] used an incomplete self-similarity approach and a combination of divergence functions to reproduce the velocity distribution with different profile shapes. However, they finally arrived with a flow resistance equation that shares the same general form as other semi-logarithmic ones. On the other hand, Katul et al. [2002] used a mixing-layer analogy for the inflectional velocity profile within and above the roughness layer, which can be represented by a hyperbolic tangent function. Their theory provided a relationship between flow velocity, flow depth and roughness size for $H_s/D < 2$, but also claimed to be applicable for $0.2 \leq H_s/D \leq 7$ (Eq. A25). Last but not least, Nikora et al. [2004] noted that other expression, such as exponential distribution, could be used for describing the velocity profiles as well.

In an earlier study, Bathurst [1981] presented a diligent process-based approach, based on an understanding of how resistance is generated from each individual contributing process. The resistance relationship combined all effects of Reynolds number, Froude number, relative roughness area, and roughness concentration to flow resistance. Later on, Ferguson (2007) and Rickenmann and Recking [2011], however, suggested that it is sufficient to use a nondimentional hydraulic geometry relation to predict the flow resistance without having to justify any particular interpretation of the dominant physical processes. They investigated several different heuristic and empirical analyses of shallow flows to find that those all converge on the linear relation of $(8/f)^{1/2} \sim H_s/D$, before arrived with their proposed Manning-Strickler-Roughness layer model.

There are also several approaches that took the additional energy loss caused by the free-surface drag associated with large roughness elements into account [e.g., Afzalimehr and Anctil [1998], Bathurst, *et al.*, [1981], Colosimo, *et al.*, [1988], Jordanova and James, [2010]]. Since this drag varies with the roughness submergence and Fr, these parameters have been taken into account. However, as pointed out by Aberle et al. [2003], caution should be made since some of these resistance equations directly estimate f from Fr. They therefore should not be considered as robust predictors as spurious self correlation may have been utilized.

Nonetheless, the majority of the approaches presented in this section have overlooked a particular concern for the (interstitial) flow in between the roughness elements, which is very important to the understanding of hydraulic resistance in flows over permeable rough bed with H_s/D generally smaller than 4–5. The effect of this portion of flow is usually grouped into the bulk flow resistance empirically. Either way, it was indirectly addressed via the theoretical flow velocity profile [e.g., Ferro and Pecoraro [2000], Katul *et al.* [2002]], or simply determined empirically [*A. D. Gupta and G. N. Paudyal*, 1985; *Tuyen et al.*, 2014]. The approach presented hereafter will attempt to combine a theoretical justification and an optimized fitting to data to derive a new resistance equation.

2.3. Main-stream velocity profile and scaling

2.3.1 Background

Generally, the shallow open channel flow is driven by a hydraulic gradient against the shear force exerting on the fluid in motion. The latter is caused by the shear-supporting boundary at the bed interface. The flow, virtually unidirectional in streamwise direction, is influenced by vertical shear giving rise to a (vertical) velocity profile.

The ability to describe the flow velocity distribution is a major concern over the past decades. To depict the velocity profiles in an open channel flow, the logarithmic law (log-law), which is inherently valid only in the wall region, has been derived independently by Prandtl and Taylor using mixing length theory, by Karman using dimensional analysis, and by Millikan using asymptotic analysis [*Buschmann and Gad-el-Hak*, 2007]. For practical purposes, it has been used to describe open channel flows since the recommendation of Keulegan. It was followed by the log-wake law [*Coles*, 1956], which accounts for the outer-zone deviations of flow profiles from the standard log-law while retaining the similarity concept of the near-wall behavior. Cole's wake function, although purely empirical, has been considered the most acceptable extension of the log-law for a long time [*Nezu and Rodi*, 1986; *Nezu and Nakagawa*, 1993]. The log-wake law can be modified to describe the flow over beds affected by wall roughness, with a coincidence with the conventional log-law in the wall region.

However, the existence of a log-law behavior, the physical meaning of the empirically found log-law parameters, and its Reynolds number dependence have become questionable despite the conventional use of the log-law. This is particularly the case of flows over rough wall with small roughness submergence, where both the roughness and surface effects are seen throughout the flow depth. Therefore it is still challenging to find a universal law for the mean velocity profile with appropriate theoretical arguments. The current debate has precluded neither a logarithmic nor power-law for scaling the mean velocity profiles of flows over rough walls/canopies [*Buschmann and Gad-el-Hak*, 2007; *Cheng et al.*, 2012b; *Manes et al.*, 2007; *Zagarola and Smits*, 1998]. Besides, the Reynolds number dependence of the mean velocity profile also adds to the complexity of the problem. Researchers have since suggested more and more complex functional forms to describe these profiles.

2.3.2 Scaling consideration

Finding a self-similar solution is among the most powerful techniques to scale flow velocity profiles as it can provide convenient, dimensionless representation for similar flow conditions. This is also the most commonly encountered problems in fluid mechanics. The technique has been widely studied for various types of flow and boundary conditions, with the ultimate aim of finding suitable coordinate transformation to collapse the measured mean velocity profiles onto a single curve.

Proper scaling of a fluid flow is a particularly powerful technique for turbulent flows where complete analytical solutions are not available. However, a review on recent developments in scaling of turbulent flows have signified the fact that none of the scaling approaches satisfactorily represent all experimental data reported in different studies, despite the large number of attempts and complicated theories developed [*Buschmann and Gad-el-Hak*, 2007; *Ghisalberti*, 2009; *Jiménez*, 2004; *Mizuno and Jiménez*, 2011; *Nezu and Nakagawa*, 1993].

2.3.3 Conventional scaling methods for flows over rough bed

Many attempts have been made to provide acceptable scaling for the velocity profiles of flows over a rough bed. This section considers some possible scaling methods that are available in the literature for the conventional boundary layers and open channel flows.

Empirically, the classical log-law has often been employed for normalizing the velocity profiles observed in the rough-bed channel flows (e.g. [*Birch and Morrison*, 2011]). If the flow depth above the porous roughness elements is large, the log-law not only applies for the inertial layer but may also provide an acceptable approximation for the entire flow. However, in the region near the wall, the bursting phenomena occur most violently and cause a local imbalance in turbulence production and dissipation. Therefore, it would not be appropriate to scale the velocity profile in the roughness layer in the same manner as implied by the log-law. In Fig. 2.3, y/k_s is plotted against u/u_* with experimental data from literature, showing that the relation between them is not unique. It varies with both the bed configuration and flow depth.

Furthermore, for the condition of small roughness submergence, the roughness layer may become relatively thick and extend up to the free surface, while the logarithmic layer would become thin and might even disappear. As a result, several studies have suggested that the boundary layer theory may fail for the flow with roughness submergence smaller than 10 [*Katul et al.*, 2002], or 40 [*Jiménez*, 2004]. In other words, the scaling that underlies the log-law would not be applicable for the open channel flow under small submergence conditions. Therefore, it is reasonable to normalize the velocity profiles observed in the surface layer with the scales that characterize the roughness layer rather than the inertial layer, where the log-law holds.

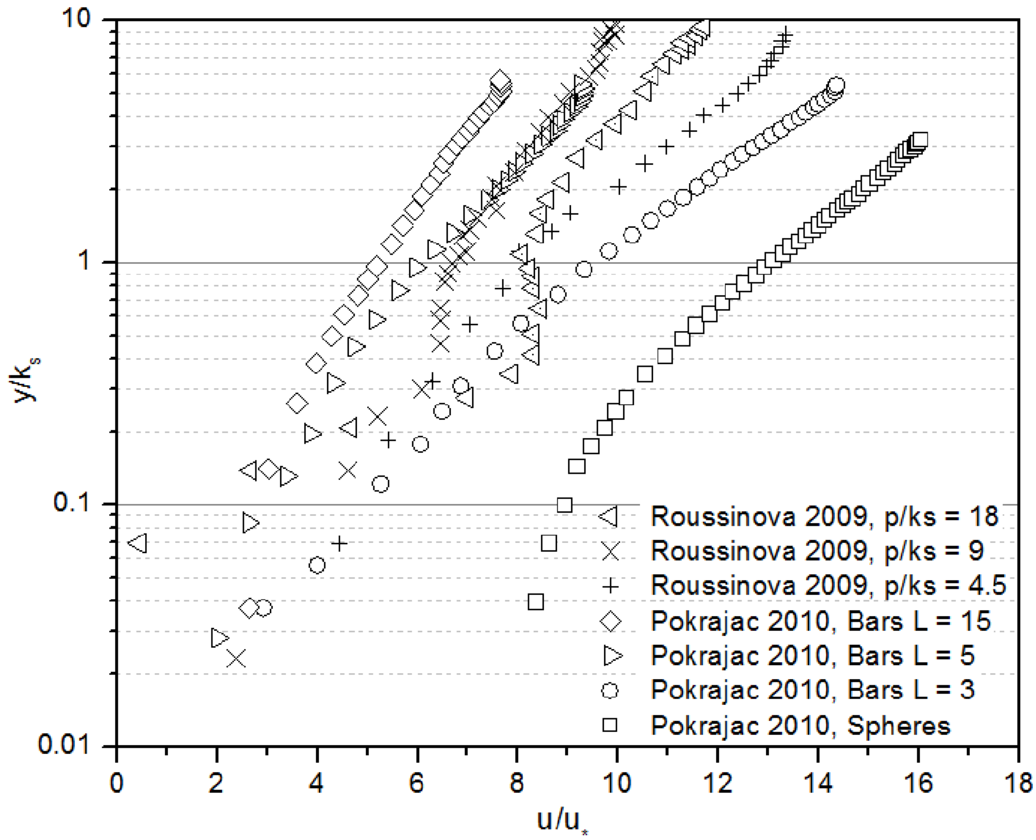

Fig. 2.3: Scaling of velocity profiles using shear velocity and roughness height

Besides the log-law, this study also considers the possibility of applying the velocity-defect law to scale the velocity profiles. Fig. 2.4 demonstrates the application of this relationship to the experiment data, showing that there is still a considerable degree of scattering associated with the data points plotted.

On the other hand, the power-law of scaling also has a rigorous basis and was even considered more fundamental than the log-law [*Afzal*, 2001; *Barenblatt*, 1993; *Cipra*, 1996]. Its envelope is claimed to enclose the log-law, recalling an issue that was previously raised by Prandtl which suggested that the log-law is a limit form that can be obtained from the power-law at sufficiently large Reynolds number [*Afzal*, 2001; *Barenblatt*, 1993; *Prandtl*, 1935]. In applying the power-law to scale the velocity profiles in the surface layer, the velocity can be normalised by the maximum velocity U_{max} (also known as the free-stream velocity), while the length scale can be represented by H_s – the depth of the flow portion above the roughness crest. It is known that the power-law in the form of $u/U_{max} = (y/H_s)^{1/m}$, with m varying from 6 to 7, may approximate to a large extent velocity profiles observed in regular open channel flows [*Cheng*, 2007].

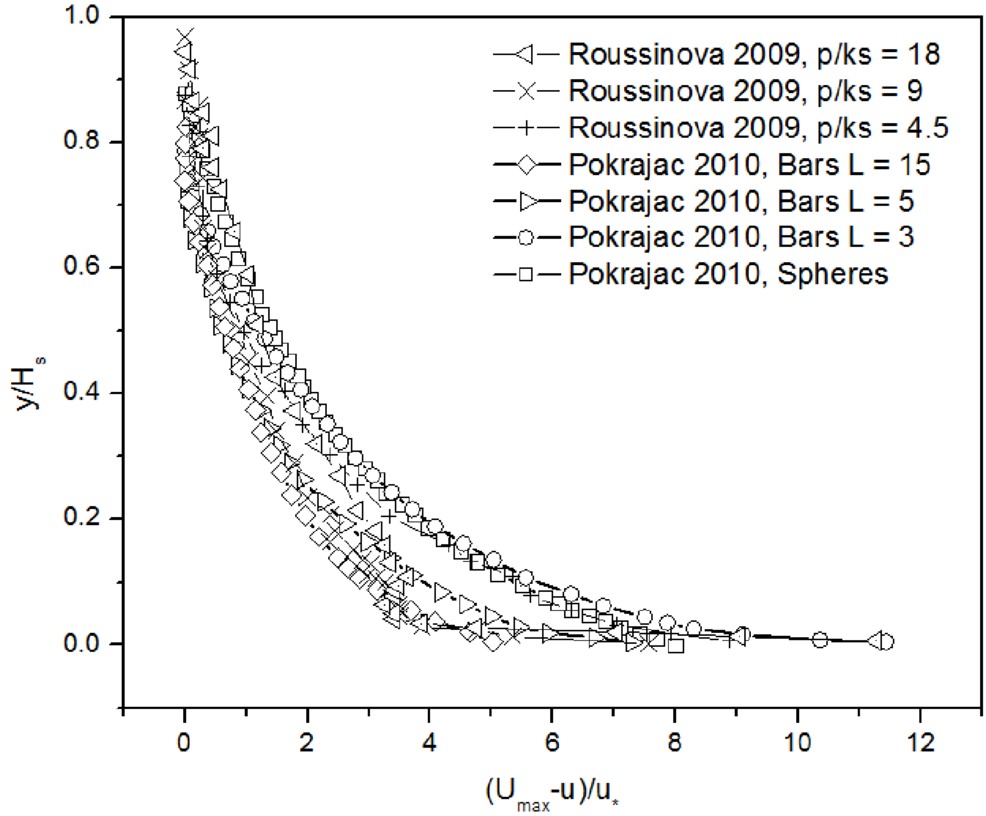

Fig. 2.4: Scaling of velocity-profiles using velocity-defect, shear velocity and flow depth

By using the free-stream velocity scale, *George and Castillo* [1997] also suggested a power-law that matches both outer and inner layer velocity profiles for a turbulent boundary layer. However, there was another problem that the outer layer slip velocity at the wall turned out to be zero and modifications are certainly needed, e.g. for permeable bed conditions [*Afzal*, 2001]. Moreover, the power-law scaling typifies the incomplete self similarity, which is also consistent with the spread of velocity data points when plotted with a narrow range of m-values [*Afzal*, 2001; *Cheng et al.*, 2012b]. The scattering of the data points plotted in Fig. 2.5 does not support the power-law with m-values in a narrow range. These facts imply that either or both of the selected velocity and length scales could be inappropriate.

Scaling in the outer layer is dependent on the global properties of the flow. For example, in a closed channel flow, the only obvious outer length scale is the channel half-height h. A proper choice of the velocity scale appears even harder and various proposals could be considered. The friction velocity u_* is the most commonly used quantity. From the analogy with pipe flow, *Zagarola and Smits* [1998] argued that the mass flux deficit, $U_{CL} - U_b$, is a true outer velocity scale, where U_{CL} is the centreline velocity and U_b is the bulk velocity. However, *Bakken et al.* [2005] showed that this velocity scale is of no advantage to the shear velocity u_* when applied to turbulent flow in a channel with rough walls.

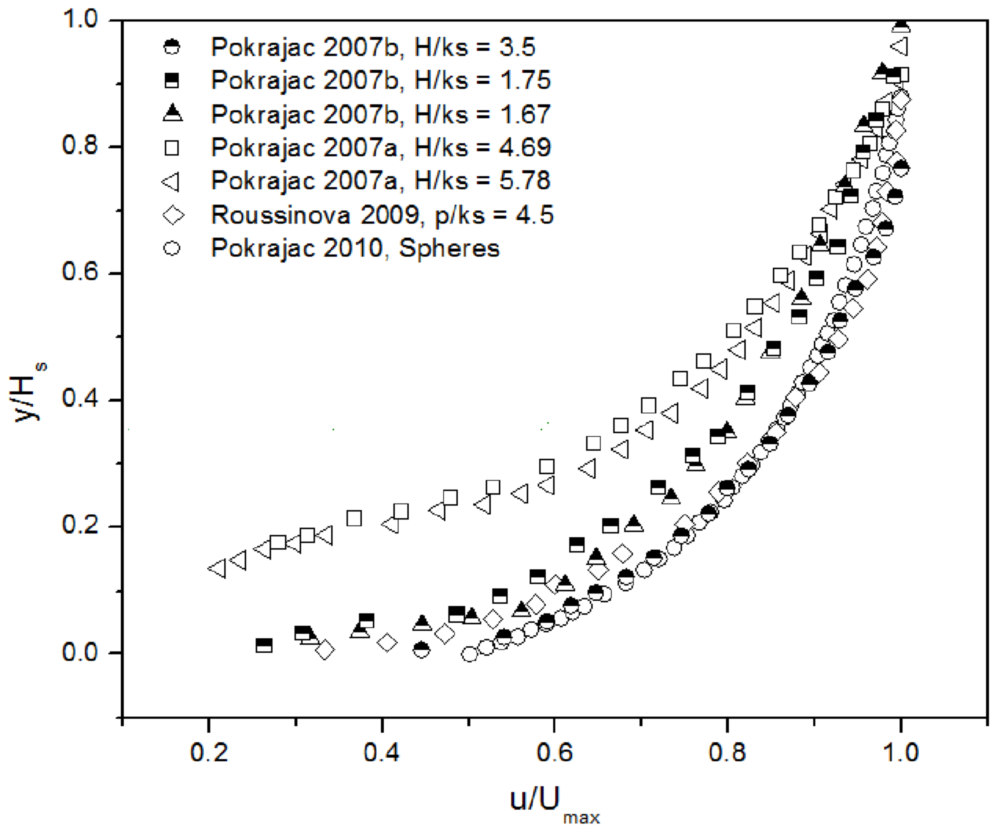

Fig. 2.5: Scaling of velocity profiles using maximum velocity and surface layer thickness

Summary

There are many characteristic length and velocity scales that have been proposed in the literature. The above review reveals that the existing scaling arguments fail to realistically describe the mean flows under the rough-bed, depth-limited conditions. In Chapter 5 , the measured velocity profiles will be normalised with a new approach proposed by this study.

2.4. Flow through permeable rough bed

2.4.1 Interaction between subsurface and surface flows

Mountain rivers typically have a rough bed comprises of gravels and/or boulders of different sizes, inside which the pores are interconnected, forming a permeable medium. Being shallow and steep, a significant portion of the total flow goes through the porous bed, especially at low flows. This subsurface flow rate was found to be proportional to the bed porosity, mean bed material size, square root of bed slope, and weakly proportional to the stage of the flow [*Codell et al.*, 1990].

For flows involving rough and permeable boundaries, the role of the bed permeability is twofold. It not only permits flow to pass through the porous medium when a pressure gradient is applied, but also gives rise to a complex interaction between the turbulent flow above the bed and the seepage flow below. As a result, a finite slip velocity U_0 occurs at the surface of the porous bed, which invalidates the no-slip condition usually applicable at the flow boundary. This is an important property of this kind of flow, which produces fundamental changes in flow characteristics [*Mendoza and Zhou*, 1992a]. For this study's tested flows, the slip velocity U_0 for each test case was obtained with the aid of PIV and PTV techniques.

Detailed simultaneous measurement of flow above and within the wall has been known as a difficult task. Hence, this study attempts to account for the subsurface flow effect on the mean-stream velocity profile by proposing an approximate solution. A schematized velocity profile of the flow has been presented in Fig. 2.6, where u_p is the bulk or superficial seepage velocity; $U_p = u_p/\varepsilon$ is the intrinsic seepage (pore) velocity of fluid in the porous medium; ε is the bed porosity; and H_s and H_p are the depth of flow above and below the permeable interface, respectively. Several studies have found that inside this permeable bed, the mean flow velocity decreases exponentially from the value of U_0 at the interface to the value of U_p away from it (e.g., the work done by *Zhou and Mendoza* [1993]).

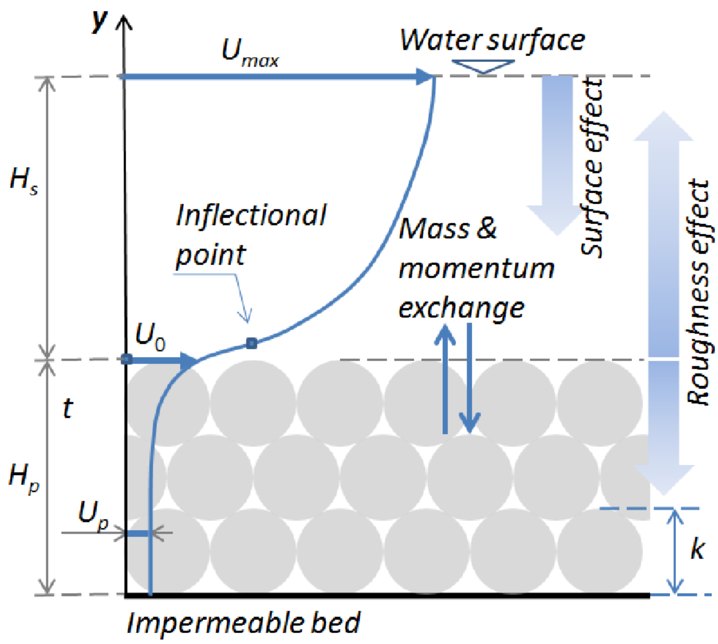

Fig. 2.6: Schematized velocity profile of the flow

On the other hand, the fluid motion in the porous bed is not only subjected to the seepage gradient, but also affected by the fluid shear stress at the interfacial level (τ_0). This shear-stress effect induced by the free stream decreases very rapidly with the depth below the bed surface, so that its effect vanishes at roughly the height of the first pore surface [*Das Gupta and Paudyal*, 1985; *Pokrajac et al.*, 2007a]. This is also consistent with a subsequent finding by *Goharzadeh et al.* [2005] and *Gualtieri [2010]*, who pointed out that the transition layer thickness is of the order of one grain diameter d rather than the square root of the permeability k. It suggests that at some distance below the interface (i.e. $y \leq -t$, where t is the thickness of the transition zone or the Brinkman layer), normal pressure-driven seepage flow occurs at a rate that can be computed from the hydraulic gradient.

Approximation of flow rate through a porous bed

Since the transition layer thickness is small, the velocity distribution in the transition zone can be reasonably approximated by a linear variation from U_0 to U_p *[Das Gupta and Paudyal, 1985; Goharzadeh et al., 2005]*. Thereby, the total underflow through the porous bed, Q_p, is estimated as

$$Q_p = B\left[H_p U_p + \frac{t}{2}\left(U_0 - U_p\right)\right] \tag{2.9}$$

where B is the channel width. In the section that follows, the estimation of the seepage velocity U_p will be discussed.

2.4.2 Characterisation of subsurface flow

At first, the flow through a porous wall with high porosity is far from creeping flow that is governed by the Darcy law. With a relatively higher seepage velocity and a substantial pore space within the wall, the deviation from the Darcy law takes place because of flow separation at the lee side of particles and the possible onset of turbulence. There are two typical formulations that are often used as extensions of the Darcy law for inertia-dominated flows through porous media, namely quadratic and power laws [*Cheng et al.*, 2008b]:

$$i_p = a_1 u_p + a_2 u_p^2 \tag{2.10}$$

$$i_p = a_3 u_p^b \tag{2.11}$$

where i_p is the hydraulic gradient; a_1, a_2 and a_3 are coefficients; and b is the power varying in the range of 1–2. In their earlier work, instead of considering various geometric simplifications of porous media, *Cheng et al.* [2008b] suggest that the situation here should involve only two parameters, namely the redefined friction factor f_p and Reynolds number Re_p that include the effects of porous media. Their dimensional analysis showed that

$$\mathrm{Re}_p = \frac{U_p R_p}{\nu} = \frac{1}{1-\varepsilon}\frac{u_p d}{\nu} \tag{2.12}$$

$$f_p = \left(\frac{u_{*p}}{U_p}\right)^2 = \frac{\varepsilon^3}{1-\varepsilon}\frac{gdi_p}{u_p^2} \tag{2.13}$$

where ν is the kinematic viscosity of fluid, $R_p = \varepsilon d/(1-\varepsilon)$ is the hydraulic radius and also a characteristic length of the cross-sectional area of the flow in a pore, and $u_{*p} = \sqrt{gR_p i_p}$ is the seepage shear velocity. Since the hydraulic gradient i_p is proportional to the squared shear velocity, u_{*p}^2, Eq. (2.12) and (2.13) can be rewritten in the following dimensionless form [*Cheng et al.*, 2008b]:

$$\left(\frac{u_{*p}R_p}{\nu}\right)^2 = C_1\left(\frac{u_p R_p}{\nu}\right) + C_2\left(\frac{u_p R_p}{\nu}\right)^2 \quad \text{or} \quad \mathrm{Re}_{*p}^2 = C_1 \mathrm{Re}_p + C_2 \mathrm{Re}_p^2 \tag{2.14}$$

$$\left(\frac{u_{*p}R_p}{\nu}\right)^2 = C_3\left(\frac{u_{*p}R_p}{\nu}\right)^M \quad \text{or} \quad \mathrm{Re}_{*p}^2 = C_3 \mathrm{Re}_p^M \tag{2.15}$$

where $\mathrm{Re}_{*p} = u_{*p}R_p/\nu$ is the seepage-related shear Reynolds number; C_1, C_2 and C_3 are coefficients; and M is the exponent. The relation given in Eq. (2.14) actually has the same form of the Ergun equation [*Ergun*, 1952], i.e.

$$i_p = C_1\frac{\nu(1-\varepsilon)^2}{gd^2\varepsilon^3}u_p + C_2\frac{1-\varepsilon}{gd^2\varepsilon^3}u_p^2 \tag{2.16}$$

where C_1 = 150 and C_2 = 1.75 are two coefficient values proposed by Ergun. In terms of the pore-based friction factor f_p and Reynolds number Re_p, Eq. (2.14) and Eq. (2.16) can both be rewritten to be

$$f_p = \frac{C_1}{\mathrm{Re}_p} + C_2 \tag{2.17}$$

This suggest that the Ergun equation with C_1 = 150 and C_2 = 1.75 can be applied to estimate the hydraulic gradient i_s, i.e. the pressure drop ΔP of flow through a porous bed of length L.

However, the Ergun equation applies only for the porous medium composed of packed spheres when the wall effects are negligible, i.e. the characteristic dimension of the cross section of the porous bed (l_p) is sufficiently larger than the sphere diameter, say, l_p/D > 40 [*Cheng*, 2011b]. Otherwise, the wall effect could cause the prediction of Eq. (2.16) to differ significantly from measurements [*Winterberg and Tsotsas*, 2000]. It has been pointed out that both the porosity and the ratio l_p/D should be used to take wall effects into account when relating f_s to Re_s [*Cheng*, 2011b; *Montillet et al.*, 2007]. A simple correction of the wall effect, i.e. the modification of the two constants involved in Eq. (2.17), has been derived based on the concept of hydraulic radius [*Mehta and Hawley*, 1969]. However, the two constants cannot be predicted correctly using the correlations available in the literature, in particular for very low values of l_p/D [*Cheng*, 2011b].

2.4.3 Influence of the subsurface flow on main-stream flow resistance

It is difficult to accurately predict the friction factor in channels with porous bed, which is often encountered in many natural stream. Generally, regardless of the thickness of a permeable bed, the friction factor has been taken as equal to that of an impermeable bed flow with the same bed materials or hydraulic roughness height, which clearly overlooks the mass exchange and energy dissipation between the surface flow and the porous bed. Intuitively, it can be expected that when the surface flow depth is comparable to the thickness of the packed bed layer with high permeability, the proportion of seepage flow is significant, and the effects of wall permeability on the flow resistance cannot be neglected.

In fact, there are important interactions occur between the surface flow and the subsurface one. These include energy dissipation, and the exchange of mass and momentum, which are responsible for additional shear stresses near the boundary [*Nezu*, 1979]. Zagni and Smith [1976] & Zippe and Graf [1983] investigated the turbulent open channel flow over permeable and impermeable rough surfaces and claimed that the permeable boundary resistance was higher than that of the impermeable boundaries having an identical surface rugosity. Meanwhile, the measurements of Gupta and Paudyal [1985] for velocity distribution and permeability of a permeable gravel bed have concluded that the logarithmic velocity distribution can be preserved if the reference datum starts from one third of the bed median diameter. They also found that the von

Karman constant may decrease to 0.28, subjected to the porous gravel bed. This indicates that the boundary resistance of permeable bed is higher compared to that of an impermeable bed with the same surface roughness. Mendoza and Zhou [1992b] reported that the presence of a passive plane porous bed in an open channel will generally cause the friction factor to be directly proportional to the Reynolds number. On the other hand, the proposed method to predict the bed permeability by measuring the hydraulic gradient over a certain reach of the bed has been proved to be very useful for investigating porous bed problems.

To the author's understanding, the existing investigations are mostly focused on the effect of the porous boundary on the characteristics of open channel turbulence flow, while very few experiments manage to test the flow within permeable layers, as it is challenging to get the detailed information concerning the flow inside the porous media. The primary reason is the limited access of standard measurement devices like Laser Doppler Velocimetry (LDV), Particle Image Velocimetry (PIV) and some intrusive current meters (e.g., Acoustic Doppler Velocimetry) to the subsurface region. Recently, Manes et al. [2006] and Manes et al. [2011a] used Ultrasonic Velocity Profile (UVP) to measure the velocity fields inside the porous medium composed of pheres packed in cubic pattern. Using an experimental arrangement that facilitate the measurement with many parallel straight pore channels inside the bed layer, they found it was impossible to apply UVP in nature random packed granular beds with complex porous patterns. The necessary instruments and techniques that can provide satisfactory information is yet to be introduced. Beside some efforts that have been paid to resistance of flow over permeable bed (Gupta and Paudyal [1985], Manes et al. [2006] and Manes et al. [2011a]), studies focused on the friction factor of flow pass through the rectangular packed porous layers are very limited.

2.5. Main-stream turbulence characteristics

Turbulence in open channel flow is considered as one of the most challenging topics and so far has not been well understood. There have been extremely different points of view presented, all of which have in common their complexity, as well as an inability to solve the problem completely [*Kundu and Cohen*, 2008; *Lesieur*, 1987]. It is even more difficult when it come to understanding the turbulence in a shallow flow in conjunction with the presence of a permeable rough bed. Such flow conditions do not allow a strict analytical study, and one would depend heavily on experimental investigation and dimensional analysis.

2.5.1 Turbulence structure in flows with small roughness submergence

Turbulence in flows with small roughness submergence has been reported to be quite different from that of flows with sufficient submergence [*Nakagawa et al.*, 1991]. The latter has been investigated to accumulate quite a substantial knowledge, but there is currently a poorer understanding of mechanics and statistical properties of turbulence in shallow flows.

Studies applying flow visualization, Particle Image Velocimetry (PIV) and cross-correlation analyses for simultaneous velocity measurements have found that turbulence in open channel flows is not simply a random field, but rather characterized by the presence of turbulent structures in highly disparate scales. These turbulent motions range from the unstructured micro scale (incoherent) structures, to the larger scale organized three-dimensional (coherent) structures generated by the vertical shear at the confining boundary, to the quasi two-dimensional horizontal wakes, which are considerably larger than the water depth, generated by transverse instabilities in the flow (e.g., Ghidaoui and Kolyshkin [2004], Chen and Jirka [1998]). Coherent flow structures such as ejections and sweeps comprise the bursts in the inner region, whilst large-scale structures such as the hairpin/horseshoe vortices occur in the outer region (e.g., [*Adrian et al.*, 2000]). Grass [1971] suggested that different modes of instability might be dominated for different boundary roughness conditions.

Under shallow flow condition, the non-homogeneity of the bed geometry, caused by the various shapes, size and orientations of discrete particles, has a significant influence on the generation, growth, and dissipation of these coherent flow structures in the main-stream flow (e.g., Hardy et al. [2009]). Whilst the limited water depth was found to prevent the development of three-dimensional wakes, the transverse growth of perturbations was found to be suppressed by bottom friction, as evident by the absence of the regular streaky structures in the case of very shallow flow conditions [*Ghidaoui and Kolyshkin*, 2004; *Hardy et al.*, 2009; 2010; *Roy et al.*, 2004; *Sarkar and Dey*, 2010].

Perhaps the most prominent turbulence motion under investigation is the strongly three-dimensional coherent structures, which scale with the typical roughness size at the boundary. Several studies using photometry measurement techniques as well as numerical models have found that these structures are quite similar to those formed through classical bursting phenomena, as illustrated in Fig. 2.7a. However, their size was found to be proportional to flow depth, Reynolds number and bed roughness [*Hardy et al.*, 2009; *Roy et al.*, 2004]. Compared to that in flows with sufficient submergence, the bursting phenomenon was found to be suppressed in the case of relatively shallow flows (see for example [*Nakagawa et al.*, 1991]).

The classical bursting phenomenon, produced by the shear effect at the channel bottom, is characterized by cycles of ejection and sweep events of the boundary layer near the solid boundary. These events were found to present in flows irrespective of the bed roughness [*Grass*, 1971]. The ejection phase is associated with ejection of low momentum fluid up and away from the boundary, while sweep phase corresponds to the transport of high momentum fluid down towards the boundary [*Grass*, 1971; *Nezu and Nakagawa*, 1993]. An example type of coherent turbulent structures is hairpin vortices as shown in Fig. 2.7b. Recent works done by *Papanicolaou et al.* [2011, 2012] have also successfully captured the eddy structure within the vicinity of individual roughness element, which provided further insight on a relevant topic.

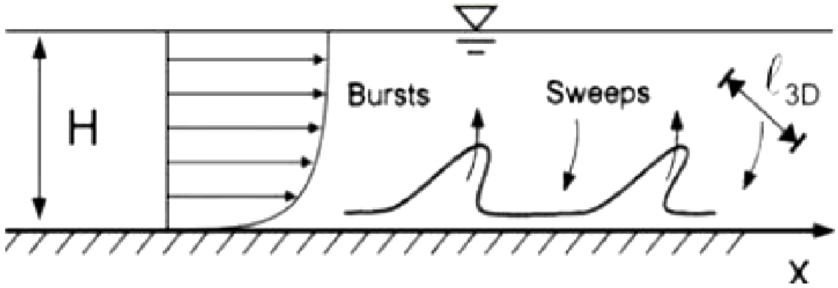

(a) Coherent flow structures in open channel - side view

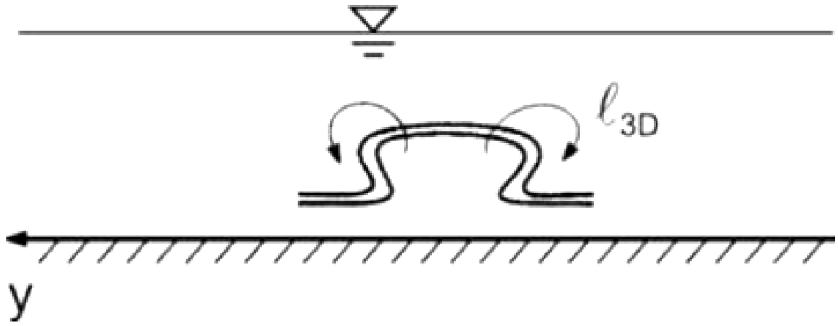

(b) Hairpin vortex - downstream view

Fig. 2.7: Schematics of turbulent shear flow (after Jirka and Uijttewaal, 2004).

Similarly, the morphology of the coherent turbulence structures in flow with rough bed and shallow conditions is characterized by intermittent ejections and sweeps. In an ejection event, small eddies move upwards from the bed, being stretched while advancing downstream above low-speed streaks and gradually decay. Such ejections are linked with sweeps (inrush events) as intertwined elements of a randomly repeating cycle, whereby inwards high-speed fluid is brought towards the boundary by weeps [*Grass*, 1971]. By investigating the correlation of the fluctuating velocity components, Nakagawa et al. [1991] found a suppression of the turbulence intensities and Reynolds stress in the roughness sublayer of flow with small roughness submergence. They suggested that the phenomenon is due solely to the suppression of ejections, which also cause the bursting on a rough bed to be indistinguishable.

Another important phenomenon regarding flows over large-scale roughness has been reported was the hairpin (or horseshoe) vortex formed upstream of individual obstacles (topographic protrusions) and shedding of vortices from the flow separation zone in the their lee side (as sketched in Fig. 2.8). In their study, Nakagawa et al. [1991] found a relatively periodical velocity fluctuation of low frequency, restricted in the roughness sublayer. They thus suggested that the momentum exchange is, to a certain extent, subjected to the organized flow structures associated with eddy-shedding from the individual roughness elements. In fact, the (topographically) protruded gravels represent various discrete obstacles that generate instabilities along the separation zone shear layer, behind which the oscillatory structures were formed, growth and breakups. This fundamental mechanism of the wake flow (also known as wake flapping) in the separation zone downstream of obstacles also induces the formation of the coherent structures near gravel beds with relatively large gravels of various shapes and orientations [*Hardy et al.*, 2009; *Kirkbride*, 1993].

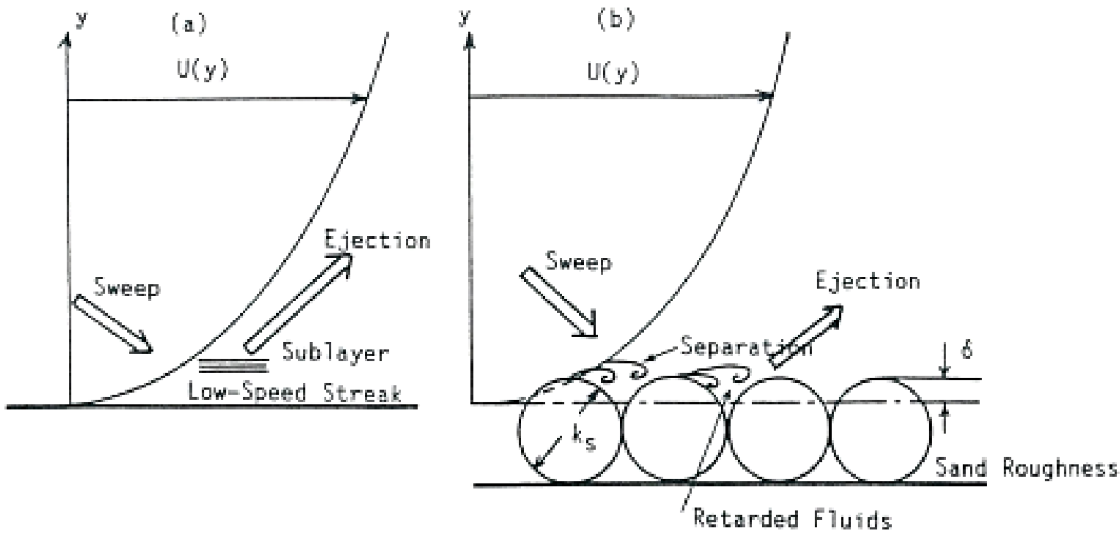

Fig. 2.8: Schematics descriptions of turbulent flow over smooth (a) and rough beds (b) (after Nezu and Nakagawa, 1993).

It is not clear to what extend each type of the turbulent structures discussed above dominates the near bed flow. On one hand it could be though that the flow over hydraulically smooth beds is dominated by the bursting phenomenon and flow over rough beds is dominated by the wake induced turbulence [*Vollmer et al.*, 2002]. On the other hand, it has been reported that coherent structures of flows over gravel beds have wall-generated turbulence origin, while the large-scale outer layer structures may be resulted from wake-flapping associated interactions in the near-bed region [*Hardy et al.*, 2009].

2.5.2 Influence of permeable rough bed on main-stream turbulence

The turbulence characteristics was induced by not only the wall roughness but also the wall permeability. From this angle, the behaviour of turbulent flow over permeable beds is also not well understood. In particular, it is not clear how the flow through the permeable bed affect the turbulence structure in the main flow, and vice versa [Manes et al., 2009]. It is possible to have different permeability with the same porosity, depending on how the pores inside a porous medium are interconnected. Typically, the composition of large-size, discrete particles causes these beds to be highly heterogeneous and permeable. Such bed configuration would strongly influence the turbulent structure of the main-stream flows [Sarkar and Dey, 2010]. With the presence of large-scale roughness, the subsurface flow that happens through the pores between solid beads is supposed to be substantial and hence, its influence on the mainstream flow should be accounted for.

The effect of bed permeability on flows over porous media could be characterized by using the permeability Reynolds number, $\mathrm{Re}_K = \sqrt{K}\, u_* / \nu$, which represents a ratio between effective pore diameter and the viscous length scale [*W P Breugem et al.*, 2006; *Manes et al.*, 2009]. In this definition, K is the permeability of the bed medium and $K^{0.5}$ is the turbulence length scale acting at the pores. The larger Re_K, the deeper turbulence eddies are able to penetrate into the wall, whereas for $\mathrm{Re}_K << 1$, the wall is considered impermeable.

Generally, the normalised Reynolds stress and turbulence intensities profiles in open channel flow over highly permeable beds are similar to those of typical open channel flows over impermeable rough beds. The measurements done by Manes et al. [2009] for open channel flows over highly permeable beds, characterized by very large value of Re_K ranging from 31.2 – 44.6, provide an example. Their finding is in agreement with Zippe and Graf [1983], who also found that the normalised vertical turbulent intensities profiles for the permeable beds collapsed reasonably well with those for impermeable beds.

However, a closer look at the turbulent flow over a highly permeable bed revealed that for the same bed roughness, the bottom-normal fluctuating velocity near the porous bed was found to increases with its permeability. This in turn yields a higher Reynolds shear stress and subsequently, an increase in friction factor of the turbulent flows over porous walls. Furthermore, the friction factor was found to be Reynolds number dependent in the hydraulically rough flow conditions. These are common conclusions resulting from the several research works, including Grass [1971], Zagni and Smith [1976], Stoesser et al. [2007], Hardy et al. [2009], Manes et al. [2009], and Suga et al. [2010].

Zagni and Smith [1976] claimed that the flow mechanism associated to shear penetration into the permeable bed is responsible for such an increase in friction factor. By facilitating a more efficient exchange of momentum between the surface and subsurface flows, a permeable bed effectively dissipate the flow energy and induces a higher flow resistance. Breugem et al. [2006] further showed that the turbulent flow over a highly permeable bed is dominated by relatively large vortices, which are known to be responsible for momentum exchange between the mainstream flow and the flow inside the permeable bed [*W P Breugem et al.*, 2006]. The presence of these vortical structures also significantly contributes to the Reynolds shear stress.

Another turbulence phenomenon is the high frequency pressure fluctuations observed in the near bed layer, induced by the periodic cycles of ejection and sweeps. It was identified irrespective of the wall roughness conditions. By using a novel measurement technique with the velocity probe positioned within the porous medium, Manes et al. [2009] found that a significant portion of turbulent kinetic energy (TKE) transported from the main-stream flow to the subsurface flow were mainly driven by pressure fluctuations, whereas turbulent velocity fluctuations only had a limited contribution to this downward transport of TKE, with their effects diminished beyond a thin layer below the interfacial layer. However, the majority of the high frequency pressure fluctuations was found to be damped at a depth of about few times the mean gravel size below the interfacial layer [*Vollmer et al.*, 2002].

In addition, it was observed that the streaks and the associated quasi-streamwise vortices are absent near a highly permeable wall. This phenomenon is claimed to be consistent with a decrease in the peak value of the normalised streamwise turbulent intensity at the permeable wall [*W P Breugem et al.*, 2006]. This effect dominates so that the peak value of the turbulent kinetic energy actually decreases despite an increase in the peak values of the transversal turbulent intensity.

Chapter 3

Experimental Setup and Procedure

To explore characteristics of shallow flows over permeable rough beds, a series of laboratory experiments were conducted with a range of flume facilities, bed materials, and bed porosities for different roughness submergences and flow conditions. This chapter describes the basic experimental facilities, measurement equipments and the raw data analysis techniques used in the present study. It comprises three main parts: Experimental setup and procedures for surface flow over gravel beds (Section 3.2), for surface flow over beds of glass spheres (Section 3.3), and for subsurface flow measurements (Section 3.4).

3.1. Test overview

Experiments were conducted in the Hydraulics Modeling Laboratory, Nanyang Technological University. Three different tilting glass rectangular flumes were utilized for the collection of a comprehensive set of data, all under depth limited conditions. There were eight sets of experiments carried out with sorted weathered gravels in two different tilting glass rectangular flumes A & B, four sets each (detailed in Section 3.2). In addition, five sets of experiments were carried out with uniform-size spherical glass beads (marbles) in Flume C (detailed in Section 3.3). Hereinafter they will be referred to as “gravel-bed tests” and “spherical-particle bed tests”, respectively.

Each set of experiments corresponds to a distinctive bed configuration, named after its number of gravel/marbles layers. A range of 0–4 layers was used in order to investigate the influence of the bed permeability and roughness on flow characteristics. For each type of granular material, the different bed configurations are characterized by the same roughness texture, and thus variations in surface flow velocities can be attributed to the effects of permeability.

To breakdown further, each set of experiments comprises of several different tests with varying flow discharge/depth. For each test case, the surface flow was characterized with the aid of either an intrusive (EMCM) or nonintrusive (PIV) measurement technique, whereas the subsurface flow was interpreted from measurements of hydraulic gradient (pressure drop) through a predefined reach of each porous medium. The measurement of subsurface flows will be detailed in Section 3.4.

3.2. Gravel-bed tests

3.2.1 Experimental facilities

Flumes (A) and its facilities

The first flume (Flume A) is made of glass. It measures 8 m in length, 0.3 m in width and 0.6 m in depth. The bed slope *S* can be adjusted by a screw-jack but was set to a fixed value of 0.001 during experiments. Bed slope was derived from longitudinal water depth variation while the flume was partially filled and water remained stationary. Generally, water depth was probed along the centre line of flume at 5–10 sections with the movable point gauge having a 0.1mm accuracy.

Water entered the flume after passing through a head tank and a flow straightener in order to stabilize the flow and minimize the entrance effect. A tail-gate installed at the end of the flume was used to adjust the flow depth and to achieve an almost uniform flow condition for each run. Measurements were then carried out at the section located between 5–6 m from the entrance. Water passing through the flume was collected by a tank position at the outlet and recirculated by two centrifugal pumps with a combined maximum discharge of 8.0 l/s. The flow rate was controlled by a mechanic valve and measured by a built-in electromagnetic flow meter. Fig. 3.1 shows a schematic drawing of the facility.

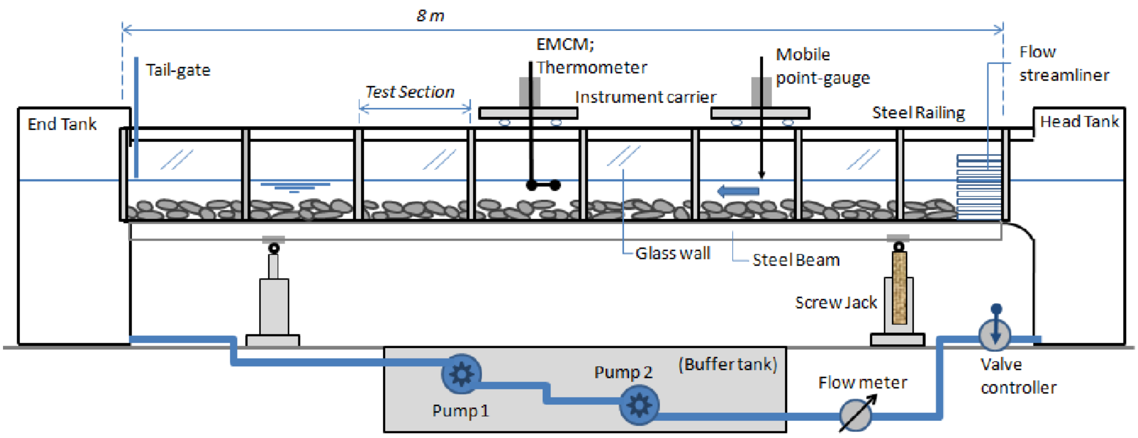

Fig. 3.1: Schematic drawing of Flume A and its facilities

Flume (B) and its facilities

The second flume (Flume B) has its sidewalls made of glass and its bottom made of galvanized steel. It measures 12 m long, 0.3 m wide and 0.45 m deep. The flume's bed slope can be manually adjusted by two screw-jack (as illustrated in Fig. 3.2) and was set to a value of S = 0.0064. The measuring section for flow velocities was located between 5–6m from the entrance. The flume was equipped with a motorized tail-gate to effectively adjust the flow depth and a centrifugal pump with a maximum capacity of 45 L/s. The flow rate can be controlled by an inverter and a mechanic valve. Flow discharges were measured by a built-in electromagnetic flow meter with standard deviations of 0.1–7.5%.

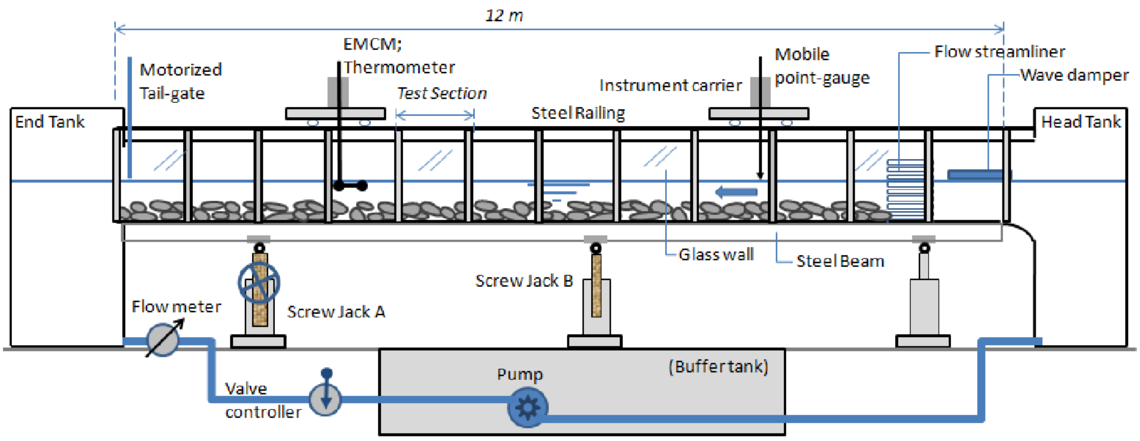

Fig. 3.2: Schematic drawing of Flume B and its facilities

An electromagnetic current meter (EMCM) and a point gauge with an accuracy of 0.1 mm were shared for both flumes to measure the flow velocity, flow depth and bed elevation. They were mounted on movable carriages running on flume rails and could be accurately positioned along the flumes.

3.2.2 Test conditions for gravel beds

All together, 40 sets of laboratory experiments were carried out under macroscopically uniform flow conditions, with varying bed configurations and roughness submergences in two flumes A & B. Various flow conditions were tested with Reynolds number Re ranging from 7×10^3–193×10^3, and Froude number Fr from 1.01–6.61. Here Re is defined as Re = $U{\cdot}H_s/\nu$, and Fr is defined as Fr = $U/(g{\cdot}H_s)^{1/2}$, in which H_s is the flow depth above the porous bed, $U = Q/(B{\cdot}H_s)$ is the estimated mean flow velocity, Q is the total discharge, B is the flume width, and g is the gravitational acceleration.

The bed slope was fixed at S = 0.001 in flume A and 0.0064 in flume B. Test conditions are summarized in Table 3.1, where 'A' and 'B' in the test names distinguish tests from the two different flumes; 'L1'–'L4' stand for different number of gravel layers placed on the flat bottom of the flumes (one to four); and 'Q1'–'Q5' stand for different flow rates in L/s. The adjacent columns list down H_0 and H_s, which are the depths measured from water surface down to the steel bottom of flume (reference elevation) and to the mean roughness surface elevation, respectively. H_p (= H_0 - H_s) is the height of the porous layer and will be clarified in a section that follows.

In these tests, the width-to-depth ratio B/H_s = 2.37–8.33, while the roughness submergence H_s/k = 1.11–3.89, k is the roughness size, taken to be D_{50}. In term of the roughness element effects [*Nezu and Nakagawa*, 1993], the flow investigated (with $k^+ = u_* k/\nu$ ranging from 86 to 200) falls into the category of completely rough bed (k^+ > 70), i.e. where the roughness elements penetrated into the fully turbulent logarithmic layer with negligible viscous effects.

Table 3.1: Experimental conditions and flow characteristics (Gravel beds)

Test	Q	S	H_0	H_s	H_s/D	U	Re	f
	l/s	-	cm	cm	-	cm/s	$x\ 10^3$	-
BL1Q1	22.431	0.0064	14.50	12.65	3.892	68.386	193.3	0.027
BL1Q2	18.545	0.0064	12.40	10.55	3.246	67.267	168.9	0.028
BL1Q3	13.190	0.0064	10.00	8.15	2.508	55.776	119.2	0.071
BL1Q4	8.239	0.0064	8.40	6.55	2.015	39.735	73.2	0.054
BL1Q5	3.468	0.0064	6.00	4.15	1.277	28.884	37.8	0.034
BL2Q1	21.870	0.0064	15.90	11.59	3.566	68.640	182.1	0.025
BL2Q2	16.980	0.0064	14.20	9.89	3.043	61.374	148.2	0.029
BL2Q3	12.710	0.0064	12.75	8.44	2.597	55.572	121.5	0.027
BL2Q4	7.120	0.0064	10.56	6.25	1.923	37.971	67.6	0.061
BL2Q5	3.250	0.0064	8.47	4.16	1.280	24.378	32.0	0.060
BL3Q1	21.624	0.0064	18.30	11.60	3.569	64.762	171.9	0.035
BL3Q2	15.677	0.0064	16.30	9.60	2.954	57.628	136.7	0.046
BL3Q3	11.924	0.0064	14.90	8.20	2.523	44.935	96.4	0.084
BL3Q4	7.304	0.0064	13.30	6.60	2.031	31.445	58.2	0.101
BL3Q5	3.464	0.0064	11.20	4.50	1.385	23.432	32.7	0.075
BL4Q1	20.575	0.0064	20.90	11.60	3.569	65.774	174.6	0.026
BL4Q2	15.636	0.0064	19.07	9.77	3.006	57.319	137.4	0.036
BL4Q3	11.529	0.0064	17.60	8.30	2.554	47.632	103.0	0.048
BL4Q4	7.148	0.0064	15.94	6.64	2.043	33.031	61.4	0.068
BL4Q5	3.388	0.0064	13.90	4.60	1.415	24.009	34.1	0.033

Test	Q	S	H_0	H_s	H_s/D	U	Re	f
	l/s	-	*cm*	*cm*	-	*cm/s*	*x* 10^3	-
AL1Q1	4.073	0.001	9.40	7.36	2.265	20.935	52.3	0.050
AL1Q2	7.097	0.001	14.50	12.46	3.834	25.155	72.6	0.034
AL1Q3	6.317	0.001	12.50	10.46	3.218	24.043	62.0	0.035
AL1Q4	2.785	0.001	7.90	5.86	1.803	17.443	29.4	0.049
AL1Q5	1.198	0.001	5.75	3.71	1.142	13.460	16.0	0.023
AL2Q1	8.127	0.001	16.20	12.20	3.754	23.532	76.0	0.069
AL2Q2	6.469	0.001	14.30	10.30	3.169	22.467	65.9	0.065
AL2Q3	4.477	0.001	12.00	8.00	2.462	19.142	48.0	0.080
AL2Q4	2.709	0.001	9.90	5.90	1.815	15.413	31.3	0.074
AL2Q5	1.127	0.001	7.90	3.90	1.200	9.766	14.5	0.053
AL3Q1	7.649	0.001	17.60	11.20	3.446	22.111	68.1	0.047
AL3Q2	6.163	0.001	16.00	9.60	2.954	22.218	62.5	0.093
AL3Q3	4.675	0.001	14.20	7.80	2.400	19.733	48.6	0.118
AL3Q4	2.549	0.001	12.00	5.60	1.723	13.849	27.1	0.060
AL3Q5	1.439	0.001	10.00	3.60	1.108	8.656	12.1	0.093
AL4Q1	6.339	0.001	19.20	10.33	3.178	19.044	46.6	0.070
AL4Q2	5.900	0.001	18.10	9.23	2.840	21.893	50.0	0.042
AL4Q3	4.174	0.001	16.15	7.28	2.240	17.183	33.7	0.076
AL4Q4	2.029	0.001	14.20	5.33	1.640	11.672	18.4	-
AL4Q5	1.043	0.001	12.50	3.63	1.117	6.017	7.0	-

The subsurface flow was estimated using a separate procedure and will be discussed in Section 3.4.

3.2.3 Characterisation of gravels and porous bed

Determination of gravels characteristics

Despite the fact that natural sorted sediments usually has a normal distribution for grain size, in laboratory experiments artificially sorted sediment is often used with uniform grain size distribution [*Garcia*, 2008]. In this study, one type of gravel was use for experiments in both flumes (see Fig. 3.3), having identical median grain size of D_{50} = 32.5 mm, determined by using Wolman pebble count procedure [*Wolman*, 1954]. The size distribution of the gravels is presented in Fig. 3.4.

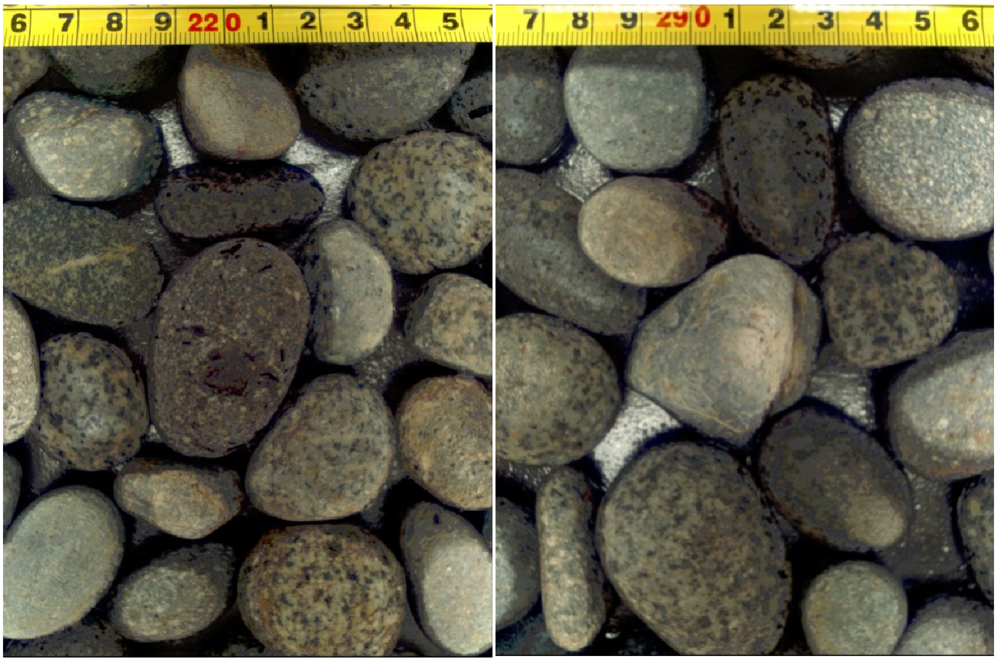

Fig. 3.3: Gravel samples

The Wolman procedure, known for its applicability to very coarse materials, was used in order to obtain an adequate representative description of the bed material. First of all, a reference grid having 100 nodes was defined within 1m length of the flume and the gravels falling under each node of the grid were picked up. The median diameter of each of these gravel grains were then meticulously measured by a Vernier caliper to the accuracy of 0.1mm. Results were subsequently sorted in terms of size and the percentages from which all the grains are finer were measured.

Other geometrical characteristics of the gravels were also obtained, namely d_{16} = 28.3mm, d_{84} = 38.0mm. The geometric standard deviation, σ = 1.16, was computed from these characteristic dimensions as $(d_{84}/d_{16})^{1/2}$. Being smaller than 1.6, it indicates that the gravel material was not poorly sorted.

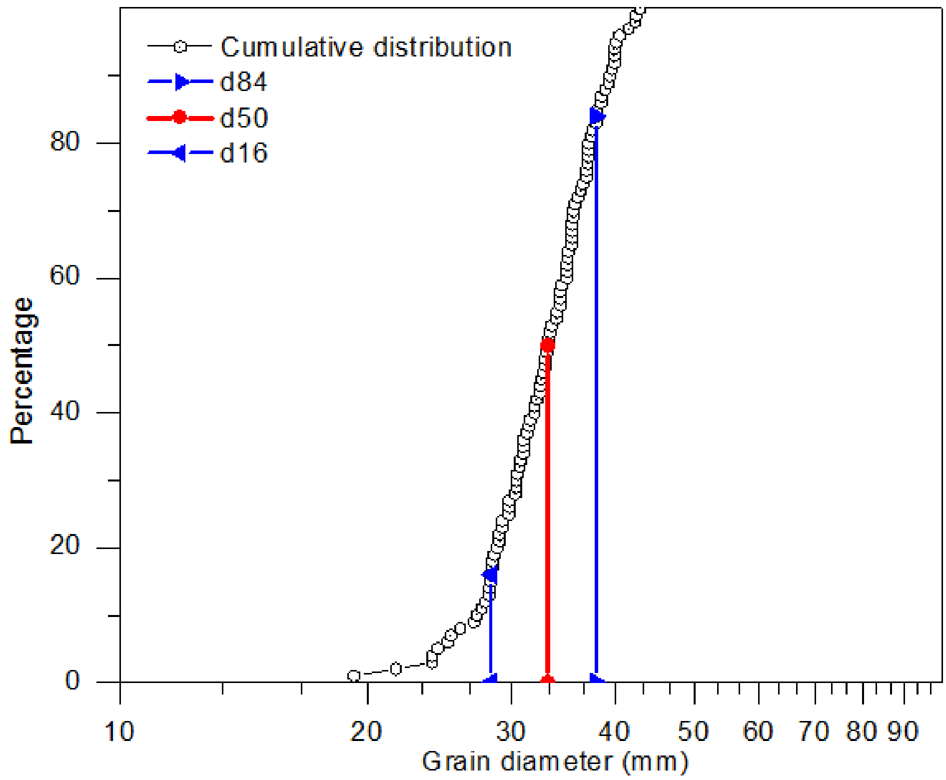

Fig. 3.4: Cumulative gravel size distribution

Determination of bed porosity

As mentioned earlier, the bed porosity is an important parameter affecting the subsurface flow. Its value varies considerably for each bed configuration due to the wall effect for small l_p/D_{50} (i.e., when the number of gravel layers are small). Generally the average porosity within the neighbouring of the wall is greater than that at a distance due to the so-called channelling effect [*Benenati and Brosilow*, 1962].

Therefore, a subsidiary test was carried out to measure the porosities of the gravel bed with considerable wall effect. In this test, a rectangular glass tank having an inner dimension of 97.4 by 47.8 cm was filled with random packed gravels. Water was then added into the tank in an incremental amount of 0.5L each time and water level readings were taken on the side walls. The porosity of the gravel medium associating with a particular layer thickness was then derived from the ratio of the voids volume (i.e., water volume V_f) to the total volume of the medium (V_0).

Repeating the test four times and the cumulative average porosity was obtained as shown in Fig. 3.5. It has a damped oscillatory wave form, which agrees with the void fraction distribution suggested by Benenati and Brosilow [1962]. For the porous media tested, which composed of naturally sorted gravels, the oscillation was found to damp out faster (2–3·D_{50}) compare to that in tests with regular spheres (4.5–5·D).

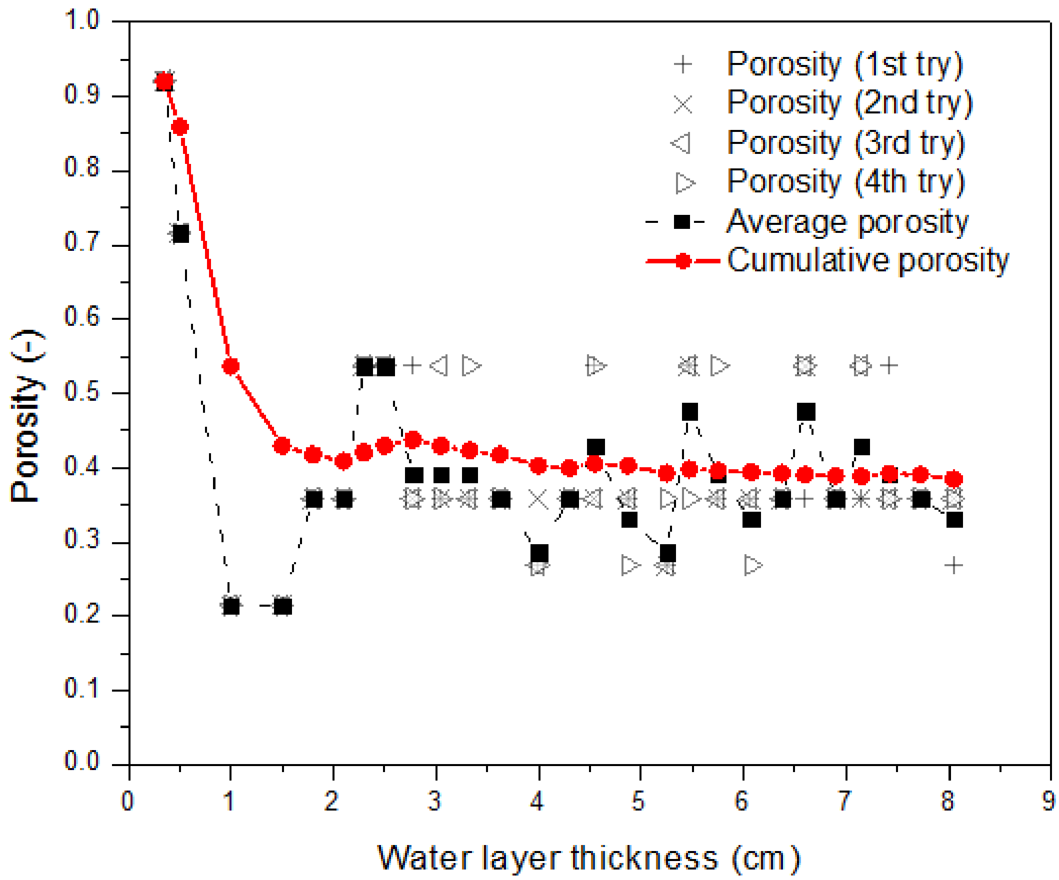

Fig. 3.5: Porosity variation with the layer thickness

The porosity values for all 8 sets of experiments using different configurations of these gravels were then interpolated using the average bed elevation values discussed in the next section. The porosities are summarized in Table 3.2 below. The porosity ε of the gravel material in this study, ranged from 0.37–0.58, is deemed typical for that of many natural gravel-bed rivers, whose ε ranged from 0.34–0.62 as reported by Darby [2005].

Table 3.2: Porosity values for different bed configurations

Case	H_p (cm)	H_p/D_{50}	ε	Case	H_p (cm)	H_p/D_{50}	ε
AL1	2.04	0.628	0.579	BL1	1.85	0.569	0.535
AL2	4.00	1.231	0.508	BL2	4.31	1.326	0.508
AL3	6.40	1.969	0.446	BL3	6.71	2.062	0.445
AL4	8.87	2.729	0.366	BL4	9.35	2.862	0.366

Determination of the average bed elevation

For each set of experiment, gravels were properly and evenly placed in the flume, covering the whole bottom from entrance to exit. Fig. 3.6 below shows a top view of the gravel bed over a stretch of 1.5m obtained with a Laser scanner (NextEngine). At the downstream of the flume, a steel mesh was installed to keep the gravels from any possible displacement.

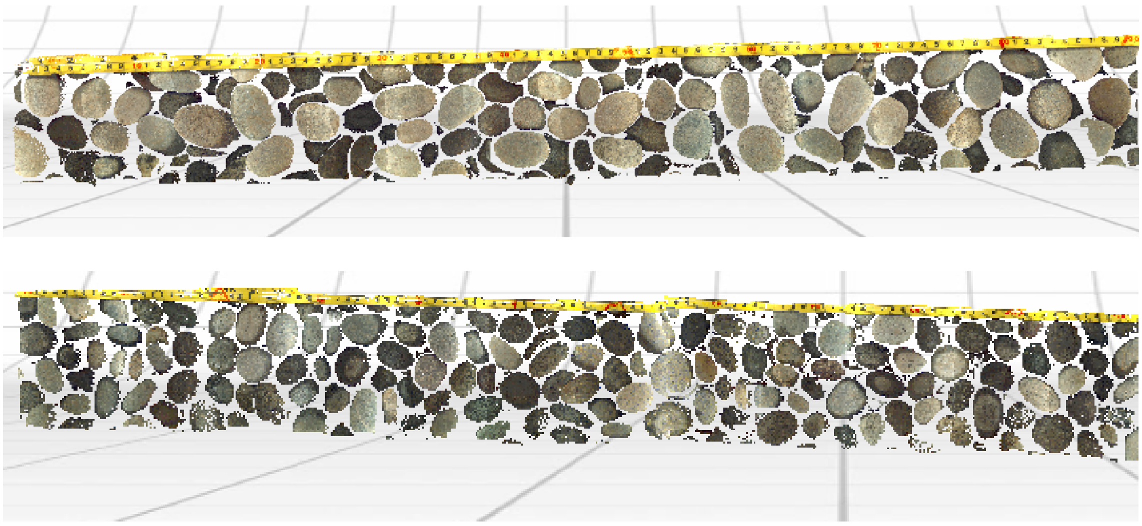

Fig. 3.6: Reconstructed images showing top view of the gravel beds (top: 2 layers; bottom: 1 layer)

Given the microscopic non-homogeneity of the bed geometry, it was important to set a datum for all subsequent velocity and depth measurements. The mean elevation (as sketched in Fig. 3.7) of the reconstructed bed surface was selected for this purpose. For each bed configuration, a point gauge with a resolution of 0.1mm was used to measure the height of the gravel layer from the flume bottom at approximately 140 equidistant verticals along the centre line of the measuring section, which were then averaged to get the mean bed elevation from the fixed flume bottom, also known as the average bed height (Hp). Table 3.2 above summarizes these base values for all 8 bed configurations.

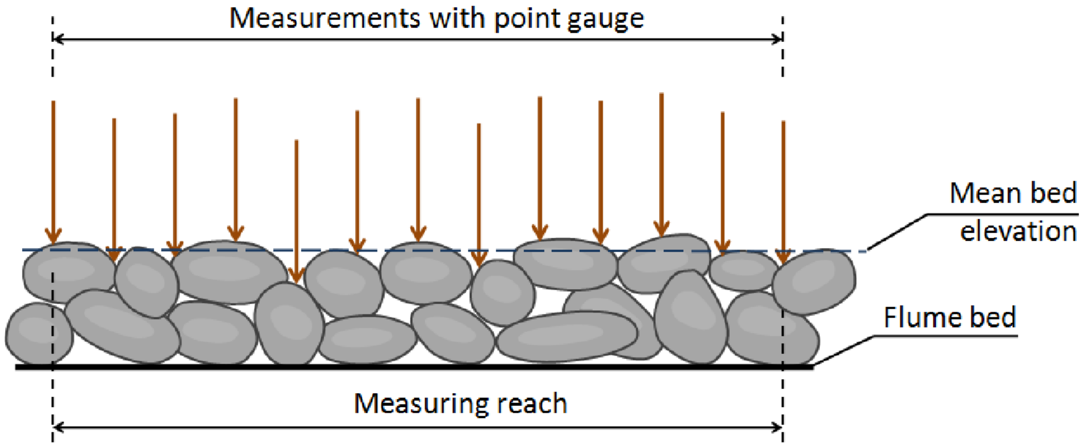

Fig. 3.7: Bed surface sampling method

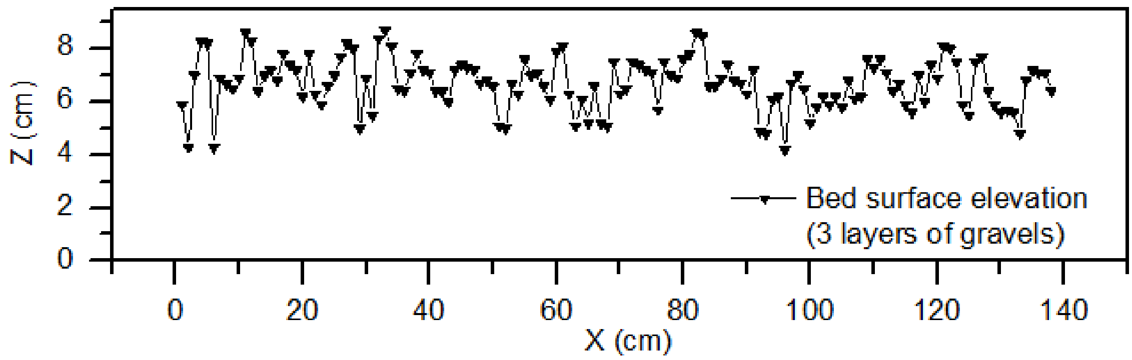

Fig. 3.8: Surface elevation of a gravel bed (3 layers)

3.2.4 Measurement of surface flow velocity

Test procedure

After the preparation of a gravel bed, the flume's pump and tailgate were adjusted to reach a macroscopically uniform flow condition in the flume at a desired flow depth. The flow depth was measured at five different locations along each flume's center line to ensure the uniformity, while flow discharge was monitored by each flume's dedicated electromagnetic flow meter to ensure its stability.

The test section located between L = 5 – 6 m from the flume entrance, sufficiently far for the flow to be considered fully developed (L/H_s ranges from 40 – 140, approximately). Experiments were conducted without influences from downstream disturbances since the test section was also far from the flume outlet and, on the other hand, all flow were supercritical.

For each test, velocity profiles were measured at nine equally spaced verticals in order to obtain a good spatial average of the velocity profiles. At each of these locations, a number of point-measurements were carried out to probe the whole flow depth. Depending on the specific flow depth, this number may vary, typically was 20–30 points. The finest resolution of 1 mm was used toward the roughness elements, while near the surface it might be as coarse as 5 mm. To gain a good temporal average of the velocity profile, each point was measured for a duration of 120 seconds, at the sampling frequency of 20 Hz. More detailed specifications of the instrument will be given in the following section.

Electro-magnetic current meter (EMCM)

To measure the streamwise and vertical components of flow velocity, a mini 2-dimensional electro-magnetic current meter (EMCM) was used (see Fig. 3.9). The device provides digital output, a high-speed sampling rate and is known for insusceptibility to electro-magnetic noise. The probe measures 4mm in diameter and 18mm in length and was positioned to point upstream. With this setting, the flow could be sampled from the gravel bottom up to 4mm below the free surface, where reading became less reliable.

Longitudinal and vertical flow velocities could be measured using one of the four ranges, namely ±25 cm/s, ±50 cm/s, ±100 cm/s, ±200 cm/s. Nominal accuracy for velocity values was ±2% of the full range adopted. The voltage signals were then translated to digital outputs through Labview system (National Instrument). With pre-calibration, they were then converted into flow velocities at a maximum sampling rate of 20 Hz.

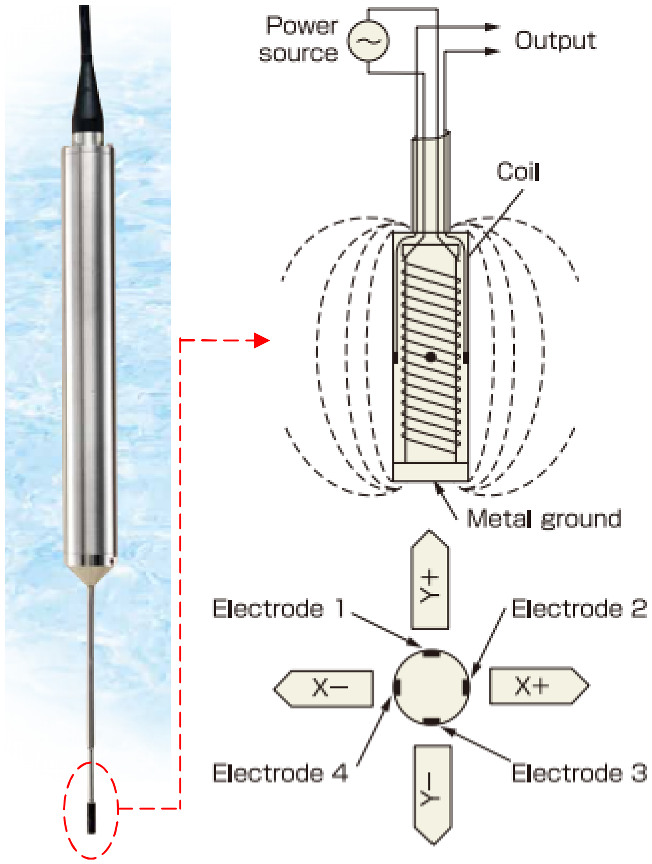

(PC & VM-802H Main Unit)

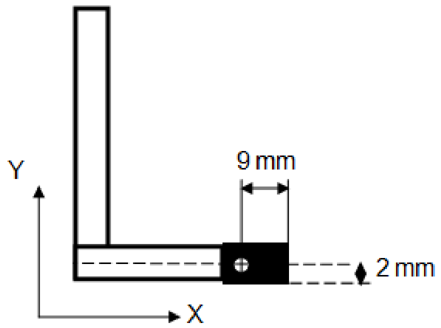

Principle of EMCM sensor (straight probe) (L-shaped probe configuration)

Source: JPE Advantech Co., Ltd.)

Fig. 3.9: Mini 2-D EMCM probe and its sampling principle

Each experimental session included a warm-up period to overcome the problem pertaining to EMCM probes' sensitivity to temperature variations. Generally half an hour was spent for both the acquisition system and flow condition to be stabilized. Prior to that, the EMCM was calibrated with a zero velocity reference by dipping the probe in a tank of still water for at least 10 minutes and subsequently set the velocity to zero on the main unit.

The small probe size of this mini EMCM made it suitable for measurements under shallow flow depths associated with this study. Other instrument such as Acoustic Doppler Velocimeters (ADV) was also made available to the study but was not as ideal because of the relatively large probe size compared to the limited flow depths. Nevertheless, comparisons were made between measurements done with EMCM, ADV and PIV to cross check the accuracy and confirm the measurement reliability. A comparison is presented in Fig. 3.10, showing that EMCM readings are reliable up to a distance of 0.02m below the free surface, which is about the probe length. This limitation had been taken into account during measurement.

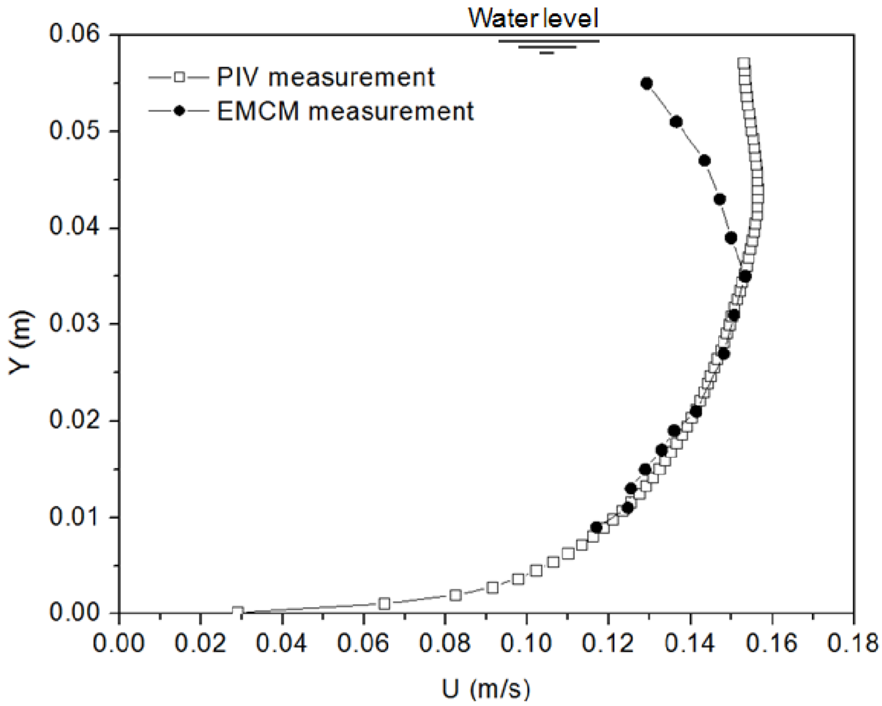

Fig. 3.10: Validation test with both EMCM and PIV measurements

3.3. Spherical-particle bed tests

Experimental set-up, installation and common facilities for tests with spherical-particle beds are generally similar to those described earlier for gravel-bed tests. The distinctive features are discussed in the following sections.

3.3.1 Experimental facilities

The experiments were conducted in a glass channel under depth limited conditions. The channel was 9.8 cm in width, 15 cm in height and 300 cm in length, as illustrated in Fig. 3.11. Both the channel wall and the impermeable fixed bed were smooth. Water was circulated by a centrifugal pump and controlled by a mechanical valve, providing a steady discharge in the range of 0-0.6 l/s. The total flow rates *Q*, measured with an electromagnetic flow meter, were then calibrated by volumetric measurement using a collecting device and a stop watch. Water temperature (*T*, in degree Celsius) was measured using a mercury thermometer to an accuracy of 0.1°C to account for the change in fluid kinematic viscosity, estimated by $\nu = \left[60/(T+40)\right]^{1.45} 10^{-6}$ (m^2/s), as proposed by *Cheng* [2008a].

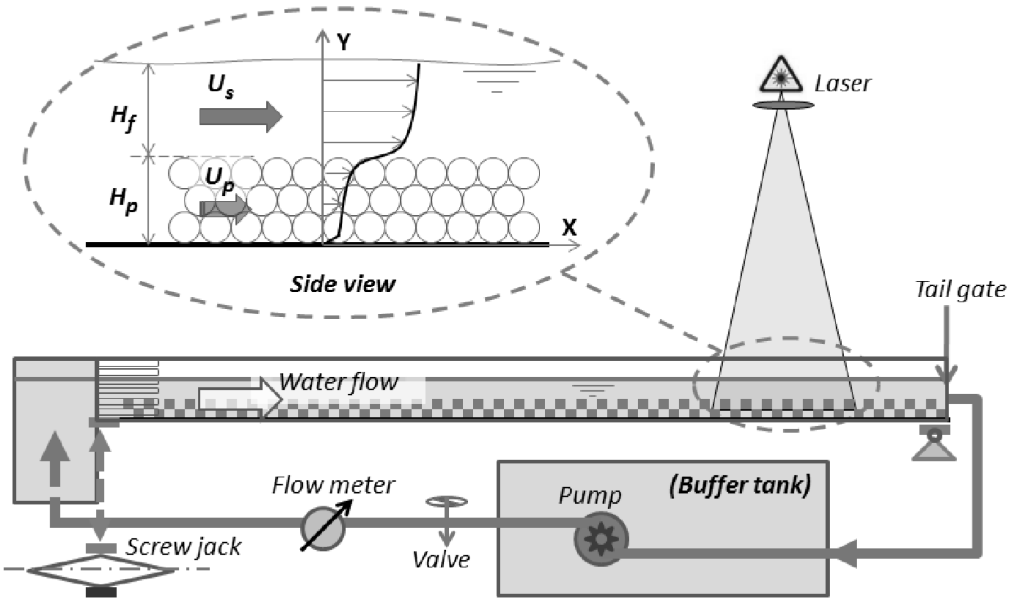

Fig. 3.11: Schematic drawing of Flume C and its facilities (Spherical-particle bed tests)

Bed preparation

The rough, permeable bed was constructed by placing layers of unisized spherical glass beads (d = 11 mm) over the impervious channel bed. The beads were packed in an alternate pattern and extended for the whole flume length. Bed configurations tested ranged from zero layers of spherical beads (impermeable bed) to four layers. The porosity ε of the artificial beds in this study, ranged between 0.35 and 0.43, is deemed typical for many natural gravel-bed rivers (whose ε ranged from 0.34–0.62, see *Darby* [2005]). Bed porosity, defined as $\varepsilon = V_f/V_m$, where V_f and V_m are the volume of fluid and the total volumes of the porous medium, were measured for each bed configuration and has been presented in Table 3.2 above. The permeability of these modeled porous beds was determined using a set of complementary tests, which will be discussed in detail in Section 3.4.

3.3.2 Test conditions for Spherical-particle beds

For measurement of the flow resistance, which is relatively more simple and straightforward, there were a separate set of 68 tests, which will be detailed in Chapter 4. Meanwhile, there were 20 more comprehensive sets of experiments for measurement of velocity profiles, which will be detailed hereafter.

These 20 tests were carried out over a range of bed configurations and roughness submergences, with bed slope fixed at S = 0.0012. All the tests were done in macroscopically uniform conditions, with the Reynolds number Re ranging from 1.29–8.87×10^3, and the Froude number Fr from 0.319–0.659. Re and Fr were defined in the same manner as that used in gravel-bed tests. These flows were found to be fully turbulent, which is consistent with the finding of *Suga et al.* [2010] who showed that the presence of a porous layer enhances the onset of turbulence so that it can take place at a Reynolds number as low as 1300.

In these tests, the width-to-depth ratio B/H_s = 4–10, where B is the flume width and H_s is the flow depth measured from the free surface down to the bead top, while the roughness submergence H_s/k_s = 0.91–2.27, where k_s is the roughness size, taken to be the same as the bead diameter. Since the flow depth and the roughness height are of the same order of magnitude, these experimental conditions can be classified under the large-scale roughness category, in the sense of *Ferro and Pecoraro* [2000]. In term of the roughness element effects, the flows investigated mainly involve hydraulically rough bed conditions (completely and incompletely rough bed). The roughness elements penetrated into the fully turbulent logarithmic layer and play a dominant role in comparison with the viscous effects [*Nezu and Nakagawa*, 1993]. It should be noted that working at these width-to-depth ratios there is the potential for secondary circulation although secondary flow is typically only a few percent of the average flow velocity [Colombini, 1993].

Test conditions are summarized in Table 3.3, in which H_p is the height of the porous layer, 'L0'–'L4' stands for the number of the layers of glass beads, and 'H10'–'H25' stands for the different flow depth (H_s) in mm.

Table 3.3: Experimental conditions and flow characteristics (Spherical-particle beds)

Test	ε	H_s	H_p	Q	T	ν	Re	Fr
	-	m	m	ls^{-1}	℃	m^2s^{-1}	-	-
L0-H25	0.0	0.025	0	0.698	29.8	8.03E-07	8869.5	0.575
L0-H20	0.0	0.020	0	0.572	30.0	8.00E-07	7298.7	0.659
L0-H15	0.0	0.015	0	0.342	30.0	8.00E-07	4363.9	0.606
L0-H10	0.0	0.010	0.0	0.166	30.0	8.00E-07	2118.1	0.541
L1-H25	0.430	0.025	0.0110	0.436	29.4	8.10E-07	5488.0	0.359
L1-H20	0.430	0.020	0.0110	0.312	29.5	8.08E-07	3934.4	0.359
L1-H15	0.430	0.015	0.0110	0.180	29.7	8.06E-07	2280.1	0.319
L1-H10	0.430	0.010	0.0110	0.102	29.7	8.06E-07	1292.1	0.332
L2-H25	0.373	0.025	0.0200	0.418	29.5	8.08E-07	5278.5	0.345
L2-H20	0.373	0.020	0.0200	0.322	29.5	8.08E-07	4059.9	0.370
L2-H15	0.373	0.015	0.0200	0.206	29.5	8.08E-07	2601.4	0.365
L2-H10	0.373	0.010	0.0200	0.108	29.5	8.08E-07	1363.8	0.352
L3-H25	0.362	0.025	0.0295	0.431	28.5	8.25E-07	5329.5	0.355
L3-H20	0.362	0.020	0.0295	0.322	28.5	8.25E-07	3981.6	0.371
L3-H15	0.362	0.015	0.0295	0.207	29.0	8.17E-07	2584.0	0.367
L3-H10	0.362	0.010	0.0295	0.107	29.3	8.12E-07	1344.1	0.349
L4-H25	0.357	0.025	0.0390	0.446	29.8	8.03E-07	5667.3	0.368
L4-H20	0.357	0.020	0.0390	0.327	29.9	8.01E-07	4163.8	0.377
L4-H15	0.357	0.015	0.0390	0.208	29.9	8.01E-07	2648.6	0.369
L4-H10	0.357	0.010	0.0390	0.102	30.1	7.98E-07	1304.2	0.332

3.3.3 Measurement of velocity profiles

Particle Image Velocimetry (PIV)

Flow velocity profiles were derived from velocity maps obtained using a two-dimensional particle image velocimetry (PIV) technique. It provides a nonintrusive, whole flow field measurement where information from multiple points on a 2-D plane and can be sampled simultaneously. The measurement of main flow and turbulence characteristics in shallow flows over large-scale roughness using PIV technique is known to be a challenging task, especially near to the rough bed where severe refraction of the laser light sheet is bound to happen due to the presence of roughness elements (see for example *Papanicolaou et al.* [2011; 2012]). The fundamental principle of PIV is given in Fig. 3.12, which basically involves three steps: to get the correct images, to extract the underlying velocity maps, and to perform further data analysis. The last step in this procedure, which largely contribute to the analysis of turbulence structure, will be discussed in Chapter 6. The majority of post-processing steps were realized by MATLAB scripts exclusively developed for this study. In general, measurement technique and post-processing methodology applied herein are similar to those previously described by Tuyen and Cheng [Tuyen and Cheng, 2012a; b].

The PIV system employed in this study was provided by Dantec Dynamics, as illustrated in Fig. 3.13. It consisted of an illumination system (Nd:YAG double-pulsed laser), a two-megapixel CCD camera with macro lenses, a synchronization board, a frame grabber, computer and dedicated software. Drivers and software from National Instrument Co., including NI-DAQ, NI-IMAQ, and MAX were used for controlling and setting the frame grabber, synchronization board and timer board. Meanwhile, Dynamic Studio version 2.1 (by Dantec) was the main software to control the image acquisition process, to render images into velocity vector maps, and to perform other post-processing analyses where deemed necessary.

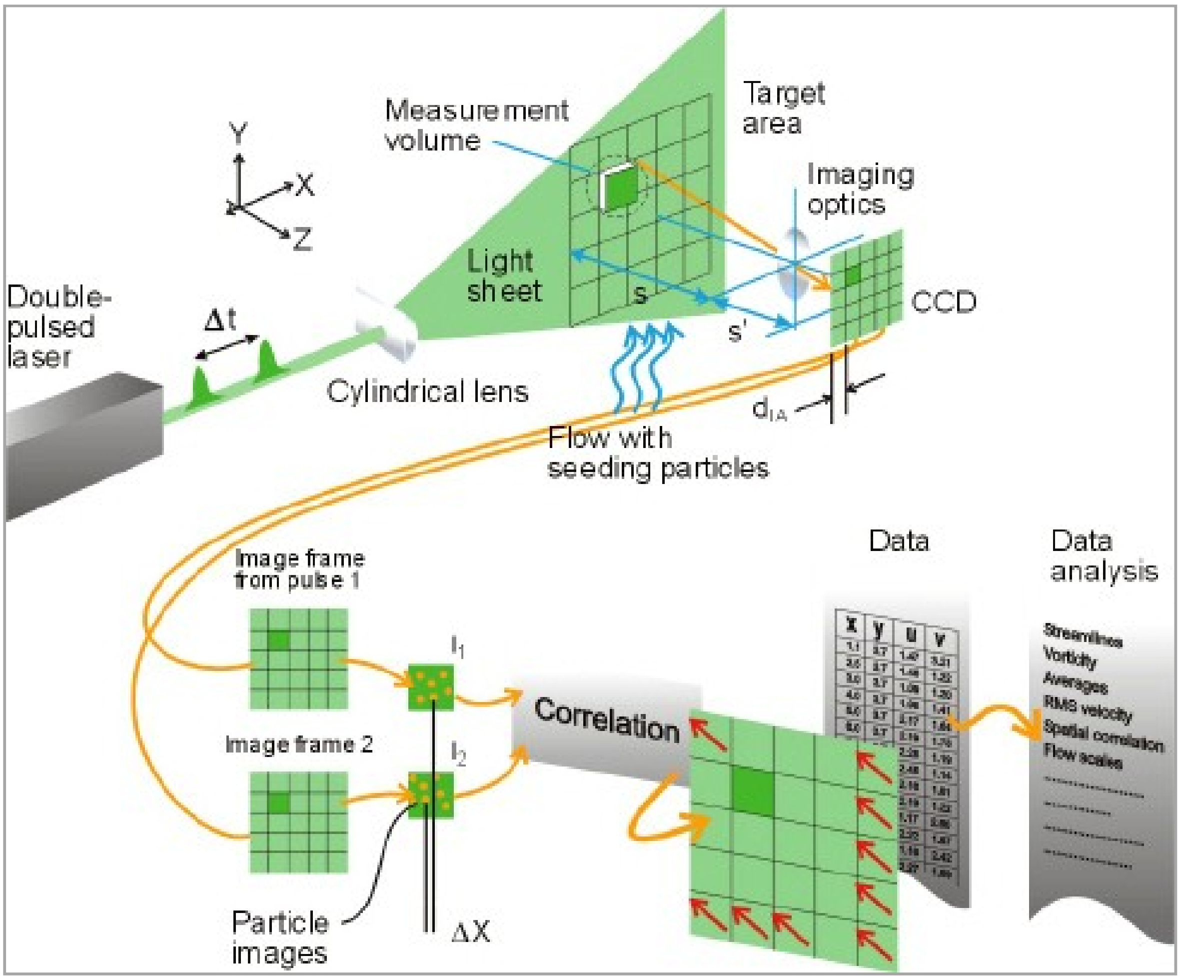

Fig. 3.12: Principle of Particle Image Velocimetry [*DantecDynamics*, 2002]

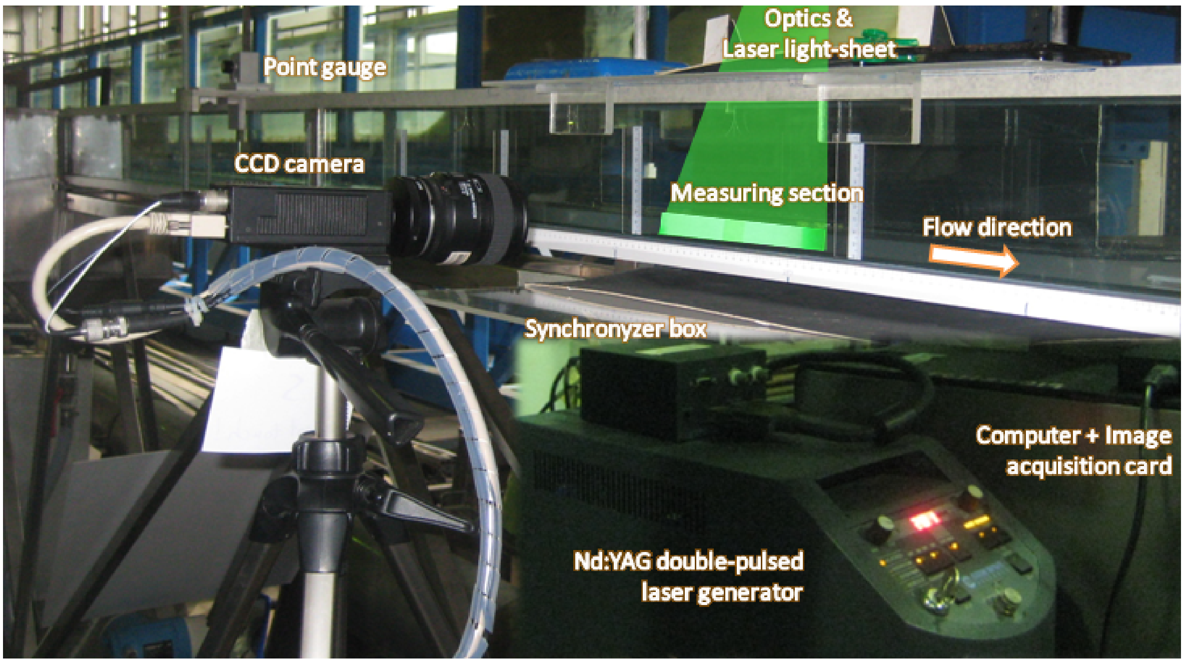

Fig. 3.13: Experimental facilities for measurements of velocity field with PIV

Polyamide seeding particles (d_t = 10μm) provided by Dantec were used as tracers. Being microporous and neutrally buoyant (ρ_t = 1.03 g/cm^3), they followed the fluid flow satisfactorily and at the same time scattered enough light to be captured by the camera sensor. The measuring section of the flow field was illuminated by the pulsed laser light sheet to produce a stroboscopic effect, adequately freezing the movement of the tracers over time. Image of the observation window was then captured by a CCD camera positioned perpendicular to the light sheet and the channel side walls. Its operation was synchronized with the illumination unit so that particle positions appeared as light specks on a dark background on each camera frame. For each test case, measurements were made at two vertical planes: one coincide with the centre-plane of the flume, and the other at a transversal offset of 0.5*D*, where *D* is the diameter of spherical glass beads (as exemplified in Fig. 3.14).

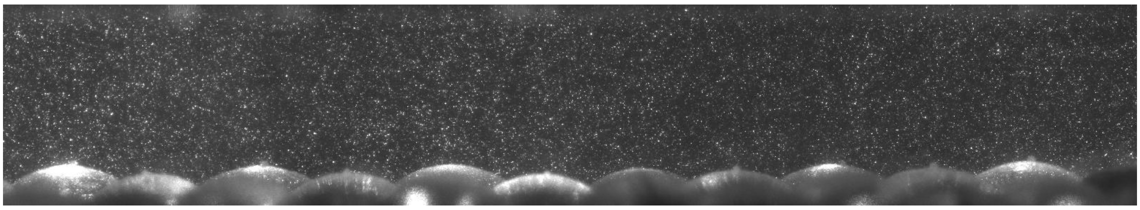

(a) Laser light-sheet positioned directly above roughness troughs

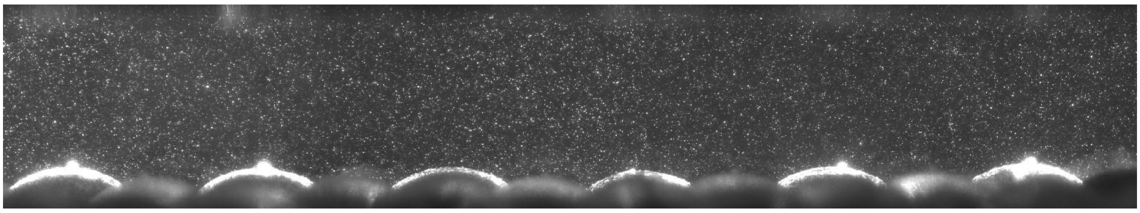

(b) Laser light-sheet positioned directly above roughness crests

Fig. 3.14: Sample image frames acquired with the PIV system (resized)

For each test, recordings were taken over a sufficiently long duration at the frequency of 15 Hz to yield a set of 1,000 double-frame, 8-bit gray-scale images. The number of images in each set has been found to provide a proper average of the flow characteristics, yet rationalizing the computational effort. For each image, its two frames were separated by an interval of Δ_p = 750 μs, providing a good impression of the instantaneous velocity field of the flow. An observation window of length 20×*D* was applied in order to obtain the statistically meaningful velocity profile from a very heterogeneous flow field. The observation window stretched 22cm in the longitudinal direction, from 251 – 263 cm from the flume entrance. This location ensured a fully developed, macroscopically uniform flow conditions for all test runs. Since the image frames had one dimension significantly larger than the other, a linear calibration was performed for each of the data set to yield almost undistorted velocity vector fields. Interrogation areas (IA) of size 16×32 px were used together with 50% overlapping cross-correlation yielding velocity vector map of 8×16 px resolution (approximately 0.32×0.64 mm). A truncated section of a typical velocity vector map obtained with PIV is shown in Fig. 3.15.

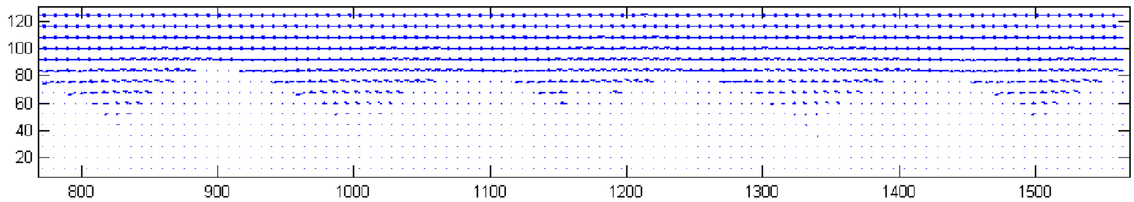

Fig. 3.15: Sample section of a velocity vector map (in pixel per frame unit)

The Cartesian co-ordinate system (*m*, *n*), as shown in Fig. 3.16, was used for the PIV analysis to transform the displacement [pixel/frame] in the image plane to velocity [m/s] in the measurement plane (*x*, *y*). For convenience, the symbols *m* and *n* were also used in MATLAB procedures to represent the matrix size (which contains information on velocities, positions, etc). An *m*-by-*n* matrix contains *m* rows and *n* columns.

Multiple PIV settings and measurement parameters were optimized via preliminary tests, including the image size, resolution, color depth, separation interval between frames, acquisition rate, and many others. The key parameters of PIV image acquisition and analysis are summarized in Table 3.4.

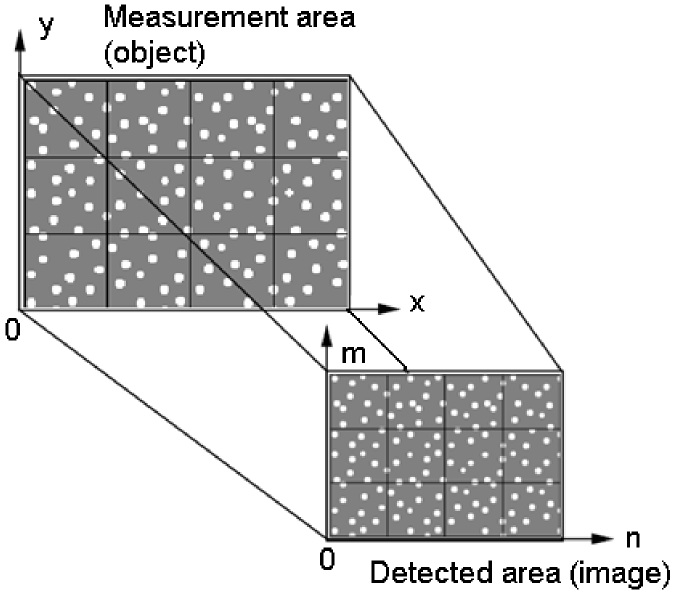

Fig. 3.16: Interrogation areas and the co-ordinate systems
for measurement plane and image plane

Table 3.4: Summary of PIV parameters

Parameter	**Dimension**	**Range**
Tracer (Polystyrene)	µm	10
Image size	$pixel^2$	(1600×330)-(1600×760)
Field of view	mm^2	(63.7×13.1)-(64.3×30.6)
Scaling constant	$mm \cdot pixel^{-1}$	0.0402 (smooth bed); 0.0401 (trough cases); 0.0398 (crest cases)
Images acquired	-	1000
Effective measurement time	s	67
Sampling rate	s^{-1}	15
Frame interval	µs	750
Interrogation area	$pixel^2$	32 (horz.)×16(vert.)
Overlap (in the horizontal direction)	%	50
Overlap (in the vertical direction)	%	50
Vector map resolution	pixel	16 (horz.)×8(vert.)
Velocity map resolution	mm	0.32×0.64
Typical number of velocity vectors (surface flow region only)	-	(99×17)-(99×44)

A problem pertaining to the use of DantecDynamics software for deriving velocity vector maps is the loss of information near the boundaries due to a finite IA size and the use of window functions. By overlapping IA, certain information near the edge of each IA could be retrieved. However, there is a permanent loss of information near the image boundaries. Fig. 3.17 illustrate a case where an overlap of 75% had been applied for the IAs of 64×64 pixel. After validations, even more velocity information is lost due to the loss-of-pair issue for tracer particles near the edges of solid roughness elements, as visible in Fig. 3.15 above. This is the major obstacle for interpreting the flow near the rough bed, and hence, the velocity measurement in this study has been enhanced by the use of particle tracking velocimetry (PTV) technique, which is briefly described in the subsequent section.

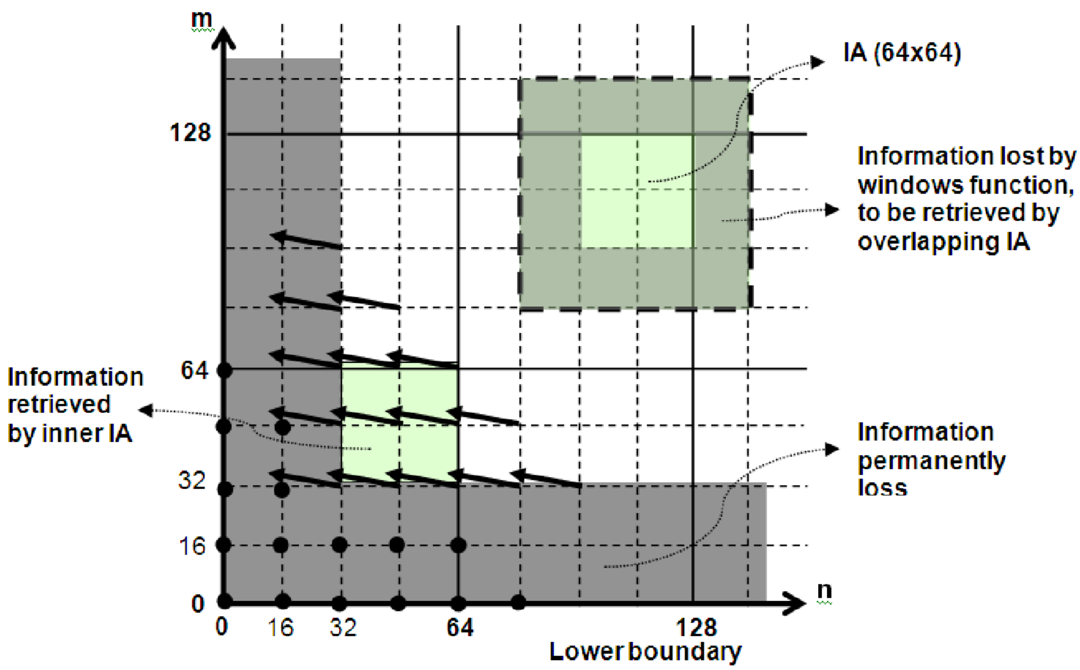

Fig. 3.17: Close-up view of information availability near the image corner, (illustrated with 64×64 pixel IA, 75% overlap)

Particle Tracking Velocimetry (PTV)

To overcome the aforementioned issue with PIV, the PTV technique was also employed in combination with a newly developed digital mask algorithm to gain details regarding the flow in the near bed region, especially the slip velocity U_0 for quantification of the subsurface flow. Compared to PIV, PTV algorithm effectively retrieve the missing information in the neighbouring of individual roughness element due to its capability to track every single tracer particle. The combined technique was developed to effectively deal with the complex bed topography, which differed from one test to another, and has previously been applied in the work done earlier by *Tuyen and Cheng* [2012b]. An example of the refined PIV and PTV results acquired is shown in Fig. 3.18, which illustrates the typical performance of the PIV and PTV techniques employed by this study. The vector maps are overlapped onto the original image for an unambiguous impression. This technique will be further discussed in the subsequent sections. Additional information and discussions regarding the PIV, PTV and relevant image processing techniques could be found in the works done earlier by the author [*Tuyen*, 2006; 2010; *Tuyen and Cheng*, 2012a; b; *Tuyen et al.*, 2014].

A quick comparisons were made between measurements done with EMCM and PIV for cross check the accuracy and confirm the measurement reliability. Results from the comparison are presented in Fig. 3.10 earlier, showing that the mean streamwise and bottom-normal velocities were well sampled. The mean velocity profiles were also validated using duplicated measurements by PTV.

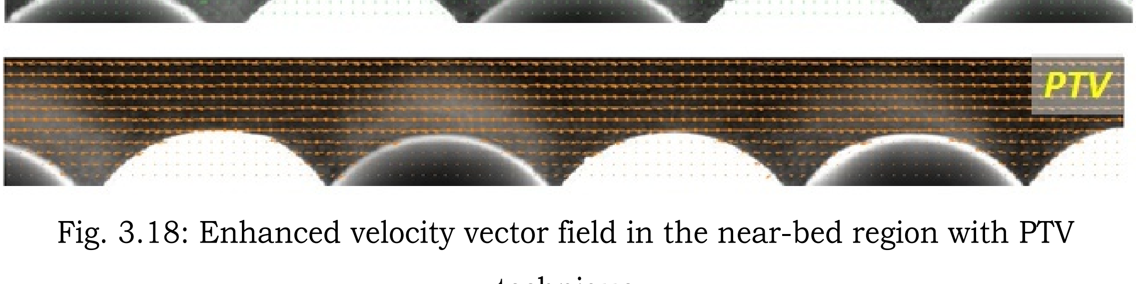

Fig. 3.18: Enhanced velocity vector field in the near-bed region with PTV technique

3.3.4 Double averaging analysis for interpreting surface flow velocity

To extract meaningful information from the large volume of raw data from measurements, statistical methods are needed. As mentioned earlier, PIV processing resulted in instantaneous whole-field velocity vector fields, thus information on spatially distributed parameters could be achieved (see for an example Fig. 3.19). Meanwhile, there were thousands of those vector fields resulting from each run (i.e. an ensemble), which made it possible to quantify the contribution of the temporal fluctuations of flow parameters. Therefore, a natural choice of analyzing technique would be the double-averaging analysis, which comprises of different temporal and spatial averaging operations.

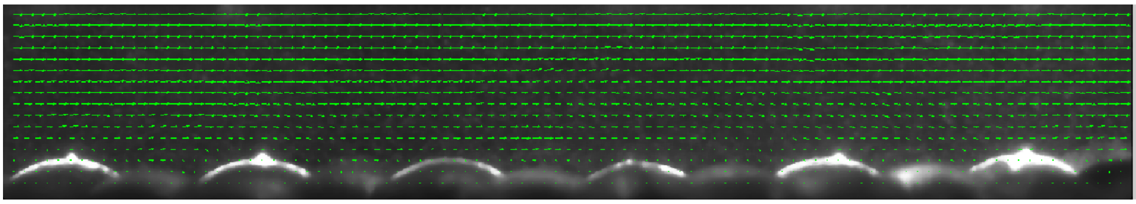

Fig. 3.19: Instantaneous velocity vector field (Spherical-particle bed test, case D1H15)

The first step involves a time-averaging operation for the velocity vector maps resulted from the PIV. For steady flows, the time average can be viewed as an approximation to the ensemble average, which is a more fundamental averaging process. It is a generalization of adding the values of the variable for each realization (a double-frame image) and dividing by the number of observations (number of images acquired for a given test case). A *realization* of the flow refers to a possible motion that could have happened, while an *ensemble* is known as the set of possible motions [*Roco*, 1993].

Generally, an infinite number of realizations of the flow is expected, which consists of variations of streamwise position, altitude, and velocities of the fluid particles (tracers). In practice, however, this ideal experimental condition should be justified and a limited quantity of realizations for each test case, usually 1,000, was adopted. This quantity of images in each test is large enough in order to provide a good statistical impression of the flow characteristics (see Fig. 3.20), yet being within the storage and processing capacity. It should be noted that due to the presence of the rough bed, this temporal average of the flow structure was three dimensional and highly heterogeneous.

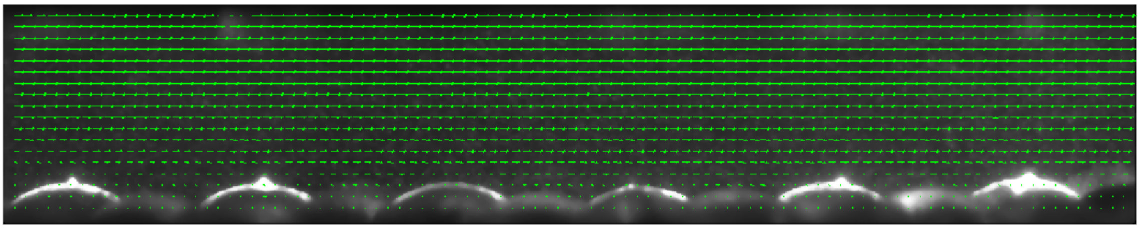

Fig. 3.20: Time-averaged velocity vector field (Spherical-particle bed test, case D1H20)

Further to the time-averaging operation, two supplementary spatial averaging steps in the longitudinal and transversal directions were then used in order to obtain the mean velocity profile over the flow depth. The first one spatially averaged the flow in the plane parallel to the bed, while the second one spatially averaged the flow over two parallel vertical planes, which were aligned with the longitudinal trough and crest of the rough bed, respectively.

The above so-called double-averaging (spatial and temporal averaging) method was conducted by a series of Matlab procedures developed along the course of the study and have successfully been applied earlier *[Tuyen and Cheng 2012a; b]*. They applied to the raw velocity vector maps (rendered by the commercial software Dantec Dynamic Studio) above the rough bed to get the bulk flow properties and other valuable information on the time-averaged turbulence characteristics of the flow. The suitability of this method for shallow flows over rough beds has been discussed previously by several researchers including *Nikora et al.[2001; 2007]*; *Manes et al.* [2007]; *Pokrajac et al.* [2009; 2007b]; and Sakar and Dey [2010].

3.3.5 Digital mask and PTV technique

To cope with the irregularity of the rough bed surfaces and the loss of accurate flow information in the neighbouring of those, the digital mask was extensively employed either

- to filter the double averaged velocity vector maps generated with PIV, or
- to subtract the roughness elements from every single image frame and subsequently perform PTV processing.

Matlab procedures were developed for the purpose of generating and applying digital masks automatically. It first applies the Sobel-edge mask algorithm, image filter and some simple arithmetic on the ensemble averaged image (shown in Fig. 3.21a) to compute the gradient magnitude map (Fig. 3.21b). The gradient is high at the edges of objects and mostly being low inside and away from them. After thresholding, the major (object) boundaries (Fig. 3.21c) were extracted from the gradient magnitude map. Another simple image processing tool was applied to remove small boundaries, which are subjected to noises (Fig. 3.21d). Subsequently, a couple of search functions based on morphology principle, originating from the mid-flow region towards the free surface and the rough bed, was applied to generate the desired digital mask in binary format (Fig. 3.21e). The generation of digital mask is illustrated with test case D4H10-trough, Spherical-particle bed test. The application of these masks is demonstrated in Fig. 3.22.

For each set of experiments corresponding with one bed configuration and a specific flow depth, a dedicated digital mask was generated. Using this technique, the rough bed elements can be effectively eliminated from the original flow image (Fig. 3.23a), resulting in so-called subtracted image (Fig. 3.23b). In binary format (0 and 1, which stand for valid and invalid pixels), it could be multiplied with image intensity map directly after conversion of the original 3-layer image frame and the pixels marked with 0 will be masked out and not taken into analysis.

(a) Ensemble averaged image

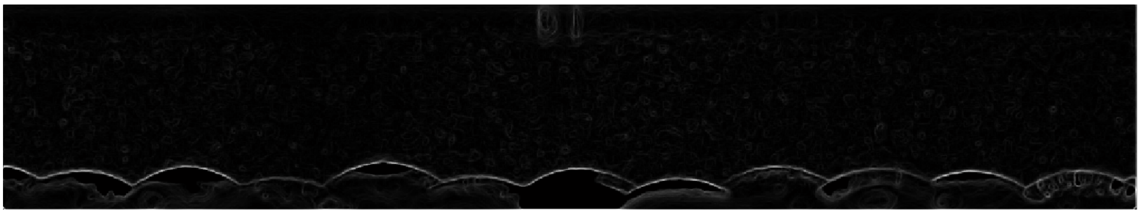

(b) Gradient magnitude map

(c) Boundary derived from gradient magnitude after thresholding

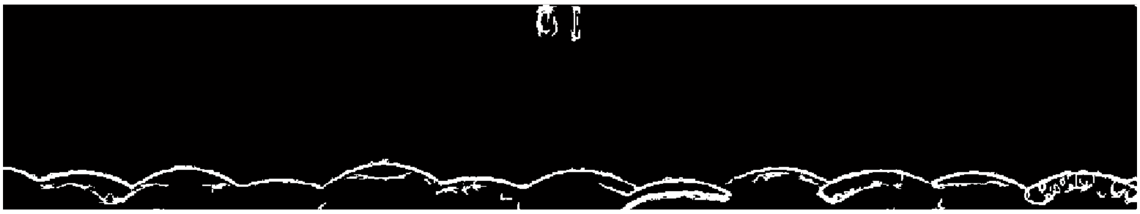

(d) Boundary after noise removal

(e) Digital mask found by morphologically searching functions

Fig. 3.21: Principle of digital mask generation

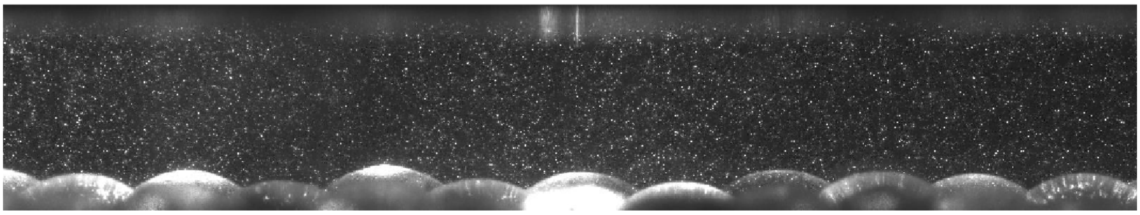

(a) Instantaneous image frame captured

(b) Instantaneous image frame with digital mask applied

Fig. 3.22: Application of digital masks in pre-processing stage

On the other hand, it could also be employed, with the aid of a supplementary procedure, to eliminated the erroneous velocity vectors in the interfacial and subsurface regions of PIV velocity vector maps (as illustrated in Fig. 3.23a & b). The effect is illustrated with the time-averaged velocity field for the same test case, which is case D4H10-trough, Spherical-particle bed test. It can be seen that PIV technique may result in certain spurious vectors in the interfacial region of the flow, subjecting to the lighting condition. However, the use of digital mask ensures that these erroneous vectors would be filtered out and not taken into further calculation of double-averaged flow velocity profile.

As discussed earlier, the PTV technique is capable to trace every individual tracer particles, providing a more detailed velocity vector field, especially in the near-bed region. This technique provides a very good impression of the instantaneous flow velocity field (Fig. 3.23a & b, for test case D4H10-trough). For the ease of double averaging subsequently, the velocity information could also be interpolated to a fixed regular grid (8-by-8 pixel) as illustrated in Fig. 3.23c & d. This figures shows an instantaneous velocity vector map, in which there are certain “white” area of no flow information. This is the nature of PTV as it tracks individual tracers for velocity information, while the tracers are randomly distributed in the flow.

A quick comparisons were made between measurements done with EMCM and PIV for cross check the accuracy and confirm the measurement reliability. Results from the comparison are presented in Fig. 3.10 earlier, showing that the mean streamwise and bottom-normal velocities were well sampled. The mean velocity profiles were also validated using duplicated measurements by PTV.

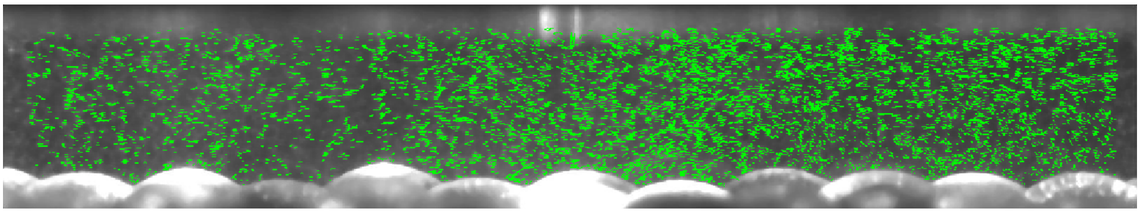

(a) Velocity vectors at individual tracer positions

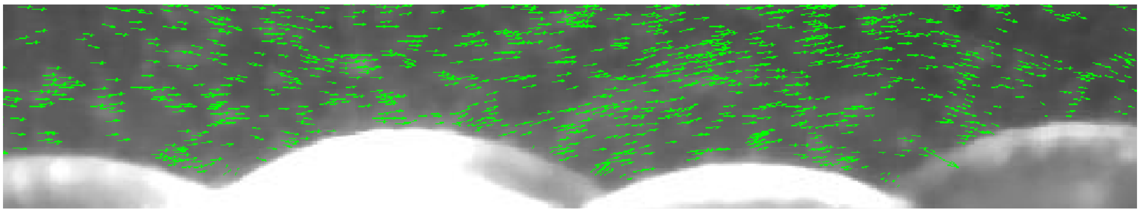

(b) Velocity vectors at individual tracer positions (close-up)

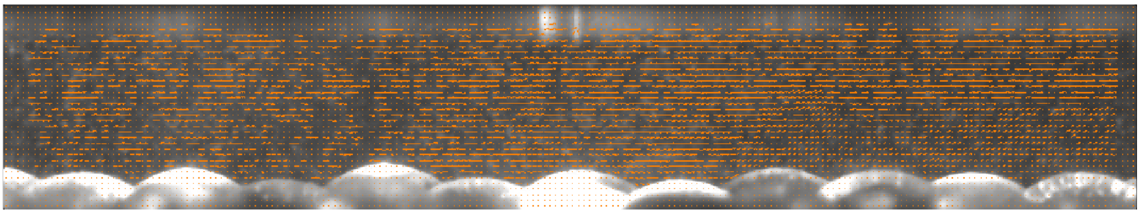

(c) Velocity vector field at fixed regular grid

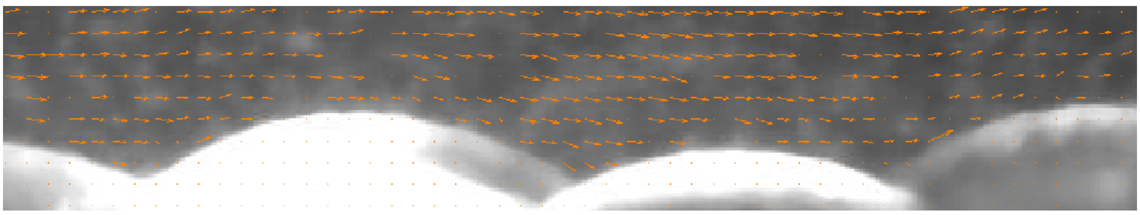

(d) After validation and integrated to fixed regular grid (close-up)

Fig. 3.23: Velocity vector maps generated with PTV technique

3.4. Quantification of sub-surface flow through the porous bed

As discussed earlier in Section 2.4.2, a typical formulation that are often used as extensions of the Darcy law for inertia-dominated flows through porous media is the Ergun equation [*Ergun*, 1952]. However, the wall effect caused the prediction to differ significantly from this study's observations, which is consistent with earlier findings by Winterberg and Tsotsas [2000] and Cheng [2011b]. By taking into account both the bed porosity (ε) and the ratio between characteristic dimension of the cross section and the sphere diameter (l_p/D), *Cheng et al.* [2008b] suggest that the governing equation can be transformed into a linear form of Eq. (2.17), which is equivalent to

$$f_p \cdot Re_p = \mathrm{C}_1 + \mathrm{C}_2 \cdot Re_p \tag{3.1}$$

where C_1 and C_2 are coefficients, $f_p = \left(gdi_p/u_p^2\right)\cdot\left[\varepsilon^3/(1-\varepsilon)\right]$ and $\mathrm{Re}_p = U_p d/\left[\nu(1-\varepsilon)\right]$ are the redefined friction factor and Reynolds number associating with flow through the porous bed, respectively. Since the two constant could not be predicted correctly using the correlations available in the literature, an additional series of experiments were carried out with the same channel facility to verify the relationship between the imposed hydraulic gradient and the flow through porous bed.

3.4.1 Investigation method

In term of laboratory test, measurement of flow inside the bed layer has been known to be a difficult task since instruments and techniques developed so far have not been able to provide satisfactory results. In order to gain an approximate estimation of the flow through porous bed, two series of complimentary experiments were carried out for both the gravel-bed (in flume A) and spherical-particle bed (in flume C). Since flume A and B has the same width and only one type of gravels was used, experiments with gravel beds were carried out in flume A only and results were interpreted for flume B where needed.

In these tests, a water-tight box was purposely placed on top of the porous layer to confine the fluid flow to the subsurface stratum (as sketched in Fig. 3.24). The fluid flow through the porous bed (Q_p) was then driven by the imposed hydraulic gradient (i_p) over the measuring section, similar in-principle to the pressure-driven flow through the permeable bed in open channel flows. It was possible to measure both of these parameters and thus empirical relationships could be established, which were subsequently used to interpret the flow rate through porous beds in the present open channel flow tests.

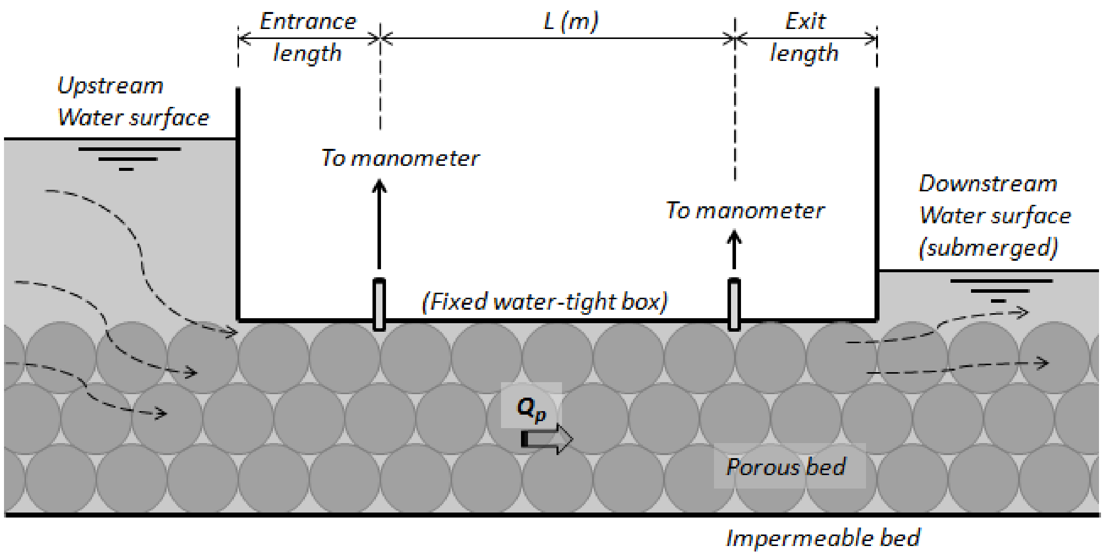

Fig. 3.24: Sketch of the subsurface flow test (not to scale)

Although the tests were designed to represent the principal mechanism of the flow through permeable beds, they were, however, unable to account for the effects caused by the turbulent shear flow that these beds exposed to in prototypical open channel flows. Therefore, deviations from the predictions of subsurface flow might arise due to momentum fluxes and coherent structures of the surface flow and thus, subjected to the relative roughness of the bed and flow conditions. Nevertheless, the proposed approach can provide useful estimation to be used for subsequent scaling of velocity profiles.

3.4.2 Experimental facilities and procedures

Four test cases corresponding to 1–4 layers of gravels were conducted in Flume B, all under a temperature of 30^0C $\pm 2^0$C. The experimental setup is illustrated in Fig. 3.25(a). The flow was channelled through a section of 2.0m of the gravel bed by placing and securing a watertight perspex box on top of the gravel bed. Outer dimensions of the box measured 200cm in length, 29.6cm in width and 56cm in height.

Flow passing through the porous medium under the box could be tested at various flow rates (Q_p) which were measured using the flume's built-in electro-magnetic flow meter. Meanwhile, two manometer taps were installed on the bottom of the box, separated by a distance of L = 1.8m, to measure the head loss (ΔH) associated. The hydraulic gradient in the direction of flow was then derived as $\Delta H/L$, or i_p.

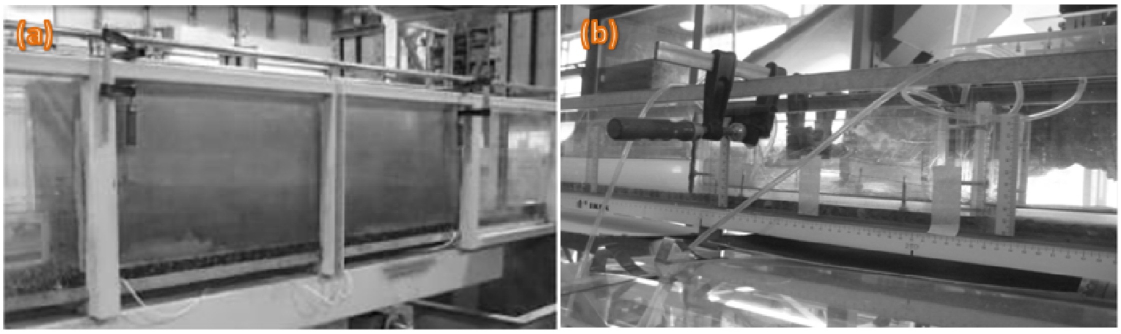

Fig. 3.25: Pressure-drop tests in Flume A (left) and Flume C (right)

Four similar sets of experiments were carried out in the same manner for the porous bed comprised 1–4 layers of packed marbles (flume C). The experimental setup is sketched in Fig. 3.25(b). A section of 0.4m of the surface flow was blocked by a watertight perspex box with two manometer taps installed, separated by a distance of L = 0.25 m. Entrance and exit effects on the manometer readings were limited by providing a transition of 0.075 m at each end of the box. For various head-loss readings (ΔH), the flow rates passing through the porous medium (Q_p) were measured using the built-in electromagnetic flow meter of flume C. Average water temperature during the tests was 30^{0}C.

For each run, the flow rate was first adjusted and head-loss reading was taken after a duration of approximately 30 minutes for the flow to be stabilized. Time sensitivity had been independently and repeatedly tested to ensure that the adopted duration would yield reliable readings since both Q_p and ΔH are typically small.

Entrance and exit effects on the manometer readings were limited by providing a transition of 0.1 m at each end of the box. On the other hand, the downstream edge of the box was always kept submerged to ensure the subsurface flows were free from air entrainment. The influence of downstream water level on head-loss reading was investigated by varying tail-gate height and repeating the measurements. Results presented in Fig. 3.26 show no marked differences between the three cases tested. This has two implications: (i) the reliability of head-loss measurement with this set-up, and (ii) the negligible effect of downstream water level on head-loss readings, given that the outlet submergence is ensured.

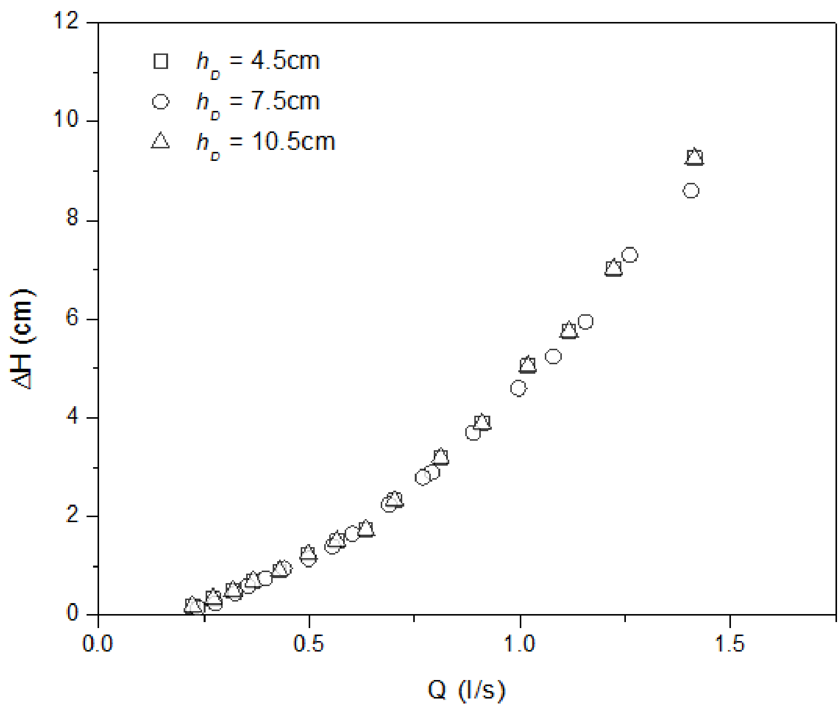

Fig. 3.26: Head-loss readings with different downstream water levels.

3.4.3 Interpretation of measured pressure drop

For each reading, the water-head loss, i.e. the piezometric pressure drop ΔH between the two manometer taps was recorded. It can also be interpreted as the unique correlation between a certain hydraulic gradient imposed on the test section and the resulting flow rate of water through the porous bed. Observations for all four bed configurations of spherical-particle bed tests are presented in Fig. 3.27.

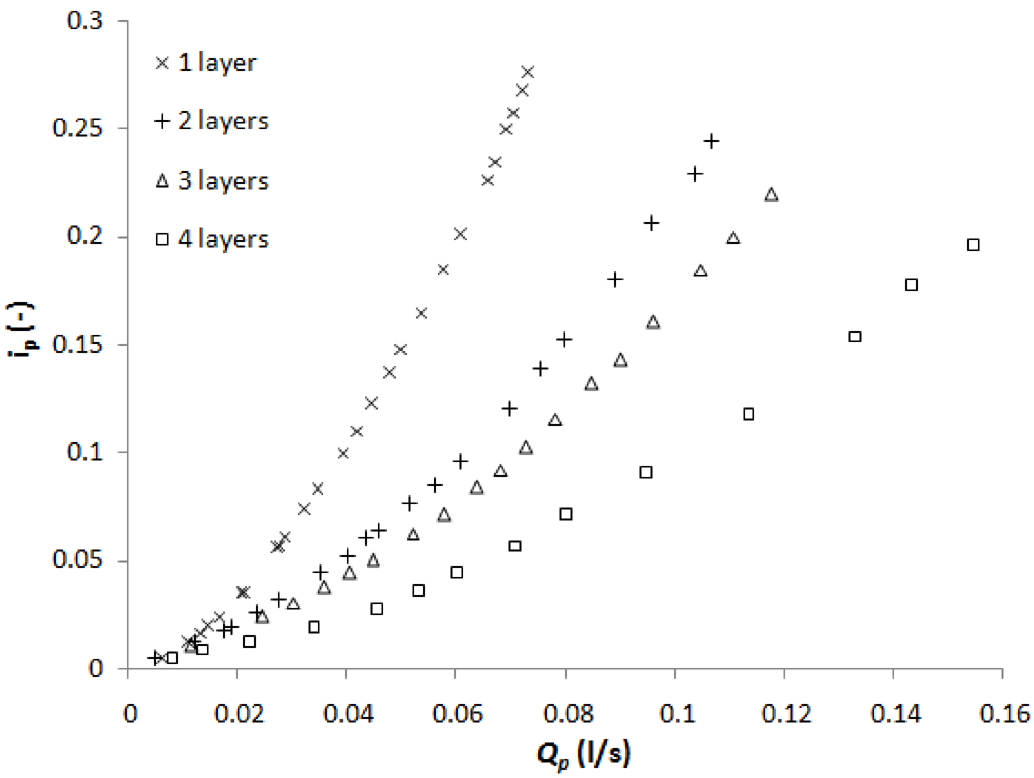

Fig. 3.27: Flow through the porous beds with varying hydraulic gradient (spherical-particle bed tests).

As discussed earlier in Section 2.4.2, by transforming Eq. (2.17) into the linear form of $f_p{\cdot}Re_p = C_1 + C_2{\cdot}Re_p$ and fitting it with the data collected, one can arrived with the specific values of the modified coefficients C_1 and C_2 for each test case (1–4 layers). Fig. 3.28 illustrates the test case with two layers of packed spheres, showing very good fit of the model proposed by Cheng et al. (2008b). Applying to the open-channel experiments, the macroscopically uniform flow over porous bed implies that the gradient of the time-averaged water surface line (S) should be the same as the hydraulic gradient imposed on the porous medium (i_p). The channel bed slope was, therefore, substituted into the modified Ergun equation [Eq. (2.16)] to solve for the corresponding average, superficial seepage velocity U_p. Thereby the intrinsic average pore velocity $u_p = U_p/\varepsilon$ can be obtained. These results are presented in Table 2.

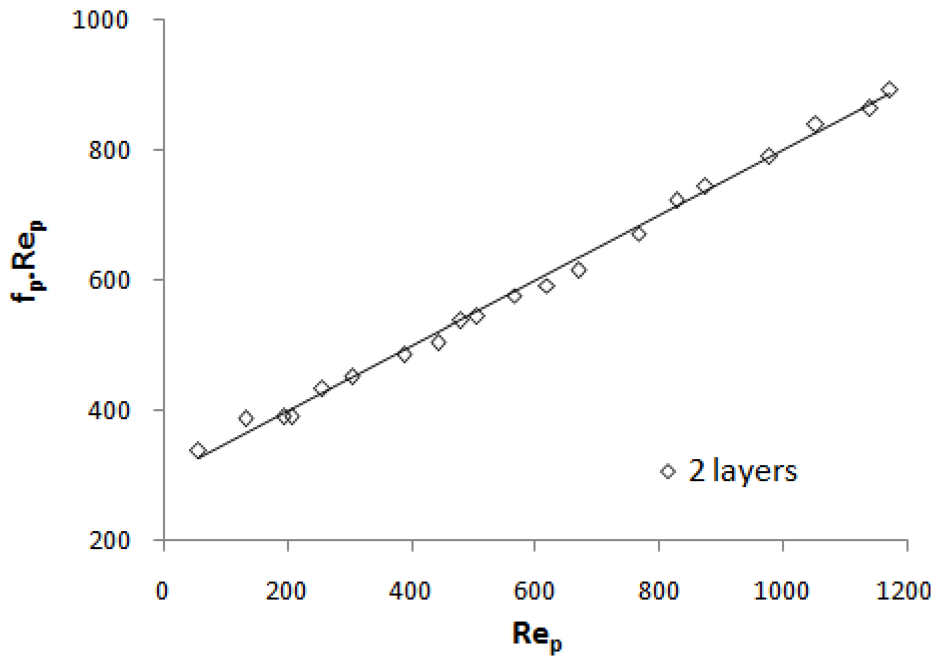

Fig. 3.28: Data fitting to find the modified A and B coefficients from experimental data

On the other hand, the slip velocity U_0 for each spherical-particle bed test was obtained with PIV and PTV measurements, as described in Section 3.3.3 earlier. Using the approximation method derived in Section 2.4.1, U_0 and U_p were substituted into Eq. (2.9) to derive the estimated subsurface flow rate (Q_p), and subsequently the corrected flow rate in the main stream (Q_s) for different test conditions. These results together are also summarized in Table 3.5. Based on the assumptions made, this approach showed that a major correction should be made for the flow above the permeable interface. The thicker the porous bed and shallower the free flow above, the higher portion of the total flow took place as underflow through the permeable bed. The portion could be as significant as 20–25% corresponding to the cases with the highest imposed hydraulic gradients.

Table 3.5: Estimation of sub-surface flow through porous bed (spherical-particle beds)

Test	C_1	C_2	U_p	u_p	U_{max}	U_0	Q_p	Q_p/Q	Q_s
	$m^{-1}s$	$m^{-2}s^2$	ms^{-1}	ms^{-1}	ms^{-1}	ms^{-1}	ls^{-1}	%	ls^{-1}
L0-H25	-	-	-	-	0.360	0	0	0	0.698
L0-H20	-	-	-	-	0.369	0	0	0	0.572
L0-H15	-	-	-	-	0.291	0	0	0	0.342
L0-H10	-	-	-	-	0.210	0	0	0	0.166
L1-H25	305.66	0.761	4.26E-04	9.91E-04	0.233	0.058	0.031	7.2	0.404
L1-H20	305.66	0.761	4.26E-04	9.92E-04	0.196	0.060	0.032	10.4	0.279
L1-H15	305.66	0.761	4.26E-04	9.92E-04	0.153	0.049	0.027	14.8	0.153
L1-H10	305.66	0.761	4.26E-04	9.92E-04	0.115	0.037	0.020	19.7	0.082
L2-H25	296.38	0.501	3.57E-04	9.58E-04	0.214	0.042	0.023	5.5	0.395
L2-H20	296.38	0.501	3.57E-04	9.58E-04	0.207	0.044	0.024	7.6	0.297
L2-H15	296.38	0.501	3.57E-04	9.58E-04	0.170	0.036	0.020	9.7	0.186
L2-H10	296.38	0.501	3.57E-04	9.58E-04	0.124	0.041	0.023	20.9	0.085
L3-H25	359.41	0.688	2.78E-04	7.69E-04	0.221	0.048	0.026	6.1	0.405
L3-H20	359.41	0.688	2.78E-04	7.69E-04	0.207	0.049	0.027	8.5	0.295
L3-H15	359.41	0.688	2.79E-04	7.71E-04	0.177	0.062	0.034	16.4	0.173
L3-H10	359.41	0.688	2.80E-04	7.73E-04	0.124	0.048	0.027	24.8	0.080
L4-H25	280.69	0.609	3.04E-04	8.53E-04	0.234	0.053	0.030	6.6	0.416
L4-H20	280.69	0.609	3.04E-04	8.53E-04	0.211	0.049	0.027	8.4	0.300
L4-H15	280.69	0.609	3.04E-04	8.53E-04	0.172	0.044	0.025	12.0	0.183
L4-H10	280.69	0.609	3.05E-04	8.54E-04	0.117	0.037	0.021	20.5	0.081

For the convenience of scaling velocity profiles in gravel-bed flows in Chapter 5, the bulk mean seepage velocity through the porous bed, defined as $U_p = Q_p/(B{\cdot}H_p{\cdot}\varepsilon)$, is used instead of the flow rate. Fig. 3.29 shows the relationships between the hydraulic gradient in the direction of flow (i_p) and the bulk mean seepage velocity (U_p) for all gravel-bed tests.

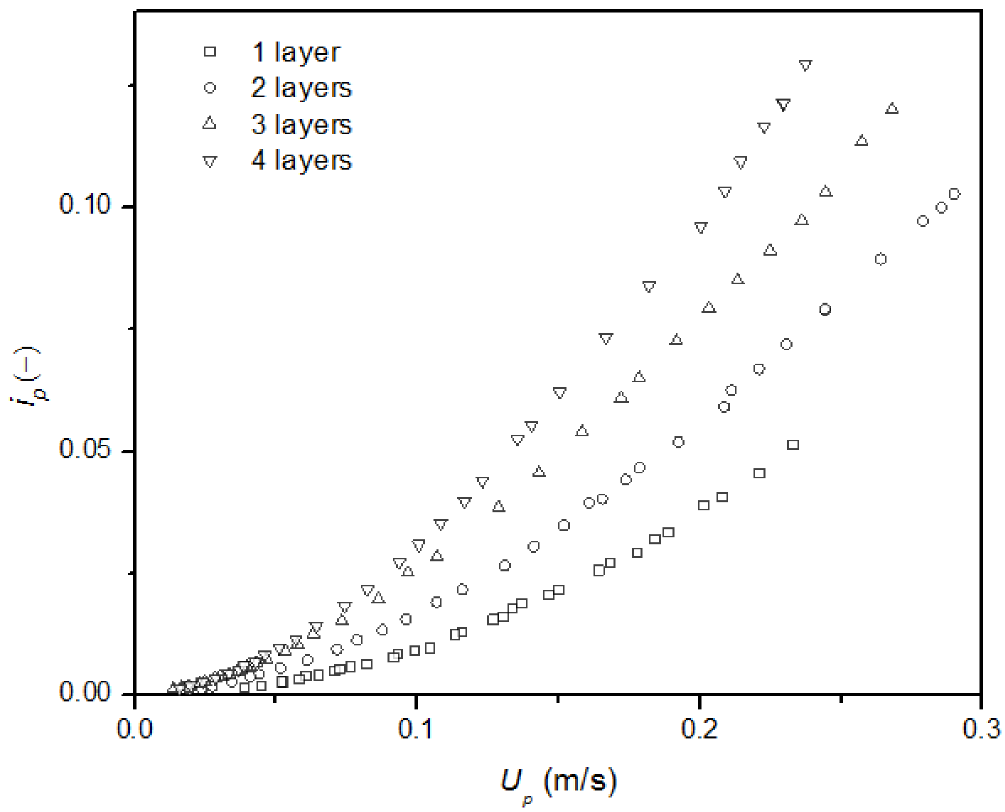

Fig. 3.29: Variation of mean seepage velocity with changing imposed hydraulic gradient (gravel-bed tests).

The trends observed are subjected to a number of parameters including the bed layer porosity (ε), the seepage Reynolds number and the wall effect. Consider the enclosed channel flow in these complimentary tests, the wall effect is accounted for by the ratios of bed hydraulic diameter to particle diameter, l_p/D, where D is the sphere diameter, $l_p = 4R_h$, and R_h is the hydraulic radius. It should be noted that even the porosity is a nonlinear function of the number of sphere layers.

3.5. Use of flow velocity data

In this thesis, the flow data obtained through the above experiments was used for different purposes, which are listed as follows:

- Chapter 3 uses the measured discharge to quantify sub-surface seepage flow velocity through the porous bed, which will be elaborated in details subsequently.

- Chapter 4 uses the mean streamwise flow velocity, obtained by integration of the double averaging velocity profiles, to calculate the friction coefficients for both gravel and spherical-particle bed tests. This integration was realized with the aid of Mathcad – an engineering calculations software.

- Chapter 5 works with the 2-D velocity profiles, obtained with double averaging technique and EMCM (for gravel-bed tests) and PIV (for spherical-particle bed tests), to justify different scaling approaches.

- Chapter 6 mainly uses the detailed velocity vector maps, obtained with PIV technique, and its corresponding turbulence statistics to investigate the influence of bed permeability and low roughness submergence on the flow.

Chapter 4

Flow Resistance

This chapter presents a new and simple calculation for resistance coefficient and mean velocity in shallow flow over permeable rough beds. An examination on the available formulations from published studies has revealed that there is currently no single standard formula for calculating flow resistance in a consistent and accurate manner. Using a heuristic approach, this study first justified a theoretical analysis that sought for the derivation of a modified Manning's formula in a dimensionally consistent form. A nondimensional exponential function of the roughness submergence was introduced to account for the shallowness effect on flow resistance. The formula was then calibrated by using a large compilation of existing data, from a wide variety of available sources and from the present study. The resulting resistance formula is expected to perform better than those currently available in literature particularly for estimating the resistance to shallow flows, of which the roughness submergence is smaller than five.

4.1. Conceptual consideration

The idea presented here is to start with a well known empirical formula, and then try to come up with a theoretical consideration that accounts for the effects of the permeable rough bed under shallow flow conditions. The resulting semi-empirical formula will then be calibrated with a large collection of data.

The formula of interest is Manning's one, which has numerous of applications in hydraulic engineering for more than a century [*Dooge*, 1992; *Yen*, 1992]

$$U = \frac{1}{n} R^{2/3} S_f^{1/2} \tag{4.1}$$

where n ($L^{-1/3}T$) is the Manning coefficient, U = mean velocity, R = hydraulic radius, S_f = friction slope. Manning's formula has gained considerable theoretical interest for its important role though it was introduced purely empirically. In a recent work, Gioia and Bombardelli [2002] have shown that Manning formula represents the asymptotic behaviour in a power-law form for a shallow flow of incomplete similarity in the roughness submergence. This study adopts his approach to extend Manning's formula for large scale roughness (low roughness submergence) condition.

Manning's empirical formula is usually presented in the dimensionally inconsistent form (Eq. (4.1), and its dimensionally homogeneous form is given as [*Chow*, 1959; *Yen*, 1992]

$$U = \frac{K_u}{\sqrt{g}} \frac{1}{n} R^{1/6} \sqrt{gRS} \tag{4.2}$$

In this consideration, R is used to characterize the cross-section geometry. There has been a wide range of measured values of n tabulated in literature for different types of channel walls. Hereafter, to characterize the large-scale roughness of the walls, the absolute roughness D is used, as also done by several others (e.g., Chow [1959], Gioia and Bombardelli [2002]). Gioia and Bombardelli, with reference to the similarity laws for turbulent shear flows [*Barenblatt*, 1986], admitted the incomplete similarity of U in D/R to arrive with a power law asymptotic in the form of

$$U = K_c \left(\frac{D}{R}\right)^{\alpha} \sqrt{RgS} + o\left[\left(\frac{D}{R}\right)^{\alpha}\right] \tag{4.3}$$

where K_c = dimensionless constant, gS = streamwise component of the gravitational acceleration, and α = similarity exponent, which could not be directly obtained by dimensional analysis. By comparing Eq. (4.1) and (4.3), it can be noted that the first term on the right hand side is compatible with Manning's formula when $\alpha = -1/6$.

Gioia and Bombardelli verified $\alpha = -1/6$ using the phenomenological theory of turbulence, first for roughness elements of uniform size D and then to the case of roughness elements in a range of sizes. This started with his crucial observation: $\left|\overline{u_n u_t}\right| \sim u_D U$, where the symbol '~' means 'equal within an order unity constant' (Frisch 1995), or simply 'scale with'; u_n and u_t are the fluctuating velocities normal and tangent to a surface T contacting with the peaks of the roughness elements (see Fig. 4.1); $\rho\left|\overline{u_n u_t}\right|$ yields the Reynolds shear stress; u_D is the characteristic velocity associated with the eddies of size D. u_n and u_t are dominated by u_D and U, respectively. Here, an assumption has been made that the spaces between top-layer roughness elements are occupied by eddies of size D. Together with the force balance in the streamwise direction, these observations gives a scaling

$$u_D U \sim \left(\frac{BH_s}{B+2H_s}\right) gS = RgS \qquad (4.4)$$

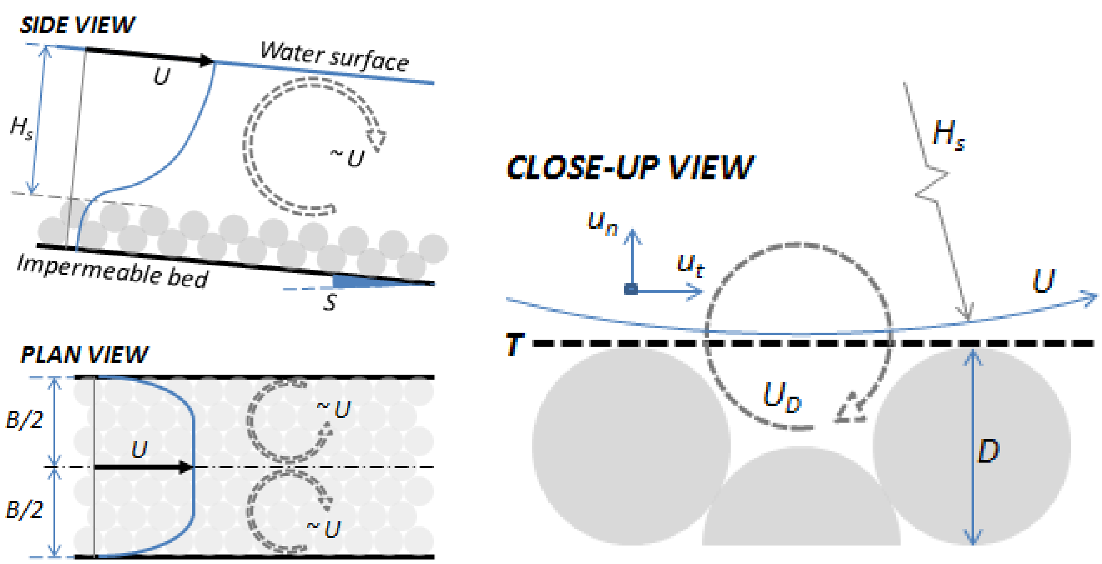

Fig. 4.1: Characteristic velocities and length-scales (after Gioia 2002)

A second assumption made is that the turbulent eddies of size D are within the inertial range, i.e. the inhomogeneous turbulence in the vicinity of the walls are governed by Kolmogorov's scaling. Thereby, $u_D^3/D \sim \varepsilon$, where ε_d is the rate of turbulent energy dissipation per unit mass. Gioia and Bombardelli further showed that the largest eddies possess an energy per unit mass ~ U^2 and noted that the eddies with horizontal and vertical vorticity vectors are characterized by turnover times of (H_s/U) and $(B/2)/U$, respectively (see Fig. 4.1). This leads to

$$\varepsilon_d \sim \frac{U^2}{H_s/U} + \frac{U^2}{B/(2U)} = U^3\left(\frac{B+2H_s}{BH_s}\right) = \frac{U^3}{R} \tag{4.5}$$

Together, the rate of dissipation of turbulent energy provides a relation for u_D and U

$$\frac{u_D^3}{D} \sim \varepsilon_d \sim \frac{U^3}{R} \tag{4.6}$$

This defines a scale for u_D in term of U, $u_D \sim (D/R)^{1/3}U$, which can be substituted into Eq. (4.4) to yield

$$U \sim \left(\frac{D}{R}\right)^{-1/6}\sqrt{RgS} \tag{4.7}$$

This is the first term in the right hand side of Eq. (4.3) with $\alpha = -1/6$, which complete the derivation for Manning's formula in its asymptotic form.

It should be noted here that the characteristic eddy turnover times in Eq. (4.5) have been proposed based on the assumption that $D/R << 1$. This is also the condition for which Manning's n is approximately constant. However, it has been widely known that when the flow depth H_s reduces to the order of D, n increases rapidly with decreasing H_s and the use of a constant n value is not acceptable [e.g., Froehlich [2012]]. Instead of using different value of n from various sources available, this study proposes to use an exponential function to account for the influence of this reduction in eddy turnover time scale, which is caused by the permeable rough bed under small roughness submergences.

According to Kolmogorov's theory of turbulence for the inertial range, the mean energy dissipation rate ε_d in Eq. (4.5) is resulted when there is neither direct energy input nor direct energy dissipation. Even though the viscous effect can be neglected, it was observed that for the conditions under investigation there should be a considerable amount of flow energy exploited by generating the momentum fluxes necessary to drive the interstitial flow in between the roughness elements. This is evident by the fact that in these flow conditions, typical vertical velocity profile has considerably departed from those logarithmic profiles, particularly in the near-bed region [*Ghisalberti*, 2009; *Goharzadeh et al.*, 2005; *Katul et al.*, 2002; *Manes et al.*, 2011b], see Fig. 4.2. The author's earlier experimental results [*Tuyen et al.*, 2014] have not only showed the inflectional velocity profile, but also pointed out that in these typical conditions, significant portion of flow discharge actually takes place in the interfacial and subsurface regions, as much as 20% of the total. Often the vortices cannot penetrate deeper beyond the first one roughness diameter below the bed surface, and the region there below is governed by a simple balance of drag and hydraulic gradient, much like a porous medium flow. These phenomena all give clues to the extra proportion of the energy being dissipated, for which a modification of the characteristic eddy turnover times is necessary, especially for those with a horizontal vorticity vector.

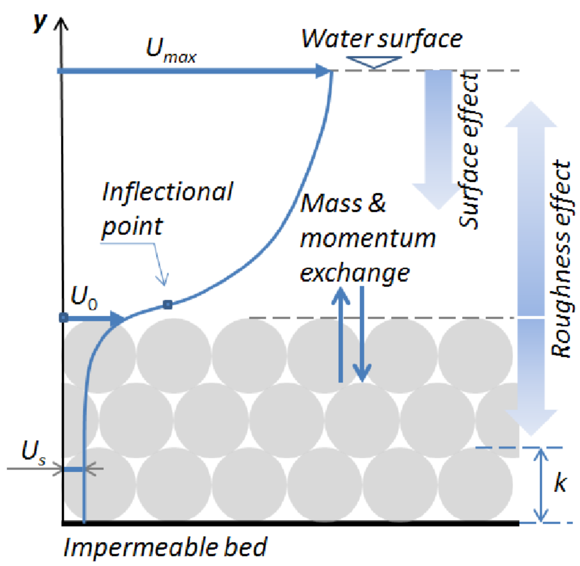

Fig. 4.2: Deviation of flow velocity from logarithmic profile

With the above considerations, this study proposes a nondimensional exponential function of (D/R) to modify the energy dissipation rate

$$\varepsilon_d \sim \frac{U^3}{R} e^{-c_1\left(\frac{D}{R}\right)^{c2}} \tag{4.8}$$

where c_i is a positive constant. Eq. (4.8) shows ε_d decreases with increasing D/R. Together with the previously mentioned scaling $u_D^3/D \sim \varepsilon_d$, yields $u_D \sim (D/R)^{1/3} U \cdot e^{-c_3(D/R)^{c4}}$. This can be substituted into Eq. (4.4) to get

$$U \sim \left(\frac{D}{R}\right)^{-1/6} \sqrt{RgS} \cdot e^{-c_5(D/R)^{c6}} \tag{4.9}$$

In the above formulations, the parameter R is often used to characterize the cross-sectional geometry. However, for stream flows with low roughness submergence, the concept of hydraulic radius based on wetted perimeter has a fractal nature and its precise determination is difficult [*Aberle and Smart*, 2003]. Furthermore, by quantifying the side-wall effect using the approach proposed by Cheng and Chua [2005] it was found that the side-wall effect is insignificant, despite its complexity. Therefore the proposed formula simply uses H_s/D instead of R/D to represent the roughness submergence. This result can also be obtained by noting that $B >> H_s$ in Eq. (4.4) – (4.7), which is reasonable for the flow conditions under consideration, as the flow generally does not 'feel' the banks. Taking this into account and rewriting Eq. (4.9) in its interchangeable form yields

$$\sqrt{\frac{8}{f}} = \frac{U}{u_*} = c_7 \left(\frac{H_s}{D}\right)^{1/6} e^{\frac{-c_8}{(H_s/D)^{c9}}} \tag{4.10}$$

This function represents a smooth curve, asymptotic to a 1/6th power relation at $H_s/D >> 1$. The coefficients c_i will then be determined by fitting this proposed model to the measurements, mainly those from available sources in literature. This step will be realized in the following sections.

4.2. Flow resistance database

This study aims to provide a semi-empirical resistance formula of good accuracy and applicability. Therefore the empirical coefficients in Eq. (4.10) were calibrated using a wide range of data sets. Two major sources of data were utilized: (i) data from the present study's measurements with gravel-bed and spherical-particle bed tests, and (ii) data from literature, which is the major portion.

4.2.1 Experimental data from the present study

A summary of experimental data from the present study, as detailed in Chapter 3, is given in Table 4.1. It includes 40 sets of measurement for gravel beds in two flumes A & B and 68 other tests carried out for spherical-particle beds in flume C, with varying bed configurations and roughness submergences. All the tests were done in macroscopically uniform conditions, with the Reynolds number Re ranging from 1.29×10^3–88.69×10^3, and the Froude number Fr from 0.156–1.115. In these tests, the width-to-depth ratio B/H_s = 2.37–10.32, where B is the flume width and H_s is the flow depth measured from the free surface down to the roughness crest, while the roughness submergence H_s/k_s = 0.86–3.89, k_s is the roughness size, taken to be the same as the bead diameter D. Different bed slopes were chosen, ranging from 0.001 to 0.023. In these tests, the friction factor f was calculated as $f = 8gH_sS/U^2$.

Table 4.1: Experimental data from gravel-bed tests, flume A

No.	Flume	Q	B	H_s	S	D	f
-		*l/s*	*m*	*m*	-	*mm*	-
1	A	4.073	0.3	0.0736	0.001	32.5	0.1697
2	A	7.097	0.3	0.1246	0.001	32.5	0.2713
3	A	6.317	0.3	0.1046	0.001	32.5	0.2026
4	A	2.785	0.3	0.0586	0.001	32.5	0.1832
5	A	1.198	0.3	0.0371	0.001	32.5	0.2513
6	A	8.127	0.3	0.122	0.001	32.5	0.1942
7	A	6.469	0.3	0.103	0.001	32.5	0.1844
8	A	4.477	0.3	0.08	0.001	32.5	0.1804
9	A	2.709	0.3	0.059	0.001	32.5	0.1977
10	A	1.127	0.3	0.039	0.001	32.5	0.3299
11	A	7.649	0.3	0.112	0.001	32.5	0.1696
12	A	6.163	0.3	0.096	0.001	32.5	0.1645
13	A	4.675	0.3	0.078	0.001	32.5	0.1534
14	A	2.549	0.3	0.056	0.001	32.5	0.1909
15	A	1.139	0.3	0.036	0.001	32.5	0.2540
16	A	6.339	0.3	0.1033	0.001	32.5	0.1938
17	A	5.900	0.3	0.0923	0.001	32.5	0.1596
18	A	4.174	0.3	0.0728	0.001	32.5	0.1564
19	A	2.029	0.3	0.0533	0.001	32.5	0.2598
20	A	1.043	0.3	0.0363	0.001	32.5	0.3106

Table 4.1 (continue): Experimental data from gravel-bed tests, flume B

No.	Flume	Q	B	H_s	S	D	f
-		*l/s*	*m*	*m*	-	*mm*	-
21	B	22.431	0.3	0.1265	0.0064	32.5	0.1819
22	B	18.545	0.3	0.1055	0.0064	32.5	0.1543
23	B	13.190	0.3	0.0815	0.0064	32.5	0.1407
24	B	8.239	0.3	0.0655	0.0064	32.5	0.1871
25	B	3.468	0.3	0.0415	0.0064	32.5	0.2686
26	B	21.870	0.3	0.1159	0.0064	32.5	0.1471
27	B	16.980	0.3	0.0989	0.0064	32.5	0.1517
28	B	12.710	0.3	0.0844	0.0064	32.5	0.1682
29	B	7.120	0.3	0.0625	0.0064	32.5	0.2177
30	B	3.250	0.3	0.0416	0.0064	32.5	0.3081
31	B	21.624	0.3	0.116	0.0064	32.5	0.1509
32	B	15.677	0.3	0.096	0.0064	32.5	0.1627
33	B	11.924	0.3	0.082	0.0064	32.5	0.1753
34	B	7.304	0.3	0.066	0.0064	32.5	0.2436
35	B	3.464	0.3	0.045	0.0064	32.5	0.3433
36	B	20.575	0.3	0.116	0.0064	32.5	0.1667
37	B	15.636	0.3	0.0977	0.0064	32.5	0.1724
38	B	11.529	0.3	0.083	0.0064	32.5	0.1945
39	B	7.148	0.3	0.0664	0.0064	32.5	0.2590
40	B	3.388	0.3	0.046	0.0064	32.5	0.3833

Table 4.1 (continue): Experimental data from spherical-particle bed tests, flume C

No.	Flume	Q	B	H_s	S	D	f
-		*l/s*	*m*	*m*	-	*mm*	-
41	C	0.436	0.098	0.025	0.0029	11	0.1801
42	C	0.312	0.098	0.02	0.0029	11	0.1802
43	C	0.180	0.098	0.015	0.0029	11	0.2277
44	C	0.102	0.098	0.01	0.0029	11	0.2101
45	C	0.418	0.098	0.025	0.0029	11	0.1955
46	C	0.322	0.098	0.02	0.0029	11	0.1692
47	C	0.206	0.098	0.015	0.0029	11	0.1738
48	C	0.108	0.098	0.01	0.0029	11	0.1874
49	C	0.431	0.098	0.025	0.0029	11	0.1839
50	C	0.322	0.098	0.02	0.0029	11	0.1687
51	C	0.207	0.098	0.015	0.0029	11	0.1722
52	C	0.107	0.098	0.01	0.0029	11	0.1909
53	C	0.446	0.098	0.025	0.0029	11	0.1717
54	C	0.327	0.098	0.02	0.0029	11	0.1635
55	C	0.208	0.098	0.015	0.0029	11	0.1705
56	C	0.102	0.098	0.01	0.0029	11	0.2101
57	C	0.662	0.098	0.019	0.01	11	0.1180
58	C	0.597	0.098	0.0179	0.01	11	0.1213
59	C	0.549	0.098	0.0168	0.01	11	0.1186
60	C	0.502	0.098	0.0161	0.01	11	0.1248
61	C	0.464	0.098	0.0155	0.01	11	0.1304
62	C	0.418	0.098	0.0145	0.01	11	0.1315
63	C	0.378	0.098	0.0139	0.01	11	0.1417
64	C	0.356	0.098	0.0133	0.01	11	0.1399
65	C	0.321	0.098	0.0125	0.01	11	0.1429
66	C	0.289	0.098	0.0118	0.01	11	0.1483
67	C	0.249	0.098	0.0109	0.01	11	0.1574
68	C	0.213	0.098	0.01	0.01	11	0.1661
69	C	0.649	0.098	0.0187	0.01	11	0.1170
70	C	0.642	0.098	0.0185	0.01	11	0.1158

Table 4.1 (continue): Experimental data from spherical-particle bed tests, flume C

No.	Flume	Q	B	H_s	S	D	f
-		*l/s*	*m*	*m*	-	*mm*	-
71	C	0.633	0.098	0.0184	0.01	11	0.1172
72	C	0.660	0.098	0.0164	0.017	11	0.1297
73	C	0.612	0.098	0.0157	0.017	11	0.1324
74	C	0.568	0.098	0.0149	0.017	11	0.1314
75	C	0.520	0.098	0.0143	0.017	11	0.1386
76	C	0.485	0.098	0.0137	0.017	11	0.1401
77	C	0.447	0.098	0.0132	0.017	11	0.1475
78	C	0.410	0.098	0.0125	0.017	11	0.1489
79	C	0.376	0.098	0.0122	0.017	11	0.1646
80	C	0.341	0.098	0.0117	0.017	11	0.1765
81	C	0.308	0.098	0.0108	0.017	11	0.1701
82	C	0.404	0.098	0.0125	0.017	11	0.1533
83	C	0.389	0.098	0.0123	0.017	11	0.1576
84	C	0.369	0.098	0.0119	0.017	11	0.1586
85	C	0.341	0.098	0.0118	0.017	11	0.1810
86	C	0.352	0.098	0.0117	0.017	11	0.1656
87	C	0.332	0.098	0.0115	0.017	11	0.1768
88	C	0.282	0.098	0.0102	0.017	11	0.1710
89	C	0.440	0.098	0.0131	0.017	11	0.1488
90	C	0.426	0.098	0.0128	0.017	11	0.1481
91	C	0.416	0.098	0.0125	0.017	11	0.1446
92	C	0.658	0.098	0.0156	0.023	11	0.1520
93	C	0.590	0.098	0.0145	0.023	11	0.1518
94	C	0.548	0.098	0.0142	0.023	11	0.1653
95	C	0.508	0.098	0.0135	0.023	11	0.1653
96	C	0.465	0.098	0.0128	0.023	11	0.1681
97	C	0.418	0.098	0.012	0.023	11	0.1714
98	C	0.393	0.098	0.0118	0.023	11	0.1844
99	C	0.372	0.098	0.0114	0.023	11	0.1856
100	C	0.350	0.098	0.0109	0.023	11	0.1833

Table 4.1 (continue): Experimental data from spherical-particle bed tests, flume C

No.	Flume	Q	B	H_s	S	D	f
-		*l/s*	*m*	*m*	-	*mm*	-
101	C	0.335	0.098	0.0108	0.023	11	0.1946
102	C	0.313	0.098	0.0102	0.023	11	0.1878
103	C	0.290	0.098	0.0095	0.023	11	0.1767
104	C	0.477	0.098	0.0129	0.023	11	0.1636
105	C	0.500	0.098	0.0134	0.023	11	0.1668
106	C	0.529	0.098	0.0137	0.023	11	0.1593
107	C	0.564	0.098	0.014	0.023	11	0.1495
108	C	0.629	0.098	0.015	0.023	11	0.1479

4.2.2 Flow resistance data from literature

For the purpose of a meaningful review, comparison and subsequent analysis, data has been meticulously collated from a variety of sources reported in published studies, restricted to gravity-driven, macroscopically uniform, fully developed, turbulent open channel flows over rough beds for low roughness submergences, H_s/D_{50} generally smaller than 5, without any bed form and any sediment transport. The Keulegan's roughness size (D_{50}) is desirable to use over other characteristic particle diameters because it is the most likely known sediment particle size.

Notwithstanding those criteria, the suitable data still covers a wide range of flow conditions, bed arrangements, and measurement methods. A summary of experimental conditions is given in Table A1 (Appendix A), whilst detailed flow resistance values are given in Table A2 (Appendix A).

Table A1 comprises the flow characteristics, bed characteristics, and relevant information regarding respective investigations. The number of tests for each set in this table should be interpreted as the number of 'relevant' tests, i.e. those satisfying the prevailing conditions of this study: (1) macroscopically uniform flow, (2) no sediment transport, (3) no bed form, and (4) the roughness submergence should be smaller than 5.

It should be noted that the data is abundant in literature, but there are, indeed, only a very small portion that is suitable for the present purpose. For example, 668 data that meet the first three requirements have been collected, but only half of them actually satisfy the last restriction. Examples can be named such as the data sets obtained from Recking [2006], Paintal [1971], Zagni and Smith [1976], Graf and Suszka [1987] and Manes *et al.*, [2011b], for which a majority of data entries has a roughness submergence in the range of 5 – 10. Those data points that merely satisfy the fourth condition will be used for the purpose of comparison and discussion on the proposed model.

Excluding this study's own data, the compilation includes 9 other data sets, contributed by Bathurst *et al.*, [1981], [*Ho*, 1984], Recking [2006], Richardson and Parr [1991], Manes *et al.*, [2011b], Gupta and Paudyal [1985], Zagni and Smith [1976], Cao [1985], Graf and Suszka [1987], Paintal [1971], and Abt *et al.*, [1987], also denoted as CSU (1987). For comparison, experimental data from the present study was also included as two separate entries. The first one corresponds to the experiments with gravels being mentioned earlier, the other corresponds to another set of experiments carried out with uniform-size marbles in another flume (Flume C). The latter set will be used for extended discussion purpose only.

Nevertheless, it should be mentioned that a preprocessing of data is needed as these data were present in very different manners in the different publications. Firstly, the units are converted to SI system, with appropriate dimensions. Thereafter, the values of D_{50} were inferred from the sources if they are not initially included, where possible. Thereby all the data entries were collated in a spreadsheet and a user-defined VBA function were utilized to classify the data by their roughness submergence.

After all, there were 534 data points useable for the calibration of proposed empirical coefficients in Eq. (4.10), among which 382 data points were for $H/D < 5$. All the data collected, including this study's own data on spherical-particle bed tests, is presented in Table A1 and A2 (Appendix A).

4.3. Analysis and discussions

4.3.1 Calibration of the proposed empirical coefficients

With the roughness size being characterized by D_{50}, all the collected data were presented in the semi-log plot of Fig. 4.3. By fitting the proposed Eq. (4.10) to all data, with the priority given to the data that satisfy the four prescribed conditions (the zone of low submergence, $H_s/D < 5$), one arrived with $c_7 = 8$, $c_8 = 0.75$ and $c_9 = 0.75$. The resulting relationship

$$\sqrt{\frac{8}{f}} = \frac{U}{u_*} = 8\left(\frac{H_s}{D}\right)^{1/6} e^{\frac{-0.75}{(H_s/D)^{0.75}}} \tag{4.11}$$

and its 1/6th-power asymptotic function (when the exponential term approaches one) are also overlapped onto this figure. In contrast with many other studies, the proposed resistance formula is dedicated only to the flow conditions where no sediment transport takes place (as addressed by Recking [2006], Yager et al. [2007], and Rickenmann and Recking [2011], for example) and no bed form, pool or riffle are present (as dealt with by Ferguson [2007], Zimmermann [2010] and many others). This explains the limitation of data available for calibration. Yet it can be seen that this study's experimental data is very consistent with other sources and the flow resistance under these typical conditions can be predicted quite well by the proposed semi-empirical formula. Eq. (4.11) leads to its equivalent formula for predicting the flow resistance

$$f = \frac{1}{8}\left(\frac{H_s}{D_{50}}\right)^{-1/3} e^{\frac{1.5}{(H_s/D_{50})^{0.75}}} \tag{4.12}$$

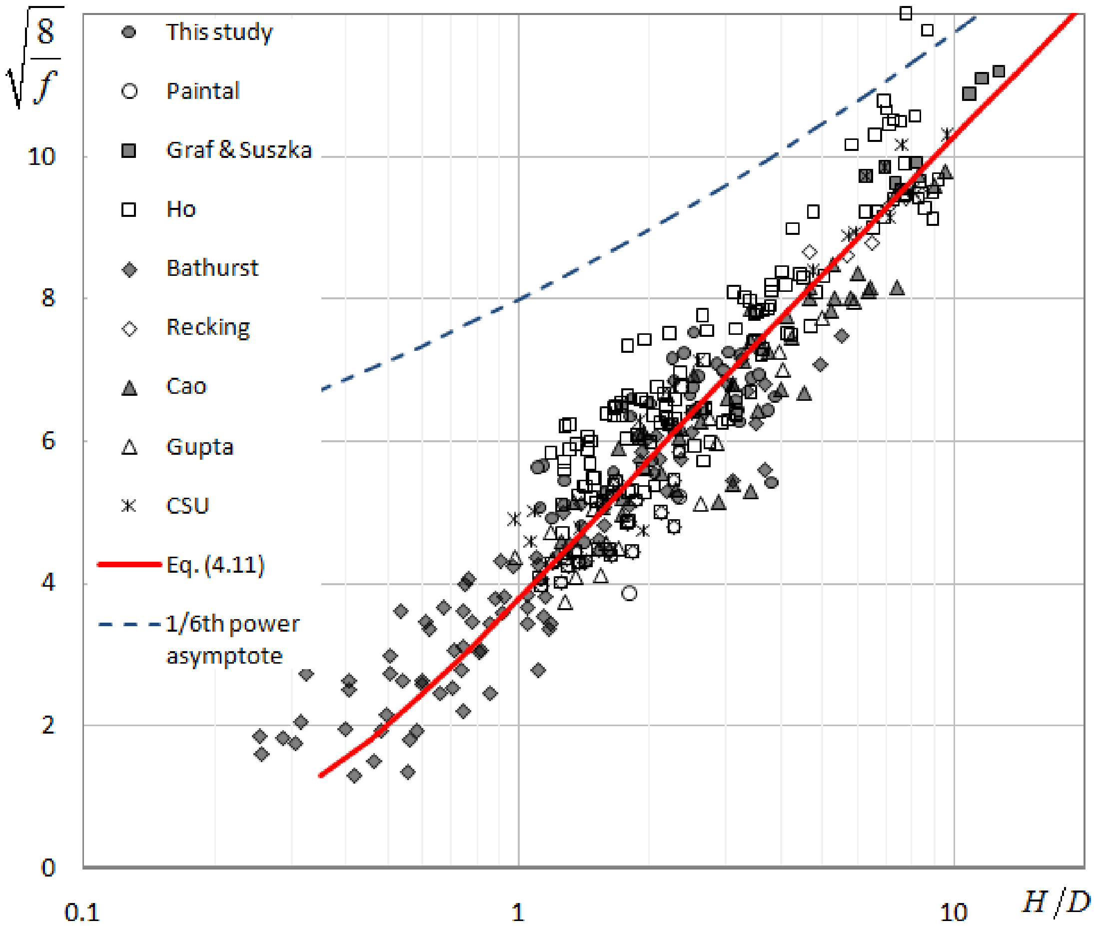

Fig. 4.3: Collection of data and fitting by the proposed model

Fig. 4.4 illustrates the relationship between f and H_s/D in log-log scale. For reference, the standard Manning-Strickler relationship is also shown. It can be seen from this figure that the Manning-Strickler formula clearly underestimates the friction factor when H_s/D falls below 4–5. Meanwhile, Eq. (4.12) follows the trend of data quite well.

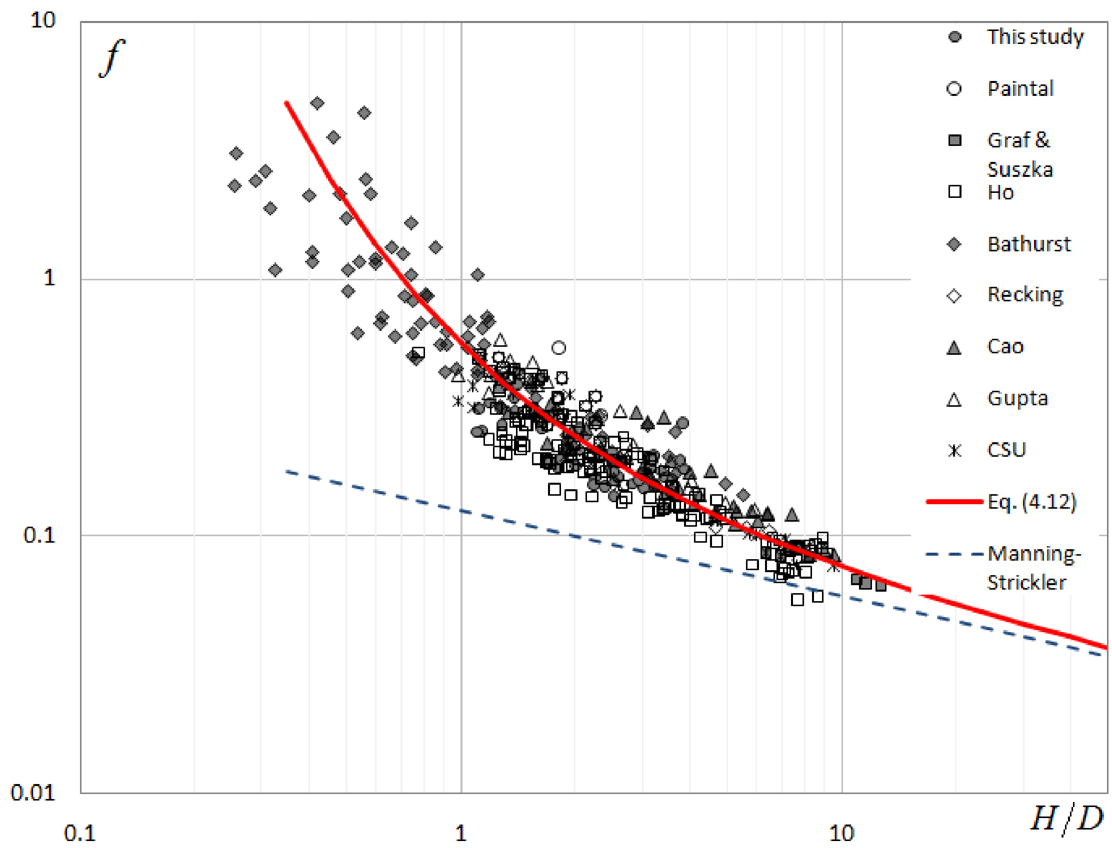

Fig. 4.4: Variation of resistance factor with the roughness submergence

4.3.2 Comparison with alternative formulae

For a broad perspective of the applicability of available formulae to the flow conditions of interest, eight formulae were selected from Table 2.1 (Chapter 2) for a comparison. They are proposed by Manning-Strickler (1), Keulegan (2), Griffiths (3), Maynord (4), Millar (5), Thompson and Campbell (6), Froehlich (7), and Katul (8). These formulae were considered either because they are widely used or they represent a different degree of complexity. Fig. 4.5 shows the correlation between $(8/f)^{1/2}$ and H_s/D for the data as a whole. It provides an overview on the performance in the region of $0.3 \le H_s/D \le 10$. The thick lines represent different logarithmic-type formulae, while the thin ones represent the power-type formulae. Since the borrowed formulae are generally not calibrated for these data, it is not surprising that they exhibit considerable deviations from the expected mean values. More importantly, their trends also show a degree of deviation from the data. Except (3) and (6) showing overshoots, all the other formulae underestimate the friction factor at low roughness submergence. This demonstrates the importance of a strong increase in flow resistance for relative flow depths. It also signifies the need of a formula dedicated for this domain of interest, i.e., shallow flow without any type of sediment transport and bed form. This comparison has demonstrated the best overall performance of the proposed relationship (Eq. (4.11).

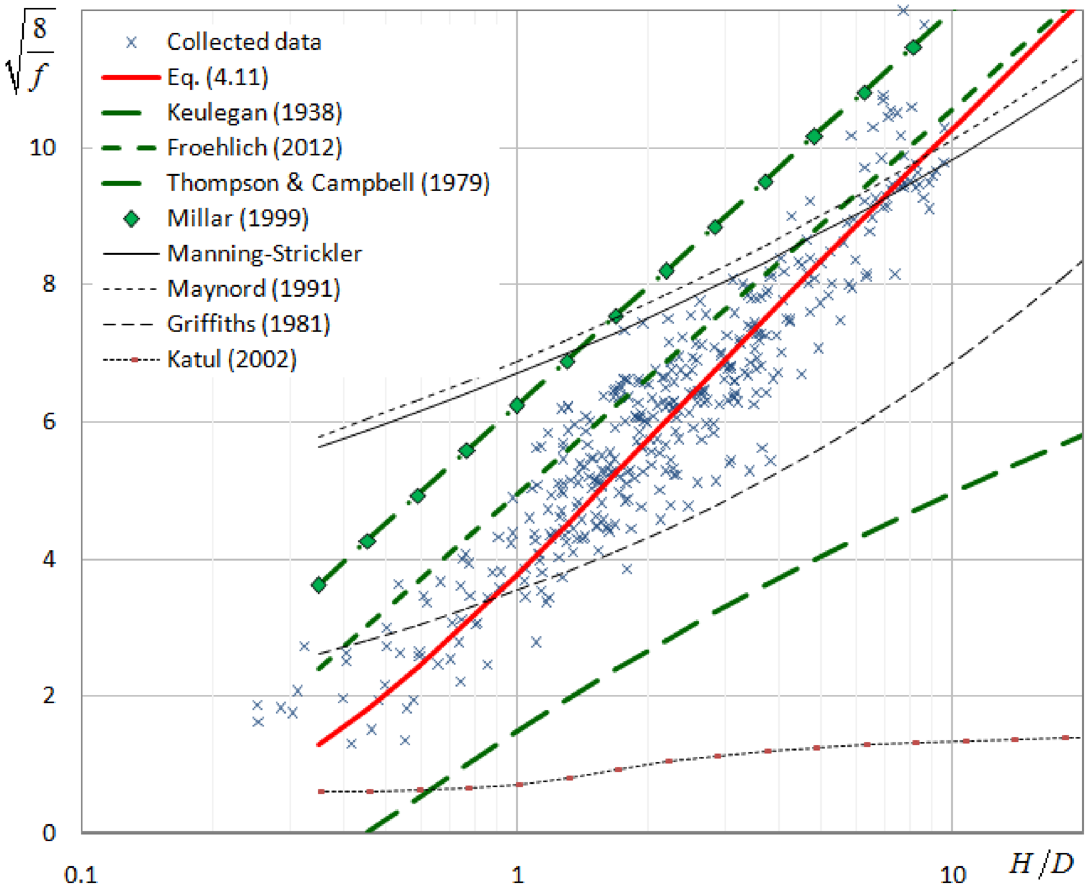

Fig. 4.5: Comparison with other power- and logarithmic-formulae in literature

4.3.3 Model verification

The performance of the proposed formula has also been assessed by comparing the measured (or calculated from measurements) and predicted values of the friction factor and bulk mean flow velocity. Fig. 4.6 shows the predicted versus observed friction factors, with an average relative error of 26.9%. Using velocity as the prediction target, Fig. 4.7 presents a comparison between the predicted velocity (U_p) and the observed one (U_m), showing better agreement. The average relative error is 10.92%, which is good for low flows subject to large-scale roughness.

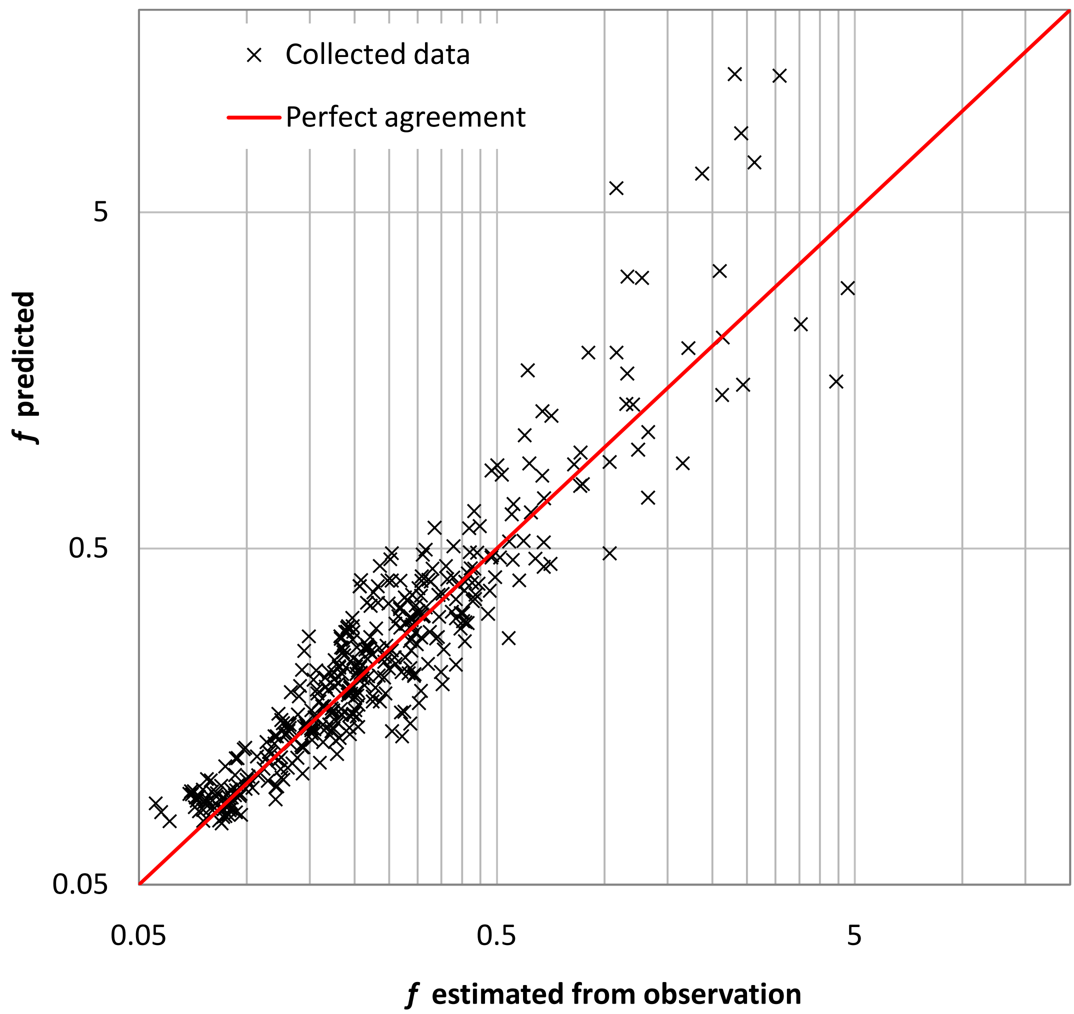

Fig. 4.6: Comparison between the predicted and estimated friction factors from measurements

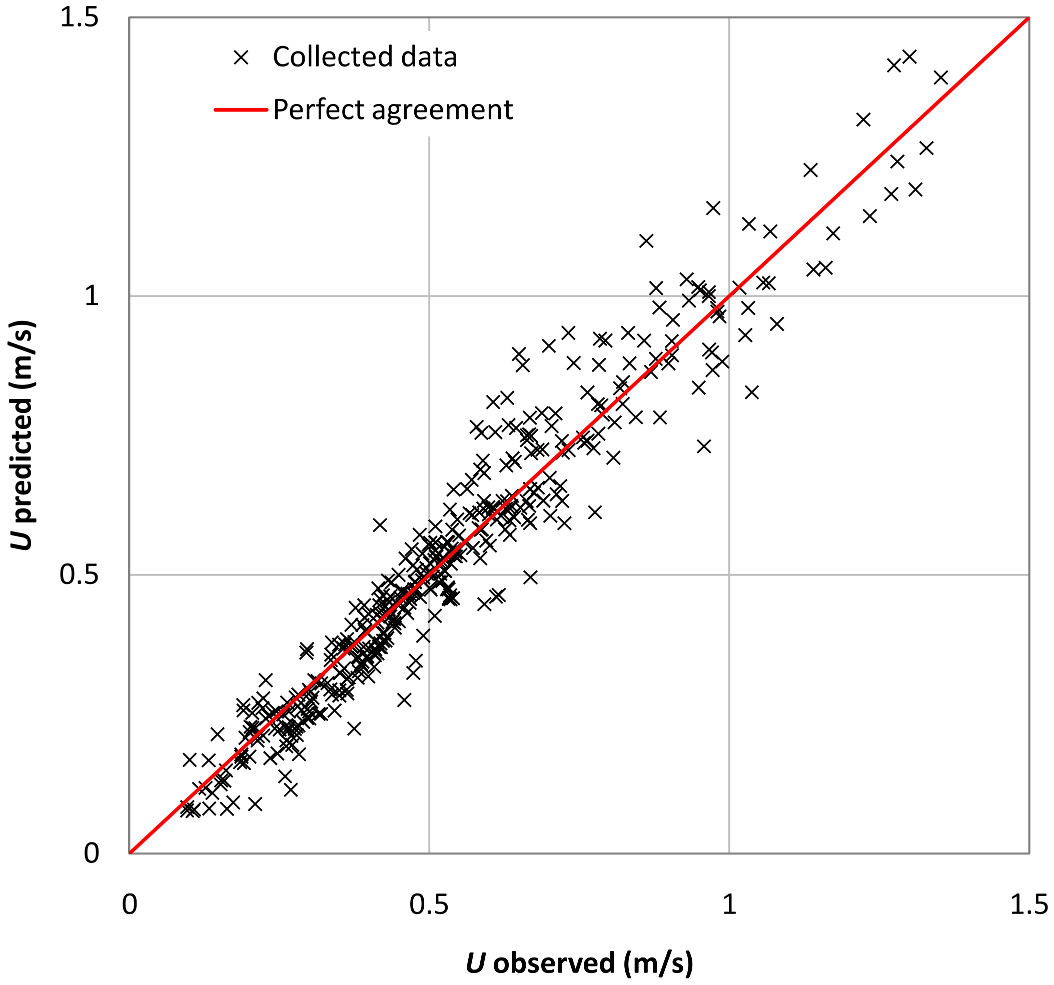

Fig. 4.7: Comparison between the predicted and observed velocities

Except for the data sets collected from the works done by Zagni & Smith [1976], Gupta & Paudyal [1985] and Manes et al [2011a] where velocity information is not available, the performance can also be assessed statistically with the other eight data sets, including this study's data (N = 401 points in total). The first parameter used for assessment is the root mean square (RMS) error, which has the dimension of the corresponding values being assessed, and it is given by

$$s_f = \sqrt{\frac{1}{N}\sum\left(f_p - f_m\right)^2}\,; \qquad s_U = \sqrt{\frac{1}{N}\sum\left(U_p - U_m\right)^2}\,; \tag{4.13}$$

The RMS errors calculated were 0.918 and 0.069 for friction factor and velocity, respectively. Another way, preferably used to assess the prediction performance in shallow flow condition, is to use the RMS logarithmic error

$$s_{\log f} = \sqrt{\frac{1}{N}\sum\left(\log f_p - \log f_m\right)^2}\ ; \qquad s_{\log U} = \sqrt{\frac{1}{N}\sum\left(\log U_p - \log U_m\right)^2} \qquad (4.14)$$

It assesses the relative error and therefore gives greater weight to over-prediction or under-prediction of the slow flows (Ferguson 2007). The RMS logarithmic errors were 0.142 and 0.071 for f and U, respectively.

To sum up, this work has introduced a semi-empirical relationship with good performance for estimating the flow resistance for the shallow flow conditions that are typically prone to highly uncertainty estimation (see for example, Bjerklie 2005, Rickenmann 2011). Nevertheless, it should be emphasized that estimations made by using this relation should be interpreted as the mean values with typical errors as discussed above.

4.3.4 Resistance to flows over rough beds of spherical elements

It is worth to note that although many natural channels have permeable beds of materials such as sand and gravels, while very little attention has been paid to the interaction of the permeable boundary and the main channel flow. In common practice, the boundary resistance of a permeable boundary has usually been taken as equal to that of an impermeable boundary of the same surface roughness, but this clearly has ignored other relevant factors (Zagni 1975). The interaction of the permeable boundary and main flow must have affected the velocity distribution and the boundary resistance. The former effect has been quantified in the author's earlier study (Tuyen et al., 2014, submitted paper). For the later one, there have been several studies carried out, in which the roughness bed was constructed from uniform-size spherical glass elements, that can facilitate the exchange between the flow above and below the bed interface. They provide a good mean to gain better understanding on the problem.

Fig. 4.8 presents data from Manes et al. (2011) and from this study's third series of experiment, which was carried out independently in Flume C. Their test conditions are shown in Table A1 and Table A2, Appendix A. By comparing with the proposed model, it can be seen that measured friction factor values are systematically smaller than the predicted ones. Since the skin friction and viscosity effects are negligible in these flows with large-scale roughness, the reduction in friction factor can most reasonably be attributed to the permeability of the bedding porous medium. Higher porosity and permeability of the bed layer must have facilitated the flow penetration into the subsurface pores and diminished the generation of coherent structures in the adjacent of top-layer roughness elements (in comparison to that in impermeable rough boundary flows). The lesser amount of energy dissipated via vortex shedding mechanism have, perhaps, yielded a reduction in the flow resistance as observed in these experiments.

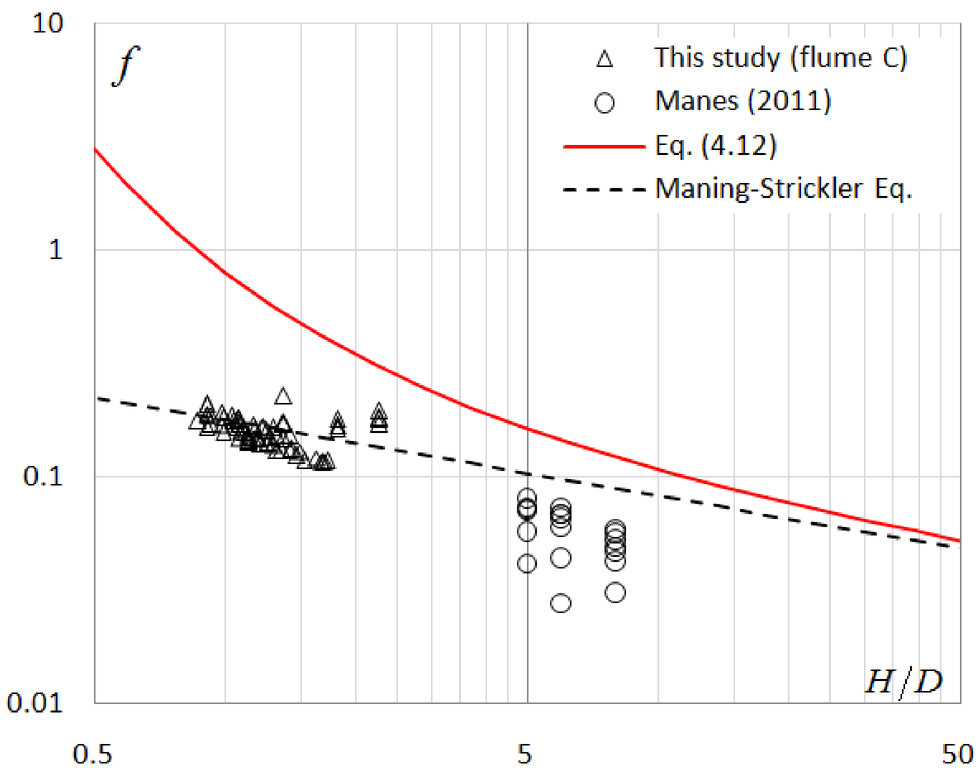

Fig. 4.8: Friction factors from experiments with glass spheres

Chapter 5

Scaling of Velocity Profiles in surface layer

This chapter presents an approach that is useful for scaling the mean velocity profiles in the outer region of turbulent open channel flows over a porous rough bed with small roughness submergence. Using the plane mixing layer analogy, scaling analysis shows that the velocity profiles can be well normalised using the maximum surface velocity and a characteristic flow depth at which the flow velocity reduces to one half of the maximum surface velocity. In order to validate the proposed scaling method, a series of velocity measurements were conducted for a range of flows over a different rough bed configurations. Comparison with measured data shows that the proposed scaling argument performs very well in collapsing the velocity profiles. Finally, an eddy viscosity model was developed to justify the scaling argument, which was validated with other datasets reported in the literature.

5.1.1 Conventional scaling methods

Many attempts have been made to provide acceptable scaling for the velocity profiles of flows over a rough bed. This section considers some possible scaling methods that are available in the literature for the conventional boundary layers and open channel flows, focusing on the physical interpretation rather than visual presentation. In another word, attention is paid to approaches that deals with the physics of the phenomenon, namely the normalisation and selection of non-dimensional parameter (or a combination of the non-dimensional parameters) rather than approaches that rely on geometrical technique such as axis transformation, or conformal transformation.

Empirically, the classical log-law has often been employed for normalizing the velocity profiles observed in the rough-bed channel flows (e.g. [*Birch and Morrison*, 2011]). If the flow depth above the porous roughness elements is large, the log-law not only applies for the inertial layer but may also provide an acceptable approximation for the entire flow. However, in the region near the wall, the bursting phenomena occur most violently and cause a local imbalance in turbulence production and dissipation. Therefore, scaling the velocity profile in a roughness layer using the log-law approach would not be appropriate. In Fig. 5.1, y/k is plotted against u/u_* with the present experimental data, showing a considerable scatter of data. The distribution varies with both the flow depth and porosity, implying that there is no unique relationship between the normalised velocity and length. Similar observation could be found when the roughness k was estimated using other method or when the velocity deflect ($u - U_0$) was used instead of u, where U_0 is the slip velocity at the bed level.

Furthermore, for the condition of small roughness submergence, the roughness layer may become relatively thick and extend up to the free surface, while the logarithmic layer would become thinner and diminish. As a result, several studies have suggested that the boundary layer theory may fail for the flow with roughness submergence smaller than 10 [*Katul et al.*, 2002], or 40

[*Jiménez*, 2004]. In other words, the scaling using log-law manner may not be suitable for the open channel flow under small submergence conditions. Therefore, it would be more appropriate to normalize the surface layer velocity profiles with a length scale that characterize the roughness layer rather than the inertial layer.

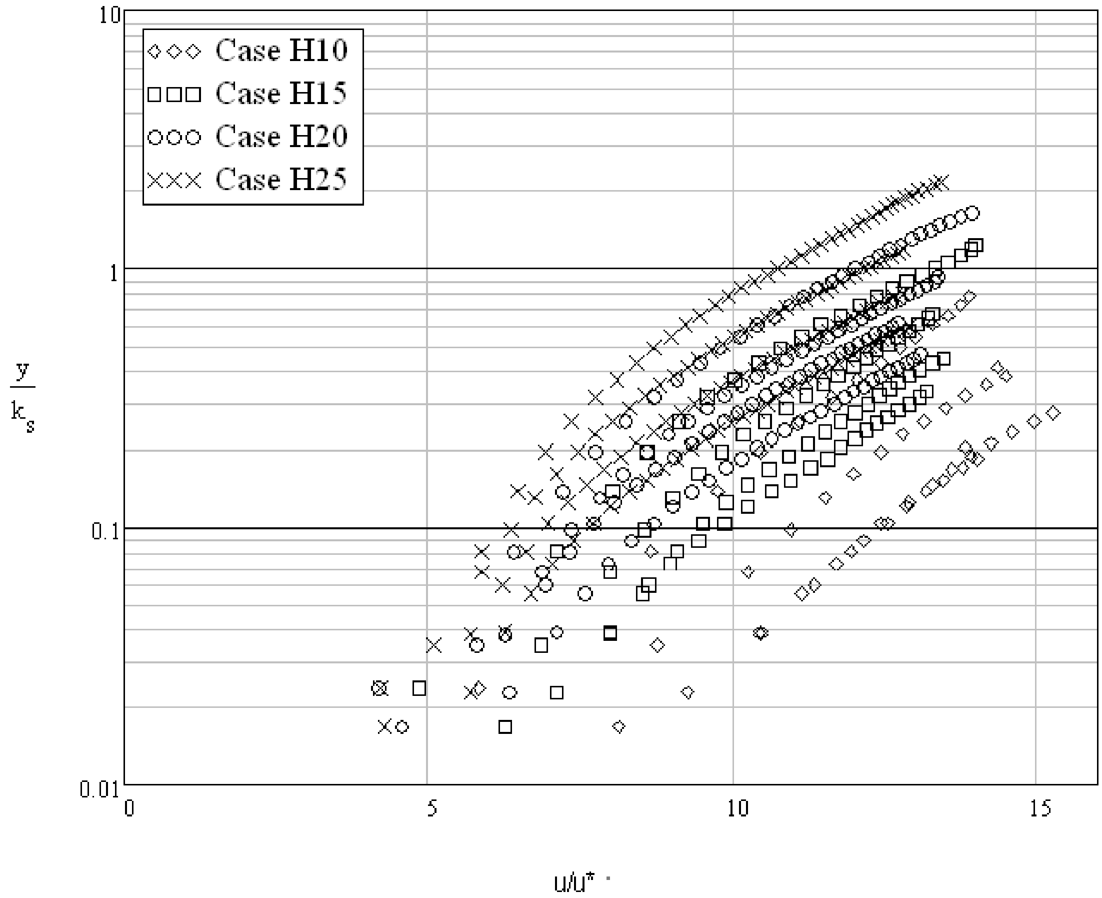

Fig. 5.1: Scaling of velocity profiles using shear velocity and roughness height

Besides the log-law consideration, this study also explored the possibility to use velocity-defect law to scale the velocity profiles. Fig. 5.2 demonstrates the scaling using of this approach for the experiment data, showing that there is still a remarkable degree of scattering associated with the data points in the surface layer.

On the other hand, the power-law of scaling also has a rigorous basis and was even considered more fundamental than the log-law [*Afzal*, 2001;

Barenblatt, 1993; *Cipra*, 1996]. Its envelope is claimed to enclose the log-law, which recalls an issue that was previously raised by Prandtl, the log-law is a limit form that can be obtained from the power-law at sufficiently large Reynolds number [*Afzal*, 2001; *Barenblatt*, 1993; *Prandtl*, 1935]. In applying the power-law to scale the velocity profiles in the surface layer, the velocity can be normalised by the maximum velocity U_{max} (also known as the free-stream velocity), while the length scale can be represented by H_s, the depth of the flow portion above the roughness crest. It is known that the power-law in the form of $u/U_{max} = (y/H_s)^{1/m}$, with m varying from 6 to 7, may approximate to a large extent velocity profiles observed in regular open channel flows [*Cheng*, 2007].

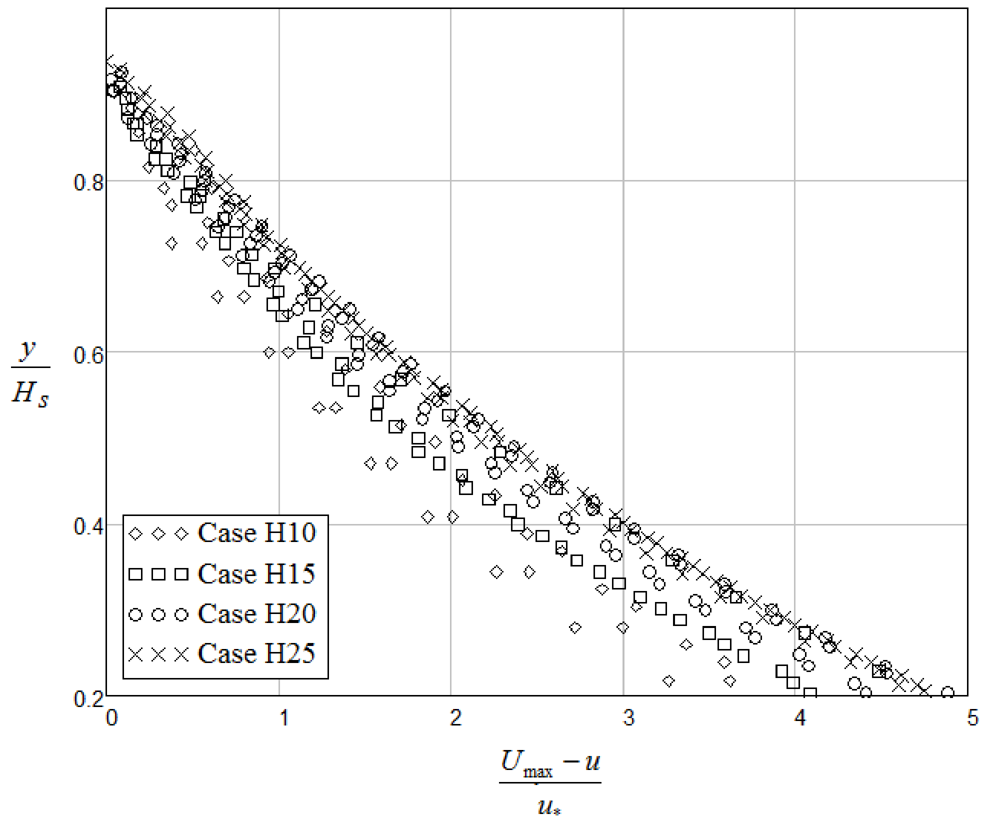

Fig. 5.2: Scaling of velocity-profiles using velocity-defect, shear velocity and flow depth

By using the free-stream velocity scale, *George and Castillo* [1997] also suggested a power-law that matches both outer and inner layer velocity profiles for a turbulent boundary layer. However, modification is needed to account for the slip velocity at the wall, such as that exists in permeable bed flows [*Afzal*, 2001]. Moreover, it was proposed by Cipra [1996] that the power-law scaling typifies the incomplete self similarity, which is also consistent with the spread of velocity data points when plotted with a narrow range of m-values [*Afzal*, 2001; *Cheng et al.*, 2012b]. The scattering of the data points plotted in Fig. 5.3 does not support the power-law with m-values in a narrow range. The data are roughly confined by the two power-laws with m = 3.5 and 7. These facts imply that either or both of the selected velocity and length scales could be inappropriate.

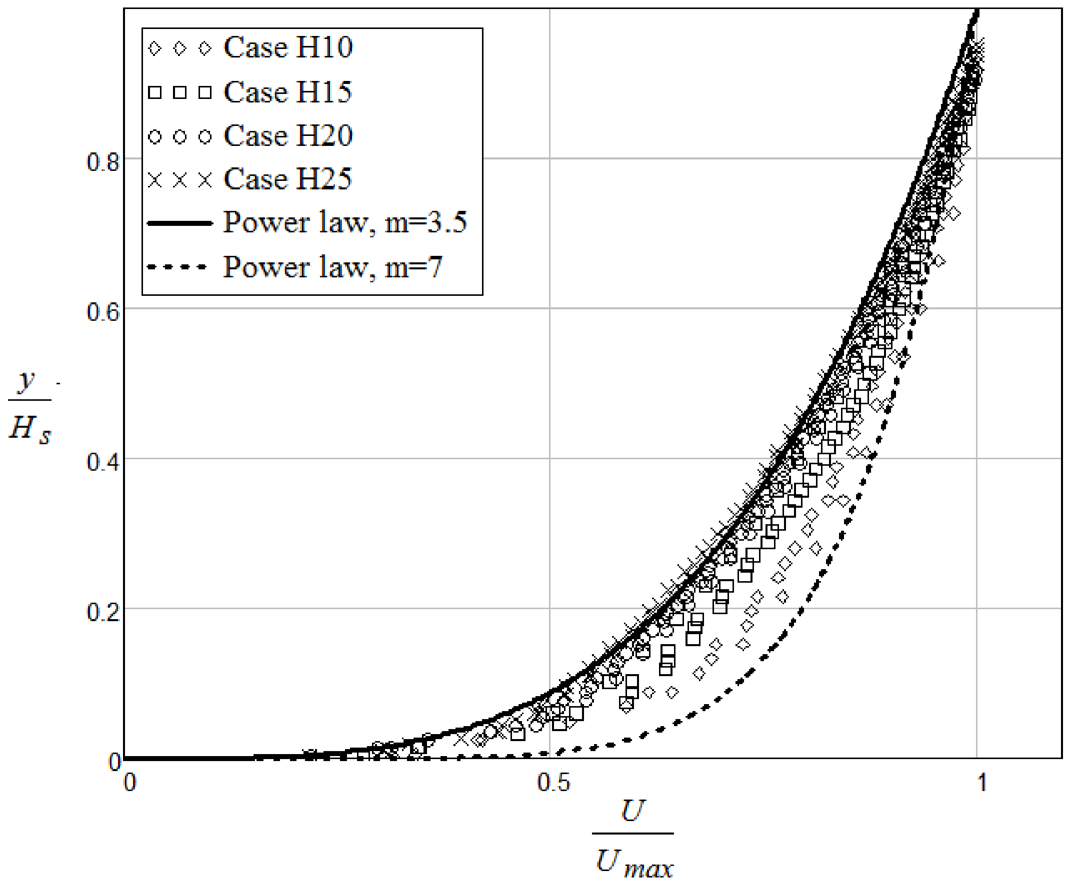

Fig. 5.3: Scaling of velocity profiles using maximum velocity and surface layer thickness

Scaling in the surface layer is dependent on the global properties of the flow. For example, in a closed channel flow, the only obvious outer length scale is the channel half-height h. A proper choice of the velocity scale appears even harder and various proposals could be considered. The friction velocity u_* is the most commonly used quantity. From the analogy with pipe flow, *Zagarola and Smits* [1998] argued that the mass flux deficit, $U_{CL} - U_b$, is a true outer velocity scale, where U_{CL} is the centerline velocity and U_b is the bulk velocity. However, *Bakken et al.* [2005] showed that this velocity scale is of no advantage to the shear velocity u_* when applied to turbulent flow in a channel with rough walls.

5.2. Proposed scaling method

5.2.1 Influences of the permeable bed on scaling

For engineering applications, the turbulent flow over porous beds is often considered equivalent to standard rough-wall turbulent boundary layers over impermeable beds [*Manes et al.*, 2009; 2011b], even though there is a substantial difference between them. With impermeable boundary, the no-slip condition applies whereas in the presence of porous bed, the flow is able to penetrate into the subsurface layer and to exchange mass, momentum and energy with the interstitial fluid. Therefore, the effects of bed permeability need to be accounted for.

It has been found that the (spatially averaged) shear stress variation has a linear distribution above the crest of the roughness elements, with a maximum at the crest level (e.g. *Nikora et al.* [2001; 2004]). The maximum kinetic energy production and dissipation occurs roughly at this level. As such, the roughness layer resembles that in a plane mixing layer theory, both sharing similar turbulence features. The turbulence over the large scale roughness is, therefore, often considered analogous to the plane mixing layer theory, with the mixing plane located roughly at the crest of the canopy [*Buffin-Bélanger and Roy*, 1998; *Finnigan*, 2000; *Ghisalberti and Nepf*, 2002; *Manes et al.*, 2011b; *Mignot et al.*, 2009; *Nepf and Ghisalberti*, 2008; *Poggi et al.*, 2004; *Raupach et al.*, 1991; *Raupach et al.*, 1996]. A detailed mixing layer explanation of the turbulence properties around submerged roughness elements can be found in the work done by *Buffin-Belanger and Roy* [1998]. It has also been documented that there exist an inflectional point in the velocity profile of a plane mixing layer, which was found to be self-similar [*Pope*, 2000].

There are several studies that have applied the concept of mixing layer to open channel flows over vegetation, e.g. *Ghisalberti and Nepf* [2004; 2006]. However, the mixing layer thickness had been chosen to be the characteristic length scale in these studies. Since the mixing layer can be strongly influenced by the velocity measured within the subsurface layer, its estimation is bound to be subjective. Depending on the strength of the flow, the penetration of coherent eddies generated in this layer into the subsurface layer may vary. The thickness of the roughness layer may neither equal nor proportional to the thickness of the outer layer, even for the flow of small submergence, as there is momentum exchange across the bed interface and turbulent eddies penetration into the subsurface layer. Therefore, the mixing layer width may vary with the strength of the flow, even though its development is restricted by the flow surface [*Cheng et al.*, 2012b].

5.2.2 Proposed length and velocity scales

To scale the mean velocity profile, both characteristic length and velocity are needed. This study proposes a scaling method based on the concept of *half-width*, defined as the flow depth at which the flow velocity reduces to one half of the maximum velocity. This approach serves as an extension from the earlier works by *Cheng et al.* [2012a; 2012b], which have been successfully applied to scaling velocity profiles in granular flows and vegetated open channel flows. The idea of half-width has also been widely used in the similarity analysis of free shear flows such as jets [*Durbin and Reif*, 2001] to quantify the spreading of those flows, where an interface with the ambient environment is indistinguishable.

At a first approximation, the maximum flow velocity, U_{max}, measured under the depth limited and permeable bed conditions is assumed to occur at the free surface. This assumption could be verified by most of the velocity profiles measured. Then, the flow velocity profiles could be considered to resemble one-half of that of the plane jet, or more precisely the compound plane jet (see Fig. 5.4 below). Both velocity profiles (at the fully developed region) exhibit self-similarity in nature and share several characteristics in common, including a maximum velocity, an inflectional point and an almost indistinguishable boundary with the surrounding environment. This is where the conventional scaling idea widely used in study of jets with the ψ axis starting at the symmetric axis of the jet (Hinze 1975, Rajaratnam 1976, Pope 2000) could be well utilized.

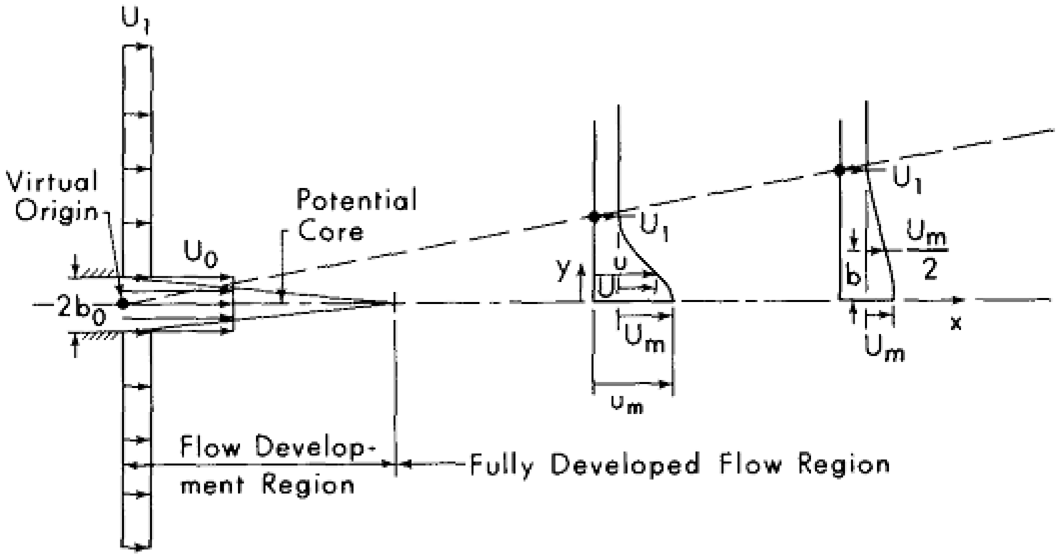

Fig. 5.4: Sketch of a compound plane jet (after Rajaratnam 1976).

More precisely, when the shallow flow takes place over a rough and porous bed, there would exist a distinct slip velocity at the permeable interface and an exchange of energy, mass and momentum across the interfacial surface. As a result, a plane mixing layer would form between two parallel streams of different velocities, one above the porous bed (U_{max}) and the other inside (U_p). In this case, $\psi_{1/2}$ should be taken to be the distance measured downwards from the free surface to the location where the velocity difference (u - U_p) reduced to one half of the maximum velocity defect (U_{max} - U_p), as sketched in Fig. 5.5.

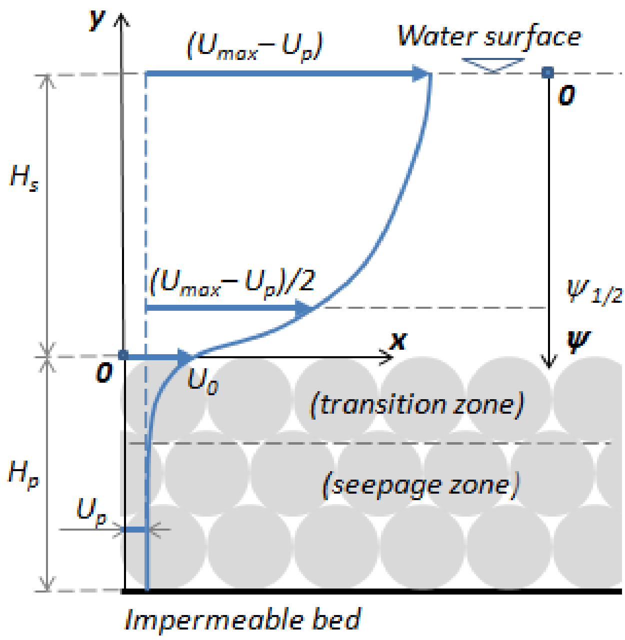

Fig. 5.5: Schematized flow velocity profile with alternative coordinate

Using $(U_{max} - U_p)$ and $\psi_{1/2}$ as characteristic velocity and length scales, the vertical profile of streamwise velocity can be normalised as $(u - U_p)/(U_{max} - U_p)$ and $\psi/\psi_{1/2}$, whereby U_p is taken to be the average velocity of the flow through porous bed, which is not significantly affected by the free surface layer and also the impermeable channel bed.

5.2.3 An eddy viscosity model for velocity distribution

Besides using the plain mixing layer analogy and the concept of half-width widely used in study of free shear flow, this study also aims to justify the scaling approach with a proposed analytical model based on eddy viscosity. In an earlier studies, *Cheng et al.* [2012a; 2012b] proposed a viscosity model to justify the scaling methods developed for vegetated open channel flows and granular sheet flows. In this section, the same approach is applied. By considering the balance of forces acting on a control volume (of length Δx in the streamwise direction and unit width in the transversal direction, as shown in Fig. 5.6), one gets $WS = \tau\Delta x = \rho g\psi S\Delta x$, where $\tau\Delta x$ is the shear force, W is the weight of the fluid being enclosed within the control volume, S is the flow surface slope and ρ is the density of water. Following the classical theory of turbulence, the shear stress exerting at the lower boundary of the control volume, τ, can be expressed as

$$\tau = -\rho(\nu + E)\frac{du}{d\psi} \approx -\rho E\frac{du}{d\psi} \tag{5.1}$$

where E is the eddy viscosity, ν is the fluid kinematic viscosity, and $E >> \nu$. The negative sign accounts for the fact that ψ is the distance measured downwards from the free surface and the velocity gradient $du/d\psi$ is negative.

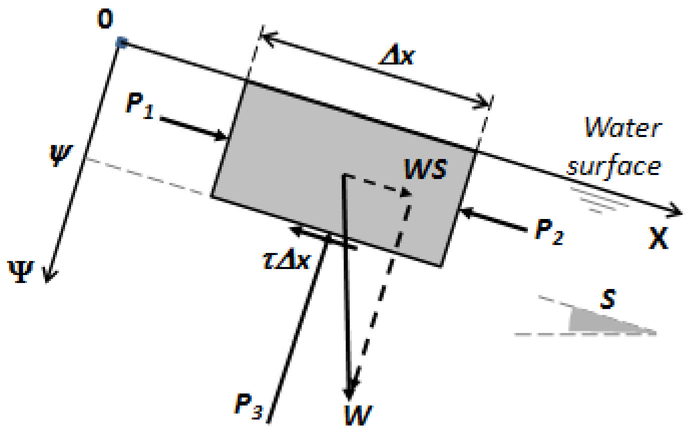

Fig. 5.6: Forces acting on a control volume

Using Eq. (5.1), the velocity distribution can be obtained by integration given that E is known. By analyzing the measured velocity profiles, an assumption similar to that by *Cheng et al.* [2012b] was adopted as a first approximation, i.e., the product of $E(u- U_p)$ is a weakly ψ-dependent function in the form of power-law. It could be represented by $E(u- U_p) \sim \psi^n$, where the exponent n is close to zero. Examples of such relation are shown in Fig. 5.7, where ψ has been normalised with the flow depth.

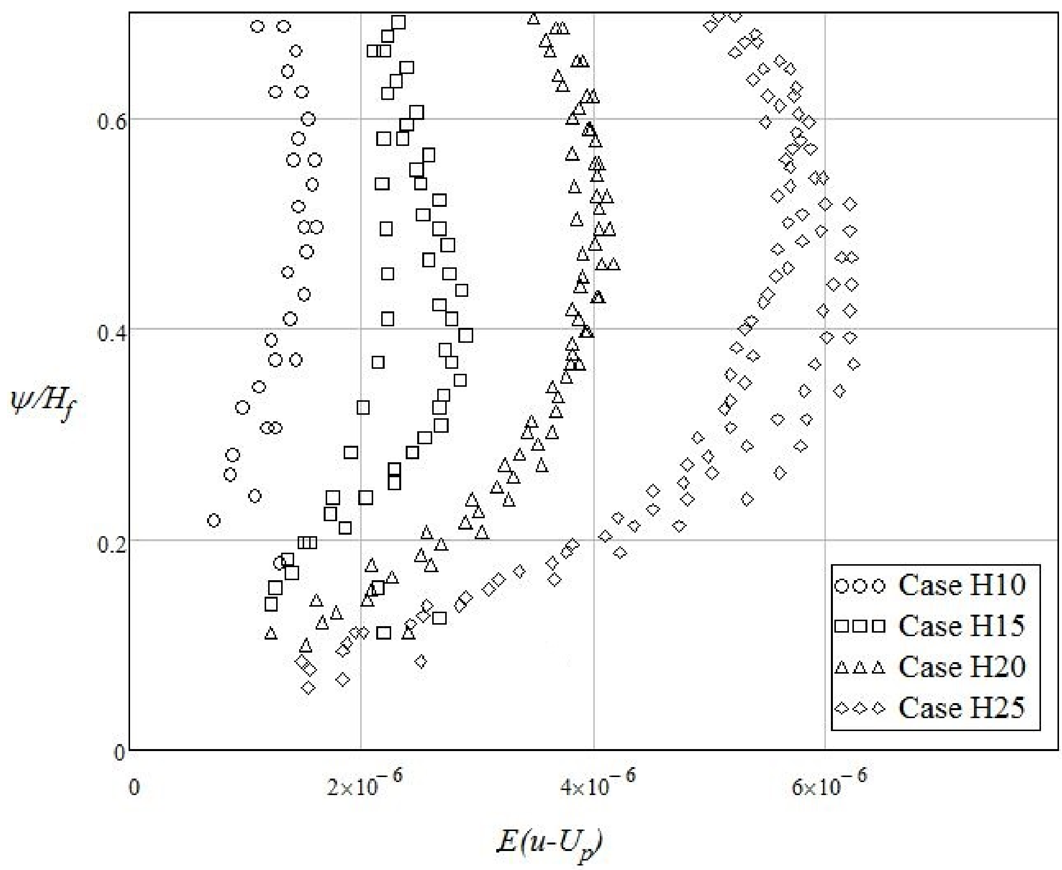

Fig. 5.7: Variation of $E{\cdot}(u - U_p)$ for all test cases, Spherical-particle bed

It is known that the eddy viscosity has a dimension of the product of velocity and length. Therefore, with the proposed half-thickness, the characteristic length and velocity can be taken to be $\psi_{1/2}$ and $(g\psi_{1/2}S)^{1/2}$, respectively. Then, E is normalised with $\psi_{1/2}\left(g\psi_{1/2}S\right)^{1/2}$ and $E(u - U_p)$ with $gS\psi_{1/2}^2$. With these considerations, Eq. (5.1) can be rewritten as

$$\frac{du^+}{d\psi^+} = -\frac{\psi^+}{E^+} \tag{5.2}$$

in which $u^+ = (u - U_p)/ (g\psi_{1/2}S)^{1/2}$, $\psi^+ = \psi/\psi_{1/2}$, and $E^+ = E/[(gS)^{1/2}(\psi_{1/2})^{3/2}]$. Integrating Eq. (5.2) taking into account $u = U_{max}$ at $\psi = 0$, and $(u - U_p) = 0.5(U_{max} - U_p)$ at $\psi = \psi_{1/2}$,

$$\frac{u - U_p}{u_{\max} - U_p} = \exp\left[-\ln(2)\left(\frac{\psi}{\psi_{1/2}} \right)^{\beta} \right] \tag{5.3}$$

where β = 2 − n. The value of β is close to 2 if n is very small. Eq. (5.3) is the proposed scaling of velocity profiles in shallow flow over large scale roughness. This method involves the length scale of $\psi_{1/2}$ and the velocity scale of (U_{max} - U_p), where the estimation of U_p has been detailed in Section 3.4. In the following sections, the proposed scaling method will be used to scale the measured velocity profiles resulting from tests with spherical-particle bed and gravel-bed. For illustrational purpose, the vertical axis is converted from $\psi/\psi_{1/2}$ to (1- $\psi/\psi_{1/2}$).

With the average subsurface flow velocity, the measured streamwise velocity above the bed can be normalised as (u - U_p)/(U_{max} - U_p). Nevertheless, it was observed that in our test condition for experiments with spherical-particle beds, U_p was about three orders smaller than U_{max}, its effect on the normalised velocity profile could be neglected. This is mainly due to the small bed slope used in our flume tests. In practice, the gradient of gravel-bed rivers are usually considerable higher and thus, U_p would play a more significant role. In the followings, (u - U_p)/(U_{max} - U_p) would be simplified as u/U_{max}. The other two parameters, $\psi_{1/2}$ and β, will be further discussed in Section 5.5.

5.3. Experimental results from spherical-particle bed tests

5.3.1 Double-averaged streamwise velocity

Using the measurement technique described in Section 3.3, a tremendous amount of data was obtained. Using PIV software, raw velocity vector maps were extracted from flow images. These vector maps were then undergone through validation, calibration and other post processing procedures to yield a meaningful velocity vector field for each test case, as depicted in Fig. 5.8.

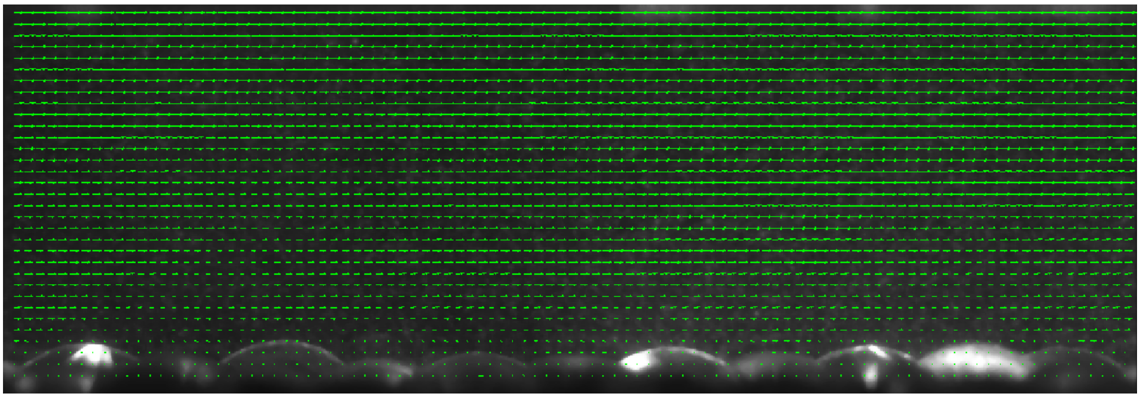

(a) Spherical-particle bed, case L3H20, vertical plane above roughness crests

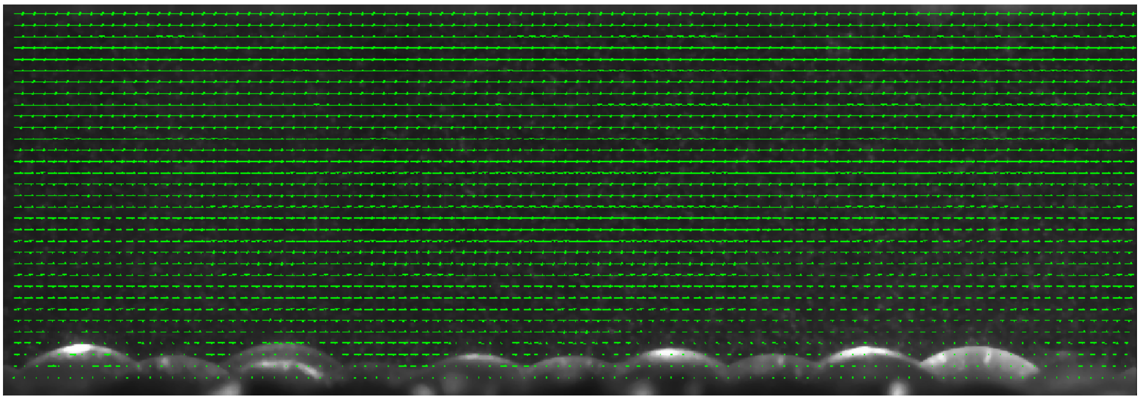

(b) Spherical-particle bed, case L3H20, vertical plane above roughness troughs

Fig. 5.8: Instantaneous velocity maps (superimposed onto original flow image)

Applying the double-averaging analysis, this spatially distributed flow velocity data was then averaged in time and space. The temporal average was carried out for all instantaneous velocity vector maps in an ensemble. Subsequently, two spatial averaging operations were performed to (i) average the velocity maps corresponding to the two planes projected on top of roughness trough and crests, respectively; and (ii) average the vertical velocity profiles over all verticals). Basically each velocity vector map is a matrix with 99 columns, representing velocity data from 99 verticals in the flow. This whole process yields the desired mean velocity profiles (for both longitudinal and bottom-normal components).

This procedure was automated with Matlab scripts and repeated for all test cases. The resulting velocity profiles for the streamwise component are shown in Fig. 5.9 below, grouped by similar flow depth. They show variations as expected. In the section that follows, the proposed scaling method will be applied and compared with conventional scaling method.

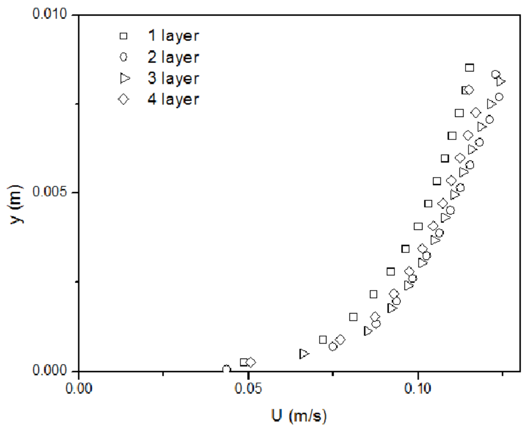

(a) H_s = 10mm

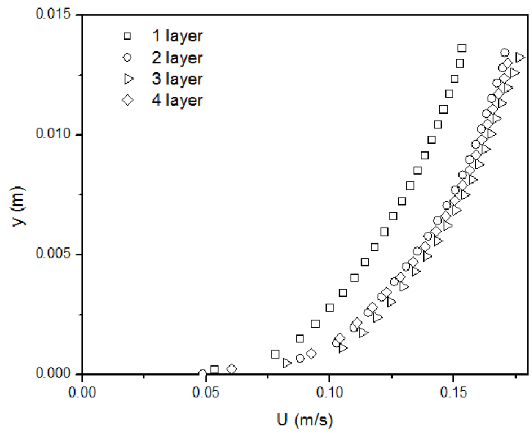

(b) H_s = 15mm

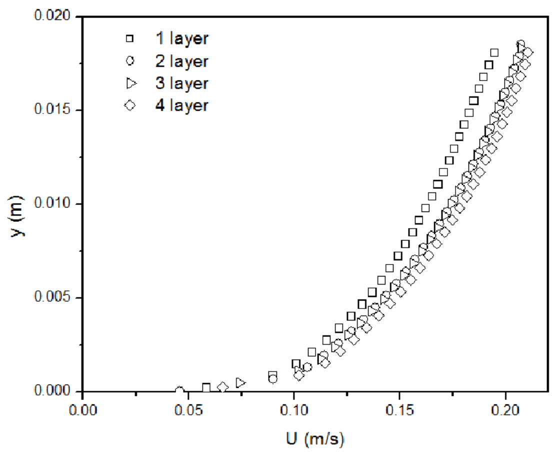

(c) H_s = 20mm

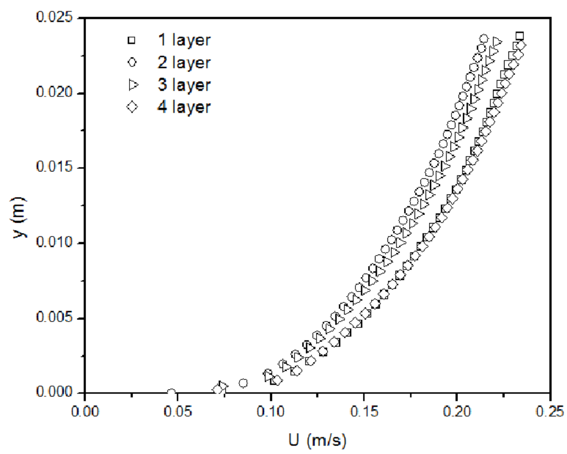

(d) H_s = 25mm

Fig. 5.9: Double-averaged velocity profiles for spherical-particle bed tests

5.3.2 Scaling of measured velocity profiles

Assuming the maximum velocity occurs at the free surface, a natural choice for scaling would be using the flow depth and this maximum velocity value as length and velocity scale. All the streamwise velocity profiles above are normalised with these scales and grouped in Fig. 5.10 below. As can be seen, they still exhibit a considerable level of scattering, implying the effects of both roughness configuration and flow depth.

Meanwhile, the proposed scaling approach has shown to be quite useful in collapsing the velocity profiles. Using the length and velocity scales proposed in section 5.2, the data are plotted in Fig. 5.11 in the form of $(1-\psi/\psi_{1/2})$ against u/U_{max} for H_s = 1.5cm. Eq. (5.3) was also superimposed onto the figure, with β = 1.88. The velocity profiles presented in this figure are those measured above the roughness crest, i.e. for $\psi < H_s$. With the same flow depth, four profiles were measured for the different porous bed configurations. From Fig. 5.11, it can be seen that the relationship between u/U_{max} and $\psi/\psi_{1/2}$ is not subject to the variation in the number of roughness layer. Similar results as shown in this figure were also observed for H_s = 10, 20 and 25 mm.

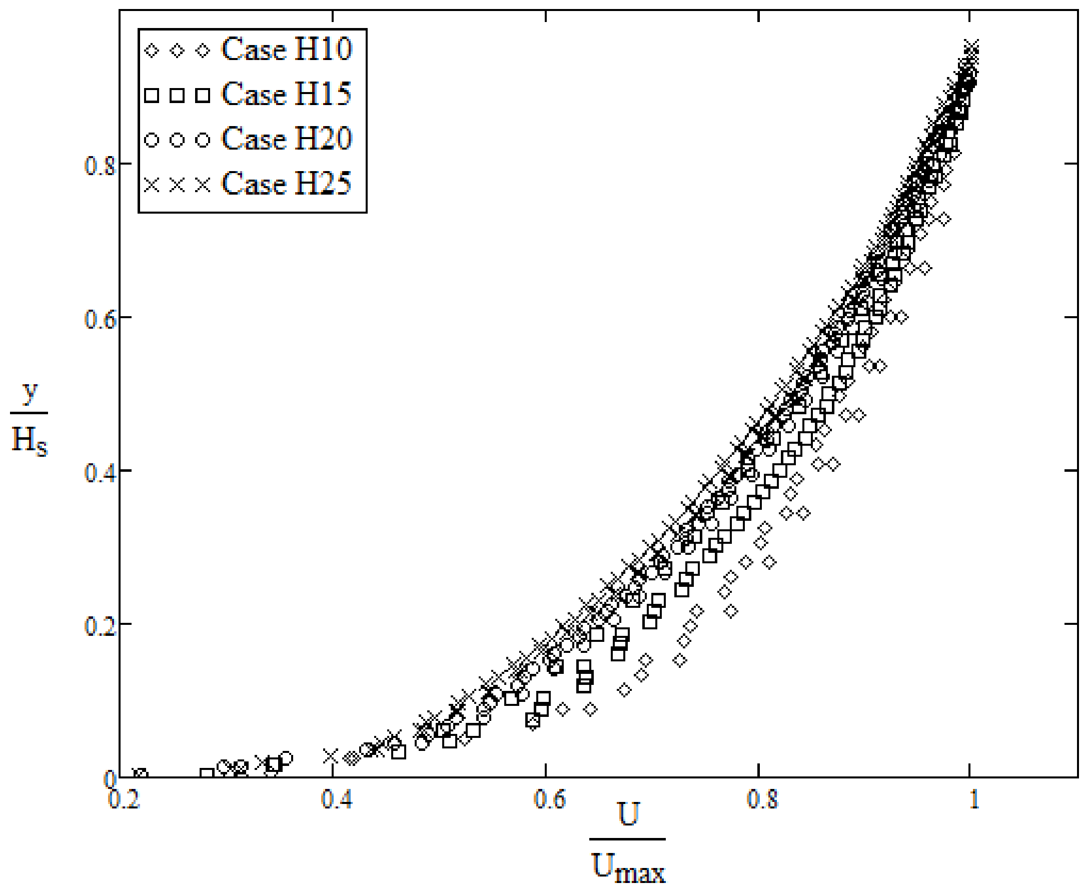

Fig. 5.10: Velocity profiles for all tests normalised with U_{max} and H_s

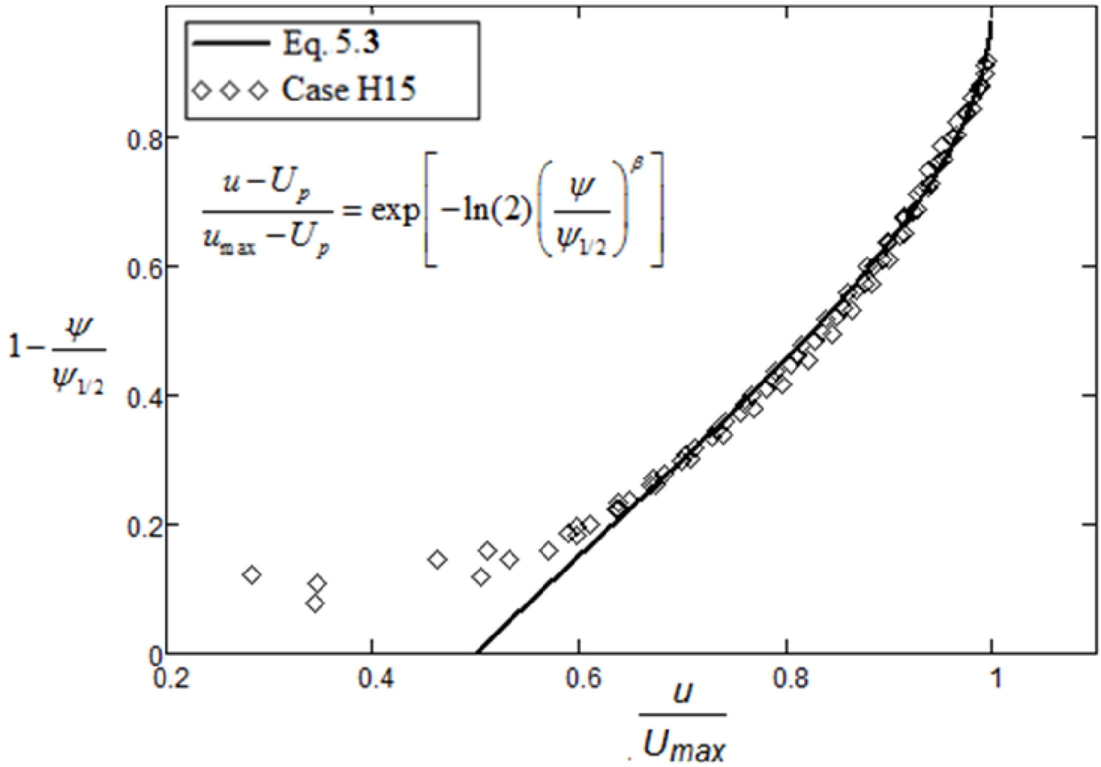

Fig. 5.11: Scaling of velocity profiles for test cases with similar flow depth (H_s = 15 mm) and different bed configurations, spherical-particle bed

On the other hand, Fig. 5.12 shows four velocity profiles measured for the case of three roughness layers, for different flow depths H10-H25 (i.e. H_s = 10, 15, 20 and 25 mm). For comparison, the upper panel presents the velocity profiles plotted with y/H_s. The lower panel shows that the new scaling method successfully collapses the data onto a single curve, for a large portion of the surface layer. The curve can be well represented by the power fit [Eq. (5.3)] with an exponent of β = 1.85, taking U_p to be zero. However, the new scaling works well only for the zone away from the roughness elements, and an obvious deviation is observed near the rough bed (approximated by $\psi \leq 0.2H_s$), where the form-induced turbulence strongly influenced the flow structure.

All the data for the 16 test cases (excluding those four cases with the impermeable smooth bed) are plotted together in Fig. 5.13, grouped by different flow depth H_s. It shows that the normalised profiles are similar to one another, independent of both the flow depth and bed configurations. This illustrates that the normalization based on (U_{max} - U_p) and $\psi_{1/2}$ yields a significant improvement in scaling the measured velocity profiles. For illustrational purpose, the vertical axis has been converted from $\psi/\psi_{1/2}$ to (1- $\psi/\psi_{1/2}$).

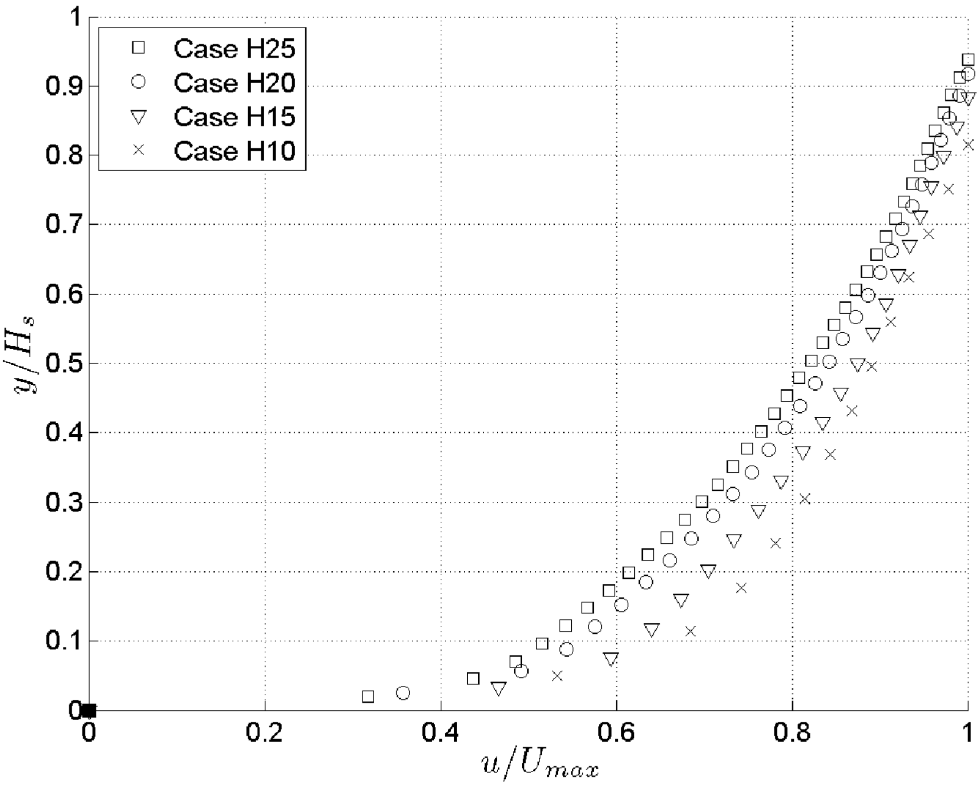

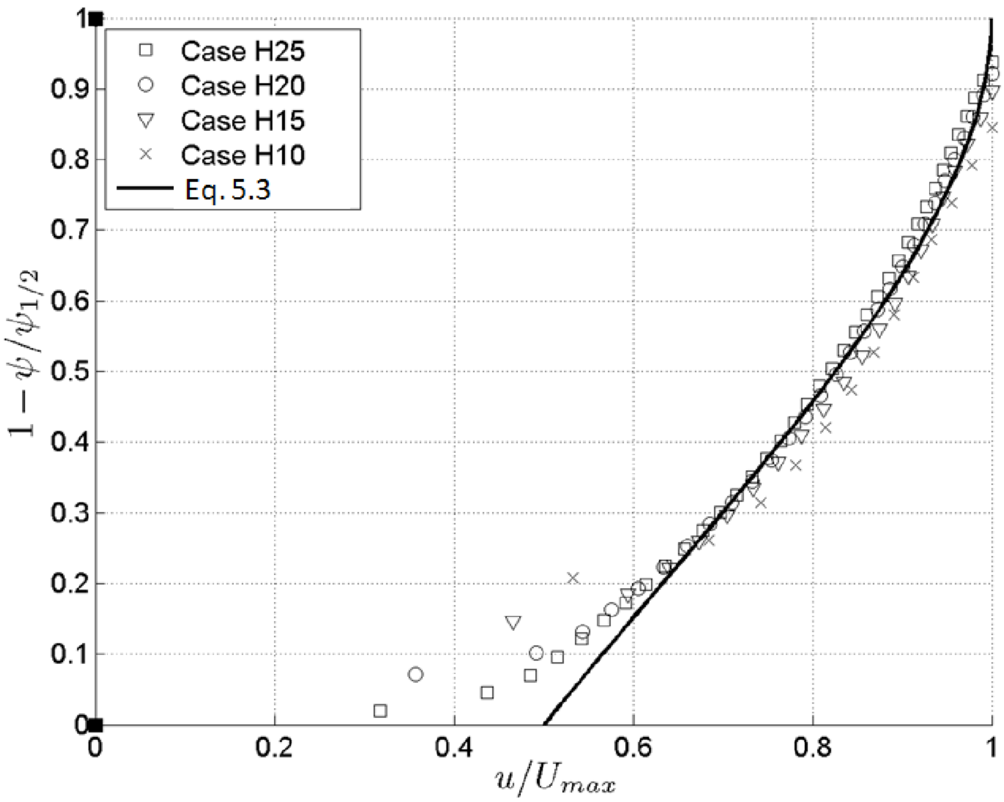

Fig. 5.12: Velocity profile for test cases with similar bed configuration (three roughness layers) and different flow depths, spherical-particle bed

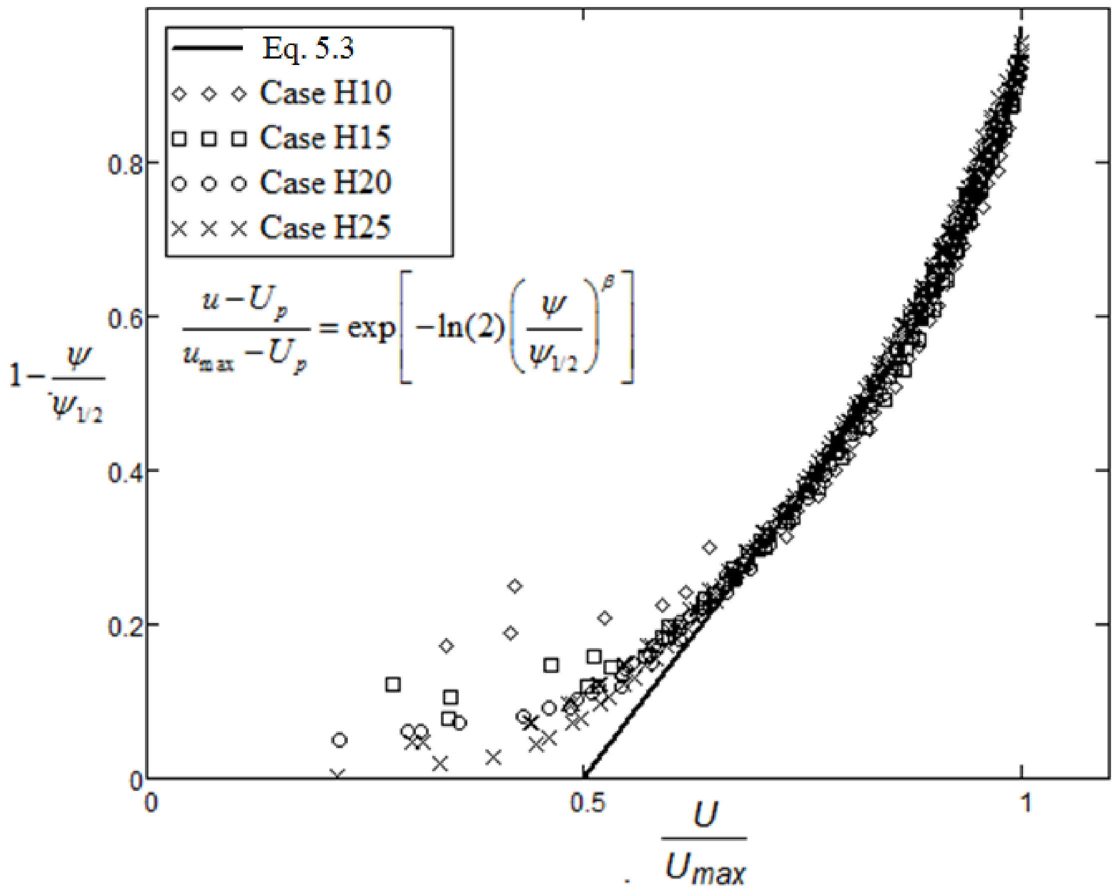

Fig. 5.13: All velocity profiles for rough-bed cases, spherical-particle beds

5.4. Experimental results from gravel-bed tests

5.4.1 Double-averaged streamwise velocity

As described in Section 3.2, 40 test cases for different gravel-bed configurations were carried out in two flumes A and B. For each test, numerous point measurements were carried out to yield nine vertical flow velocity profiles at nine equi-distant verticals, as illustrated in Fig. 5.14 for the test case with 4 layer of gravels and Q = 6.639 l/s in Flume A. Each point measurement had already been averaged out over a period of 120 seconds. Therefore, a subsequent averaging over these nine spatially distributed profiles resulted in a double-averaged velocity profile, as exemplified in Fig. 5.15 (3 layer of gravels, Q = 7.649 l/s, Flume A).

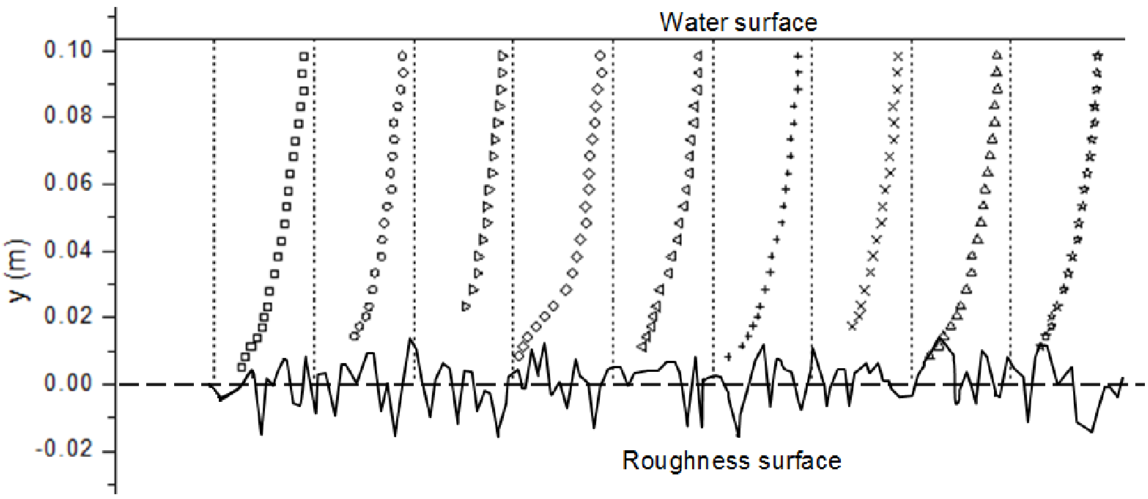

Fig. 5.14: Velocity profiles for nine verticals, test AL4Q1, gravel bed

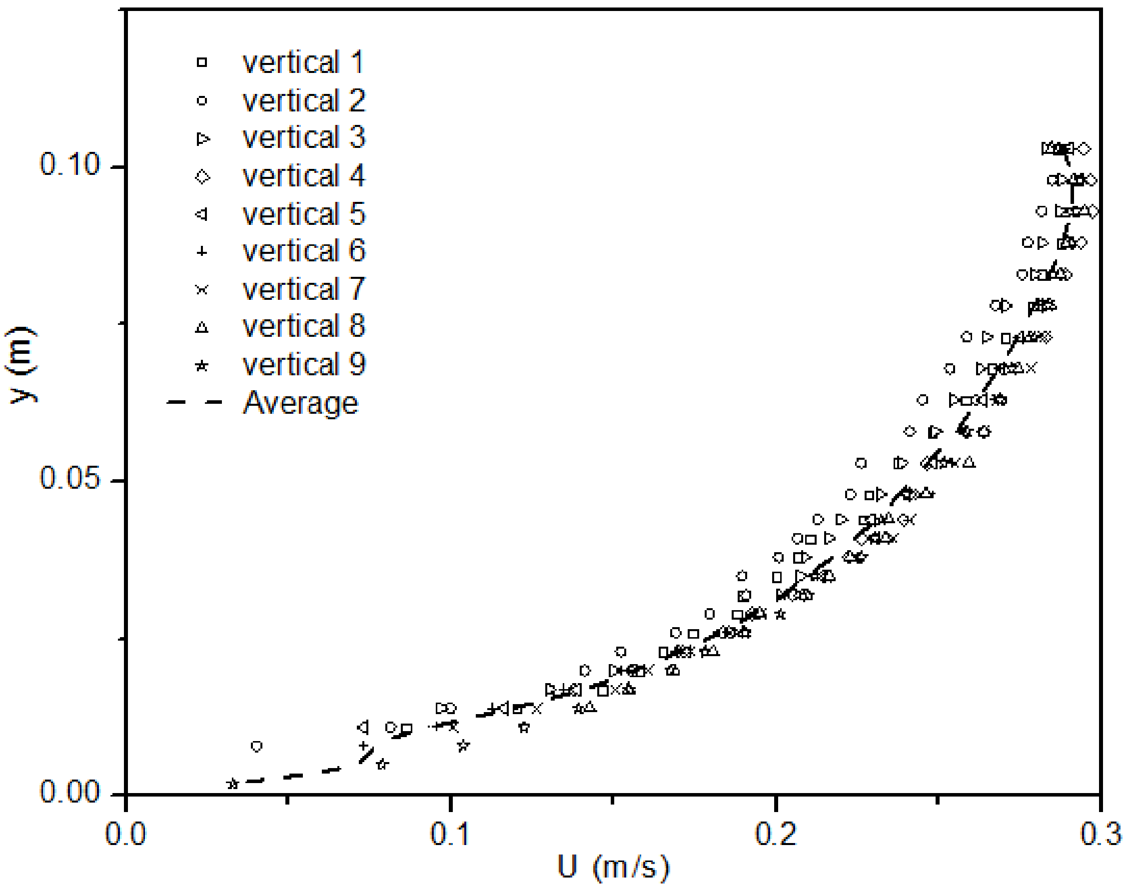

Fig. 5.15: Velocity measurements and spatial averaging, test AL3Q1, gravel bed

Due to the irregularity of the roughness surface, flow velocity in the near bed region is subjected to a noticeable fluctuation. A higher number of verticals would, therefore, be desired to get a more meaningful average. However, due to limitations of the point measurement, a finite number of 9 verticals had been adopted, which resulted in reliable measurement and acceptable results. Nevertheless, for engineering application it could be noted that the major portion of the surface flow takes place in the region above the roughness sublayer and thus, this miniature fluctuation of velocity near the bed would have a minimal effect in the mean flow velocity.

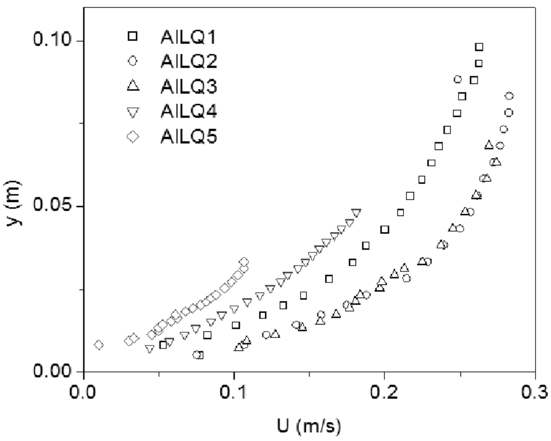

(a) 1 layer, flume A

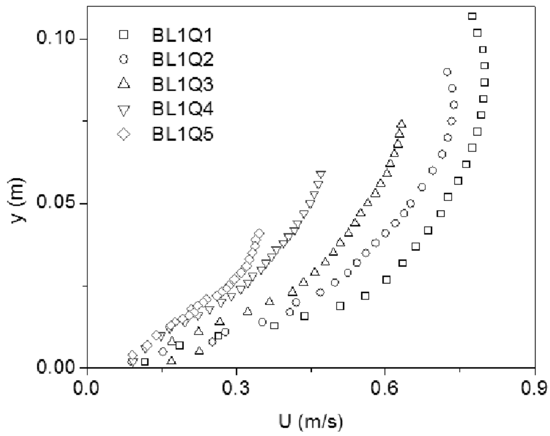

(b) 1 layer, flume B

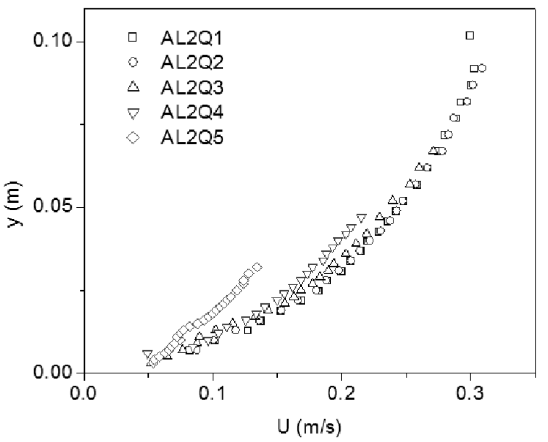

(c) 2 layer, flume A

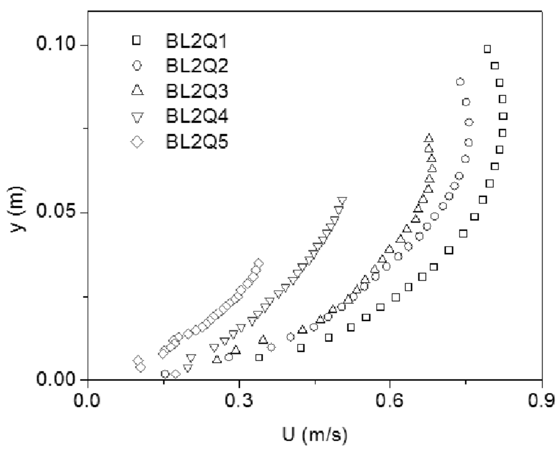

(d) 2 layer, flume B

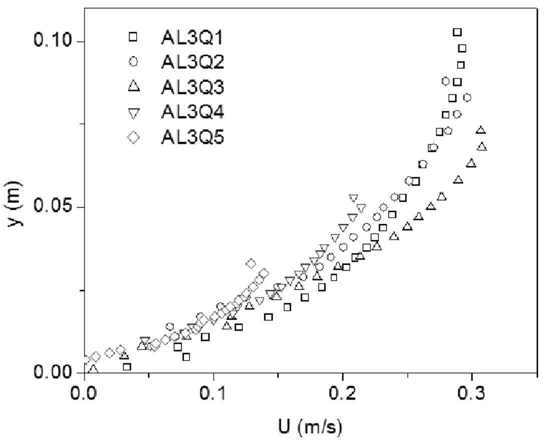

(e) 3 layer, flume A

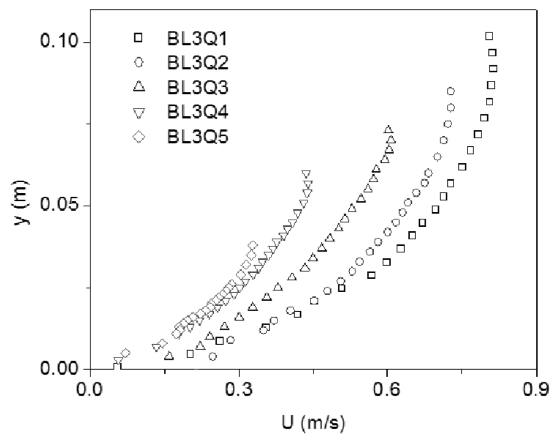

(f) 3 layer, flume B

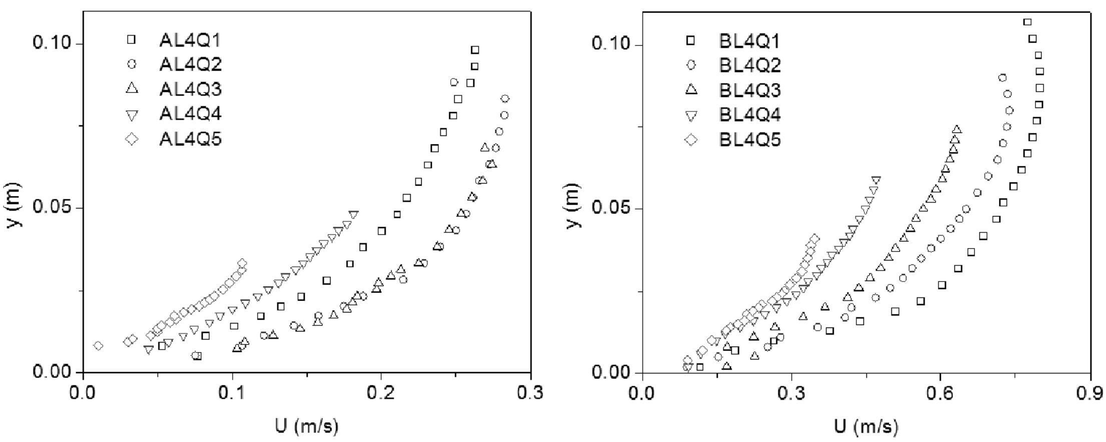

(g) 4 layer, flume A (h) 4 layer, flume B

Fig. 5.16: Double-averaged velocity profiles for gravel-bed tests

5.4.2 Scaling of the measured velocity profiles

Similarly to the scaling exercise for data from spherical-particle bed tests, those from gravel-bed tests could be normalised using the same approach. By normalizing with the length and velocity scales proposed, the velocity data for gravel-bed tests are plotted in Fig. 5.17 in the form of ($1-\psi/\psi_{1/2}$) against u/U_{max} for different flow conditions, test cases with two layer of gravels. Eq. (5.3) was also superimposed onto the figure, with β = 2.3, showing that the relationship between u/U_{max} and $\psi/\psi_{1/2}$ is not subject to the variation in the flow depth.

Similar results as shown in this figure were also observed for the other bed configurations with different number of gravel layers and different flume set up, as exemplified in Fig. 5.18 and Fig. 5.19, implying that the scaling method is suitable for different bed configuration as set out in this study. In comparison to the test cases with spherical-particle beds, there is a higher degree of scattering for velocity data near to the bed surface, which is expected due to the higher irregularity of the gravel bed.

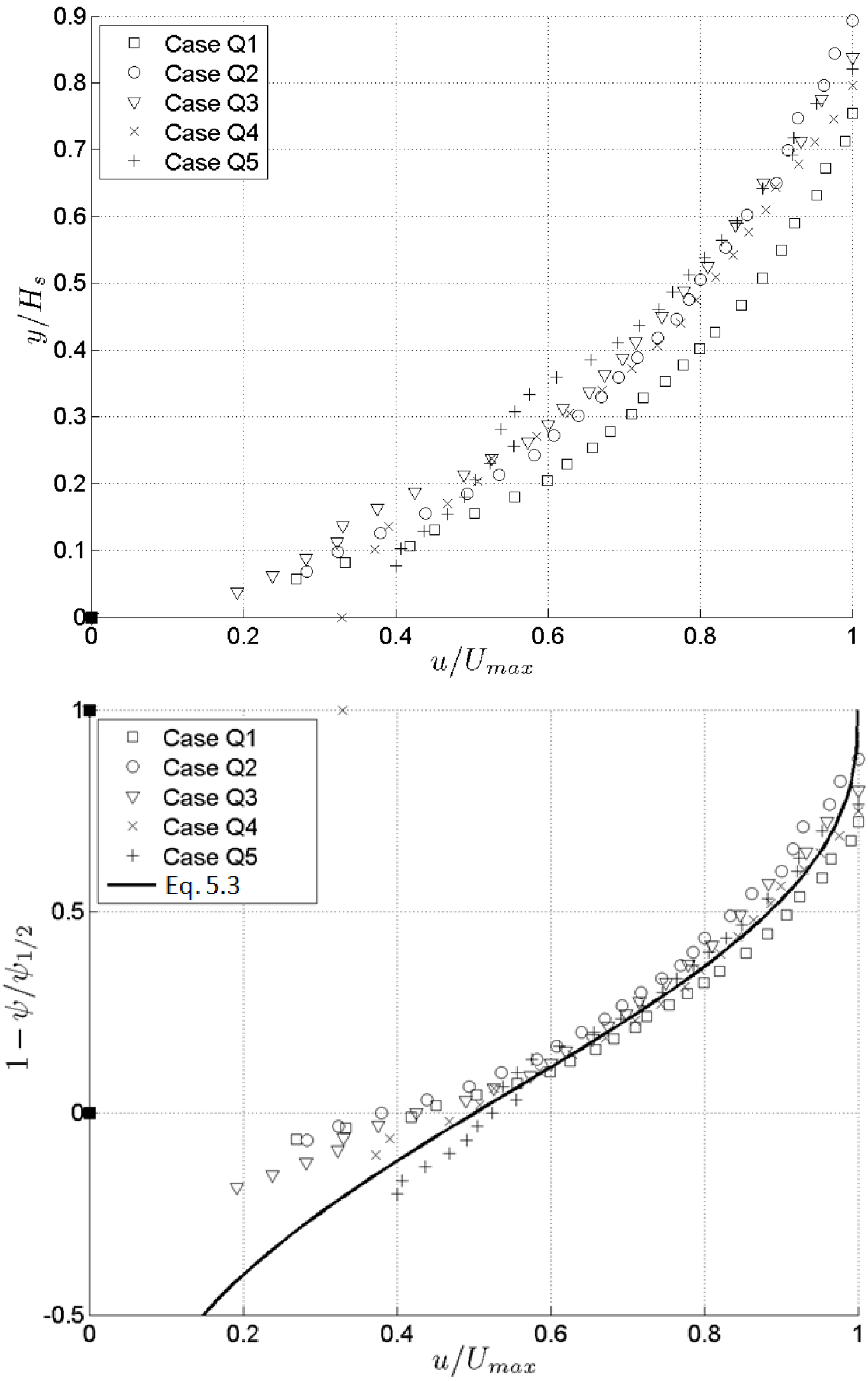

Fig. 5.17: Scaling of velocity profiles for test cases with two layer of gravels and varying flow discharges, Flume A

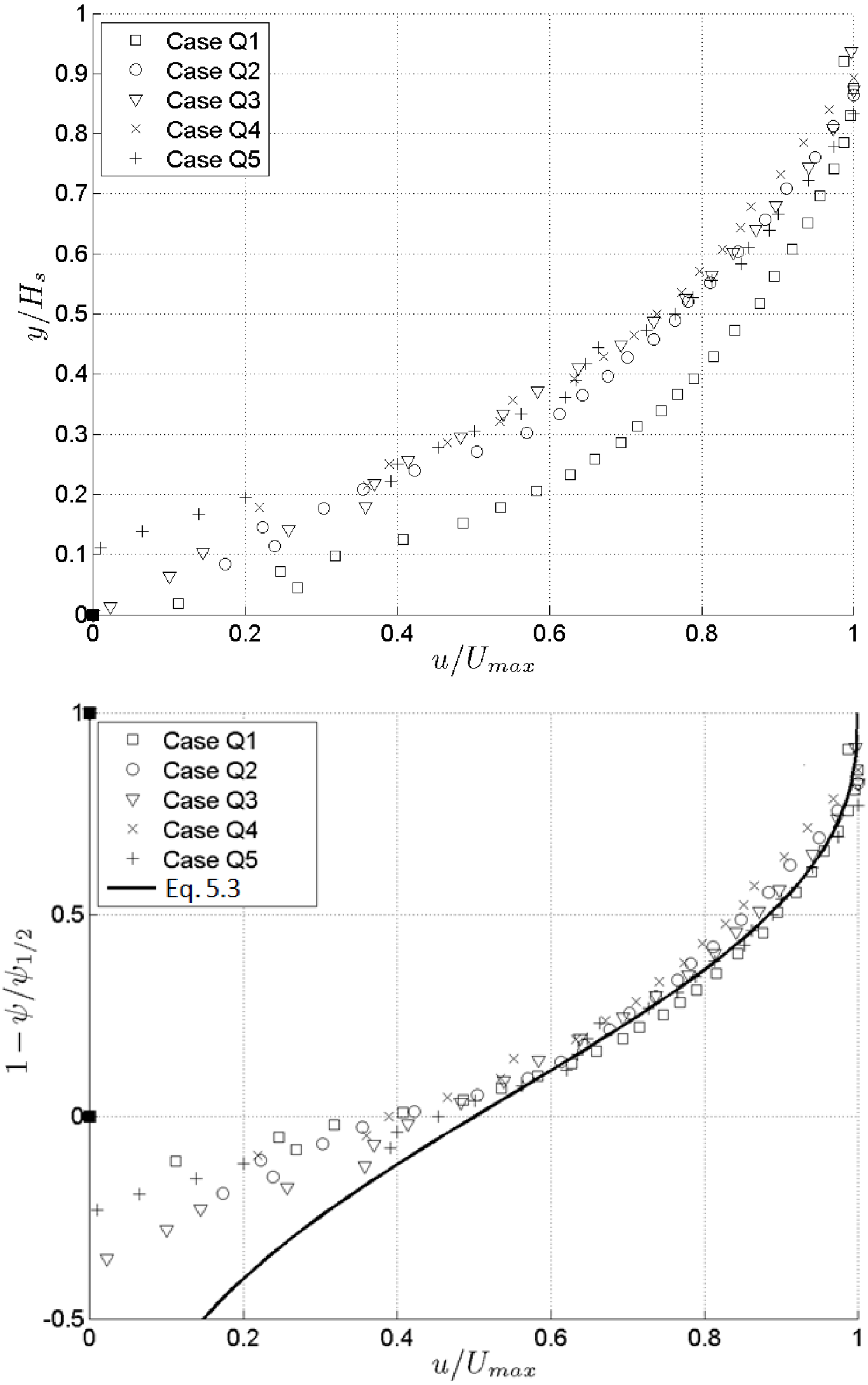

Fig. 5.18: Scaling of velocity profiles for test cases with three layers of gravels and varying flow discharges, Flume A

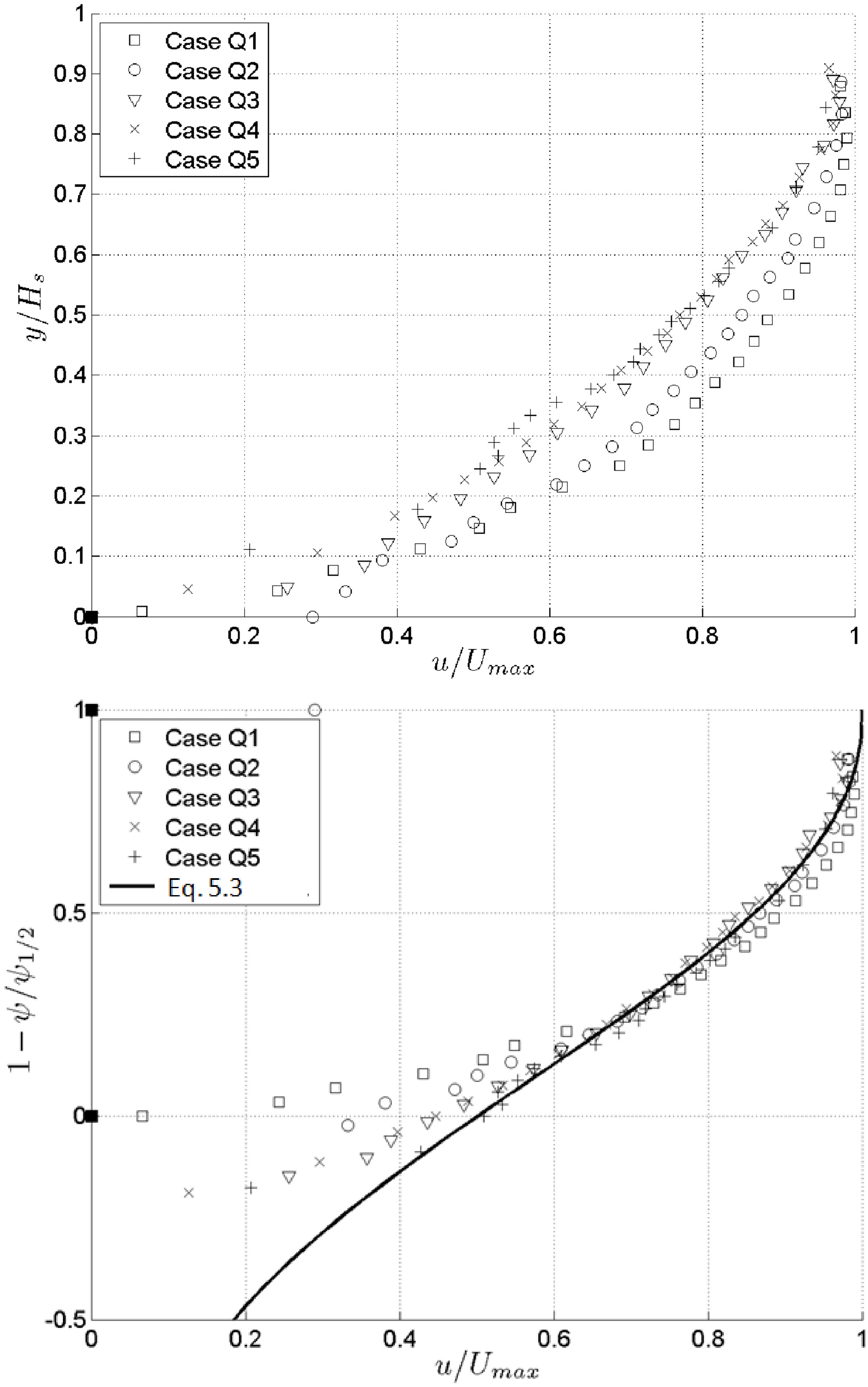

Fig. 5.19: Scaling of velocity profiles for test cases with three layers of gravels and varying flow discharges, Flume B

Table 5.1 and Table 5.2 summarize the scaling parameters obtained by fitting the proposed relationships with the measured data.

Table 5.1: Scaling parameters for test cases carried out in flume A

Test case	H_s (m)	U_{max} (m/s)	$\psi_{1/2}$ (m)	$\psi_{1/2}/H_s$ (-)	U_{mean} (m/s)	β (-)
AL1Q1	0.074	0.274	0.064	0.8696	0.205	2.35
AL1Q2	0.125	0.301	0.122	0.9791	0.246	2.95
AL1Q3	0.105	0.296	0.104	0.9943	0.236	2.25
AL1Q4	0.059	0.223	0.051	0.8618	0.171	2.53
AL1Q5	0.037	0.176	0.034	0.9164	0.131	1.90
AL2Q1	0.122	0.308	0.108	0.8853	0.237	2.60
AL2Q2	0.103	0.311	0.090	0.8738	0.227	1.90
AL2Q3	0.080	0.273	0.065	0.8063	0.198	2.20
AL2Q4	0.059	0.217	0.048	0.8136	0.156	2.30
AL2Q5	0.039	0.140	0.030	0.7692	0.098	1.90
AL3Q1	0.112	0.293	0.099	0.8795	0.225	2.72
AL3Q2	0.096	0.297	0.074	0.7708	0.202	2.23
AL3Q3	0.078	0.310	0.057	0.7244	0.204	2.24
AL3Q4	0.056	0.216	0.042	0.7518	0.140	1.90
AL3Q5	0.036	0.142	0.026	0.7278	0.089	2.25
AL4Q1	0.103	0.262	0.091	0.8809	0.193	2.20
AL4Q2	0.092	0.283	0.086	0.9317	0.224	2.95
AL4Q3	0.073	0.275	0.064	0.8791	0.209	2.30
AL4Q4	0.053	0.182	0.038	0.713	0.118	1.87
AL4Q5	0.036	0.108	0.023	0.6198	0.062	2.20

Fig. 5.20 shows the plot of the data for various tests performed in flume A, normalised by $\psi_{1/2}$ and (U_{max} - U_p), the latter being simplified as U_{max} in these cases as U_p was much smaller than U_{max}. Fifteen profiles were presented for different bed configurations and flow conditions. For comparison, the plot using U_{max} and H_s as velocity and length scales was also shown. It can be seen that the normalization using U_{max} and $\psi_{1/2}$ yields a considerable improvement in collapsing the measured velocity profiles onto a single curve, although there

were certain deviation near the gravel bed surface due to its strong irregularity. Similar observation was found with the normalised velocity profiles resulted from the various tests with Flume B, as shown in Fig. 5.21. All the data for the 20 test cases, grouped by different bed configuration, were normalised with (U_{max} - U_p) and $\psi_{1/2}$. Eq. (5.3) was also superimposed onto the figure, with β = 2.4. As usual, the vertical axis has been converted from to (1- $\psi / \psi_{1/2}$) for the ease of comparison.

Table 5.2: Scaling parameters for test cases carried out in flume B

Test case	H_s (m)	U_{max} (m/s)	$\psi_{1/2}$ (m)	$\psi_{1/2}/H_s$ (-)	U_{mean} (m/s)	β (-)
BL1Q1	0.127	0.800	0.140	1.102	0.673	2.9
BL1Q2	0.106	0.800	0.115	1.085	0.675	2.9
BL1Q3	0.082	0.710	0.072	0.878	0.563	2.7
BL1Q4	0.066	0.520	0.056	0.855	0.400	2.7
BL1Q5	0.042	0.410	0.033	0.795	0.299	2.7
BL2Q1	0.116	0.830	0.120	1.035	0.693	2.9
BL2Q2	0.099	0.770	0.095	0.961	0.614	2.6
BL2Q3	0.084	0.700	0.080	0.948	0.560	2.6
BL2Q4	0.063	0.510	0.054	0.864	0.386	2.1
BL2Q5	0.042	0.350	0.031	0.745	0.248	2.1
BL3Q1	0.116	0.820	0.105	0.905	0.634	2.7
BL3Q2	0.096	0.740	0.090	0.938	0.576	2.2
BL3Q3	0.078	0.620	0.068	0.829	0.451	2.0
BL3Q4	0.056	0.450	0.053	0.803	0.315	2.0
BL3Q5	0.036	0.340	0.034	0.756	0.236	2.2
BL4Q1	0.103	0.800	0.120	1.034	0.644	2.7
BL4Q2	0.092	0.750	0.085	0.870	0.574	2.7
BL4Q3	0.073	0.640	0.072	0.867	0.477	2.3
BL4Q4	0.053	0.470	0.051	0.797	0.331	2.4
BL4Q5	0.036	0.350	0.033	0.717	0.242	2.3

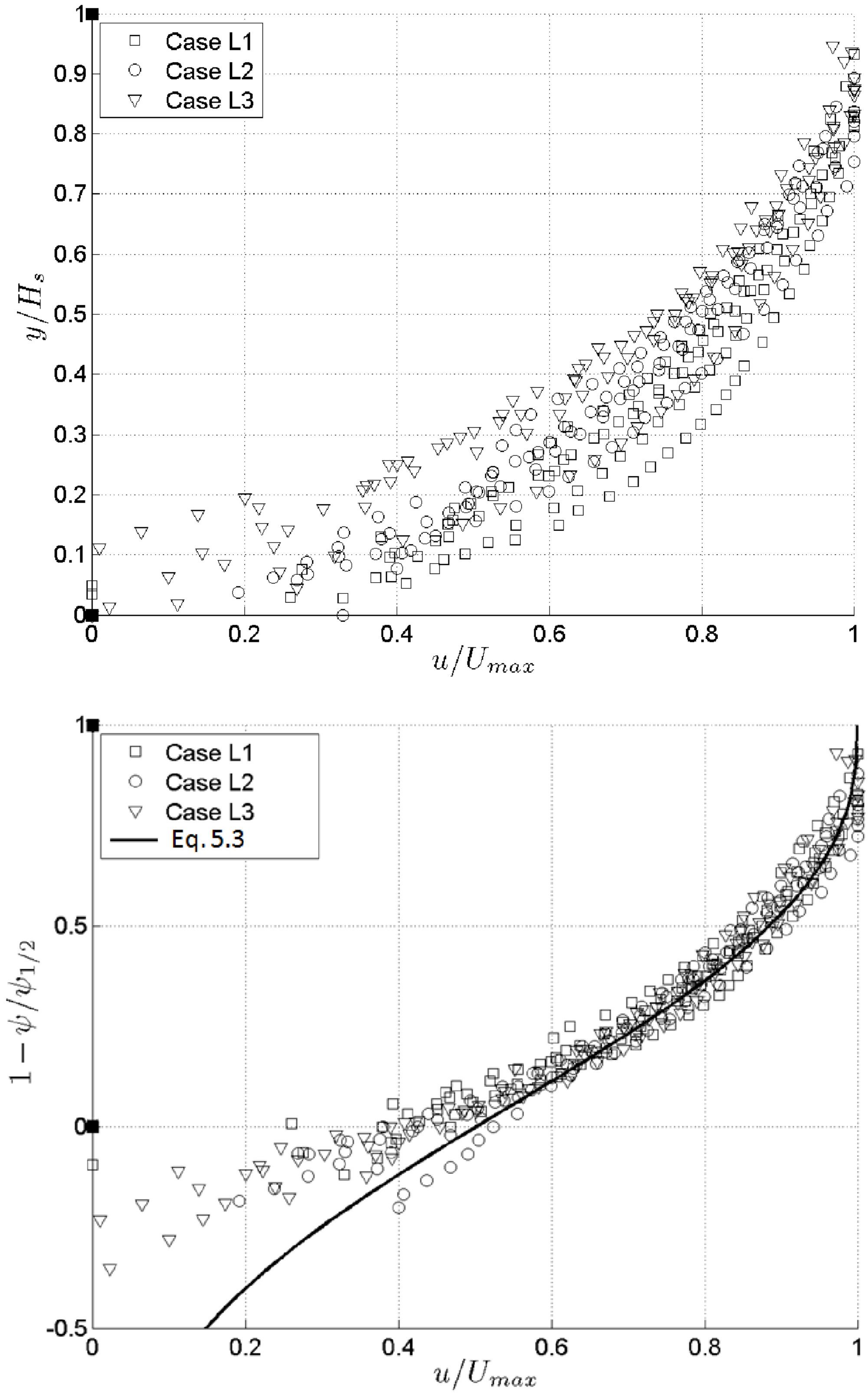

Fig. 5.20: Scaling of velocity profiles for test cases with varying bed configurations and flow discharges, gravel beds, Flume A

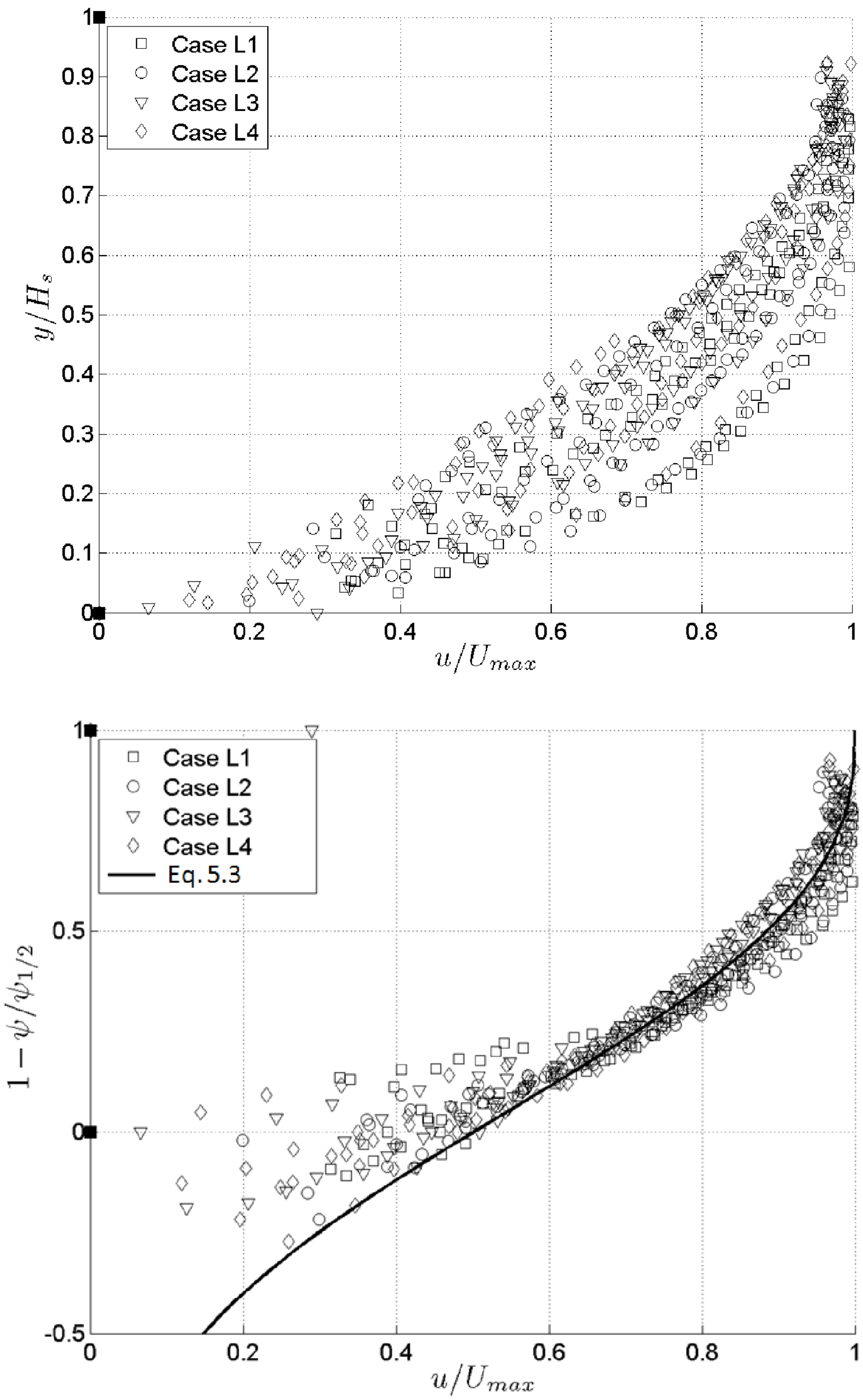

Fig. 5.21: Scaling of velocity profiles for test cases with varying bed configurations and flow discharges, gravel beds, Flume B

5.5. Discussions and Concluding remarks

5.5.1 Discussion on the viscosity model's parameters

To normalize the measured velocity profiles based on Eq. (5.3), the two parameters, $\psi_{1/2}$ and β, must be known. As can be seen in the preceding sections, the value of β varied slightly from case to case and was found by fitting Eq. (5.3) to each individual velocity profile (see Fig. 5.22). From the velocity profiles measured in the test cases with spherical-particle beds, an average value of β = 1.86 was found. Meanwhile, an average value of β = 2.45 was obtained for the tests with gravel beds. Similar process was applied for data from literature for shallow flow over large scale roughness (Pokrajac 2007b; 2010) and the resulting β values were plotted on the same figure for comparison.

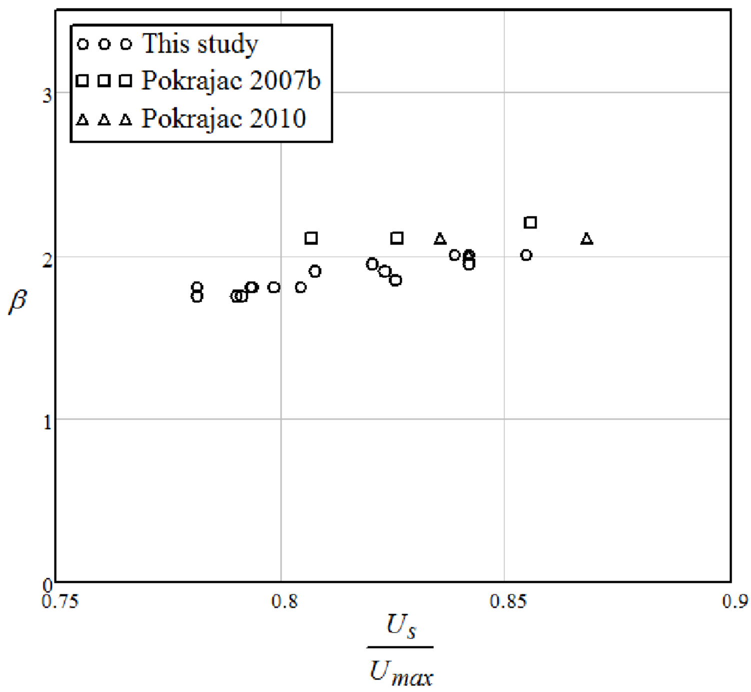

Fig. 5.22: Variation of the exponent β with U_s/U_{max}

On the other hand, $\psi_{1/2}$ can be evaluated using other parameters including U_{max} and U_s, where U_s is the average flow velocity in the surface layer. By integrating Eq. (5.3) from ψ = 0 to ψ = H_s, *Cheng et al.* [2012b] arrived with the simplified relationship to determine $\psi_{1/2}$ in the form of

$$\frac{\psi_{1/2}}{H_s} = c \frac{U_s - U_p}{U_{max} - U_p} \exp\left[\left(\frac{U_s - U_p}{U_{max} - U_p} \right)^p \right] \tag{5.4}$$

where c and p are constants. Fig. 5.23 shows that with c = 0.9 and p = 4.5, Eq. (5.4) fits well to the data points obtained using the values of U_p, $\psi_{1/2}$ and U_{max}, which were all estimated from the measured velocity profiles. Eq. (5.3) has been superimposed on the normalised velocity profiles in the preceding sections, showing that the measurements can be described reasonably well using the eddy viscosity model presented.

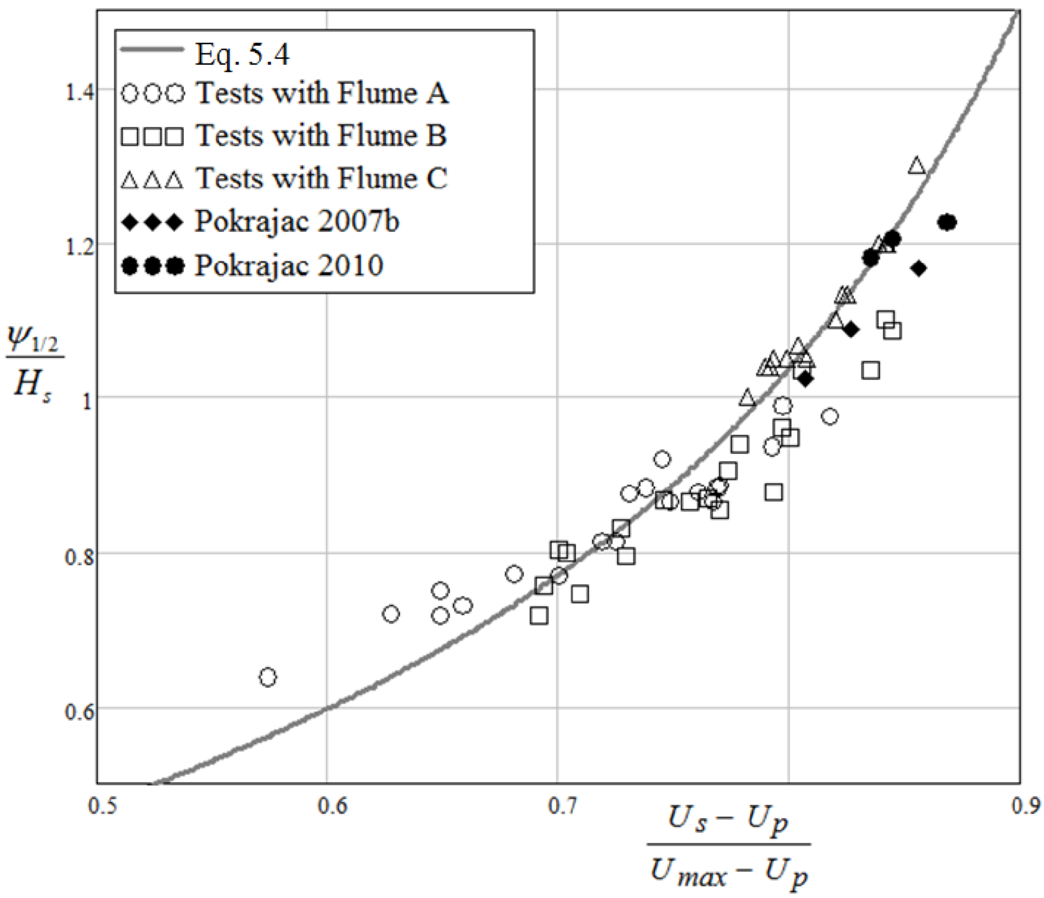

Fig. 5.23: Dependence of the normalised half-thickness $\psi_{1/2}/H_s$ on $(U_s - U_p)/(U_{max} - U_p)$

5.5.2 Validation with other datasets

Laboratory and field data published in the literature were also used to further validate the proposed scaling approach. These are research works carried out by Pokrajac [2007a, 2—7b, 2010] for fully rough turbulent flows in open channels, under relatively shallow flow conditions ($H_s/k < 5$). As this type of data is limited in literature, only five velocity profiles were digitized and plotted in Fig. 5.24 using $(u - U_p)/(U_{max} - U_p)$ and $\psi/\psi_{1/2}$. The main parameters for these experiments are shown in Table 5.3. The figure shows a good agreement between Eq. (5.3) (with $\beta = 2.1$) and the velocity profiles, for a large portion of the surface layer.

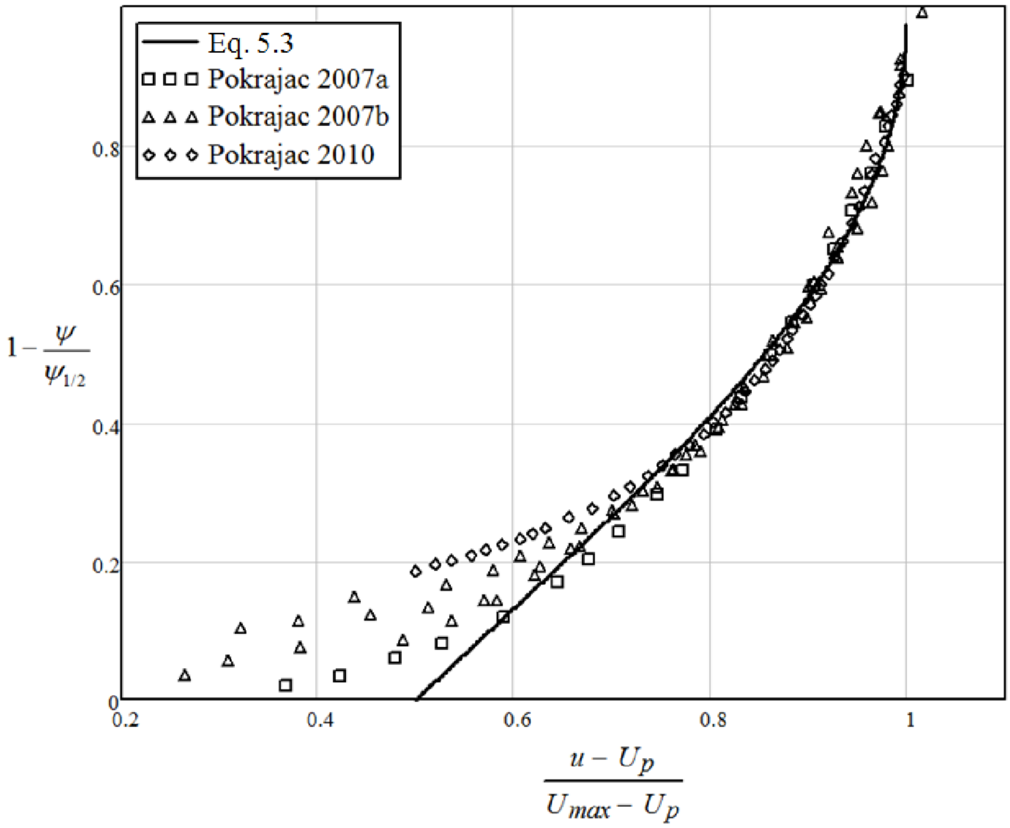

Fig. 5.24: Scaling of velocity profiles from other studies

Table 5.3: Data collected from literature

Investigator	**Roughness type**	H_s/k	β
Pokrajac (2007a)	Bars, L = 8 (k-type)	4.69	2.20
Pokrajac (2007b)	Sphere	1.67	2.10
	Sphere	1.75	2.00
	Sphere	3.5	2.10
Pokrajac (2010)	Sphere	3.67	2.05

5.5.3 An alternative length scale

For some situations, the smallest velocity measured above the sediment bed could be larger than $0.5U_{\max}$. For such a case, to find the half-thickness, it is necessary to extrapolate the velocity profile to the point of $0.5U_{max}$ by using an algorithm such as bi-cubic extrapolation. However, such extrapolation of the profile is purely mathematic and has no physical base. Therefore, to ensure the applicability of the proposed scaling method, it is worth to note that there are other comparable characteristic lengths and velocities to use as well. In fact, with a slight modification, other sufficient large portion of U_{max} and its corresponding location ψ would work as well.

For example, an alternative velocity and length scales can be taken to be $U_{3/4}$ (equals $0.75U_{max}$) and its corresponding $\psi_{3/4}$, which also work well for scaling all the observed velocity profiles. Fig. 5.25 illustrates the results for four test cases with two roughness layers, plotted with β = 1.6. The upper panel presents all velocity profiles with the normal scaling, showing that for some cases it is unreliable to determine the $U_{1/2}$ (= $0.5U_{max}$) directly from the measured profiles. Therefore it is advisable to use the alternative velocity and length scale for such cases. The modified relationship has the form of

$$\frac{u}{U_{\max}} = \exp\left[-\ln\left(\frac{4}{3}\right)\left(\frac{\psi}{\psi_{3/4}}\right)^{\beta}\right] \tag{5.5}$$

where $\psi_{3/4}$ follows the relationship similar to that of $\psi_{1/2}$,

$$\frac{\psi_{3/4}}{H_s} = c\frac{U_s}{U_{\max}}\exp\left[\left(\frac{U_s}{U_{\max}}\right)^{p}\right] \tag{5.6}$$

with c = 0.57 and p = 4.5.

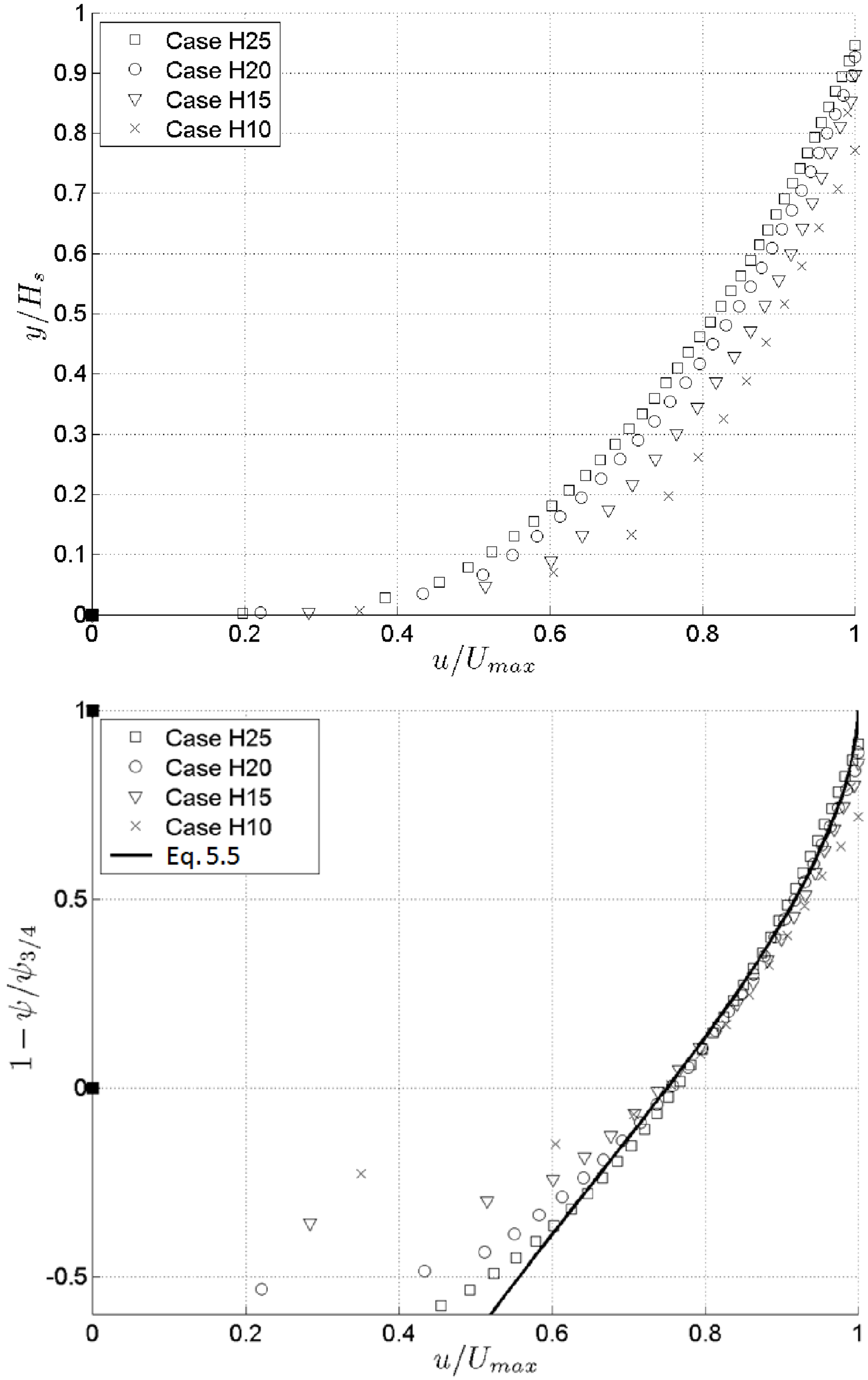

Fig. 5.25: Velocity profiles normalised with U_{max} and $\psi_{3/4}$ (test cases with two roughness layers)

5.5.4 Concluding remarks

The scaling approach proposed has allowed the collapse of velocity data onto a single curve. The experiments carried out in this study focused on very shallow flow, where the roughness submergence ranged from 0.91–2.27. However, validation tests with several other data sources available in literature show that the proposed scaling method is also applicable for other boundary layer flows. By using an empirical exponent $\beta \approx 2$ and a characteristic length $\psi_{1/2}$ determined by Eq. (5.4), it is possible to scale these flow velocity profiles in the outer region using the present approach.

Investigating the data collected, one may find no critical ratio of H_s/k, beyond which this method ceases to work. Rather, with increasing H_s/k, the effect of the roughness layer gradually reduces, resulting in an ever decreasing portion of the velocity profile that the present scaling formula can fit. This is in agreement with the conclusion of *Flack et al.* [2007], who investigated the turbulent boundary layer flows with the ratio of the boundary layer thickness to roughness height varying from 16 to 110, and found that a critical roughness height does not exist. They, however, proposed a region confined within the distance of 3–5·k from the wall, which will be directly modified by the roughness. This is also what was implied by Townsend's hypothesis [*Townsend*, 1976], that the roughness layer typically extends 5·k from the wall. In other words, this should be the prevailing range where this study's scaling method would be favorable.

An advantage of the scaling method proposed here is that the half-thickness can be easily defined using the velocity profile largely observed in the surface layer. Using the downward bed-normal coordinate, with the origin at the free surface, it can inherently waive the need to find an appropriately-defined origin of the bed-normal coordinate, as has been raised by many others.

Nevertheless, further studies can be carried out to confirm the applicability of the scaling method for other porous beds, including natural-gravel and fibrous beds, urban and terrestrial-vegetation canopies. The hydrodynamic similarities between flows over these different types of permeable media, including the existence of an inflection point in the mean velocity profile roughly at the interface, have been shown by *Katul et al.* [2002] and *Ghisalberti* [2009]. Their suggestion of a single framework to describe a range of flow systems and scales, based on the good collapse of experimental data, has also implied the predictive capability of the proposed scaling method here for flows over other permeable media. This has been proved to be true by the earlier work done by *Cheng et al. [2012b]*, where the scaling method has been effectively applied to the flow over submerged vegetation (simulated by arrays of rigid rods), regardless of its density.

Chapter 6

Turbulence Characteristics

This chapter investigates characteristics of turbulence in shallow flows over permeable rough beds and discusses effects of the bed permeability as well as the small roughness submergence. Investigation mainly utilized the measurements carried out with spherical-particle beds. The statistical properties of turbulence parameters exhibit a difference from the prevailing knowledge about turbulence structure in flow with sufficient submergence. Also, by focusing on their coherent structures (organized behaviour) such as bursting, the mechanics of turbulence in such shallow flows and very rough bed conditions is also explored.

6.1. Interpretation of measured data

6.1.1 Mean and fluctuating velocity components

In chapter 3, the major steps of the double-averaging (spatial and temporal averaging) technique have been described. This section elaborate the application of the technique to the instantaneous flow velocity vector maps obtained with the PIV measurement and its associated post processing. Main results include the bulk flow properties and other valuable information on the time-averaged turbulence characteristics of the flow.

When calculating a properties ξ of the flow, the mean value was generated by taking average over the homogeneous direction (streamwise), and over all instantaneous realizations in the ensemble. Taking advantage of the steady uniform character of the flows, the flow was first divided into 17-44 non-overlapping parallel equal layers of thickness 8 pixels, depending on the image size of each experiment case. The mean value of each of these layers were then determined by

$$\bar{\xi}(y_i) = \frac{1}{N_s(y_i)N_r}\sum_{j=1}^{N_s}\sum_{k=1}^{N_r}\xi\left(x_j, y_i, k\right) \tag{6.1}$$

where $N_s(y_i)$ is the number of samples (vectors) contained within the box of length L in the streamwise direction (equals the length of a image size) and height Δy_i at one instant in time; N_r is the number of realizations within the ensemble; the total of samples within the i^{th} layer would then be $N_t = N_s(y_i) \cdot N_r$. Δy_i correspond to the bottom-normal vector spacing, and is uniform throughout the region under consideration.

Once a mean has been defined, the variance of the above quantity follows the standard definition

$$\xi_{rms} = \sqrt{\frac{1}{N_t}\sum_{j=1}^{N_t}\left(\xi - \bar{\xi}\right)} \tag{6.2}$$

For any plane parallel to the side wall (and thus parallel to the flow direction), u represents the streamwise instantaneous component of the flow velocity, and v is the bottom-normal velocity component. Reynolds-based decomposition was used to separate the time-averaged part of a velocity component ($\bar{u}$ and $\bar{v}$) from the fluctuating part (u' and v'), such that $u = \bar{u} + u'$ and $v = \bar{v} + v'$.

6.1.2 Total fluid shear stress and Shear velocity

The shear velocity has been widely known to provide a good velocity scale for the mean velocity profiles as well as higher velocity moments (e.g., *Nikora et al.[2001; 2007]*; *Manes et al.* [2007]; *Pokrajac et al.* [2009; 2007b]; and Sakar and Dey [2010]). It is originated from theoretical arguments to find an appropriate velocity scale for the logarithmic layer of zero pressure gradient boundary layers. In these context, the total bed shear stress is constant and the shear velocity is usually defined as $u_* = \sqrt{\tau_0 / \rho}$, where τ_0 is the total fluid shear stress at the roughness crest level (y = 0), estimated by extrapolating the double averaged Reynolds shear stress profile down to the bead top.

Flows in open channels, on the other hand, are driven by gravity and the total shear stress is not constant. The viscous shear stress is negligible in the surface region of the flow, but increases towards the bed. The shear velocity could then be estimated from the bed slope or the directly measured Reynolds stress. Different from the smooth bed, the presence of momentum exchange between the flow above and inside the porous rough bed makes the bed shear stress at a virtual bed level different from the fluid shear stress at the roughness crest. The difference is negligible for rough bed flows with high submergence, but becomes significant when the flows becomes relatively shallow.

There is no consensus about what value should be formally used to determine the shear velocity (*Manes et al.*, 2007). In this study, we used the total fluid shear stress acting at the roughness crest level (denoted as τ_0 hereafter) to derive u_*. This choice provide a unique velocity scale for each test case that is able to collapse fairly well the measurement of higher velocity moments. τ_0 is estimated by extrapolating the double averaged Reynolds shear stress profile down to the bead top (y = 0). These profiles are shown in Fig. 6.1 – Fig. 6.5, each representing a test case and was derived from averaging in the transversal direction of two respective double-averaged profiles for trough and crest case measurements. These values will subsequently be used to scale the turbulent intensities and Reynolds shear-stress profiles.

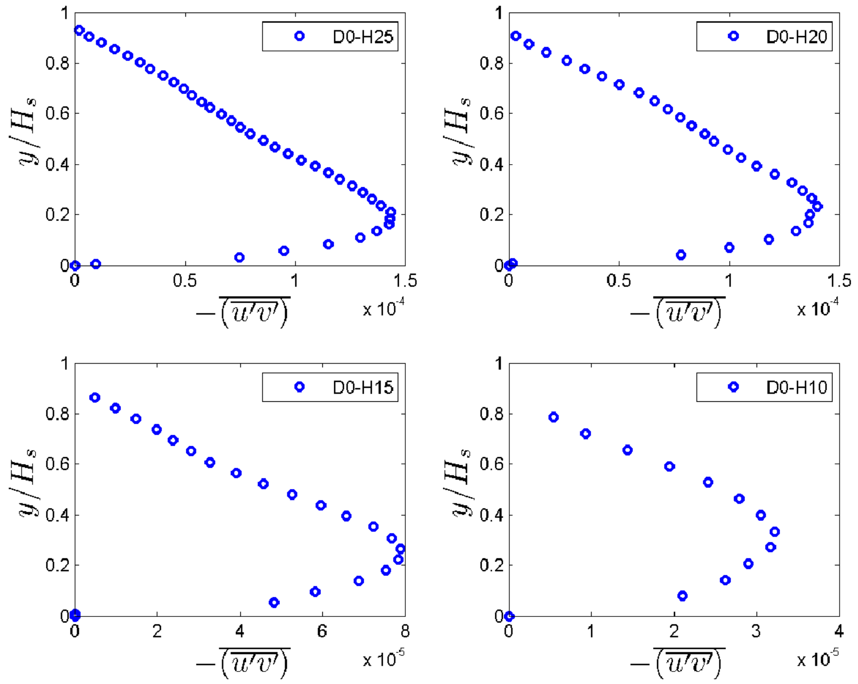

Fig. 6.1: Reynolds shear stress profile, smooth bed

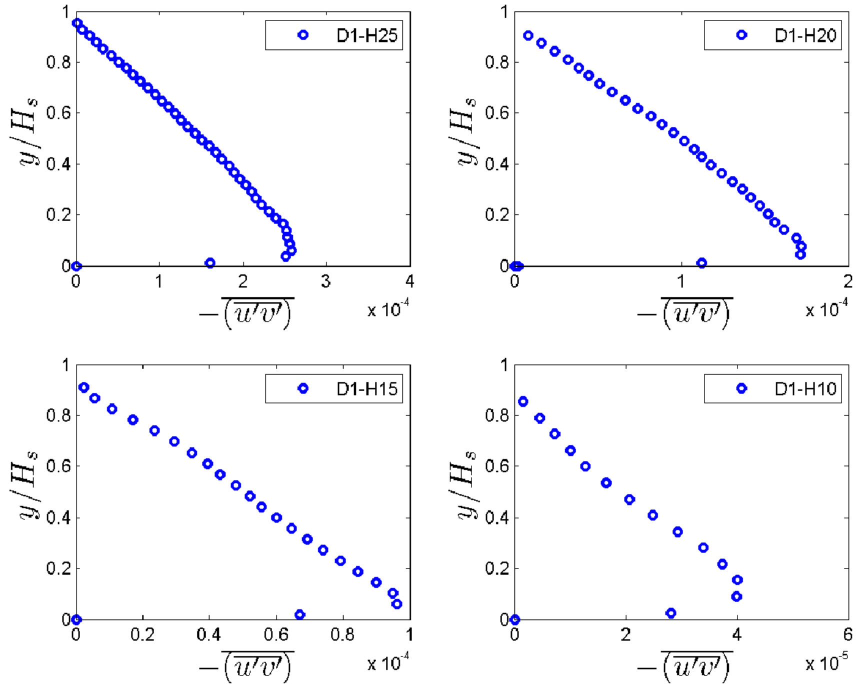

Fig. 6.2: Reynolds shear stress profile, one roughness layers

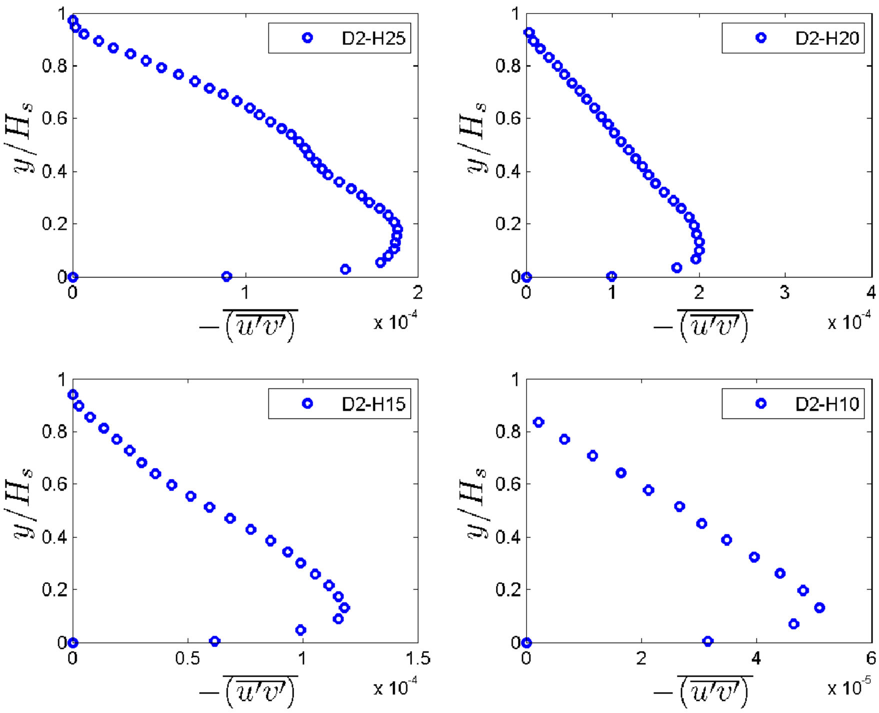

Fig. 6.3: Reynolds shear stress profile, two roughness layers

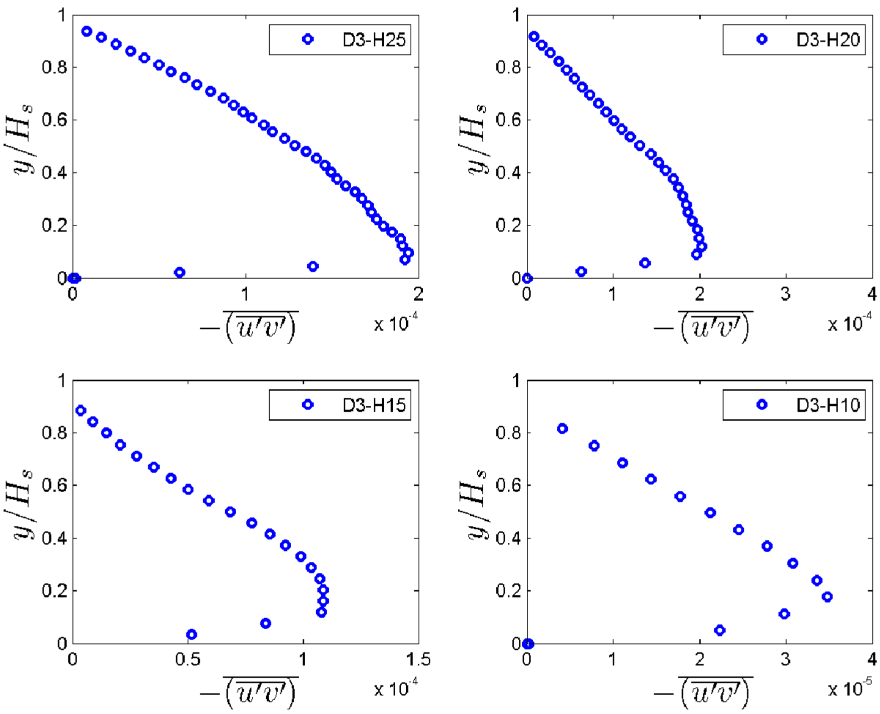

Fig. 6.4: Reynolds shear stress profile, three roughness layers

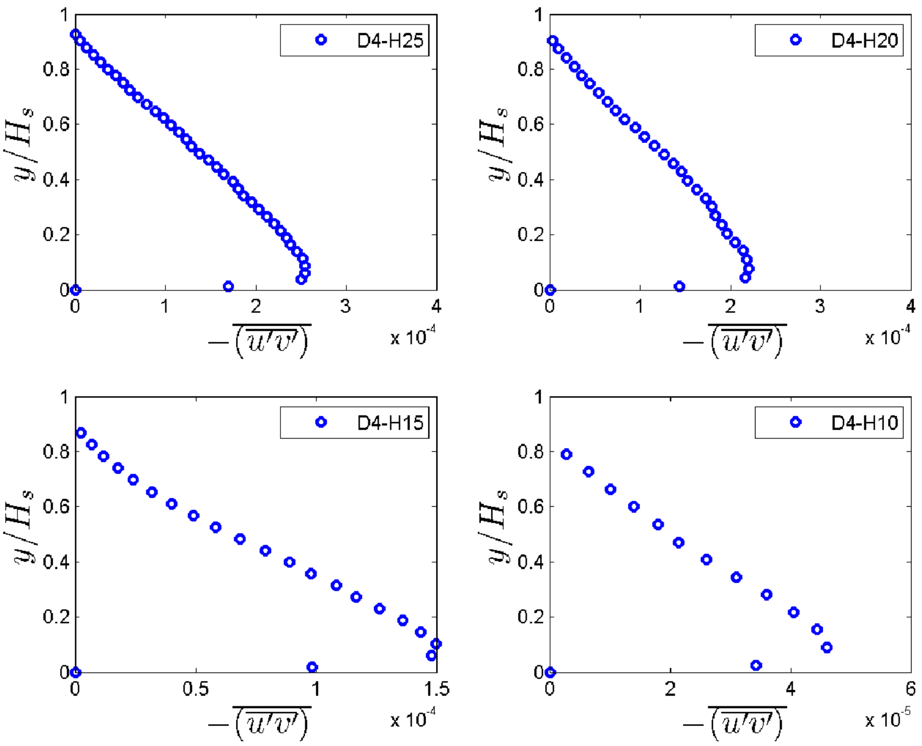

Fig. 6.5: Reynolds shear stress profile, four roughness layers

Shear velocity values derived from these mean bed shear stress profiles at the defined bed level are summarized in Table 6.1.

Table 6.1: Shear velocity values estimated from Reynolds shear stress profile

Test case	H_s *(m)*	u_* (trough)	u_* (crest)	u_* (avg.)	**Test case**	H_s *(m)*	u_* (trough)	u_* (crest)	u_* (avg.)
D0-H25	0.025	-	-	0.0136	D3-H25	0.025	0.0164	0.0182	0.0173
D0-H20	0.020	-	-	0.0140	D3-H20	0.020	0.0164	0.0161	0.0163
D0-H15	0.015	-	-	0.0134	D3-H15	0.015	0.0124	0.0138	0.0131
D0-H10	0.010	-	-	0.0079	D3-H10	0.010	0.0069	0.0094	0.0081
D1-H25	0.025	0.0179	0.0169	0.0174	D4-H25	0.025	0.0173	0.0190	0.0181
D1-H20	0.020	0.0145	0.0134	0.0140	D4-H20	0.020	0.0167	0.0155	0.0161
D1-H15	0.015	0.0105	0.0114	0.0109	D4-H15	0.015	0.0130	0.0130	0.0130
D1-H10	0.010	0.0071	0.0095	0.0083	D4-H10	0.010	0.0075	0.0091	0.0083
D2-H25	0.025	0.0170	0.0164	0.0167					
D2-H20	0.020	0.0158	0.0152	0.0155					
D2-H15	0.015	0.0122	0.0134	0.0128					
D2-H10	0.010	0.0079	0.0092	0.0085					

6.2. Observations and discussions

6.2.1 Turbulence intensities and Reynolds shear stresses

The streamwise and wall-normal (or so called 'vertical' for unambiguous nomenclature) double-averaged Reynolds normal stresses are calculated by $\overline{u'_{RMS}} = \left[-\rho\overline{u'u'}\right]^{1/2}$ and $\overline{v'_{RMS}} = \left[-\rho\overline{v'v'}\right]^{1/2}$. They were normalised by u_* to be $\sigma_u^+ = \overline{u'_{RMS}}/u_*$ and $\sigma_v^+ = \overline{v'_{RMS}}/u_*$, respectively. Meanwhile, the Reynolds shear stress is calculated by $-\left(\overline{u'v'}\right)$ and normalised by u_*^2 for all cases. Fig. 6.6 – Fig. 6.9 show the distribution of Reynolds stresses for each individual test, grouped by test cases with the same flow depth for ease of comparison. From left to right, the sub-plots show σ_u^+, σ_v^+ and Reynolds shear stress, with the vertical axis normalised by the surface flow depth H_s. The empirical curves as suggested by Nezu and Rodi [1986] were also plotted for comparison.

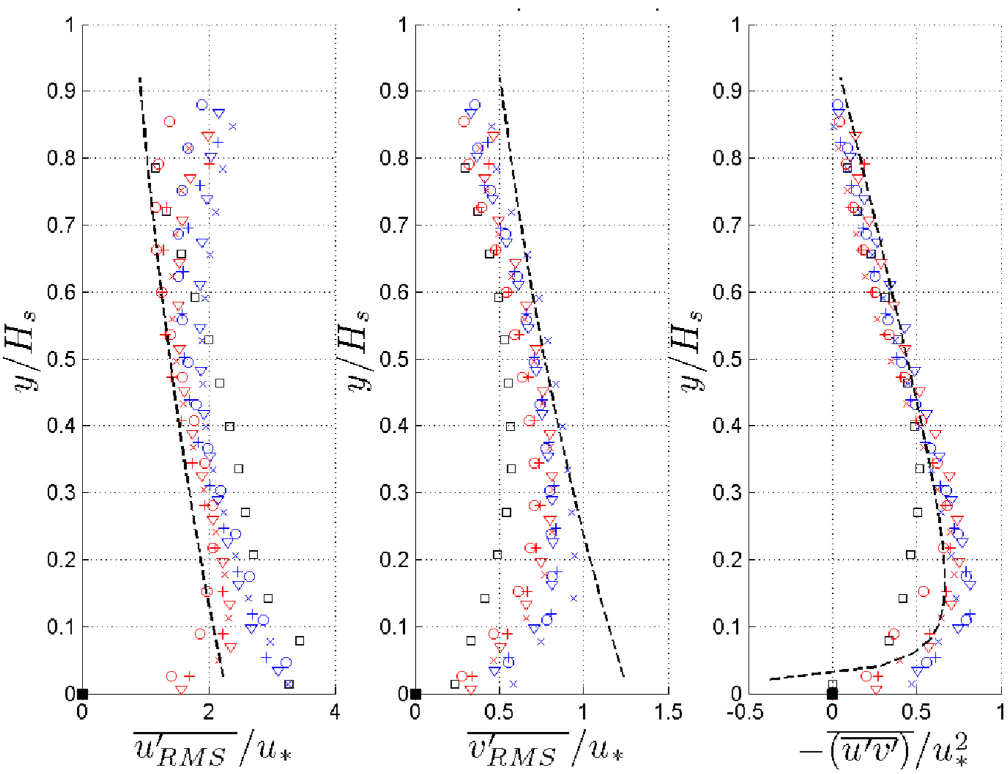

Fig. 6.6: Reynolds stresses for test cases with H_s = 1.0 cm (□, D0; o, D1-crest; ∇, D2-crest; ×, D3-crest; +, D4-crest, o, D1- trough; ∇, D2- trough; ×, D3-trough; +, D4-trough; Dashed lines indicate the empirical relationship)

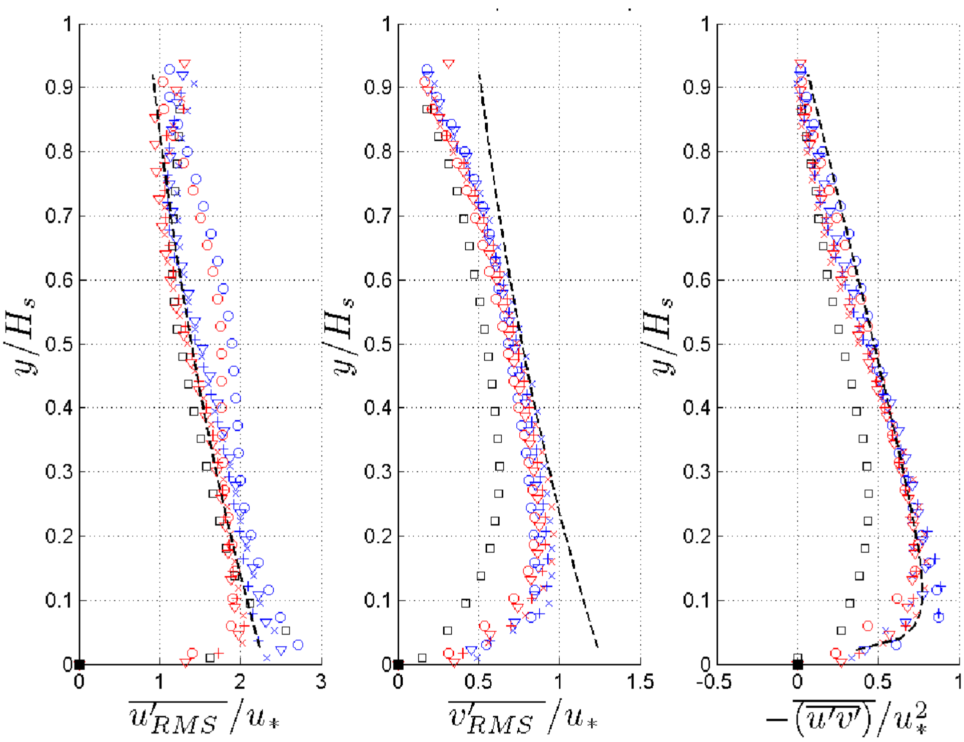

Fig. 6.7: Reynolds stresses for test cases with H_s = 1.5 cm (□, D0; o, D1-crest; ∇, D2-crest; ×, D3-crest; +, D4-crest, o, D1- trough; ∇, D2- trough; ×, D3-trough; +, D4-trough; Dashed lines indicate the empirical relationship)

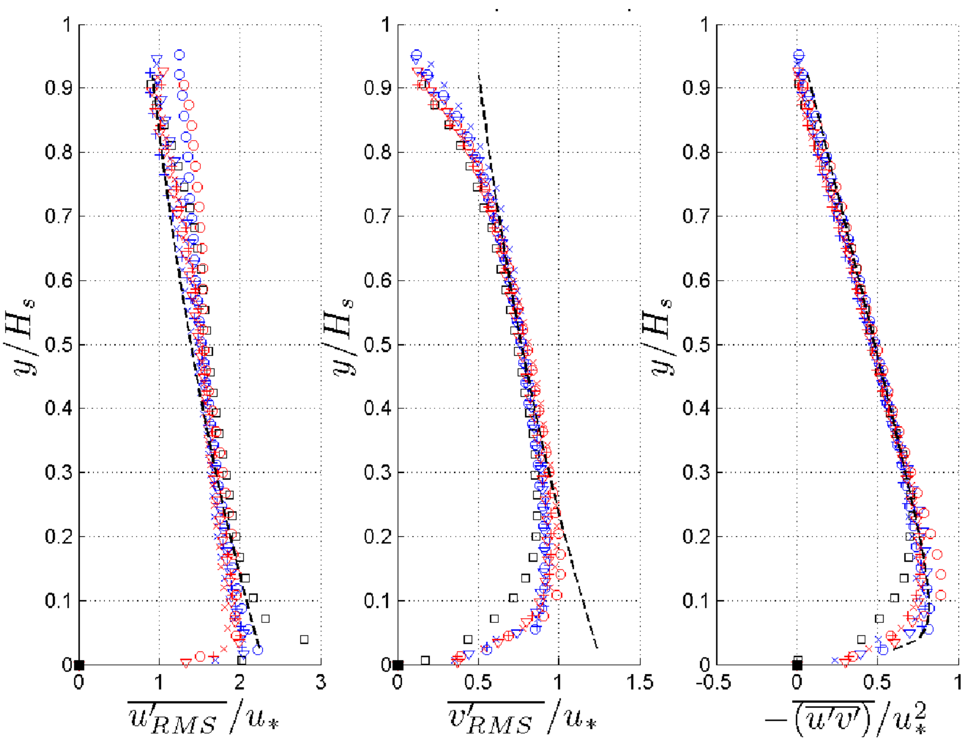

Fig. 6.8: Reynolds stresses for test cases with H_s = 2.0 cm (□, D0; o, D1-crest; ∇, D2-crest; ×, D3-crest; +, D4-crest, o, D1- trough; ∇, D2- trough; ×, D3-trough; +, D4-trough; Dashed lines indicate the empirical relationship)

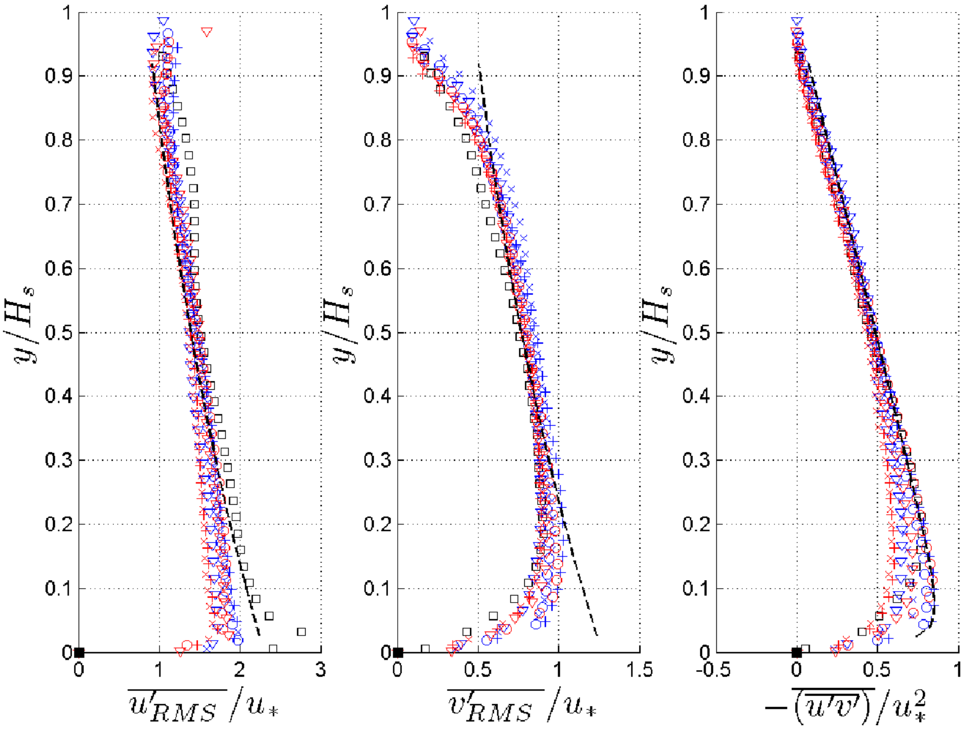

Fig. 6.9: Reynolds stresses for test cases with H_s = 2.5 cm (□, D0; o, D1-crest; ∇, D2-crest; ×, D3-crest; +, D4-crest, o, D1- trough; ∇, D2- trough; ×, D3-trough; +, D4-trough; Dashed lines indicate the empirical relationship)

In general, the profiles exhibit a similar characteristics with the Reynolds stresses linearly increase towards the bed and attain their peak value just above the roughness top, at a height of approximately $D/5$, where D is the roughness size. The normalised profiles reach a maxima of roughly 2 and 1 for the normal and the shear tresses, respectively. There is a rapid decrease of turbulent intensities below this level, which could be attributed to the increasing significance of viscous shear stress and form-induced shear stress. A comparison with *Manes et al.* [2009]; *Sarkar and Dey* [2010] and *Dey and Das* [2012] shows similar trends. The turbulence intensity could be well normalised with the shear velocity and is quite independent of the boundary condition for y/H_s > 0.2. However, the data spread immediately adjacent to the bed, which implies the roughness effect.

Compared to the smooth bed cases (denoted as D0 in the figures), the streamwise normal stress in rough bed flows experiences a noticeable depression. Meanwhile, the vertical normal stress and shear stress are signified, especially towards the bed. This emphasizes the influence of the permeable rough bed on the momentum balance in the near-bed region. Interestingly, Fig. 6.6 – Fig. 6.9 show no obvious impact of the bed configuration on the Reynolds stress profiles, except for the streamwise turbulence intensity, which shows a decreases in σ_u^+ with increasing number of roughness layers.

For the same bed configuration, the influence of different flow depth is illustrated in Fig. 6.10 and Fig. 6.11 for one and two roughness layers, respectively. Away from the roughness layer, at the height of approximately $D/5$ and above, The Reynolds shear stress follows a linear distribution and shows little influence of the flow depth. Meanwhile, the streamwise normal stress exhibits a slight decrease and the vertical normal stress shows an increase in magnitude with increasing flow depth.

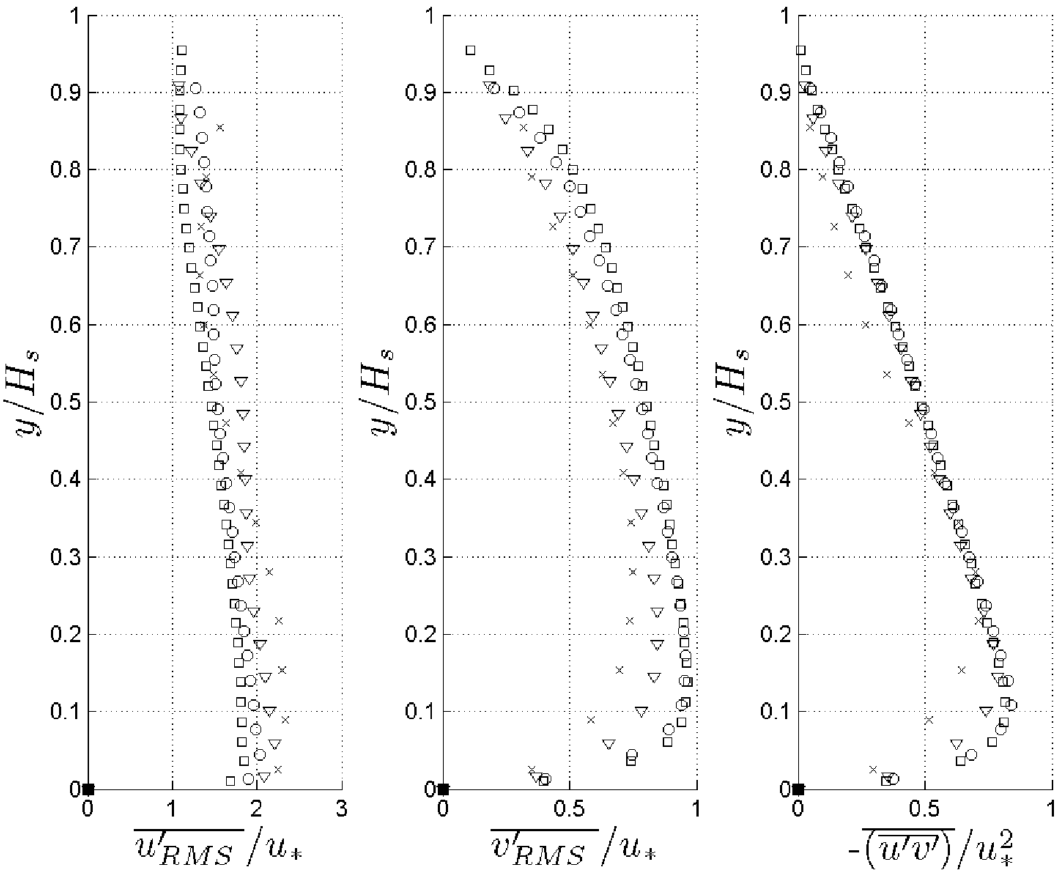

Fig. 6.10: Reynolds stresses for test cases with 1 layer of roughness

(□, Case H25; o, Case H20; ∇, Case H15; ×, Case H10)

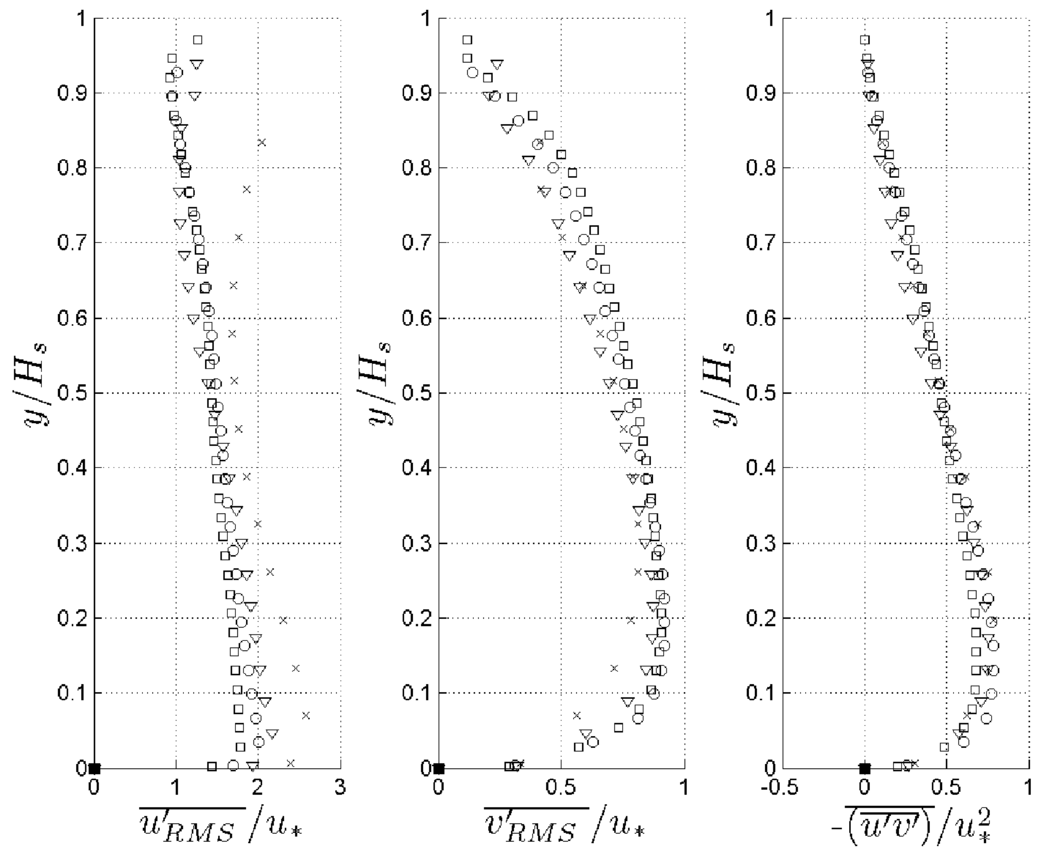

Fig. 6.11: Reynolds stresses for test cases with 2 layers of roughness
(□, Case H25; o, Case H20; ∇, Case H15; ×, Case H10)

6.2.2 Flow visualization and coherent turbulence structures

The time-averaged flow velocity field clearly shows the influence of the rough bed. Due to the large-scale roughness elements, the flow exhibits a strong in homogeneity in the neighbourhood of the bed. For the width-to-depth ratio of less than five, the main flow could be affected by secondary currents and become three-dimensional. However, as measurements were carried out in the vicinity of the flume centreline, the effect of secondary current could be considered to be minor and a 2-D plot would be suitable for investigation of the flow characteristics.

Fig. 6.12 shows an example of the flow velocity field in a shallow flow over permeable rough bed, test case D4H10. Although the time-averaged velocity components do not reveal individual coherent flow structures, they do illustrate the effect of topographic irregularity, with clear influence of roughness protrusion on the localized flow field. The time-averaged streamwise velocity increases with flow depth and the effect of individual roughness elements generally diminishes at about 0.2*D*. Analysis of the time-averaged streamwise velocity component shows areas of low flow velocity in the wake region behind protruding roughness elements.

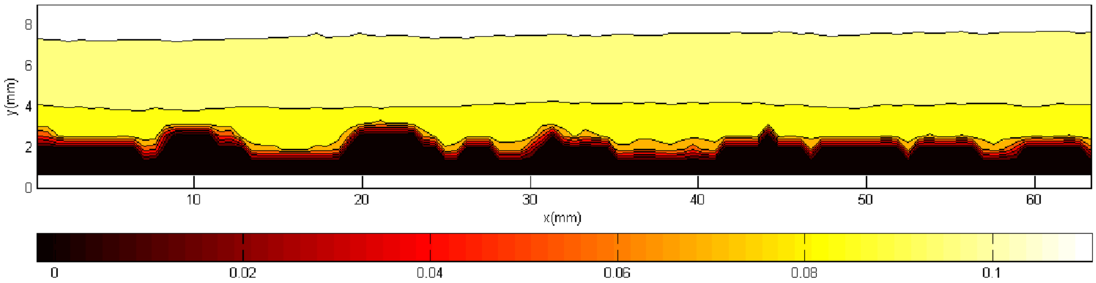

(a) Streamwise velocity component (m/s)

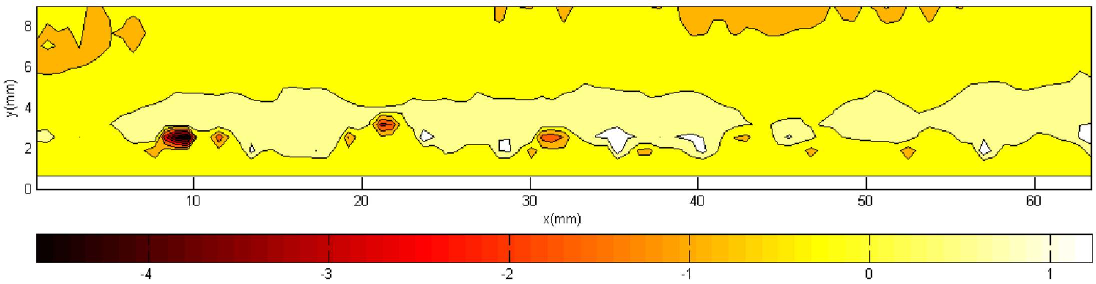

(b) Bottom-normal velocity component ($\times 10^{-4}$ m/s)

Fig. 6.12: Time-averaged velocity vector field (Spherical-particle bed test, case D1H10)

Whilst the influence of the roughness elements appears to be mainly confined to a region close to the boundary, the extend of the coherent structures is far more extensive, as will be exemplified herebelow. Fig. 6.13 and Fig. 6.14 show three consecutive flow velocity maps for $\bar{u}$ and $\bar{v}$, respectively. Each flow instant was separated with the adjacent one by 1/15 second. The observed ejection and inrush events are sufficiently strong to travel the whole flow depth and facilitate momentum exchange. The low momentum fluid was originated from the interstices of the roughness elements, ejects from this interfacial/roughness sublayer and travels outwards. Meanwhile, for the sweep (inrush) events, the high speed fluid elements, originated from the outer region, were swept toward the porous bed and bring high momentum fluid to penetrate into the porous layer to exchange with the more stagnant water herein.

These two randomly repeating events happen intermittently and intertwined with each other, as can be seen in these figures. They contribute to the rise in vertical normal stress and Reynolds shear stress at points remote from the boundary, and to the higher turbulence production near the permeable rough bed. For such shallow flows, the coherent structures are sufficiently strong to affect the entire surface flow region and could represent the dominant mode of momentum transport outside the roughness sublayer.

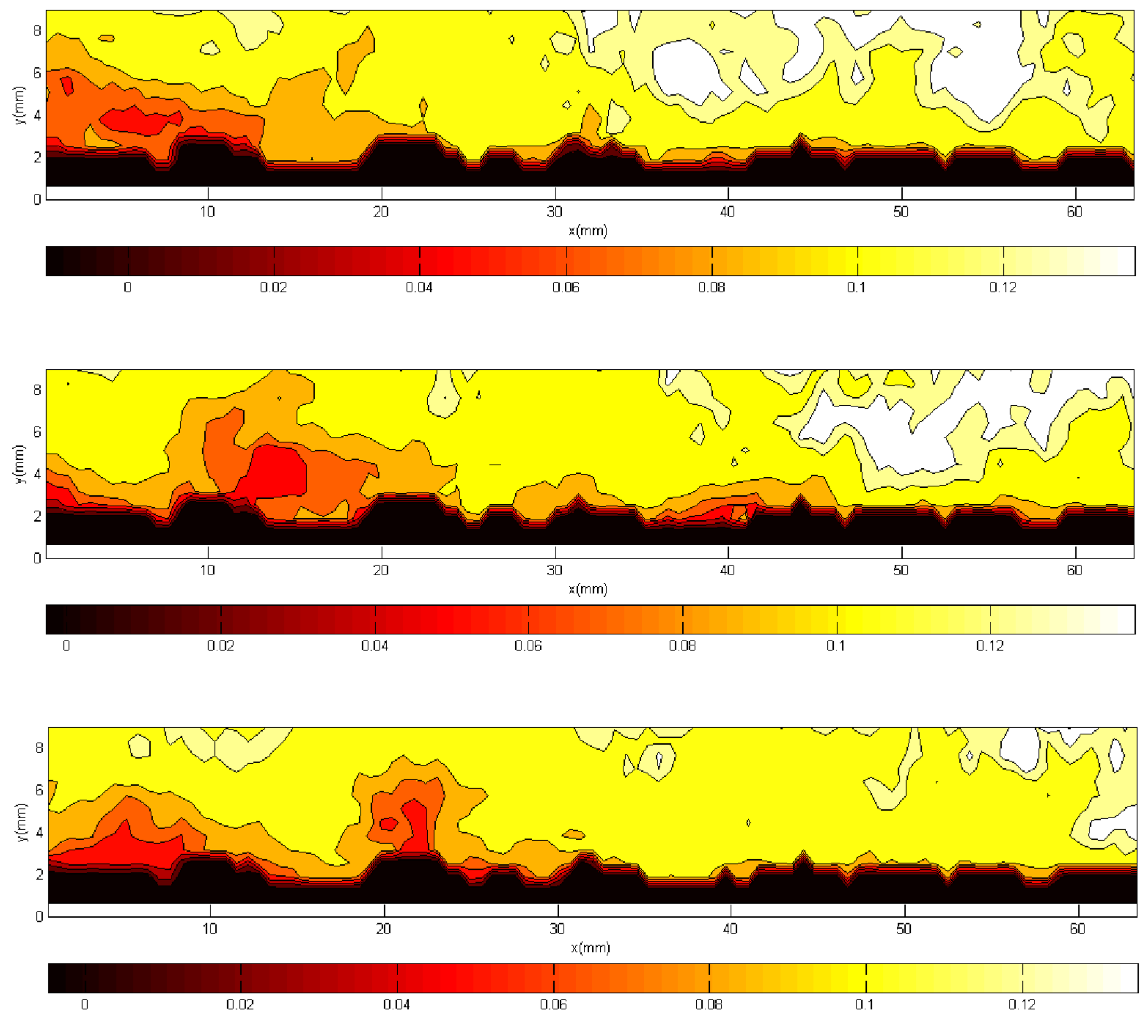

Fig. 6.13: Instantaneous streamwise velocity field (Spherical-particle bed test, case D1H10)

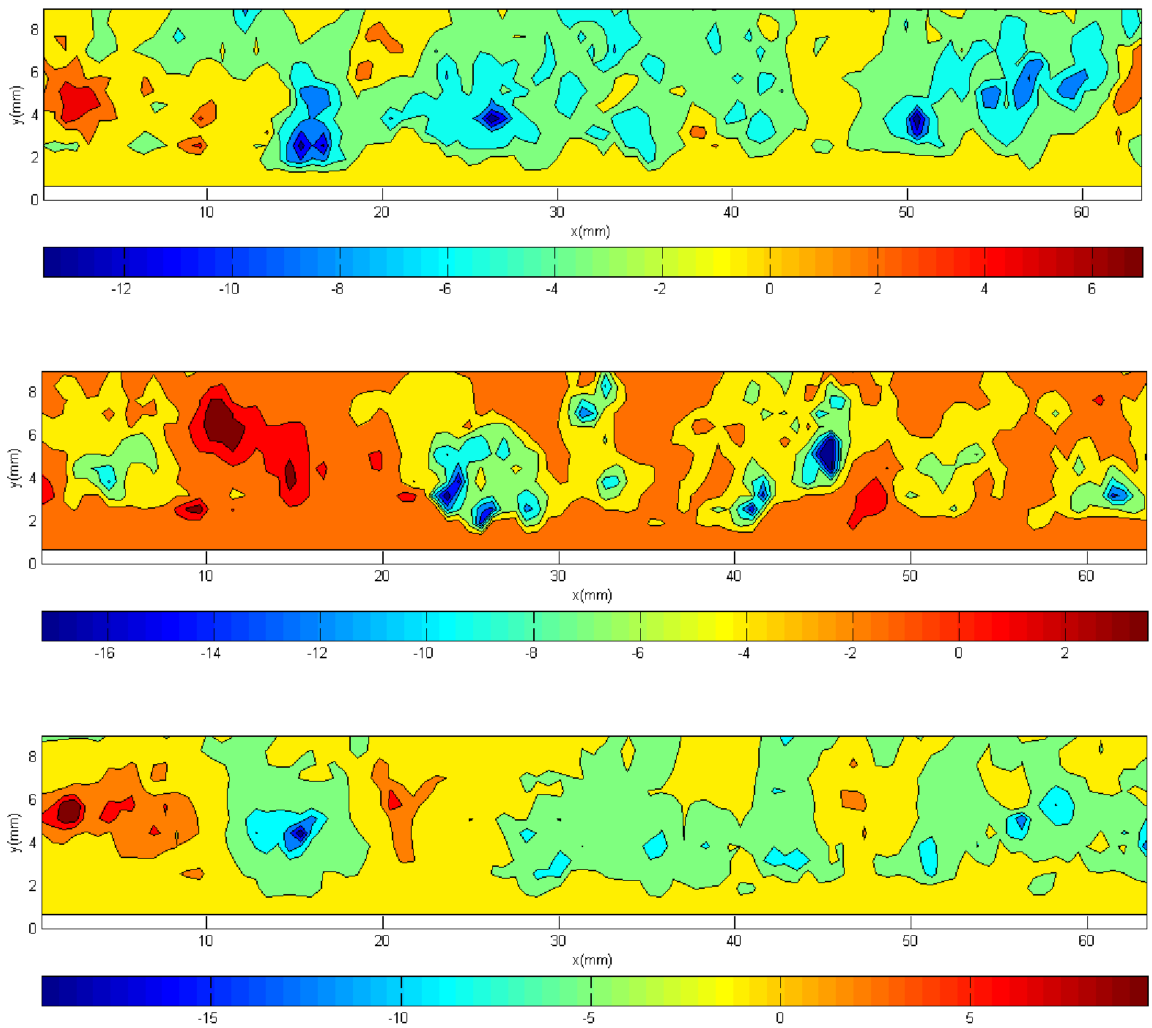

Fig. 6.14: Instantaneous bottom-normal velocity field ($\times 10^{-4}$ m/s, case D1H10)

6.2.3 Quadrant analysis

Besides investigating the mean flow characteristics, additional insight can be obtained by studying the flow velocity fluctuations. Fig. 6.15a gives an impression of the flow fluctuations by showing a resultant vector map for

$u' = u - \bar{\bar{u}}$ and $v' = v - \bar{\bar{v}}$. Meanwhile, Fig. 6.15b shows the colour map for only the streamwise fluctuating component.

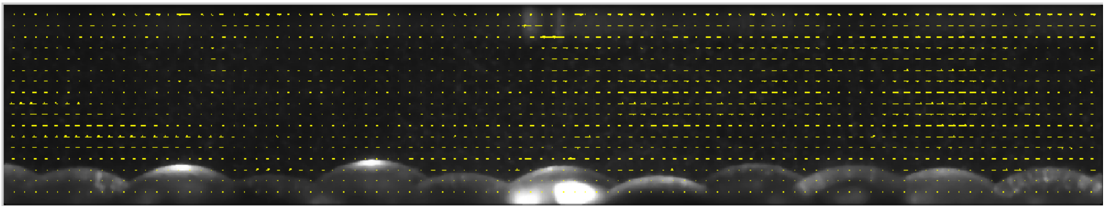

(a) Resultant velocity vectors (consist of *u'* and *v'*)

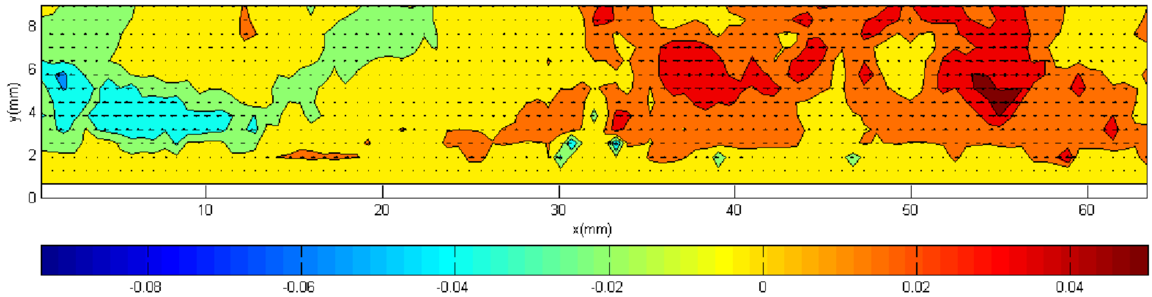

(b) Streamwise fluctuating velocity component (*u'*)

Fig. 6.15: The fluctuating components of flow velocity

These fluctuating velocities (u' and v') can be sorted according to the four quadrants defined by the relevant plane (u', v'). Turbulent events associated with each quadrant are called outward interactions (Q_1, u' > 0 and v' > 0), ejections (Q_1, u' < 0 and v' > 0), inward interactions (Q_1, u' < 0 and v' < 0), and sweeps (Q_1, u' > 0 and v' < 0). Interesting insight can be obtained by mapping the probability distribution functions for these fluctuating velocity components and investigating their interaction. This is known as quadrant analysis, and has been used in many studies to characterize the flow structure and investigating the interactions between the moving fluid and the solid boundary [*W A Breugem and Uijttewaal*, 2007; *Kiger and Pan*, 2002; *Lelouvetel et al.*, 2009; *Muste et al.*, 2009; *Nezu and Azuma*, 2004; *Noguchi and Nezu*, 2009]. This useful technique would be employed to further analyze the flow structure and the underlying physical mechanisms.

Fig. 6.16 illustrates the mapping of the probability distribution function for u' and v' of fluid flow at different elevations for Spherical-particle bed test case D4H10. It shows that for the relatively shallow flow over permeable bed of large-scale roughness in the present study, the dominant structures for the fluid are quadrant 1 (ejection) and 4 (sweep or inrush) events. Particularly, near the roughness element (y/H_s = 0.06 and 0.41), the ejections happens significantly more frequent. Meanwhile, moving away from the roughness, the role of sweep (inrush) events gradually takes over.

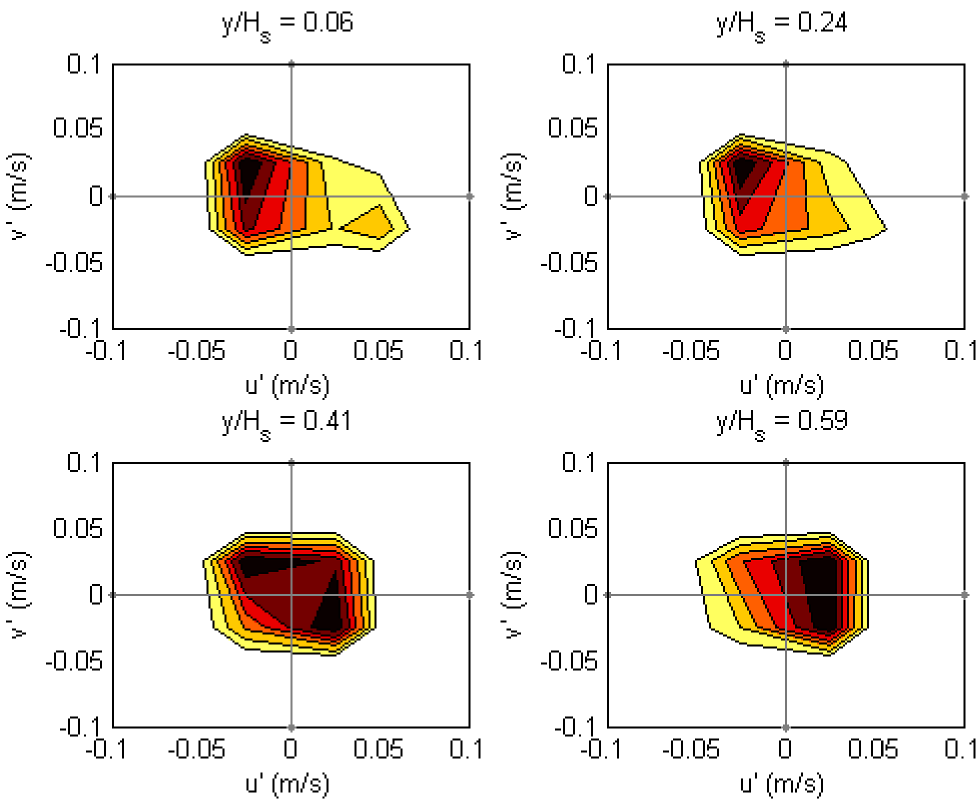

Fig. 6.16: Mapping of the probability distribution function for u' and v' of fluid flow at different elevations, Spherical-particle bed test case D4H10

With the aid of PIV and digital masking technique, the observations have confirmed the dominant of ejection-type momentum transport mechanism. This could possibly extend across the surface sublayer. In comparison, the findings are in agreement with an earlier suggestion by *Grass et al.* [1971]. There are apparently evidence of strong 3-D instability that give rise to the inrush and ejection sequences as also presented in both the similar studies in literature.

Chapter 7

Conclusions

7.1. Concluding remarks

7.1.1 Flow resistance

This study has focused on the hydraulic resistance of shallow flows with large-scale roughness, but without sediment mobility (fixed bed) and bed form. To minimize the complexity of the very challenging topic, the investigation has been limited to channel flows in rectangular flumes, which to a large extent, represents the conditions as observed in mountain streams.

Theoretical consideration have shown that the resistance relationship can be approximated using a power law function. By extending the work done by Gioia and Bombardelli [2002], which based on a phenomenological theory of turbulence, this study has proposed a simple exponential function of the roughness submergence to account for the effect of shallowing on flows with large-scale roughness. This heuristic approach resulted in a resistance equation in dimensionally consistent form. To calibrate the proposed model, this study then exemplarily organized existing databases, covering a wide variety of slopes, discharges, depths and bed configurations.

The resulting formula yields improved predictions of resistance and bulk mean velocity for shallow flows, of which the roughness submergence is smaller than 5–10. Although most of the data used for the analyses in this study were collected for low roughness submergence and flows with no bed forms, the application of the proposed formula for the cases of higher submergence also shows acceptable results.

7.1.2 Scaling of velocity profiles

Turbulent flows over permeable rough beds in shallow flow conditions are of practical importance in environmental and hydraulic engineering. However, a proper scaling for the mean velocity profile of such flows is still a major concern. Based on the mixing length analogy, this study has proposed a simple scaling method using the maximum velocity defect and a length scale denoted as half-thickness. The empirical half-thickness, similar to those widely used in study of jets, performs well in collapsing of the velocity profiles measured under a wide range of flow and bed configurations.

Validation tests with velocity measurements for flows over a range of permeable rough beds for shallow flow conditions have shown that the scaling argument performs well in collapsing all these velocity data onto a single curve, providing an effective way to represent the flow velocity profile from the more readily observable flow parameters. Finally an eddy viscosity model has been developed to theoretically describe the normalised velocity profile. The model compares well with the data collected from the laboratory experiments conducted in this study and also those reported in the literature. It should be mentioned that this scaling method is limited to the shallow flow conditions, where the roughness submergence H_S/k_s is generally smaller than 5. The approach presented in this study may provide convenient, dimensionless representation of flows in similar cases, for which analytical solutions derived from basic principles are not possible.

7.1.3 Turbulence characteristics

This study made use of the state-of-the-art non-intrusive measurement techniques such as PIV, PTV and other image processing tools to study the flow structure. Measurements resulted in an enormous amount of data spanning in both temporal and spatial domains. These data was subsequently studied by employing the double-averaging technique to get the averaged velocity profiles and higher flow velocity statistics.

Observations from spherical-particle bed tests have found that the shear velocity derived from the total fluid shear stress acting at the roughness crest level could well be used to scale and collapse the measurement of higher velocity moments. The turbulence intensity and Reynolds shear stress are quite independent of the boundary condition for $y/H_s > 0.2$. Generally, the normalised turbulent intensities linearly increase towards the bed and attain their peak value just above the roughness top, at a height of approximately $D/5$, where D is the roughness size. Furthermore, investigation has found that a decrease in streamwise turbulence intensity with increasing number of roughness layers.

Instantaneous visualization of shallow flows over permeable rough bed also revealed the extensive action of coherent structures in the first and fourth quadrant, i.e. the ejection and sweep events. Near to the roughness element, the ejections happens significantly more frequent, while the role of sweep events gradually takes over when moving away from the bed.

7.2. Recommendations for further research

For future research, this study recommends a modified experimental configuration to study the complex flow structure in shallow flow over permeable rough bed of gravels. It would make use of the glass-bottom flume and digital PIV/PTV technique to effectively carry out mass collection of flow velocity data instead of point measurement. Not only does it improve the measurement efficiency and accuracy, but also provide unprecedented spatial distributed data for studying the form-induced stress.

In order to perform PIV measurement for gravel-bed flows, it is proposed that a narrow slit made of thin steel rods would be deployed into the gravel bottom along the center line of the flume. The short and narrow slit would allow laser light to pass through and illuminate the surface flow above. General arrangement of the experiment set-up is illustrated in Fig. 7.1 and early result is shown in Fig. 7.2. The gravels were masked out using the same principle, resulting in the remaining unobstructed detailed flow information.

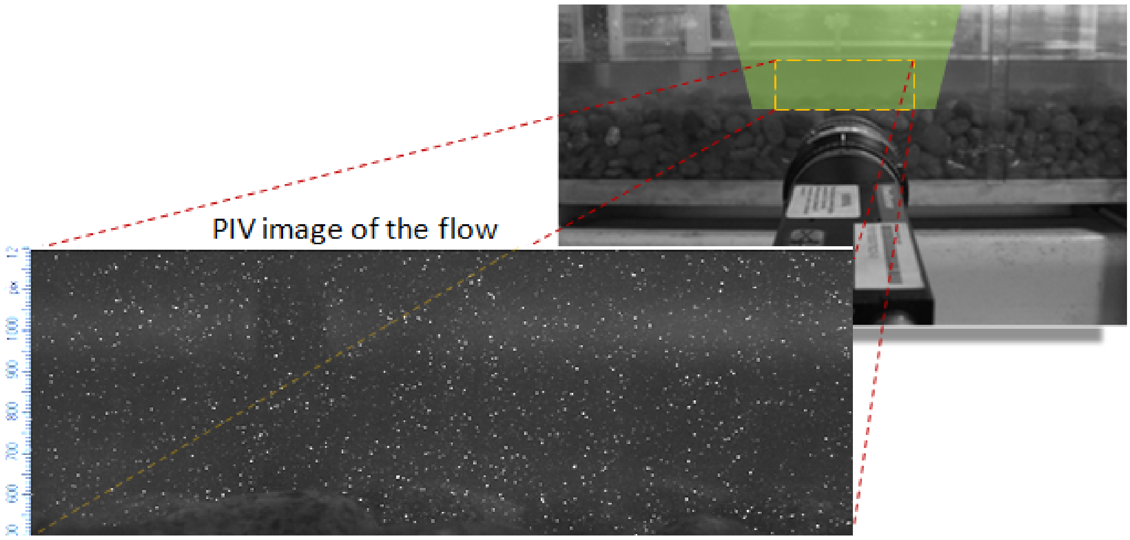

Fig. 7.1: PIV application in rough-bed open channel flow over gravel beds

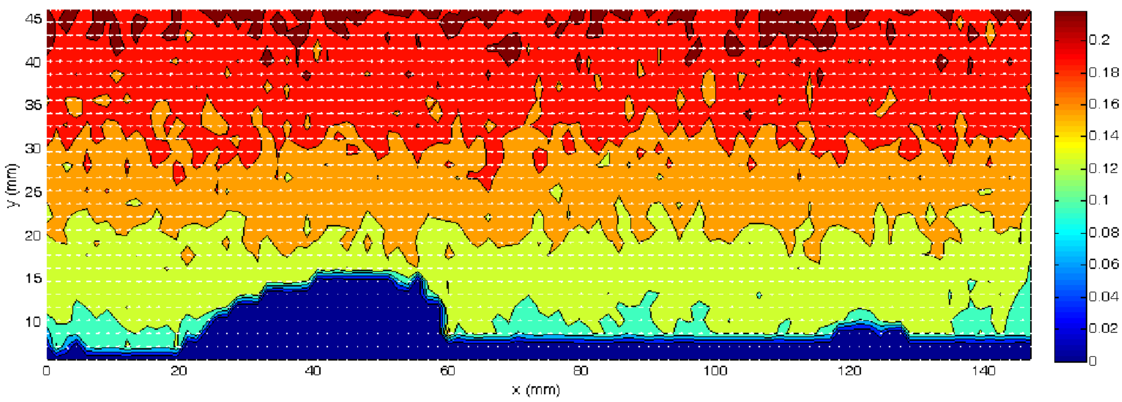

Fig. 7.2: Preliminary test results – streamwise velocity distribution

References

1. Aberle, J., and G. M. Smart (2003), The influence of roughness structure on flow resistance on steep slopes, *L'influence de la structure de rugosité sur la résistance à des écoulements en fortes pentes*, *41*(3), 259-269.
2. Abt, S. R., M. S. Khattak, J. D. Nelson, J. F. Ruff, R. Shaikh, R. J. Wittler, D. W. Lee, and N. E. Hinkle (1987), Development of riprap design criteria by riprap testing in flumes: Phase I – Initial Flume Study*Rep.*, Colorado State University.
3. Adrian, R. J., C. D. Meinhart, and C. D. Tomkins (2000), Vortex organization in the outer region of the turbulent boundary layer, *Journal of Fluid Mechanics*, *422*, 1-54.
4. Afzal, N. (2001), Power law and log law velocity profiles in turbulent boundary-layer flow: Equivalent relations at large Reynolds numbers, *Acta Mechanica*, *151*(3-4), 195-216.
5. Afzalimehr, H., and F. Anctil (1998), Estimation of gravel-bed river flow resistance, *Journal of Hydraulic Engineering*, *124*(10), 1054-1058.
6. Alonso, R. L., J. B. Fernández, and M. A. C. Cugat (2009), Flow resistance equations for mountain rivers, *Ecuaciones de resistencia al flujo para ríos de montaña*, *18*(1), 81-91.
7. Bakken, O. M., P. Å. Krogstad, A. Ashrafian, and H. I. Andersson (2005), Reynolds number effects in the outer layer of the turbulent flow in a channel with rough walls, *Physics of Fluids*, *17*(6), 1-16.
8. Barenblatt, G. I. (1986), *Scaling, Self-Similarity, and Intermediate Asymptotics*, University Press, Cambridge.
9. Barenblatt, G. I. (1993), Scaling laws for fully developed turbulent shear flows. Part 1. Basic hypotheses and analysis, *Journal of Fluid Mechanics*, *248*, 513-520.
10. Bathurst, J. C. (1985), Flow resistance estimation in mountain rivers (Britain, friction factor), *Journal of Hydraulic Engineering - ASCE*, *111*(4), 625-643.
11. Bathurst, J. C. (2002), At-a-site variation and minimum flow resistance for mountain rivers, *Journal of Hydrology*, *269*(1-2), 11-26.
12. Bathurst, J. C., R. M. Li, and D. B. Simons (1981), Resistance equation for large-scale roughness, *Journal of the Hydraulics Division, ASCE*, *107*(HY12, Proc. Paper 16743), 1593-1613.

13. Benenati, R. F., and C. B. Brosilow (1962), Void fraction distribution in beds of spheres, *AIChE Journal*, *8*(3), 359-361.
14. Birch, D. M., and J. F. Morrison (2011), Similarity of the streamwise velocity component in very-rough-wall channel flow, *Journal of Fluid Mechanics*, *668*, 174-201.
15. Bjerklie, D. M., S. L. Dingman, and C. H. Bolster (2005), Comparison of constitutive flow resistance equations based on the Manning and Chezy equations applied to natural rivers, *Water Resources Research*, *41*(11), 1-7.
16. Bray, D. I. (1979), Estimating average velocity in gravel-bed rivers, (Alberta), *Journal of the Hydraulics Division, ASCE*, *105*(HY9, Proc.Paper, 14810), 1103-1122.
17. Breugem, W. A., and W. S. J. Uijttewaal (2007), *Sediment transport by coherent structures in a turbulent open channel flow experiment*, Springer Netherlands.
18. Breugem, W. P., B. J. Boersma, and R. E. Uittenbogaard (2006), The influence of wall permeability on turbulent channel flow, *Journal of Fluid Mechanics*, *562*, 35-72.
19. Buffin-Bélanger, T., and A. G. Roy (1998), Effects of a pebble cluster on the turbulent structure of a depth-limited flow in a gravel-bed river, *Geomorphology*, *25*(3-4), 249-267.
20. Buschmann, M. H., and M. Gad-el-Hak (2007), Recent developments in scaling of wall-bounded flows, *Progress in Aerospace Sciences*, *42*(5-6), 419-467.
21. Cao, H. H. (1985), Resistance hydraulique d'un lit à gravier mobile à pente raide; étude expérimentale, Ecole PolytechniqueFederale de Lausane, Lausanne.
22. Carson, M. A., and M. J. Kirkby (1972), *Hillslope Form and Process*, 473 pp., Cambridge Univ. Press, New York.
23. Charlton, F. G., P. M. Brown, and R. W. Benson (1978), *The Hydraulic Geometry of Some Gravel Rivers in Britain*, Hydraulics Research Station (Great Britain).
24. Chen, D., and G. H. Jirka (1998), Linear stability analysis of turbulent mixing layers and jets in shallow water layers, *Journal of Hydraulic Research*, *36*(5), 815-830.
25. Cheng, N. S. (2007), Power-law index for velocity profiles in open channel flows, *Advances in Water Resources*, *30*(8), 1775-1784.
26. Cheng, N. S. (2008a), Formula for the viscosity of a glycerol-water mixture, *Industrial and Engineering Chemistry Research*, *47*(9), 3285-3288.
27. Cheng, N. S. (2011b), Wall effect on pressure drop in packed beds, *Powder Technology*, *210*(3), 261-266.

28. Cheng, N. S. (2012a), Scaling law for velocity profiles of surface granular flows observed in rotating cylinders, *Powder Technology*, *218*, 11-17.
29. Cheng, N. S., and L. H. C. Chua (2005), Comparisons of sidewall correction of bed shear stress in open-channel flows, *Journal of Hydraulic Engineering*, *131*(7), 605-609.
30. Cheng, N. S., Z. Hao, and S. K. Tan (2008b), Comparison of quadratic and power law for nonlinear flow through porous media, *Experimental Thermal and Fluid Science*, *32*(8), 1538-1547.
31. Cheng, N. S., H. T. Nguyen, S. K. Tan, and S. Shao (2012b), Scaling of velocity profiles for depth-limited open channel flows over submerged rigid vegetation, *Journal of Hydraulic Engineering, ASCE.*
32. Chow, V. T. (1959), *Open Channel Hydraulics*, 680 pp., McGraw-Hill, New York.
33. Cipra, B. (1996), A new theory of turbulence causes a stir among experts, *Science*, *272*(5264), 951.
34. Codell, R. B., S. R. Abt, T. Johnson, and J. Ruff (1990), Estimation of flow through and over armored slopes, *Journal of Hydraulic Engineering*, *116*(10), 1252-1269.
35. Coles, D. (1956), The law of the wake in the turbulent boundary layer *J. Fluid Mech.*, *1*, 191-226.
36. Colombini, M. (1993), Turbulence-driven secondary flows and formation of sand ridges, *Journal of Fluid Mechanics*, *254*, 701-719.
37. Colosimo, C., V. A. Copertino, and M. Veltri (1988), Friction Factor Evaluation in Gravel-bed Rivers, *J. Hydraulic Engineering*, *114*(8), 861-876.
38. DantecDynamics (2002), Flow Manager software and introduction to PIV instrumentation, in *Software user's guide*, edited, Skovlunde, Denmark.
39. Darby, S. E. (2005), Refined hydraulic geometry data for British gravel-bed rivers, *Journal of Hydraulic Engineering*, *131*(1), 60-64.
40. Das Gupta, A., and G. N. Paudyal (1985), Characteristics of free surface flow over a gravel bed, *Journal of Irrigation and Drainage Engineering*, *111*(4), 299-318.
41. Dey, S., and R. Das (2012), Gravel-bed hydrodynamics: Double-averaging approach, *Journal of Hydraulic Engineering*, *138*(8), 707-725.
42. Dooge, J. C. I. (1992), The Manning formula in context, in *Channel Flow Resistance: Centennial of Manning's Formula*, edited by B. C. Yen, pp. 136-185.
43. Durbin, P. A., and B. A. P. Reif (2001), *Statistical theory and modeling for turbulent flows*, John Wiley & Sons, Chichester, Singapore.
44. Ergun, S. (1952), Fluid Flow through Packed Columns, *Chemical Engineering and Processing: Process Intensification*, *48*(2), 89-94.

45. Ferguson, R. (2007), Flow resistance equations for gravel- and boulder-bed streams, *Water Resources Research*, *43*(5).
46. Ferro, V., and R. Pecoraro (2000), Incomplete self-similarity and flow velocity in gravel bed channels, *Water Resources Research*, *36*(9), 2761-2769.
47. Finnigan, J. (2000), Turbulence in plant canopies, *Annual Review of Fluid Mechanics*, *32*, 519-571.
48. Flack, K. A., M. P. Schultz, and J. S. Connelly (2007), Examination of a critical roughness height for outer layer similarity, *Physics of Fluids*, *19*(9).
49. Froehlich, D. C. (2012), Resistance to Shallow Uniform Flow in Small, Riprap-Lined Drainage Channels, *Journal of Irrigation and Drainage Engineering*, *138*(2), 203-210.
50. Garcia, M. (2008), *Sedimentation engineering: processes, measurements, modeling, and practice*, ASCE, Reston.
51. George, W. K., and L. Castillo (1997), Zero-pressure-gradient turbulent boundary layer, *Applied Mechanics Reviews*, *50*(12 PART I), 689-728.
52. Ghidaoui, M. S., and A. A. Kolyshkin (2004), On coherent structures in shallow flows, in *Shallow Flows*, edited, pp. 39-46, Taylor & Francis.
53. Ghisalberti, M. (2009), Obstructed shear flows: Similarities across systems and scales, *Journal of Fluid Mechanics*, *641*, 51-61.
54. Ghisalberti, M., and H. M. Nepf (2002), Mixing layers and coherent structures in vegetated aquatic flows, *Journal of Geophysical Research C: Oceans*, *107*(2), 3-1.
55. Ghisalberti, M., and H. M. Nepf (2004), The limited growth of vegetated shear layers, *Water Resources Research*, *40*(7), W075021-W0750212.
56. Ghisalberti, M., and H. Nepf (2006), The structure of the shear layer in flows over rigid and flexible canopies, *Environmental Fluid Mechanics*, *6*(3), 277-301.
57. Gioia, G., and F. A. Bombardelli (2002), Scaling and similarity in rough channel flows, *Physical Review Letters*, *88*(1), 145011-145014.
58. Goharzadeh, A., A. Khalili, and B. B. Joørgensen (2005), Transition layer thickness at a fluid-porous interface, *Physics of Fluids*, *17*(5), 1-10.
59. Graf, W. H., and L. Suszka (1987), Sediment transport in steep channels, *Journal of Hydroscience and Hydraulic Engineering*, *5*(1), 11-26.
60. Grass, A. J. (1971), Structural features of turbulent flow over smooth and rough boundaries, *Journal of Fluid Mechanics*, *50*(02), 233-255.
61. Griffiths, G. A. (1981), Flow resistance in coarse gravel bed rivers, *Journal of the Hydraulics Division, ASCE*, *107*(HY7, Proc. Paper 16363), 899-918.
62. Gualtieri, C. (2010), Numerical simulation of transition layer at a fluid-porous interface, Ottawa, ON.

63. Gupta, A. D., and G. N. Paudyal (1985), Characteristics of free surface fow over gravel bed, *J. of Irrigation and Drainage Engineering*, *111*(4), 299-318.
64. Gupta, A. D., and G. N. Paudyal (1985), Characteristics of free surface flow over gravel bed, *Journal of irrigation and drainage engineering*, *111*, 299.
65. Hardy, R. J., J. L. Best, S. N. Lane, and P. E. Carbonneau (2009), Coherent flow structures in a depth-limited flow over a gravel surface: The role of near-bed turbulence and influence of Reynolds number, *Journal of Geophysical Research F: Earth Surface*, *114*(1).
66. Hardy, R. J., J. L. Best, S. N. Lane, and P. E. Carbonneau (2010), Coherent flow structures in a depth-limited flow over a gravel surface: The influence of surface roughness, *Journal of Geophysical Research F: Earth Surface*, *115*(3).
67. Hey, R. D. (1979), Flow resistance in gravel bed rivers, *J. HYDRAUL. DIV. : PROC. ASCE*, *105 , no.HY4, Apr.1979*, 365-379.
68. Hinze, J. O. (1975), *Turbulence*, McGraw-Hill, New York.
69. Ho, C. M. (1984), Study of bedload transport in turbulent open channel flows, National Taiwan University, Taiwan.
70. Jarrett, R. D. (1984a), Hydraulics of high-gradient streams, *Journal of Hydraulic Engineering - ASCE*, *110*(11), 1519-1539.
71. Jarrett, R. D. (1984b), Hydraulics of high-gradient streams, *J. HYDRAUL. ENGNG. (ASCE)*, *110*(11 , Nov.), 1519-1539.
72. Jiménez, J. (2004), Turbulent flows over rough walls, edited, pp. 173-196.
73. Jirka, G. H., and W. S. J. Uijttewaal (2004), *Shallow Flows: Research Presented at the International Symposium on Shallow Flows, Delft, Netherlands, 2003*, Taylor & Francis.
74. Jordanova, A. A., and C. S. James (2010), Resistance Prediction for Streams under Low Flow Conditions, paper presented at River Flow 2010.
75. Katul, G., P. Wiberg, J. Albertson, and G. Hornberger (2002), A mixing layer theory for flow resistance in shallow streams, *Water Resources Research*, *38*(11), 321-328.
76. Keulegan, G. H. (1938), Laws of Turbulent Flow in Open Channels, *J. of Res. of the Nat. Bur. of Standards*, *21*, 707-741.
77. Kiger, K. T., and C. Pan (2002), Suspension and turbulence modification effects of solid particulates on a horizontal turbulent channel flow, *Journal of Turbulence*, *3*.
78. Kirkbride, A. (1993), Observations of the influence of bed roughness on turbulence structure in depth limited flows over gravel beds, *Turbulence: perspectives on flow and sediment transfer*, 185-196.
79. Kundu, P. K., and I. M. Cohen (2008), *Fluid Mechanics*, Academic Press.

80. Lawrence, D. S. L. (1997), Macroscale surface roughness and frictional resistance in overland flow, *Earth Surface Processes and Landforms*, *22*(4), 365-382.
81. Lelouvetel, J., F. Bigillon, D. Doppler, I. Vinkovic, and J. Y. Champagne (2009), Experimental investigation of ejections and sweeps involved in particle suspension, *Water Resources Research*, *45*(2).
82. Lesieur, M. (1987), *Turbulence in Fluids*, Martinus Nijhoff Publishers, Dordrecht, Netherlands.
83. Manes, C., D. Pokrajac, and I. McEwan (2007), Double-averaged open-channel flows with small relative submergence, *Journal of Hydraulic Engineering*, *133*(8), 896-904.
84. Manes, C., D. Pokrajac, I. McEwan, and V. Nikora (2009), Turbulence structure of open channel flows over permeable and impermeable beds: A comparative study, *Physics of Fluids*, *21*(12), 1-12.
85. Manes, C., D. Pokrajac, I. McEwan, V. Nikora, and L. Campbell (2006), Application of UVP within porous beds, *Journal of Hydraulic Engineering*, *132*, 983.
86. Manes, C., D. Pokrajac, V. Nikora, L. Ridolfi, and D. Poggi (2011a), Turbulent friction in flows over permeable walls, *Geophysical Research Letters*, *38*(3), L03402.
87. Manes, C., D. Pokrajac, V. I. Nikora, L. Ridolfi, and D. Poggi (2011b), Turbulent friction in flows over permeable walls, *Geophysical Research Letters*, *38*(3).
88. McKay, S. K., and J. C. Fischenich (2011), Robust Prediction of Hydraulic Roughness, (ERDC/CHL CHETN-VII-11).
89. Mehta, D., and M. C. Hawley (1969), Wall effect in packed columns, *Industrial and Engineering Chemistry Design and Development*, *8*(2), 280-282.
90. Mendoza, C., and D. Zhou (1992a), Effects of porous bed on turbulent stream flow above the bed, *Journal of Hydraulic Engineering - ASCE*, *118*(9), 1222-1240.
91. Mendoza, C., and D. Zhou (1992b), Effects of porous bed on turbulent stream flow above bed, *Journal of Hydraulic Engineering*, *118*(9), 1222-1240.
92. Mignot, E., E. Barthelemy, and D. Hurther (2009), Double-averaging analysis and local flow characterization of near-bed turbulence in gravel-bed channel flows, *Journal of Fluid Mechanics*, *618*, 279-303.
93. Millar, R. G. (1999), Grain and form resistance in gravel-bed rivers, *Résistances de grain et de forme dans les rivières à graviers*, *37*(3), 303-312.
94. Mizuno, Y., and J. Jiménez (2011), Mean velocity and length-scales in the overlap region of wall-bounded turbulent flows, *Physics of Fluids*, *23*(8).

95. Montes, S. (1998), *Hydraulics of open channel flow*, 697 pp., ASCE Press, Reston, VA
96. Montillet, A., E. Akkari, and J. Comiti (2007), About a correlating equation for predicting pressure drops through packed beds of spheres in a large range of Reynolds numbers, *Chemical Engineering and Processing: Process Intensification*, *46*(4), 329-333.
97. Muste, M., K. Yu, I. Fujita, and R. Ettema (2009), Two-phase flow insights into open-channel flows with suspended particles of different densities, *Environmental Fluid Mechanics*, *9*(2), 161-186.
98. Nakagawa, H., T. Tsujimoto, and Y. Shimizu (1991), *Turbulent flow with small relative submergence*, Springer-Verlag, Berlin, Germany.
99. Nepf, H., and M. Ghisalberti (2008), Flow and transport in channels with submerged vegetation, *Acta Geophysica*, *56*(3), 753-777.
100. Nezu, I. (1979), Turbulent structure in open-channel flows, Department of Civil Engineering, Kyoto University.
101. Nezu, I., and W. Rodi (1986), Open-channel flow measurements with a Laser Doppler Anenometer, *Journal of Hydraulic Engineering - ASCE*, *112*(5), 335-355.
102. Nezu, I., and H. Nakagawa (1993), *Turbulence in open-channel flows*, A. A. Balkema.
103. Nezu, I., and R. Azuma (2004), Turbulence characteristics and interaction between particles and fluid in particle-laden open channel flows, *Journal of Hydraulic Engineering*, *130*(10), 988-1001.
104. Nikora, V., D. Goring, I. McEwan, and G. Griffith (2001), Spatially averaged open-channel flow over rough bed, *Journal of Hydraulic Engineering*, *127*(2), 123-133.
105. Nikora, V., K. Koll, I. McEwan, S. McLean, and A. Dittrich (2004), Velocity distribution in the roughness layer of rough-bed flows, *Journal of Hydraulic Engineering*, *130*(10), 1036-1042.
106. Nikora, V., I. McEwan, S. McLean, S. Coleman, D. Pokrajac, and R. Walters (2007), Double-averaging concept for rough-bed open-channel and overland flows: Theoretical background, *Journal of Hydraulic Engineering*, *133*(8), 873-883.
107. Noguchi, K., and I. Nezu (2009), Particle-turbulence interaction and local particle concentration in sediment-laden open-channel flows, *Journal of Hydro-Environment Research*, *3*(2), 54-68.
108. Paintal, A. S. (1971), Concept of critical shear stress in loose boundary open channels, *J. of Hydraulic Research*, *1*, 90-113.
109. Papanicolaou, A. N., D. C. Dermisis, and M. Elhakeem (2011), Investigating the role of clasts on the movement of sand in gravel bed rivers, *Journal of Hydraulic Engineering*, *137*(9), 871-883.

110. Papanicolaou, A. N., C. M. Kramer, A. G. Tsakiris, T. Stoesser, S. Bomminayuni, and Z. Chen (2012), Effects of a fully submerged boulder within a boulder array on the mean and turbulent flow fields: Implications to bedload transport, *Acta Geophysica*, *60*(6), 1502-1546.
111. Parker, G. (1991), Selective sorting and abrasion of river gravel. II. Applications, *Journal of Hydraulic Engineering*, *117*(2), 150-171.
112. Poggi, D., A. Porporato, L. Ridolfi, J. D. Albertson, and G. G. Katul (2004), The effect of vegetation density on canopy sub-layer turbulence, *Boundary-Layer Meteorology*, *111*(3), 565-587.
113. Pokrajac, D., and C. Manes (2009), Velocity measurements of a free-surface turbulent flow penetrating a porous medium composed of uniform-size spheres, *Transport in Porous Media*, *78*(3 SPEC. ISS.), 367-383.
114. Pokrajac, D., C. Manes, and I. McEwan (2007a), Peculiar mean velocity profiles within a porous bed of an open channel, *Physics of Fluids*, *19*(9).
115. Pokrajac, D., L. J. Campbell, V. Nikora, C. Manes, and I. McEwan (2007b), Quadrant analysis of persistent spatial velocity perturbations over square-bar roughness, *Experiments in Fluids*, *42*(3), 413-423.
116. Pope, S. B. (2000), *Turbulent Flows*, Cambridge University Press.
117. Prandtl, L. (1935), The mechanics of viscous fluid, *In: Aerodynamic theory III (Durand, W. F., ed.)* 34-208.
118. Raupach, M. R., R. A. Antonia, and S. Rajagopalan (1991), Rough-wall turbulent boundary layers, *Applied Mechanics Reviews*, *44*, 1-25.
119. Raupach, M. R., J. J. Finnigan, and Y. Brunet (1996), Coherent eddies and turbulence in vegetation canopies: the mixing-layer analogy, *Boundary-Layer Meteorology*, *78*(3-4), 351-382.
120. Recking, A. (2006), An experimental study of grain sorting effects on bedload, Institut National des Siences Appliquees de Lyon, Lyon.
121. Richardson, C. P., and A. D. Parr (1991), Friction and free-surface flow over porous media, *Journal of Hydraulic Engineering*, *117*(11), 1496-1512.
122. Rickenmann, D. (1991), Hyperconcentrated flow and sediment transport at steep slopes, *Journal of Hydraulic Engineering*, *117*(11), 1419-1439.
123. Rickenmann, D., and A. Recking (2011), Evaluation of flow resistance in gravel-bed rivers through a large field data set, *Water Resources Research*, *47*(7).
124. Roco, M. C. (1993), *Particulate two-phase flow*, xxii, 1,002 p. pp., Butterworth-Heinemann, Boston.
125. Roy, A. G., T. Buffin-Bélanger, H. Lamarre, and A. D. Kirkbride (2004), Size, shape and dynamics of large-scale turbulent flow structures in a gravel-bed river, *Journal of Fluid Mechanics*(500), 1-27.

126. Sarkar, S., and S. Dey (2010), Double-averaging turbulence characteristics in flows over a gravel bed, *Journal of Hydraulic Research*, *48*(6), 801-809.
127. Simões, J. M. F. (2010), Flow resistance in open channels with fixed and movable bed, in *2nd Joint Federal Interagency Conference*, edited, Las vegas, NV.
128. Smart, G. M. (1984), Sediment transport formula for steep channels, *Journal of Hydraulic Engineering - ASCE*, *110*(3), 267-276.
129. Stoesser, T., J. Fröhlich, and W. Rodi (2007), Turbulent open channel flow over a permeable bed, paper presented at 32th IAHR Congress, Venice, Italy
130. Suga, K., Y. Matsumura, Y. Ashitaka, S. Tominaga, and M. Kaneda (2010), Effects of wall permeability on turbulence, *International Journal of Heat and Fluid Flow*, *31*(6), 974-984.
131. Thompson, S. M., and P. L. Campbell (1979), Hydraulics of a large channel paved with boulders, *Journal of Hydraulic Research*, *17*(4), 341-354.
132. Townsend, A. A. (1961), Equilibrium layers and wall turbulence, *Journal of Fluid Mechanics*, *11*(Part 1), 97-120.
133. Townsend, A. A. (1976), *The Structure of Turbulent Shear Flow*, Cambridge University Press, New York.
134. Tuyen, N. B. (2006), Flow over oblique weirs, Master of Science Thesis thesis, Delft University of Technology.
135. Tuyen, N. B. (2010), Experimental investigation of open-channel two-phase flows by means of a combination of PIV and PTV*Rep.*, Confirmation of Candidature Report, submitted to the Nanyang Technological University.
136. Tuyen, N. B., and N. S. Cheng (2012a), Flow Resistance in Smooth Rectangular Open Channels with Low Aspect Ratios, *J. Hydraul. Eng.-ASCE*, *138*(9), 817-821.
137. Tuyen, N. B., and N. S. Cheng (2012b), A single-camera technique for simultaneous measurement of large solid particles transported in rapid shallow channel flows, *Experiments in Fluids*, *53*(5), 1269-1287.
138. Tuyen, N. B., N. S. Cheng, C. Qiao, and X. Liu (2014), Scaling for velocity profiles in shallow flows over a permeable rough bed, *Water Resources Research*(Submitted paper).
139. Vollmer, S., F. D. L. S. Ramos, H. Daebel, and G. Kühn (2002), Micro scale exchange processes between surface and subsurface water, *Journal of Hydrology*, *269*(1-2), 3-10.
140. Winterberg, M., and E. Tsotsas (2000), Impact of tube-to-particle-diameter ratio on pressure drop in packed beds, *AIChE Journal*, *46*(5), 1084-1088.
141. Wohl, E. E. (2000), *Mountain Rivers*, American Geophysical Union, Washington, D. C.
142. Wolman, M. G. (1954), A method of sampling coarse river-bed material, *American Geophysical union*, *35*(6), 951-956.

143. Yager, E. M., J. W. Kirchner, and W. E. Dietrich (2007), Calculating bed load transport in steep boulder bed channels, *Water Resources Research*, *43*(7).

144. Yen, B. C. (1992), *Hydraulic resistance in open channels, in Channel Flow Resistance: Centennial of Manning's Formula, edited by B. C. Yen*, Water Resour. Publ., Highlands Ranch, Colo.

145. Yen, B. C. (2002), Open channel flow resistance, *Journal of Hydraulic Engineering*, *128*(1), 20-39.

146. Zagarola, M. V., and A. J. Smits (1998), Mean-flow scaling of turbulent pipe flow, *Journal of Fluid Mechanics*, *373*, 33-79.

147. Zagni, A. F. E., and K. V. H. Smith (1976), Channel flow over permeable beds of graded spheres, *ASCE J Hydraul Div*, *102*(2), 207-222.

148. Zagni, A. F. E., and K. V. H. Smith (1976), Channel flow over permeable beds of graded spheres, *Journal of the Hydraulics Division*, *102*(2), 207-222.

149. Zhou, D., and C. Mendoza (1993), Flow through porous bed of turbulent stream, *Journal of Engineering Mechanics - ASCE*, *119*(2), 365-383.

150. Zimmermann, A. (2010), Flow resistance in steep streams: An experimental study, *Water Resources Research*, *46*(9).

151. Zippe, H. J., and W. H. Graf (1983), Turbulent boundary-layer flow over permeable and non-permeable rough surfaces, *Journal of Hydraulic Research*, *21*(1), 51-65.

APPENDIX

Appendix A - Collected flow resistance data from literature and the present study

Table A1 (to be continued)**:** Summary of data sets collected

Reference	***Q***	***B***	***H_s***	***S***	***U***	**Fr**	**Re**	***f***	***D50***	***H_s/D_{50}***
-	*m3/s*	*m*	*m*	-	*m/s*	-	-	-	*mm*	-
This study (for gravels)	0.00325 – 0.022	0.3	0.042 – 0.127	0.0064	0.234 – 0.686	0.353 – 0.661	1.20×10^4 – 1.03×10^5	0.117 – 0.412	32.5	1.28 – 3.89
This study (for spherical-particles)	0.0001 – 0.00066	0.098	0.0077 – 0.025	0.0029 – 0.031	0.104 – 0.484	0.319 – 1.356	1.29×10^3 – 8.19×10^4	0.116 – 0.228	11	0.7 – 2.27
Manes (2011)	NA	0.4	0.05 – 0.08	NA	NA	NA	2.94×10^4 – 1.53×10^5	0.028 – 0.08	10	5 – 8

Recking (2006)	0.0003 – 0.02	0.1 – 0.25	0.011 – 0.083	0.01 – 0.05	0.194 – 0.96	0.496 – 1.255	2.40×10^3 – 5.82×10^4	0.066 – 0.396	2.3 – 9	1.26 – 36.22
H0 (1984)	0.000192 – 0.0216	0.3 – 0.6	0.0026 – 0.079	0.002 – 0.1	0.242 – 0.904	0.55 – 2.82	6.78×10^2 – 5.33×10^4	0.02 – 0.509	2.2 – 15	1.12 – 35.91
Richardson (1991)	NA	0.152	0.009 – 0.01	0	NA	NA	2.64×10^2 – 2.97×10^3	0.021 – 0.069	0.11 – 3	3.25 – 94.09
Graf and Suszka (1987)	0.039 – 0.09	0.6	0.077 – 0.154	0.005 – 0.01	0.774 – 0.983	0.768 – 0.993	5.45×10^4 – 1.14×10^5	0.064 – 0.088	12.2	6.31 – 12.62
Gupta (1985)	0.0013 – 0.0145	0.3	0.026 – 0.116	0.0021 – 0.012	NA	NA	4.86×10^3 – 5.80×10^4	0.06 – 0.398	9.8	2.7 – 8
Cao (1985)	0.007 – 0.2	0.6	0.022 – 0.262	0.005 – 0.09	0.314 – 1.353	0.435 – 1.509	1.09×10^4 – 2.00×10^5	0.066 – 0.576	11.5 – 44.3	0.98 – 12.50
Bathurst (1981)	0.00143 – 0.0802	1.168	0.008 – 0.09	0.02 – 0.08	0.100 – 1.301	0.19 – 1.93	1.05×10^3 – 5.86×10^4	0.143 – 4.797	8.8 – 54.25	0.26 – 5.53
Zagni and Smith (1976)	NA	0.46	0.023 – 0.133	0.0005 – 0.008	NA	NA	2.84×10^3 – 1.34×10^5	0.023 – 0.077	4	5.8 – 33.2
Paintal (1971)	0.017 – 0.227	0.914 – 0.924	0.045 – 0.187	0.0012 – 0.0092	0.388 – 1.329	0.431 – 0.982	1.78×10^4 – 1.92×10^5	0.038 – 0.098	2.5 – 22.2	4.32 – 33.04

Table A1 (continued): Summary of data sets collected

Reference	Roughness element	Bed preparation method	No. of layers	No. of tests	Measurement	Notes
-	-	-	-	-	-	-
This study (for gravels)	One type of gravels.	Gravels were randomly placed onto the flume bottom and leveled with a still water surface.	1 – 4	20	Gauged flow depth and metered discharge; Sub-critical flow conditions; No sediment motion.	Flume tests, with complimentary EMCM measurements
This study (for spherical-particles)	Glass spheres (marbles).	Layers of alternate marbles on top of each other	1 – 4	103	Gaged depth and discharge; U determined by flow-area method.	Flume tests, with complimentary PIV measurements
Manes (2011)	One type of gravels.	6 cm-thick of gravel grains.	Approx. 6 – 7	20	Gauged flow depth and metered discharge; Sub-critical flow conditions; No sediment motion.	Constant flow depth, varying bed slope; Complimentary UVP measurements for velocity.
Recking (2006)	Four types of materials, including sieved sand and gravels.	10 cm-thick of sand/gravel grains;	Approx. 12 – 50	60	Gaged depth and discharge; Bed infiltration rate was measured separately and deduced from total flow rate.	Selected tests with no bed load; equilibrium bed slope. Complimentary salt velocity technique.
Ho (1984)	Five sizes of sediments	Sediment layer thickness of 5 – 10 cm	-	186	Uniform flow; Sediment motion close to threshold condition	Flume test; 9 different bed slopes; Measured flow depth and discharge;
Richardson (1991)	Five permeable media; uniform-size glass beads.	2.54 cm of randomly dumped glass beads.	Approx. 9 – 250	90	Mettered flow; Lory depth gages; Percolation effect was not examined;	Zero-slope; non-uniform flow with longitudinally varying depth and velocity.
Graf and Suszka	-	-	-	8	-	As reported by Recking (2006)

(1987)						
Gupta (1985)	Angular gravels of uniform size.	5.5 cm-thick gravel bed.	Approx. 6	37	Gaged flow depth and gauged discharge;	Hotwire anemometer for velocity profile measurements;
Cao (1985)	-	-	-	51	-	As reported by Recking (2006)
Bathurst (1981)	Cobbles & crushing cobbles, 0.5 – 2.5 inch.	One layer of material, glued to bottom	1	88	Gaged depth at a single cross-section (large B/H); U determined by flow-area method	Flume tests; flat bed; macroscopically uniform flow; R ~= H
Zagni and Smith (1976)	Spherical lead shots or steel balls.	6 cm-thick of bed materials; Permeable beds, formed by laying bed material evenly with no surface undulation and grain segregation.	Approx. 17	45	Gauged flow depth and metered discharge; Permeability tests were performed separately.	Grading of bed material was varied extensively; Complimentary surface-scan tests.
Paintal (1971)	Sub-rounded to sub-angular unigravels.	3-5 inch layer of gravels	Approx. 6 – 30	32	Uniform depth prevailed thorough; measured depth, discharge and slope.	Data points as reported by Recking (2006)

Table A2: Summary of flow resistance data collected

S/N	Investigator	Q	B	H_s	U_s	S	D	ν	H_s/D	f	Re
-	-	m^3/s	m	m	m/s	-	mm	m^2/s	-	-	-
1	Bathurst 1981	0.00241	1.168	0.014	0.146	0.0200	12.70	1.17E-06	1.110	1.038	1755
2	Bathurst 1981	0.01274	1.168	0.028	0.391	0.0200	12.70	1.17E-06	2.197	0.286	9300
3	Bathurst 1981	0.03046	1.168	0.045	0.584	0.0200	12.70	1.17E-06	3.512	0.205	22205
4	Bathurst 1981	0.05746	1.168	0.063	0.785	0.0200	12.70	1.17E-06	4.937	0.160	41960
5	Bathurst 1981	0.07197	1.168	0.070	0.877	0.0200	12.70	1.17E-06	5.528	0.143	52485
6	Bathurst 1981	0.00143	1.168	0.008	0.161	0.0500	12.70	1.17E-06	0.598	1.151	1043
7	Bathurst 1981	0.00522	1.168	0.015	0.296	0.0500	12.70	1.17E-06	1.189	0.676	3810
8	Bathurst 1981	0.01737	1.168	0.024	0.619	0.0500	12.70	1.17E-06	1.890	0.246	12665
9	Bathurst 1981	0.03249	1.168	0.034	0.823	0.0500	12.70	1.17E-06	2.661	0.196	23715
10	Bathurst 1981	0.04896	1.168	0.041	1.017	0.0500	12.70	1.17E-06	3.244	0.156	35721
11	Bathurst 1981	0.00196	1.168	0.008	0.201	0.0800	12.70	1.17E-06	0.661	1.305	1439
12	Bathurst 1981	0.00610	1.168	0.013	0.392	0.0800	12.70	1.17E-06	1.047	0.543	4445
13	Bathurst 1981	0.01355	1.168	0.021	0.563	0.0800	12.70	1.17E-06	1.622	0.408	9887
14	Bathurst 1981	0.03576	1.168	0.032	0.965	0.0800	12.70	1.17E-06	2.496	0.214	26079
15	Bathurst 1981	0.06061	1.168	0.042	1.225	0.0800	12.70	1.17E-06	3.339	0.177	44280
16	Bathurst 1981	0.07065	1.168	0.047	1.301	0.0800	12.70	1.17E-06	3.661	0.172	51574
17	Bathurst 1981	0.00580	1.168	0.022	0.222	0.0200	19.05	1.17E-06	1.171	0.710	4220
18	Bathurst 1981	0.01181	1.168	0.029	0.348	0.0200	19.05	1.17E-06	1.522	0.376	8604
19	Bathurst 1981	0.02482	1.168	0.044	0.484	0.0200	19.05	1.17E-06	2.304	0.294	18114
20	Bathurst 1981	0.04047	1.168	0.059	0.586	0.0200	19.05	1.17E-06	3.102	0.270	29525
21	Bathurst 1981	0.05348	1.168	0.070	0.656	0.0200	19.05	1.17E-06	3.664	0.255	39036
22	Bathurst 1981	0.00381	1.168	0.014	0.230	0.0500	19.05	1.17E-06	0.740	1.046	2765
23	Bathurst 1981	0.00843	1.168	0.020	0.363	0.0500	19.05	1.17E-06	1.045	0.593	6158
24	Bathurst 1981	0.02037	1.168	0.030	0.583	0.0500	19.05	1.17E-06	1.570	0.345	14861
25	Bathurst 1981	0.03333	1.168	0.037	0.782	0.0500	19.05	1.17E-06	1.916	0.234	24333

S/N	Investigator	Q	B	H_s	U_s	S	D	ν	H_s/D	f	Re
-	-	*m^3/s*	*m*	*m*	*m/s*	-	*mm*	*m^2/s*	-	-	-
26	Bathurst 1981	0.04586	1.168	0.043	0.904	0.0500	19.05	1.17E-06	2.278	0.208	33447
27	Bathurst 1981	0.05460	1.168	0.048	0.979	0.0500	19.05	1.17E-06	2.504	0.195	39811
28	Bathurst 1981	0.00207	1.168	0.010	0.186	0.0800	19.05	1.17E-06	0.499	1.724	1506
29	Bathurst 1981	0.00631	1.168	0.014	0.380	0.0800	19.05	1.17E-06	0.745	0.617	4600
30	Bathurst 1981	0.01007	1.168	0.020	0.430	0.0800	19.05	1.17E-06	1.050	0.679	7332
31	Bathurst 1981	0.02825	1.168	0.030	0.807	0.0800	19.05	1.17E-06	1.570	0.288	20571
32	Bathurst 1981	0.04518	1.168	0.038	1.032	0.0800	19.05	1.17E-06	1.969	0.221	32992
33	Bathurst 1981	0.04879	1.168	0.039	1.064	0.0800	19.05	1.17E-06	2.058	0.217	35557
34	Bathurst 1981	0.00250	1.168	0.018	0.116	0.0200	38.10	1.17E-06	0.483	2.146	1820
35	Bathurst 1981	0.00868	1.168	0.031	0.239	0.0200	38.10	1.17E-06	0.816	0.855	6337
36	Bathurst 1981	0.01893	1.168	0.043	0.375	0.0200	38.10	1.17E-06	1.134	0.482	13811
37	Bathurst 1981	0.04352	1.168	0.063	0.587	0.0200	38.10	1.17E-06	1.664	0.289	31727
38	Bathurst 1981	0.06763	1.168	0.080	0.721	0.0200	38.10	1.17E-06	2.108	0.242	49357
39	Bathurst 1981	0.08020	1.168	0.090	0.764	0.0200	38.10	1.17E-06	2.360	0.242	58554
40	Bathurst 1981	0.00181	1.168	0.012	0.132	0.0500	38.10	1.17E-06	0.307	2.635	1317
41	Bathurst 1981	0.00636	1.168	0.021	0.264	0.0500	38.10	1.17E-06	0.541	1.160	4636
42	Bathurst 1981	0.01456	1.168	0.030	0.419	0.0500	38.10	1.17E-06	0.782	0.666	10645
43	Bathurst 1981	0.03073	1.168	0.042	0.625	0.0500	38.10	1.17E-06	1.102	0.422	22379
44	Bathurst 1981	0.06061	1.168	0.060	0.869	0.0500	38.10	1.17E-06	1.567	0.310	44228
45	Bathurst 1981	0.07421	1.168	0.068	0.932	0.0500	38.10	1.17E-06	1.787	0.308	54108
46	Bathurst 1981	0.00389	1.168	0.012	0.267	0.0800	38.10	1.17E-06	0.325	1.092	2823
47	Bathurst 1981	0.01092	1.168	0.020	0.457	0.0800	38.10	1.17E-06	0.535	0.613	7948
48	Bathurst 1981	0.02100	1.168	0.029	0.616	0.0800	38.10	1.17E-06	0.766	0.483	15334
49	Bathurst 1981	0.03126	1.168	0.037	0.721	0.0800	38.10	1.17E-06	0.974	0.448	22804
50	Bathurst 1981	0.05498	1.168	0.048	0.971	0.0800	38.10	1.17E-06	1.270	0.322	40065

S/N	Investigator	Q	B	H_s	U_s	S	D	ν	H_s/D	f	Re
-	-	m^3/s	m	m	m/s	-	mm	m^2/s	-	-	-
51	Bathurst 1981	0.05574	1.168	0.054	0.883	0.0800	38.10	1.17E-06	1.417	0.435	40650
52	Bathurst 1981	0.00329	1.168	0.028	0.100	0.0200	50.80	1.17E-06	0.555	4.426	2404
53	Bathurst 1981	0.00837	1.168	0.038	0.189	0.0200	50.80	1.17E-06	0.744	1.661	6091
54	Bathurst 1981	0.01158	1.168	0.044	0.227	0.0200	50.80	1.17E-06	0.858	1.328	8438
55	Bathurst 1981	0.02541	1.168	0.058	0.377	0.0200	50.80	1.17E-06	1.138	0.638	18577
56	Bathurst 1981	0.04047	1.168	0.067	0.519	0.0200	50.80	1.17E-06	1.315	0.389	29556
57	Bathurst 1981	0.04949	1.168	0.071	0.601	0.0200	50.80	1.17E-06	1.388	0.306	36121
58	Bathurst 1981	0.00329	1.168	0.021	0.132	0.0500	50.80	1.17E-06	0.419	4.797	2397
59	Bathurst 1981	0.00713	1.168	0.029	0.214	0.0500	50.80	1.17E-06	0.561	2.442	5199
60	Bathurst 1981	0.01413	1.168	0.036	0.331	0.0500	50.80	1.17E-06	0.707	1.286	10130
61	Bathurst 1981	0.02068	1.168	0.041	0.431	0.0500	50.80	1.17E-06	0.809	0.868	15102
62	Bathurst 1981	0.02941	1.168	0.047	0.542	0.0500	50.80	1.17E-06	0.915	0.621	21486
63	Bathurst 1981	0.04368	1.168	0.058	0.643	0.0500	50.80	1.17E-06	1.146	0.552	31903
64	Bathurst 1981	0.00247	1.168	0.013	0.162	0.0800	50.80	1.17E-06	0.256	3.110	1795
65	Bathurst 1981	0.00565	1.168	0.024	0.205	0.0800	50.80	1.17E-06	0.465	3.526	4124
66	Bathurst 1981	0.01017	1.168	0.030	0.313	0.0800	50.80	1.17E-06	0.581	1.891	7872
67	Bathurst 1981	0.02187	1.168	0.036	0.515	0.0800	50.80	1.17E-06	0.715	0.859	15937
68	Bathurst 1981	0.03249	1.168	0.044	0.631	0.0800	50.80	1.17E-06	0.860	0.689	23508
69	Bathurst 1981	0.03724	1.168	0.045	0.712	0.0800	50.80	1.17E-06	0.882	0.555	27193
70	Bathurst 1981	0.00409	1.168	0.025	0.138	0.0200	63.50	1.17E-06	0.400	2.093	2988
71	Bathurst 1981	0.00993	1.168	0.038	0.223	0.0200	63.50	1.17E-06	0.600	1.203	7243
72	Bathurst 1981	0.01671	1.168	0.048	0.301	0.0200	63.50	1.17E-06	0.748	0.823	12189
73	Bathurst 1981	0.02799	1.168	0.059	0.409	0.0200	63.50	1.17E-06	0.923	0.550	20433
74	Bathurst 1981	0.04110	1.168	0.070	0.500	0.0200	63.50	1.17E-06	1.107	0.441	29966
75	Bathurst 1981	0.04967	1.168	0.078	0.543	0.0200	63.50	1.17E-06	1.231	0.416	36200

S/N	Investigator	Q	B	H_s	U_s	S	D	ν	H_s/D	f	Re
-	-	m^3/s	*m*	*m*	*m/s*	-	*mm*	m^2/s	-	-	-
76	Bathurst 1981	0.00369	1.168	0.018	0.173	0.0500	63.50	1.17E-06	0.288	2.399	2699
77	Bathurst 1981	0.00855	1.168	0.026	0.283	0.0500	63.50	1.17E-06	0.408	1.269	6249
78	Bathurst 1981	0.01282	1.168	0.032	0.342	0.0500	63.50	1.17E-06	0.506	1.077	9359
79	Bathurst 1981	0.02176	1.168	0.039	0.478	0.0500	63.50	1.17E-06	0.614	0.670	15893
80	Bathurst 1981	0.03403	1.168	0.048	0.611	0.0500	63.50	1.17E-06	0.751	0.501	24846
81	Bathurst 1981	0.04896	1.168	0.058	0.725	0.0500	63.50	1.17E-06	0.910	0.432	35725
82	Bathurst 1981	0.00397	1.168	0.016	0.210	0.0800	63.50	1.17E-06	0.255	2.306	2900
83	Bathurst 1981	0.00605	1.168	0.020	0.259	0.0800	63.50	1.17E-06	0.315	1.872	4416
84	Bathurst 1981	0.01128	1.168	0.026	0.374	0.0800	63.50	1.17E-06	0.406	1.158	8226
85	Bathurst 1981	0.01775	1.168	0.032	0.474	0.0800	63.50	1.17E-06	0.506	0.897	12971
86	Bathurst 1981	0.02737	1.168	0.040	0.592	0.0800	63.50	1.17E-06	0.624	0.709	19986
87	Bathurst 1981	0.03319	1.168	0.043	0.669	0.0800	63.50	1.17E-06	0.669	0.596	24239
88	Bathurst 1981	0.04485	1.168	0.050	0.775	0.0800	63.50	1.17E-06	0.780	0.517	32705
89	Ho (1984)	0.00062	0.3	0.007	0.295	0.0200	2.20	1.00E-06	3.136	0.124	2036
90	Ho (1984)	0.00069	0.3	0.008	0.307	0.0200	2.20	1.00E-06	3.409	0.125	2303
91	Ho (1984)	0.00066	0.3	0.007	0.303	0.0200	2.20	1.00E-06	3.318	0.125	2212
92	Ho (1984)	0.00080	0.3	0.008	0.319	0.0200	2.20	1.00E-06	3.773	0.128	2648
93	Ho (1984)	0.00094	0.3	0.009	0.352	0.0200	2.20	1.00E-06	4.045	0.113	3133
94	Ho (1984)	0.00109	0.3	0.009	0.378	0.0200	2.20	1.00E-06	4.273	0.103	3553
95	Ho (1984)	0.00130	0.3	0.010	0.417	0.0200	2.20	1.00E-06	4.727	0.094	4337
96	Ho (1984)	0.00031	0.3	0.004	0.261	0.0333	2.20	1.00E-06	1.773	0.150	1018
97	Ho (1984)	0.00036	0.3	0.004	0.279	0.0333	2.20	1.00E-06	1.955	0.145	1200
98	Ho (1984)	0.00044	0.3	0.005	0.300	0.0333	2.20	1.00E-06	2.227	0.142	1470
99	Ho (1984)	0.00045	0.3	0.005	0.304	0.0333	2.20	1.00E-06	2.364	0.147	1581
100	Ho (1984)	0.00060	0.3	0.006	0.345	0.0333	2.20	1.00E-06	2.727	0.132	2070

S/N	Investigator	Q	B	H_s	U_s	S	D	ν	H_s/D	f	Re
-	-	m^3/s	m	m	m/s	-	mm	m^2/s	-	-	-
101	Ho (1984)	0.00059	0.3	0.006	0.336	0.0333	2.20	1.00E-06	2.636	0.134	1949
102	Ho (1984)	0.00020	0.3	0.003	0.242	0.0500	2.20	1.00E-06	1.318	0.194	702
103	Ho (1984)	0.00034	0.3	0.004	0.295	0.0500	2.20	1.00E-06	1.773	0.176	1151
104	Ho (1984)	0.00038	0.3	0.004	0.301	0.0500	2.20	1.00E-06	1.909	0.182	1264
105	Ho (1984)	0.00031	0.3	0.004	0.277	0.0500	2.20	1.00E-06	1.682	0.189	1025
106	Ho (1984)	0.00032	0.3	0.004	0.294	0.0500	2.20	1.00E-06	1.727	0.173	1117
107	Ho (1984)	0.00020	0.3	0.003	0.242	0.0500	2.20	1.00E-06	1.318	0.194	702
108	Ho (1984)	0.00034	0.3	0.004	0.295	0.0500	2.20	1.00E-06	1.773	0.176	1151
109	Ho (1984)	0.00019	0.3	0.003	0.261	0.0700	2.20	1.00E-06	1.182	0.210	679
110	Ho (1984)	0.00023	0.3	0.003	0.250	0.0700	2.20	1.00E-06	1.273	0.246	700
111	Ho (1984)	0.00023	0.3	0.003	0.271	0.0700	2.20	1.00E-06	1.318	0.217	786
112	Ho (1984)	0.00024	0.3	0.003	0.270	0.0700	2.20	1.00E-06	1.364	0.226	810
113	Ho (1984)	0.00026	0.3	0.003	0.282	0.0700	2.20	1.00E-06	1.455	0.221	902
114	Ho (1984)	0.00169	0.3	0.015	0.389	0.0100	2.20	1.00E-06	6.591	0.075	5641
115	Ho (1984)	0.00140	0.3	0.013	0.362	0.0100	2.20	1.00E-06	5.864	0.077	4670
116	Ho (1984)	0.00190	0.3	0.015	0.414	0.0100	2.20	1.00E-06	6.955	0.070	6334
117	Ho (1984)	0.00193	0.3	0.016	0.410	0.0100	2.20	1.00E-06	7.136	0.073	6437
118	Ho (1984)	0.00209	0.3	0.017	0.423	0.0100	2.20	1.00E-06	7.500	0.072	6980
119	Ho (1984)	0.00236	0.3	0.018	0.443	0.0100	2.20	1.00E-06	8.091	0.071	7885
120	Ho (1984)	0.00500	0.6	0.017	0.490	0.0100	2.20	1.00E-06	7.727	0.056	8333
121	Ho (1984)	0.00580	0.6	0.019	0.509	0.0100	2.20	1.00E-06	8.636	0.058	9667
122	Ho (1984)	0.00306	0.3	0.024	0.433	0.0100	3.60	1.00E-06	6.556	0.099	10219
123	Ho (1984)	0.00323	0.3	0.024	0.448	0.0100	3.60	1.00E-06	6.667	0.094	10752
124	Ho (1984)	0.00296	0.3	0.023	0.434	0.0100	3.60	1.00E-06	6.306	0.095	9852
125	Ho (1984)	0.00339	0.3	0.025	0.456	0.0100	3.60	1.00E-06	6.944	0.094	11400

S/N	Investigator	Q	B	H_s	U_s	S	D	ν	H_s/D	f	Re
-	-	m^3/s	m	m	m/s	-	mm	m^2/s	-	-	-
126	Ho (1984)	0.00370	0.3	0.026	0.472	0.0100	3.60	1.00E-06	7.222	0.092	12272
127	Ho (1984)	0.00404	0.3	0.028	0.478	0.0100	3.60	1.00E-06	7.639	0.094	13145
128	Ho (1984)	0.00417	0.3	0.028	0.494	0.0100	3.60	1.00E-06	7.778	0.090	13832
129	Ho (1984)	0.00453	0.3	0.030	0.511	0.0100	3.60	1.00E-06	8.250	0.089	15165
130	Ho (1984)	0.00510	0.3	0.032	0.532	0.0100	3.60	1.00E-06	8.889	0.089	17024
131	Ho (1984)	0.00544	0.3	0.033	0.547	0.0100	3.60	1.00E-06	9.167	0.087	18051
132	Ho (1984)	0.00078	0.3	0.009	0.277	0.0200	3.60	1.00E-06	2.611	0.192	2604
133	Ho (1984)	0.00137	0.3	0.013	0.366	0.0200	3.60	1.00E-06	3.472	0.146	4575
134	Ho (1984)	0.00150	0.3	0.013	0.392	0.0200	3.60	1.00E-06	3.556	0.131	5018
135	Ho (1984)	0.00175	0.3	0.014	0.422	0.0200	3.60	1.00E-06	3.833	0.122	5824
136	Ho (1984)	0.00176	0.3	0.014	0.425	0.0200	3.60	1.00E-06	3.833	0.120	5865
137	Ho (1984)	0.00196	0.3	0.015	0.441	0.0200	3.60	1.00E-06	4.111	0.119	6527
138	Ho (1984)	0.00224	0.3	0.016	0.465	0.0200	3.60	1.00E-06	4.444	0.116	7440
139	Ho (1984)	0.00229	0.3	0.016	0.469	0.0200	3.60	1.00E-06	4.528	0.116	7645
140	Ho (1984)	0.00078	0.3	0.008	0.329	0.0333	3.60	1.00E-06	2.194	0.191	2599
141	Ho (1984)	0.00092	0.3	0.009	0.356	0.0333	3.60	1.00E-06	2.389	0.178	3062
142	Ho (1984)	0.00115	0.3	0.010	0.400	0.0333	3.60	1.00E-06	2.667	0.157	3840
143	Ho (1984)	0.00046	0.3	0.005	0.294	0.0500	3.60	1.00E-06	1.444	0.237	1527
144	Ho (1984)	0.00063	0.3	0.006	0.346	0.0500	3.60	1.00E-06	1.667	0.197	2076
145	Ho (1984)	0.00065	0.3	0.006	0.348	0.0500	3.60	1.00E-06	1.722	0.201	2158
146	Ho (1984)	0.00079	0.3	0.007	0.382	0.0500	3.60	1.00E-06	1.917	0.186	2636
147	Ho (1984)	0.00083	0.3	0.007	0.399	0.0500	3.60	1.00E-06	1.972	0.175	2833
148	Ho (1984)	0.00085	0.3	0.007	0.382	0.0500	3.60	1.00E-06	2.056	0.199	2827
149	Ho (1984)	0.00092	0.3	0.008	0.408	0.0500	3.60	1.00E-06	2.083	0.177	3060
150	Ho (1984)	0.00044	0.3	0.005	0.313	0.0700	3.60	1.00E-06	1.278	0.258	1440

S/N	Investigator	Q	B	H_s	U_s	S	D	ν	H_s/D	f	Re
-	-	m^3/s	m	m	m/s	-	mm	m^2/s	-	-	-
151	Ho (1984)	0.00044	0.3	0.005	0.319	0.0700	3.60	1.00E-06	1.278	0.248	1467
152	Ho (1984)	0.00057	0.3	0.005	0.367	0.0700	3.60	1.00E-06	1.444	0.212	1908
153	Ho (1984)	0.00058	0.3	0.005	0.363	0.0700	3.60	1.00E-06	1.472	0.221	1924
154	Ho (1984)	0.00068	0.3	0.006	0.400	0.0700	3.60	1.00E-06	1.583	0.196	2280
155	Ho (1984)	0.00074	0.3	0.006	0.409	0.0700	3.60	1.00E-06	1.667	0.197	2454
156	Ho (1984)	0.00800	0.6	0.025	0.533	0.0100	3.60	1.00E-06	6.944	0.069	13333
157	Ho (1984)	0.00830	0.6	0.026	0.532	0.0100	3.60	1.00E-06	7.222	0.072	13832
158	Ho (1984)	0.00870	0.6	0.028	0.518	0.0100	3.60	1.00E-06	7.778	0.082	14498
159	Ho (1984)	0.00940	0.6	0.030	0.522	0.0100	3.60	1.00E-06	8.333	0.086	15666
160	Ho (1984)	0.00950	0.6	0.031	0.511	0.0100	3.60	1.00E-06	8.611	0.093	15835
161	Ho (1984)	0.00980	0.6	0.032	0.510	0.0100	3.60	1.00E-06	8.889	0.096	16333
162	Ho (1984)	0.00264	0.3	0.019	0.461	0.0200	6.00	1.00E-06	3.167	0.140	8759
163	Ho (1984)	0.00303	0.3	0.021	0.478	0.0200	6.00	1.00E-06	3.517	0.145	10086
164	Ho (1984)	0.00311	0.3	0.022	0.478	0.0200	6.00	1.00E-06	3.633	0.150	10420
165	Ho (1984)	0.00394	0.3	0.025	0.524	0.0200	6.00	1.00E-06	4.167	0.143	13100
166	Ho (1984)	0.00405	0.3	0.026	0.529	0.0200	6.00	1.00E-06	4.250	0.143	13490
167	Ho (1984)	0.00481	0.3	0.028	0.566	0.0200	6.00	1.00E-06	4.717	0.139	16018
168	Ho (1984)	0.00574	0.3	0.030	0.622	0.0200	6.00	1.00E-06	5.000	0.122	18660
169	Ho (1984)	0.00183	0.3	0.014	0.442	0.0333	6.00	1.00E-06	2.300	0.185	6100
170	Ho (1984)	0.00199	0.3	0.016	0.425	0.0333	6.00	1.00E-06	2.667	0.232	6800
171	Ho (1984)	0.00215	0.3	0.016	0.438	0.0333	6.00	1.00E-06	2.733	0.224	7183
172	Ho (1984)	0.00286	0.3	0.019	0.502	0.0333	6.00	1.00E-06	3.167	0.197	9538
173	Ho (1984)	0.00192	0.3	0.015	0.419	0.0333	6.00	1.00E-06	2.550	0.228	6411
174	Ho (1984)	0.00248	0.3	0.018	0.475	0.0333	6.00	1.00E-06	2.917	0.203	8313
175	Ho (1984)	0.00268	0.3	0.018	0.489	0.0333	6.00	1.00E-06	3.050	0.200	8949

S/N	Investigator	Q	B	H_s	U_s	S	D	ν	H_s/D	f	Re
-	-	m^3/s	*m*	*m*	*m/s*	-	*mm*	m^2/s	-	-	-
176	Ho (1984)	0.00283	0.3	0.019	0.500	0.0333	6.00	1.00E-06	3.150	0.198	9450
177	Ho (1984)	0.00140	0.3	0.012	0.401	0.0500	6.00	1.00E-06	1.950	0.286	4692
178	Ho (1984)	0.00165	0.3	0.012	0.457	0.0500	6.00	1.00E-06	2.000	0.225	5484
179	Ho (1984)	0.00207	0.3	0.013	0.525	0.0500	6.00	1.00E-06	2.167	0.185	6825
180	Ho (1984)	0.00082	0.3	0.008	0.366	0.0700	6.00	1.00E-06	1.250	0.308	2745
181	Ho (1984)	0.00099	0.3	0.008	0.396	0.0700	6.00	1.00E-06	1.383	0.291	3287
182	Ho (1984)	0.00116	0.3	0.009	0.430	0.0700	6.00	1.00E-06	1.500	0.267	3870
183	Ho (1984)	0.00103	0.3	0.008	0.410	0.0700	6.00	1.00E-06	1.400	0.275	3444
184	Ho (1984)	0.00114	0.3	0.009	0.426	0.0700	6.00	1.00E-06	1.483	0.269	3791
185	Ho (1984)	0.00175	0.3	0.012	0.503	0.0700	6.00	1.00E-06	1.933	0.252	5835
186	Ho (1984)	0.00666	0.3	0.035	0.641	0.0200	10.00	1.00E-06	3.460	0.132	22179
187	Ho (1984)	0.00725	0.3	0.037	0.663	0.0200	10.00	1.00E-06	3.650	0.130	24200
188	Ho (1984)	0.00759	0.3	0.038	0.674	0.0200	10.00	1.00E-06	3.750	0.130	25275
189	Ho (1984)	0.01140	0.3	0.048	0.787	0.0200	10.00	1.00E-06	4.830	0.122	38012
190	Ho (1984)	0.00360	0.3	0.022	0.538	0.0333	10.00	1.00E-06	2.240	0.202	12051
191	Ho (1984)	0.00635	0.3	0.032	0.670	0.0333	10.00	1.00E-06	3.160	0.184	21172
192	Ho (1984)	0.00442	0.3	0.025	0.582	0.0333	10.00	1.00E-06	2.530	0.195	14725
193	Ho (1984)	0.00474	0.3	0.026	0.598	0.0333	10.00	1.00E-06	2.640	0.193	15787
194	Ho (1984)	0.00489	0.3	0.027	0.606	0.0333	10.00	1.00E-06	2.690	0.192	16301
195	Ho (1984)	0.00491	0.3	0.027	0.606	0.0333	10.00	1.00E-06	2.700	0.192	16362
196	Ho (1984)	0.00718	0.3	0.034	0.703	0.0333	10.00	1.00E-06	3.400	0.180	23902
197	Ho (1984)	0.00843	0.3	0.036	0.781	0.0333	10.00	1.00E-06	3.600	0.154	28116
198	Ho (1984)	0.00234	0.3	0.017	0.472	0.0500	10.00	1.00E-06	1.650	0.291	7788
199	Ho (1984)	0.00267	0.3	0.018	0.496	0.0500	10.00	1.00E-06	1.800	0.287	8928
200	Ho (1984)	0.00275	0.3	0.018	0.502	0.0500	10.00	1.00E-06	1.830	0.285	9187

S/N	Investigator	Q	B	H_s	U_s	S	D	ν	H_s/D	f	Re
-	-	m^3/s	m	m	m/s	-	mm	m^2/s	-	-	-
201	Ho (1984)	0.00329	0.3	0.020	0.539	0.0500	10.00	1.00E-06	2.040	0.276	10996
202	Ho (1984)	0.00399	0.3	0.021	0.629	0.0500	10.00	1.00E-06	2.100	0.208	13209
203	Ho (1984)	0.00426	0.3	0.022	0.649	0.0500	10.00	1.00E-06	2.180	0.203	14148
204	Ho (1984)	0.00461	0.3	0.023	0.669	0.0500	10.00	1.00E-06	2.300	0.202	15387
205	Ho (1984)	0.00461	0.3	0.023	0.669	0.0500	10.00	1.00E-06	2.300	0.202	15387
206	Ho (1984)	0.00489	0.3	0.034	0.684	0.0500	10.00	1.00E-06	3.400	0.285	23256
207	Ho (1984)	0.00167	0.3	0.013	0.439	0.0700	10.00	1.00E-06	1.270	0.362	5575
208	Ho (1984)	0.00227	0.3	0.014	0.515	0.0700	10.00	1.00E-06	1.430	0.296	7365
209	Ho (1984)	0.00230	0.3	0.015	0.520	0.0700	10.00	1.00E-06	1.470	0.299	7644
210	Ho (1984)	0.00240	0.3	0.015	0.526	0.0700	10.00	1.00E-06	1.520	0.302	7995
211	Ho (1984)	0.00240	0.3	0.015	0.526	0.0700	10.00	1.00E-06	1.520	0.302	7995
212	Ho (1984)	0.00265	0.3	0.016	0.548	0.0700	10.00	1.00E-06	1.600	0.293	8768
213	Ho (1984)	0.00355	0.3	0.018	0.669	0.0700	10.00	1.00E-06	1.780	0.218	11908
214	Ho (1984)	0.00389	0.3	0.019	0.695	0.0700	10.00	1.00E-06	1.880	0.214	13066
215	Ho (1984)	0.00389	0.3	0.019	0.695	0.0700	10.00	1.00E-06	1.880	0.214	13066
216	Ho (1984)	0.00504	0.3	0.022	0.762	0.0700	10.00	1.00E-06	2.200	0.208	16764
217	Ho (1984)	0.00143	0.3	0.011	0.434	0.1000	10.00	1.00E-06	1.120	0.467	4861
218	Ho (1984)	0.00168	0.3	0.012	0.466	0.1000	10.00	1.00E-06	1.200	0.434	5592
219	Ho (1984)	0.00187	0.3	0.013	0.481	0.1000	10.00	1.00E-06	1.300	0.441	6253
220	Ho (1984)	0.00207	0.3	0.014	0.511	0.1000	10.00	1.00E-06	1.350	0.406	6899
221	Ho (1984)	0.00295	0.3	0.016	0.635	0.1000	10.00	1.00E-06	1.550	0.302	9843
222	Ho (1984)	0.00292	0.3	0.016	0.628	0.1000	10.00	1.00E-06	1.550	0.308	9734
223	Ho (1984)	0.00335	0.3	0.016	0.683	0.1000	10.00	1.00E-06	1.640	0.276	11195
224	Ho (1984)	0.00353	0.3	0.017	0.697	0.1000	10.00	1.00E-06	1.680	0.271	11710
225	Ho (1984)	0.00317	0.3	0.021	0.510	0.0700	15.00	1.00E-06	1.380	0.437	10563

S/N	Investigator	Q	B	H_s	U_s	S	D	ν	H_s/D	f	Re
-	-	*m^3/s*	*m*	*m*	*m/s*	-	*mm*	*m^2/s*	-	-	-
226	Ho (1984)	0.00419	0.3	0.025	0.576	0.0700	15.00	1.00E-06	1.633	0.406	14107
227	Ho (1984)	0.00503	0.3	0.028	0.611	0.0700	15.00	1.00E-06	1.833	0.405	16789
228	Ho (1984)	0.00537	0.3	0.027	0.664	0.0700	15.00	1.00E-06	1.800	0.337	17917
229	Ho (1984)	0.00711	0.3	0.032	0.764	0.0700	15.00	1.00E-06	2.133	0.301	24461
230	Ho (1984)	0.00746	0.3	0.034	0.779	0.0700	15.00	1.00E-06	2.267	0.308	26469
231	Ho (1984)	0.00848	0.3	0.034	0.837	0.0700	15.00	1.00E-06	2.267	0.266	28465
232	Ho (1984)	0.00949	0.3	0.035	0.904	0.0700	15.00	1.00E-06	2.327	0.235	31550
233	Ho (1984)	0.00261	0.3	0.017	0.512	0.1000	15.00	1.00E-06	1.133	0.509	8704
234	Ho (1984)	0.00308	0.3	0.019	0.546	0.1000	15.00	1.00E-06	1.253	0.495	10265
235	Ho (1984)	0.00348	0.3	0.019	0.592	0.1000	15.00	1.00E-06	1.293	0.434	11485
236	Ho (1984)	0.00405	0.3	0.022	0.629	0.1000	15.00	1.00E-06	1.433	0.426	13524
237	Ho (1984)	0.00462	0.3	0.023	0.673	0.1000	15.00	1.00E-06	1.533	0.399	15479
238	Ho (1984)	0.00499	0.3	0.024	0.687	0.1000	15.00	1.00E-06	1.613	0.402	16625
239	Ho (1984)	0.00627	0.3	0.027	0.781	0.1000	15.00	1.00E-06	1.780	0.344	20853
240	Ho (1984)	0.00721	0.3	0.028	0.856	0.1000	15.00	1.00E-06	1.867	0.300	23968
241	Recking 2006	0.00030	0.1	0.011	0.280	0.0100	2.30	1.12E-06	4.652	0.107	2681
242	Recking 2006	0.00040	0.1	0.013	0.308	0.0100	2.30	1.15E-06	5.652	0.108	3488
243	Recking 2006	0.00050	0.1	0.015	0.336	0.0100	2.30	1.17E-06	6.478	0.104	4279
244	Recking 2006	0.00060	0.1	0.016	0.370	0.0100	2.30	1.17E-06	7.043	0.093	5126
245	Recking 2006	0.00070	0.1	0.018	0.393	0.0100	2.30	1.19E-06	7.739	0.090	5895
246	Recking 2006	0.00080	0.1	0.019	0.412	0.0100	2.30	1.20E-06	8.435	0.090	6655
247	Recking 2006	0.00090	0.1	0.021	0.433	0.0100	2.30	1.21E-06	9.043	0.087	7422
248	Recking 2006	0.00100	0.1	0.022	0.455	0.0100	2.30	1.22E-06	9.565	0.084	8197
249	Recking 2006	0.00040	0.1	0.011	0.374	0.0200	2.30	1.13E-06	4.652	0.120	3531
250	Recking 2006	0.00050	0.1	0.012	0.413	0.0200	2.30	1.15E-06	5.261	0.111	4359

S/N	Investigator	Q	B	H_s	U_s	S	D	ν	H_s/D	f	Re
-	-	m^3/s	m	m	m/s	-	mm	m^2/s	-	-	-
251	Recking 2006	0.00060	0.1	0.014	0.435	0.0200	2.30	1.17E-06	6.000	0.115	5128
252	Recking 2006	0.00080	0.1	0.017	0.471	0.0200	2.30	1.22E-06	7.391	0.120	6582
253	Recking 2006	0.00200	0.25	0.019	0.421	0.0100	2.30	1.09E-06	8.261	0.084	7342
254	Recking 2006	0.00030	0.1	0.012	0.242	0.0100	4.90	1.17E-06	2.531	0.166	2564
255	Recking 2006	0.00040	0.1	0.015	0.263	0.0100	4.90	1.21E-06	3.102	0.172	3305
256	Recking 2006	0.00050	0.1	0.017	0.299	0.0100	4.90	1.22E-06	3.408	0.146	4099
257	Recking 2006	0.00070	0.1	0.021	0.337	0.0100	4.90	1.27E-06	4.245	0.144	5502
258	Recking 2006	0.00100	0.1	0.026	0.392	0.0100	4.90	1.32E-06	5.204	0.130	7560
259	Recking 2006	0.00120	0.1	0.028	0.423	0.0100	4.90	1.35E-06	5.796	0.125	8883
260	Recking 2006	0.00140	0.1	0.031	0.449	0.0100	4.90	1.38E-06	6.367	0.122	10161
261	Recking 2006	0.00075	0.1	0.017	0.449	0.0200	4.90	1.22E-06	3.408	0.130	6162
262	Recking 2006	0.00098	0.1	0.020	0.488	0.0200	4.90	1.27E-06	4.102	0.133	7720
263	Recking 2006	0.00123	0.1	0.023	0.537	0.0200	4.90	1.30E-06	4.673	0.125	9487
264	Recking 2006	0.00148	0.1	0.026	0.571	0.0200	4.90	1.33E-06	5.286	0.124	11100
265	Recking 2006	0.00200	0.1	0.031	0.639	0.0200	4.90	1.39E-06	6.388	0.120	14350
266	Recking 2006	0.00080	0.1	0.017	0.460	0.0300	4.90	1.26E-06	3.551	0.194	6345
267	Recking 2006	0.00100	0.1	0.020	0.510	0.0300	4.90	1.29E-06	4.000	0.177	7769
268	Recking 2006	0.00120	0.1	0.022	0.541	0.0300	4.90	1.33E-06	4.531	0.179	9035
269	Recking 2006	0.00500	0.25	0.036	0.560	0.0100	4.90	1.18E-06	7.286	0.089	16948
270	Recking 2006	0.00030	0.1	0.016	0.194	0.0100	9.00	1.25E-06	1.722	0.325	2396
271	Recking 2006	0.00060	0.1	0.021	0.282	0.0100	9.00	1.31E-06	2.367	0.211	4564
272	Recking 2006	0.00100	0.1	0.028	0.357	0.0100	9.00	1.39E-06	3.111	0.172	7201
273	Recking 2006	0.00140	0.1	0.034	0.417	0.0100	9.00	1.44E-06	3.733	0.152	9704
274	Recking 2006	0.00030	0.1	0.012	0.250	0.0200	9.00	1.19E-06	1.333	0.301	2518
275	Recking 2006	0.00060	0.1	0.017	0.351	0.0200	9.00	1.26E-06	1.900	0.218	4756

S/N	Investigator	Q	B	H_s	U_s	S	D	ν	H_s/D	f	Re
-	-	m^3/s	m	m	m/s	-	mm	m^2/s	-	-	-
276	Recking 2006	0.00100	0.1	0.024	0.426	0.0200	9.00	1.35E-06	2.611	0.204	7394
277	Recking 2006	0.00160	0.1	0.030	0.542	0.0200	9.00	1.41E-06	3.278	0.157	11344
278	Recking 2006	0.00030	0.1	0.011	0.265	0.0300	9.00	1.19E-06	1.256	0.377	2522
279	Recking 2006	0.00060	0.1	0.015	0.395	0.0300	9.00	1.24E-06	1.689	0.230	4854
280	Recking 2006	0.00080	0.1	0.019	0.417	0.0300	9.00	1.31E-06	2.133	0.260	6112
281	Recking 2006	0.00100	0.1	0.021	0.476	0.0300	9.00	1.33E-06	2.333	0.218	7539
282	Recking 2006	0.00160	0.1	0.027	0.590	0.0300	9.00	1.40E-06	3.011	0.183	11408
283	Recking 2006	0.00150	0.1	0.026	0.579	0.0500	9.00	1.43E-06	2.878	0.303	10521
284	Recking 2006	0.00175	0.1	0.028	0.629	0.0500	9.00	1.45E-06	3.089	0.275	12056
285	Recking 2006	0.00200	0.1	0.031	0.649	0.0500	9.00	1.50E-06	3.422	0.287	13311
286	Recking 2006	0.00051	0.1	0.014	0.370	0.0500	9.00	1.24E-06	1.533	0.396	4113
287	Recking 2006	0.00071	0.1	0.016	0.455	0.0500	9.00	1.26E-06	1.733	0.296	5650
288	Recking 2006	0.00091	0.1	0.018	0.520	0.0500	9.00	1.28E-06	1.944	0.254	7097
289	Recking 2006	0.00110	0.1	0.021	0.534	0.0500	9.00	1.34E-06	2.289	0.283	8216
290	Cao 1985	0.01000	0.6	0.040	0.418	0.0300	22.20	1.12E-06	1.797	0.538	14844
291	Cao 1985	0.02000	0.6	0.052	0.645	0.0300	22.20	1.15E-06	2.329	0.293	28906
292	Cao 1985	0.02000	0.6	0.055	0.606	0.0300	22.20	1.17E-06	2.477	0.353	28605
293	Cao 1985	0.02000	0.6	0.049	0.680	0.0300	22.20	1.14E-06	2.207	0.249	29155
294	Cao 1985	0.03000	0.6	0.063	0.794	0.0300	22.20	1.18E-06	2.838	0.235	42318
295	Cao 1985	0.03000	0.6	0.060	0.833	0.0300	22.20	1.17E-06	2.703	0.203	42671
296	Cao 1985	0.04000	0.6	0.070	0.948	0.0300	22.20	1.20E-06	3.167	0.184	55726
297	Cao 1985	0.04000	0.6	0.069	0.966	0.0300	22.20	1.19E-06	3.108	0.174	55976
298	Cao 1985	0.04900	0.6	0.079	1.032	0.0300	22.20	1.22E-06	3.563	0.175	66768
299	Cao 1985	0.05000	0.6	0.078	1.068	0.0300	22.20	1.22E-06	3.514	0.161	68567
300	Cao 1985	0.01000	0.6	0.029	0.585	0.0500	22.20	1.08E-06	1.284	0.327	15381

S/N	Investigator	Q	B	H_s	U_s	S	D	ν	H_s/D	f	Re
-	-	m^3/s	m	m	m/s	-	mm	m^2/s	-	-	-
301	Cao 1985	0.01500	0.6	0.035	0.718	0.0500	22.20	1.10E-06	1.568	0.265	22666
302	Cao 1985	0.02000	0.6	0.048	0.699	0.0500	22.20	1.14E-06	2.149	0.383	29142
303	Cao 1985	0.03000	0.6	0.058	0.862	0.0500	22.20	1.17E-06	2.613	0.306	42597
304	Cao 1985	0.03000	0.6	0.049	1.027	0.0500	22.20	1.13E-06	2.194	0.181	44085
305	Cao 1985	0.03000	0.6	0.051	0.980	0.0500	22.20	1.15E-06	2.297	0.208	43649
306	Cao 1985	0.00700	0.6	0.022	0.535	0.0700	22.20	1.07E-06	0.982	0.418	10921
307	Cao 1985	0.01000	0.6	0.026	0.634	0.0700	22.20	1.08E-06	1.185	0.360	15400
308	Cao 1985	0.01300	0.6	0.034	0.632	0.0700	22.20	1.10E-06	1.545	0.472	19653
309	Cao 1985	0.01500	0.6	0.035	0.710	0.0700	22.20	1.11E-06	1.586	0.383	22575
310	Cao 1985	0.01500	0.6	0.033	0.758	0.0700	22.20	1.10E-06	1.486	0.316	22764
311	Cao 1985	0.01000	0.6	0.028	0.589	0.0900	22.20	1.09E-06	1.275	0.576	15309
312	Cao 1985	0.01200	0.6	0.030	0.667	0.0900	22.20	1.09E-06	1.351	0.477	18328
313	Cao 1985	0.01000	0.6	0.053	0.314	0.0100	44.30	1.16E-06	1.199	0.423	14379
314	Cao 1985	0.05000	0.6	0.126	0.663	0.0100	44.30	1.36E-06	2.837	0.224	61486
315	Cao 1985	0.05000	0.6	0.121	0.688	0.0100	44.30	1.34E-06	2.734	0.201	62189
316	Cao 1985	0.10000	0.6	0.179	0.929	0.0100	44.30	1.49E-06	4.050	0.163	112035
317	Cao 1985	0.10000	0.6	0.175	0.951	0.0100	44.30	1.47E-06	3.957	0.152	113408
318	Cao 1985	0.15000	0.6	0.220	1.136	0.0100	44.30	1.57E-06	4.968	0.134	158847
319	Cao 1985	0.20000	0.6	0.262	1.274	0.0100	44.30	1.67E-06	5.905	0.126	199542
320	Cao 1985	0.03000	0.6	0.069	0.723	0.0300	44.30	1.21E-06	1.562	0.312	41459
321	Cao 1985	0.03000	0.6	0.075	0.668	0.0300	44.30	1.23E-06	1.691	0.396	40730
322	Cao 1985	0.05000	0.6	0.086	0.971	0.0300	44.30	1.25E-06	1.937	0.214	66772
323	Cao 1985	0.05000	0.6	0.084	0.989	0.0300	44.30	1.24E-06	1.903	0.203	67307
324	Cao 1985	0.07000	0.6	0.101	1.161	0.0300	44.30	1.28E-06	2.269	0.176	90935
325	Cao 1985	0.09000	0.6	0.115	1.310	0.0300	44.30	1.31E-06	2.585	0.157	114069

S/N	Investigator	Q	B	H_s	U_s	S	D	ν	H_s/D	f	Re
-	-	m^3/s	m	m	m/s	-	mm	m^2/s	-	-	-
326	Cao 1985	0.11000	0.6	0.136	1.353	0.0300	44.30	1.38E-06	3.059	0.174	132745
327	Cao 1985	0.02000	0.6	0.048	0.702	0.0500	44.30	1.15E-06	1.072	0.378	29100
328	Cao 1985	0.03000	0.6	0.061	0.822	0.0500	44.30	1.18E-06	1.372	0.353	42282
329	Cao 1985	0.05000	0.6	0.086	0.974	0.0500	44.30	1.26E-06	1.932	0.354	66312
330	Cao 1985	0.03000	0.6	0.057	0.877	0.0700	44.30	1.17E-06	1.287	0.407	42576
331	Cao 1985	0.02500	0.6	0.044	0.958	0.0900	44.30	1.13E-06	0.982	0.335	36833
332	Cao 1985	0.03000	0.6	0.048	1.037	0.0900	44.30	1.14E-06	1.088	0.316	43781
333	Cao 1985	0.02000	0.6	0.066	0.506	0.0050	11.50	1.16E-06	5.730	0.101	28834
334	Cao 1985	0.03500	0.6	0.088	0.667	0.0050	11.50	1.19E-06	7.609	0.077	48860
335	Cao 1985	0.05000	0.6	0.110	0.756	0.0050	11.50	1.24E-06	9.583	0.076	66988
336	Cao 1985	0.02000	0.6	0.054	0.613	0.0100	11.50	1.13E-06	4.730	0.114	29390
337	Cao 1985	0.03000	0.6	0.068	0.732	0.0100	11.50	1.17E-06	5.939	0.100	42891
338	Cao 1985	0.04000	0.6	0.082	0.818	0.0100	11.50	1.20E-06	7.087	0.096	55702
339	Cao 1985	0.05000	0.6	0.092	0.904	0.0100	11.50	1.22E-06	8.017	0.089	68313
340	Graf & S. 1987	0.03900	0.6	0.084	0.774	0.0075	12.20	1.19E-06	6.885	0.083	54451
341	Graf & S. 1987	0.04400	0.6	0.093	0.789	0.0075	12.20	1.22E-06	7.615	0.088	60161
342	Graf & S. 1987	0.03900	0.6	0.077	0.844	0.0100	12.20	1.18E-06	6.311	0.085	55059
343	Graf & S. 1987	0.04800	0.6	0.089	0.899	0.0100	12.20	1.21E-06	7.295	0.086	66085
344	Graf & S. 1987	0.05900	0.6	0.100	0.983	0.0100	12.20	1.23E-06	8.197	0.081	79771
345	Paintal 1971	0.07079	0.914	0.096	0.807	0.0085	22.20	1.16E-06	4.324	0.098	66836
346	Paintal 1971	0.08500	0.914	0.105	0.884	0.0088	22.20	1.17E-06	4.739	0.093	79253
347	Paintal 1971	0.09911	0.914	0.114	0.949	0.0087	22.20	1.19E-06	5.149	0.087	91482
348	Paintal 1971	0.11043	0.914	0.125	0.967	0.0088	22.20	1.21E-06	5.631	0.093	100179
349	Paintal 1971	0.13025	0.914	0.132	1.080	0.0089	22.20	1.21E-06	5.946	0.079	117778
350	Paintal 1971	0.14158	0.914	0.147	1.057	0.0088	22.20	1.24E-06	6.604	0.090	124871

S/N	Investigator	Q	B	H_s	U_s	S	D	ν	H_s/D	f	Re
-	-	m^3/s	m	m	m/s	-	mm	m^2/s	-	-	-
351	Paintal 1971	0.15574	0.914	0.149	1.141	0.0089	22.20	1.24E-06	6.730	0.080	137550
352	Paintal 1971	0.16990	0.914	0.159	1.173	0.0091	22.20	1.25E-06	7.140	0.082	148150
353	Paintal 1971	0.18405	0.914	0.163	1.235	0.0092	22.20	1.26E-06	7.347	0.077	160058
354	Paintal 1971	0.19821	0.914	0.171	1.270	0.0092	22.20	1.27E-06	7.689	0.076	171046
355	Paintal 1971	0.21520	0.919	0.183	1.280	0.0091	22.20	1.29E-06	8.239	0.079	181618
356	Paintal 1971	0.22653	0.914	0.187	1.329	0.0091	22.20	1.29E-06	8.401	0.076	191525
357	Paintal 1971	0.02605	0.914	0.054	0.532	0.0047	7.95	1.07E-06	6.742	0.070	26529
358	Paintal 1971	0.03681	0.914	0.068	0.595	0.0049	7.95	1.10E-06	8.516	0.074	36645
359	Paintal 1971	0.02605	0.914	0.053	0.535	0.0049	7.95	1.15E-06	6.704	0.071	24825
360	Paintal 1971	0.04672	0.914	0.077	0.668	0.0045	7.95	1.10E-06	9.623	0.061	46314
361	Paintal 1971	0.02832	0.924	0.079	0.388	0.0021	7.95	1.11E-06	9.925	0.085	27493
362	CSU 1988	0.49525	3.6576	0.061	1.704	0.2000	104.14		0.585	0.324	
363	CSU 1988	0.61637	3.6576	0.067	2.018	0.2000	104.14		0.644	0.259	
364	CSU 1988	0.32290	3.6576	0.049	0.887	0.2000	129.54		0.376	0.976	
365	CSU 1988	0.74118	3.6576	0.079	1.990	0.2000	129.54		0.612	0.315	
366	CSU 1988	0.55100	3.6576	0.079	1.295	0.2000	157.48		0.503	0.743	
367	CSU 1988	0.56034	3.6576	0.070	1.500	0.2000	157.48		0.445	0.489	
368	CSU 1988	0.88013	3.6576	0.107	1.804	0.2000	157.48		0.677	0.514	
369	CSU 1988	0.15791	3.6576	0.030	1.052	0.2000	55.88		0.545	0.433	
370	CSU 1988	0.17122	3.6576	0.034	1.064	0.2000	55.88		0.600	0.465	
371	CSU 1988	0.69618	2.4384	0.198	1.628	0.0200	55.88		3.550	0.088	
372	CSU 1988	1.37538	2.4384	0.292	2.231	0.0200	55.88		5.231	0.066	
373	CSU 1988	1.23388	2.4384	0.282	2.063	0.0200	55.88		5.044	0.079	
374	CSU 1988	1.32727	2.4384	0.296	2.094	0.0200	55.88		5.293	0.081	
375	CSU 1988	1.49141	2.4384	0.324	2.158	0.0200	55.88		5.792	0.082	

S/N	Investigator	Q	B	H_s	U_s	S	D	ν	H_s/D	f	Re
-	-	*m^3/s*	*m*	*m*	*m/s*	-	*mm*	*m^2/s*	-	-	-
376	CSU 1988	1.60178	2.4384	0.348	2.155	0.0200	55.88		6.228	0.086	
377	CSU 1988	1.01880	2.4384	0.258	1.865	0.0200	55.88		4.608	0.091	
378	CSU 1988	0.28526	2.4384	0.111	1.192	0.0200	25.91		4.298	0.100	
379	CSU 1988	0.43016	2.4384	0.143	1.402	0.0200	25.91		5.507	0.093	
380	CSU 1988	0.51789	2.4384	0.164	1.484	0.0200	25.91		6.313	0.094	
381	CSU 1988	0.25187	2.4384	0.104	1.113	0.0200	25.91		4.030	0.111	
382	CSU 1988	0.24055	2.4384	0.108	1.049	0.0200	25.91		4.164	0.128	
383	CSU 1988	0.33960	2.4384	0.132	1.192	0.0200	25.91		5.104	0.121	
384	CSU 1988	0.42450	2.4384	0.150	1.326	0.0200	25.91		5.776	0.109	
385	CSU 1988	0.50374	2.4384	0.146	1.615	0.0200	25.91		5.642	0.070	
386	CSU 1988	0.33960	2.4384	0.118	1.344	0.0200	25.91		4.567	0.083	
387	CSU 1988	0.42450	2.4384	0.139	1.445	0.0200	25.91		5.373	0.085	
388	CSU 1988	0.50657	2.4384	0.146	1.637	0.0200	25.91		5.642	0.069	
389	CSU 1988	0.28300	2.4384	0.143	0.936	0.0100	25.91		5.507	0.101	
390	CSU 1988	0.33960	2.4384	0.164	0.981	0.0100	25.91		6.313	0.104	
391	CSU 1988	0.07641	2.4384	0.028	1.250	0.1000	25.91		1.075	0.127	
392	CSU 1988	0.07018	2.4384	0.038	0.866	0.1000	25.91		1.478	0.339	
393	CSU 1988	0.09481	2.4384	0.049	0.908	0.1000	25.91		1.881	0.415	
394	CSU 1988	0.25470	2.4384	0.080	1.570	0.1000	55.88		1.432	0.234	
395	CSU 1988	0.28300	2.4384	0.087	1.524	0.1000	55.88		1.557	0.224	
396	Manes 2011		0.4	0.050			10.00		5.000	0.041	
397	Manes 2011		0.4	0.050			10.00		5.000	0.057	
398	Manes 2011		0.4	0.050			10.00		5.000	0.072	
399	Manes 2011		0.4	0.050			10.00		5.000	0.072	
400	Manes 2011		0.4	0.050			10.00		5.000	0.073	

S/N	Investigator	Q	B	H_s	U_s	S	D	ν	H_s/D	f	Re
-	-	m^3/s	m	m	m/s	-	mm	m^2/s	-	-	-
401	Manes 2011		0.4	0.050			10.00		5.000	0.080	
402	Manes 2011		0.4	0.060			10.00		6.000	0.028	
403	Manes 2011		0.4	0.060			10.00		6.000	0.044	
404	Manes 2011		0.4	0.060			10.00		6.000	0.060	
405	Manes 2011		0.4	0.060			10.00		6.000	0.066	
406	Manes 2011		0.4	0.060			10.00		6.000	0.068	
407	Manes 2011		0.4	0.060			10.00		6.000	0.068	
408	Manes 2011		0.4	0.060			10.00		6.000	0.073	
409	Manes 2011		0.4	0.080			10.00		8.000	0.031	
410	Manes 2011		0.4	0.080			10.00		8.000	0.042	
411	Manes 2011		0.4	0.080			10.00		8.000	0.047	
412	Manes 2011		0.4	0.080			10.00		8.000	0.049	
413	Manes 2011		0.4	0.080			10.00		8.000	0.053	
414	Manes 2011		0.4	0.080			10.00		8.000	0.057	
415	Manes 2011		0.4	0.080			10.00		8.000	0.059	
416	Zagni & S. 1976								5.800	0.035	
417	Zagni & S. 1976								5.900	0.035	
418	Zagni & S. 1976								8.700	0.041	
419	Zagni & S. 1976								5.900	0.068	
420	Zagni & S. 1976								6.000	0.051	
421	Zagni & S. 1976								6.000	0.050	
422	Zagni & S. 1976								6.000	0.032	
423	Zagni & S. 1976								8.100	0.044	
424	Zagni & S. 1976								8.900	0.044	
425	Zagni & S. 1976								8.900	0.028	

S/N	Investigator	Q	B	H_s	U_s	S	D	ν	H_s/D	f	Re
-	-	m^3/s	m	m	m/s	-	mm	m^2/s	-	-	-
426	Gupta 1985								2.850	0.398	
427	Gupta 1985								2.850	0.274	
428	Gupta 1985								2.850	0.208	
429	Gupta 1985								2.850	0.228	
430	Gupta 1985								2.850	0.302	
431	Gupta 1985								3.500	0.097	
432	Gupta 1985								3.500	0.164	
433	Gupta 1985								3.500	0.150	
434	Gupta 1985								3.500	0.149	
435	Gupta 1985								3.500	0.199	
436	Gupta 1985								3.500	0.226	
437	Gupta 1985								3.500	0.249	
438	Gupta 1985								4.500	0.136	
439	Gupta 1985								4.500	0.080	
440	Gupta 1985								4.500	0.114	
441	Gupta 1985								4.500	0.109	
442	Gupta 1985								4.500	0.119	
443	Gupta 1985								4.500	0.138	
444	Gupta 1985								4.500	0.194	
445	Gupta 1985								4.500	0.178	
446	Gupta 1985								5.500	0.070	
447	Gupta 1985								5.500	0.130	
448	Gupta 1985								5.500	0.074	
449	Gupta 1985								5.500	0.090	
450	Gupta 1985								5.500	0.098	

S/N	Investigator	Q	B	H_s	U_s	S	D	ν	H_s/D	f	Re
-	-	m^3/s	m	m	m/s	-	mm	m^2/s	-	-	-
451	Gupta 1985								5.500	0.120	
452	Gupta 1985								5.500	0.152	
453	Gupta 1985								5.500	0.151	
454	Gupta 1985								7.000	0.072	
455	Gupta 1985								7.000	0.060	
456	Gupta 1985								7.000	0.094	
457	Gupta 1985								7.000	0.081	
458	Gupta 1985								7.000	0.073	
459	Gupta 1985								7.000	0.084	
460	Gupta 1985								7.000	0.090	
461	Gupta 1985								7.000	0.139	
462	Gupta 1985								7.000	0.109	